Anna Regoutz

Structural and Electronic Properties of Metal Oxides

A thesis submitted in partial fulfilment of the requirements for the degree of Doctor of Philosophy at the University of Oxford



Inorganic Chemistry Laboratory
Department of Chemistry
University of Oxford
and
Trinity College

Hilary Term 2014

Für Mama, Papa und Steffi

Abstract

Structural and Electronic Properties of Metal Oxides
Anna Regoutz, Trinity College
DPhil
Hilary 2014

Metal oxides are of immense technological importance. Their wide variety of structural and electronic characteristics leads to a flexibility unrivalled by other groups of materials. However, there is still much debate about the fundamental properties of some of the most widely used oxides, including TiO_2 and In_2O_3. This work presents high quality, in-depth characterisation of these two oxides in pure and doped form, including soft and hard X-ray photoelectron spectroscopy and X-ray diffraction. Bulk samples as well as thin film samples were prepared analysed. For the preparation of thin films a high quality sol-gel dip-coating method was developed, which resulted in epitaxial films.

In more detail the organisation of the thesis is as follows: Chapter 1 provides an introduction to key ideas related to metal oxides and presents the metal oxides investigated in this thesis, In_2O_3, Ga_2O_3, Tl_2O_3, TiO_2, and SnO_2. Chapter 2 presents background information and Chapter 3 gives the practical details of the experimental techniques employed.

Chapters 4 presents reciprocal space maps of MBE-grown In_2O_3 thin films and nanorods on YSZ substrates. Chapters 5 and 6 investigate the doping of In_2O_3 bulk samples with gallium and thallium and introduce a range of solid state characterisation techniques. Chapter 7 describes the development of a dip-coating sol-gel method for the growth of thin films of TiO_2 and shows 3D reciprocal space maps of the resulting films. Chapter 8 concerns hard x-ray photoelectron spectroscopy of undoped and Sn-doped TiO_2. Chapter 9 interconnects previous chapters by presenting 2D reciprocal space maps of nano structured epitaxial samples of In_2O_3 grown by the newly developed sol-gel based method. Chapter 10 concludes this thesis with a summary of the results.

Keywords: metal oxides, transparent conducting oxides, photocatalysis, X-ray diffraction, reciprocal space mapping, X-ray photoelectron spectroscopy, sol-gel

Acknowledgements

Foremost I would like to thank my supervisor Professor Russell G. Egdell for his guidance, encouragement and friendship throughout my doctorate and the entire process of completing this thesis.

Secondly, I would like to thank Dave, Hongliang, Freddy and Geoff for their help and all the good times we had in the basement. I am also utterly grateful for starting my DPhil at the same time as the best Part IIs imaginable, Debs and Wanzhen.

I would also like to thank all my collaborators who have contributed to the results presented in this thesis. Dr. Didier Wermeille at the ESRF and Dr. Steve Collins at Diamond for their help with the complex reciprocal space mapping experiments. David Hesp for his support at Diamond. The SPring-8 team, Ku-Ding Tsuei, Stefano Agrestini, Yuki Utsumi, and Liu Hao Tjeng, for their support with the HAXPES measurements. Dr. Danny Law at NCESS Daresbury, Dr. David Morgan at Cardiff University, and Dr. Robert Palgrave at University College London for helping with XPS measurements and Prof. Giancarlo Panaccione and Dr. Francesco Borgatti for bearing with my rudimentary Italian and the intense discussions on HAXPES. Dr. David Scanlon for his calculations and for making me work with thallium, and Prof. Graeme Watson for his calculations on TiO_2. Finally, Joe Paddison for his Fortran code.

I will always be grateful for the many happy moments I shared with members of my College, especially during my two years as MCR President. I am immensely grateful to Kevin for his "cheerful" words and the financial support he made possible. Special thanks have to go to Caitlin, Amanda, Julia, Marc, Ben, Jonathan, Harry, Lina & Dave, Richard, and the Jeune Street chemists, to name but a few. You, the frequent G&Ts, and many cups of Starbucks have kept me sane and made Trinity College a home.

Finally, I wish to thank my family. My parents, Christine and Egon, have to receive special thanks for their love and support and without them this thesis would not exist. Further thanks go to my uncle and aunt, Harald and Gerda, who supported me financially throughout my time at Oxford. I am immensely grateful for Nat's patience and acceptance of my workaholic traits and overpowering enthusiasm for all things chemistry. And last but not least, I wish to thank my sister, whose unfiltered honesty was what I needed when everything seemed a bit to surreal.

Anna Regoutz

Oxford, 2014

Publications in blue are from work directly contributing to this thesis.

1. **Determination of the Poisson ratio of (001) and (111) oriented thin films of In_2O_3 by synchrotron-based x-ray diffraction.**

   K. H. L. Zhang, A. Regoutz, R. G. Palgrave, D. J. Payne, R. G. Egdell, A. Walsh, S. P. Collins, D. Wermeille, and R. A. Cowley, *Physical Review B* **84**, 233301, 2011.

2. **A study of (111) oriented epitaxial thin films of In_2O_3 on cubic Y-doped ZrO_2 by synchrotron-based x-ray diffraction.**

   A. Regoutz, K. H. L. Zhang, R. G. Egdell, D. Wermeille, and R. A. Cowley, *Journal of Materials Research* **27**, 2257, 2012.

3. **Growth of epitaxial anatase nano islands on $SrTiO_3$(001) by dip coating.**

   F. Oropeza, K. H. L. Zhang, A. Regoutz, V. K. Lazarov, D. Wermeille, C. G. Poll, and R. G. Egdell, *Crystal Growth & Design* **13**, 1438, 2013.

4. **Strain and tilt during epitaxial growth of highly ordered In_2O_3 nanorods.**

   A. Regoutz, R. G. Egdell, D. Wermeille, R. A. Cowley, and K. H. L. Zhang, *Nanoscale* **5**, 7445, 2013.

5. **Electronic structure of epitaxial Sn-doped anatase grown on $SrTiO_3$ (001) by dip coating.**

   F. E. Oropeza, K. H. L. Zhang, R. G. Palgrave, A. Regoutz, and R. G. Egdell, *The Journal of Physical Chemistry C* **117**, 15221, 2013.

6. **Band gap engineering of In_2O_3 by alloying with Tl_2O_3.**

   D. O. Scanlon, A. Regoutz, R. G. Egdell, D. J. Morgan, and G. W. Watson, *Applied Physics Letters* **103**, 262108, 2013.

7. **Understanding the electronic structure of IrO_2 using hard X-ray photoelectron spectroscopy and density functional theory.**

   J. M. Kahk, C. G. Poll, F. E. Oropeza, J. M. Ablett, D. Colin, J-P. Rueff, S. Agrestini, Y. Utsumi, K. D. Tsuei, Y. F. Liao, F. Borgatti, G. Panaccione, A. Regoutz, R. G. Egdell, B. J. Morgan, D. O. Scanlon, and D. J. Payne, *Physical Review Letters*, in press.

8. **Electronic and surface properties of Ga-doped In_2O_3 ceramics.**

   A. Regoutz, D. J. Morgan, R. G. Palgrave, H. Telles-Lozano, S. J. Skinner, D. J. Payne, D. O. Scanlon, G. W. Watson, and R. G. Egdell, *Applied Physics Letters*, in preparation.

9. **A study of anatase thin films by synchrotron based X-ray diffraction.**

   A. Regoutz, D. Wermeille, C. Poll, F. Oropeza, and R. G. Egdell, in preparation.

10. **Polarisation dependence in hard X-ray photoemission of Sn-doped anatase.**

    A. Regoutz, G. Panaccione, F. Borgatti, K.-D. Tsuei, S. Agrestini, Y. Utsumi, L. H. Tjeng, C. Poll, D. Payne, and R. G. Egdell, in preparation.

Science is a way of trying not to fool yourself.
The first principle is that you must not fool yourself,
and you are the easiest person to fool.

Richard P. Feynman

Contents

1 Introduction to Metal Oxides **1**

1.1 Metal Oxides - Importance and Challenges 1

1.2 Electronic Structure of Metal Oxides 1

1.2.1 Ionic Model 2

1.2.2 Band Theory of Crystalline Solids 4

1.3 Crystal Structure of Metal Oxides 9

1.3.1 In_2O_3 9

1.3.2 Ga_2O_3 11

1.3.3 Tl_2O_3 13

1.3.4 TiO_2 15

1.3.5 SnO_2 18

1.4 Technological Importance of Metal Oxides 19

1.4.1 Transparent Conducting Oxides 19

1.4.2 Photocatalysis in Transition Metal Oxides 22

1.5 Scope and Organisation of this Thesis 23

1.6 References 24

2 Background to Experimental Techniques **31**

2.1 Molecular Beam Epitaxy 31

2.1.1 Principles 32

2.1.2 Instrumentation 33
2.2 Sol-Gel Dip-Coating 34
2.2.1 Principles 35
2.2.2 Instrumentation 35
2.3 X-Ray Diffraction 36
2.3.1 Principles and Theoretical Considerations 37
2.3.1.1 Reciprocal Space 38
2.3.1.2 Absences and the Structure Factor 39
2.3.2 Instrumentation 40
2.3.2.1 Four-Circle Diffractometers 41
2.4 X-Ray Photoelectron Spectroscopy 42
2.4.1 Principles and Theoretical Considerations 43
2.4.1.1 Inelastic Mean Free Path 44
2.4.1.2 Chemical Shift 45
2.4.1.3 Spin-orbit Splitting 46
2.4.2 Photoionisation Cross Section 47
2.4.3 Instrumentation 50
2.4.4 Hard X-ray Photoemission Spectroscopy (HAXPES) 51
2.4.4.1 Polarisation Dependent Cross Sections 52
2.5 Diffuse Reflectance Spectroscopy (DRS) 53
2.5.1 The Kubelka-Munk Theory 54
2.5.2 Instrumentation 55
2.6 Raman Spectroscopy 56
2.6.1 Principles and Theoretical Considerations 56
2.6.2 Instrumentation 58
2.7 Low Energy Ion Scattering 59
2.7.1 Principles 59

2.7.2 Instrumentation 60
2.8 Atomic Force Microscopy 61
2.8.1 Principles 61
2.8.2 Instrumentation 63
2.9 Ellipsometry 63
2.9.1 Principles 64
2.9.2 Instrumentation 64
2.10 References 66

3 Experimental Apparatus and Techniques 68

3.1 Molecular Beam Epitaxy 68
3.2 Sol-Gel Dip-Coating 69
3.3 X-Ray Diffraction 70
3.3.1 XMaS, Beam Line BM28, European Synchrotron Radiation Facility (ESRF), Grenoble, France 71
3.3.2 Beam Line I16, Diamond Light Source (DLS), Rutherford-Appleton Laboratory, Harwell, UK 72
3.4 X-Ray Photoelectron Spectroscopy 73
3.4.1 Scienta ESCA 300 Spectrometer, Daresbury Laboratory, UK . 73
3.4.2 Kratos Axis Ultra-DLD, Cardiff University, UK 75
3.4.3 Thermo Scientific K-Alpha, University College London, UK . 76
3.4.4 Beam Line BL12XU, SPring-8, Hyogo, Japan 76
3.5 Diffuse Reflectance Spectroscopy (DRS) 77
3.6 Raman Spectroscopy 78
3.7 Low Energy Ion Scattering (LEIS) 78
3.8 Atomic Force Miscroscopy 79
3.9 Ellipsometry 79
3.10 References 81

4 Reciprocal Space Mapping of In_2O_3 on Y-doped ZrO_2 (111) and (110) 82

4.1 Introduction . . . 82

4.2 Experimental . . . 84

4.3 Thin films of In_2O_3 on Y-doped ZrO_2 (111) . . . 85

4.4 In_2O_3 Nanorods on Y-doped ZrO_2 (110) . . . 96

4.5 Concluding Remarks . . . 109

4.6 References . . . 110

5 Electronic and Surface Properties of Ga-doped In_2O_3 Ceramics 113

5.1 Introduction . . . 113

5.2 Experimental . . . 116

5.3 Computational Methods . . . 117

5.4 Results and Discussion . . . 117

5.4.1 Solubility Limit of Ga in In_2O_3 and Changes in Crystal Structure 117

5.4.2 Band Gaps from Diffuse Reflectance Spectroscopy . . . 125

5.4.3 Band Gaps from Valence Band X-ray Photoemission Spectroscopy . . . 128

5.4.4 Core-level X-ray Photoemission Spectroscopy and Gallium Surface Segregation . . . 133

5.4.5 Influence of Ion Bombardment on Valence and Core Level XPS of Ga_2O_3 . . . 138

5.4.6 Surface Atomic Composition from Low Energy Ion Scattering (LEIS) . . . 141

5.5 Concluding Remarks . . . 145

5.6 References . . . 147

6 Electronic and Surface Properties of Tl-doped In_2O_3 Ceramics 153

6.1 Introduction . . . 153

6.2 Experimental . . . 154
6.3 Results and Discussion . . . 155
6.3.1 Calculations . . . 155
6.3.2 Surface versus Bulk Incorporation of Thallium . . . 156
6.3.3 Valence Band X-ray Photoemission Spectroscopy . . . 159
6.3.4 Influence of Ion Bombardment on Valence and Core Levels XPS of Tl-doped In_2O_3 . . . 161
6.3.5 Concluding Remarks . . . 163
6.4 References . . . 164

7 A Sol-Gel Approach to Growth of High Quality TiO_2 Thin Films 165
7.1 Introduction . . . 165
7.2 Experimental . . . 168
7.3 Results and Discussion . . . 171
7.3.1 Exploratory Setup . . . 171
7.3.2 High Quality Thin Films of TiO_2 on $SrTiO_3$ (001) . . . 174
7.3.3 Reciprocal Space Mapping of TiO_2 Thin Films . . . 180
7.3.4 Influence of Temperature on Thin Films Probed by Synchrotron Based Diffraction . . . 185
7.3.5 Influence of the Substrate on Thin Films of TiO_2 . . . 189
7.3.6 The Effect of Sn-Doping on TiO_2 Thin Films . . . 193
7.4 Concluding Remarks . . . 194
7.5 References . . . 196

8 Hard X-Ray Photoemission Spectroscopy of TiO_2 and Sn-doped TiO_2 Thin Films 199
8.1 Introduction . . . 199
8.2 Experimental . . . 201

8.3 Computational 202
8.4 Results and Discussion 203
8.4.1 Core Level Spectra 203
8.4.2 Satellites in the Ti $2p$ and O $1s$ Core Levels 209
8.4.3 Valence Band Spectra 215
8.4.4 Polarisation in Valence Band Spectra 217
8.5 Concluding Remarks 222
8.6 References 224

9 A Sol-Gel Approach to Growth of In_2O_3 Thin Films 228

9.1 Introduction 228
9.2 Experimental 229
9.3 Results and Discussion 230
9.3.1 Influence of the Substrate on Surface Morphology of Thin Films of In_2O_3 230
9.3.2 Reciprocal Space Maps of Thin Films Grown on YSZ (110) . . 231
9.3.3 Reciprocal Space Maps of Thin Films Grown on YSZ (100) . . 237
9.4 Concluding Remarks 238

10 Conclusions 240

10.1 References 243

1 Introduction to Metal Oxides

1.1 Metal Oxides - Importance and Challenges

Metal oxides exhibit a diverse range of electronic properties, extending across insulators, semiconductors, metallic conductors, and superconductors. Their technological importance is enormous. However, the underlying basic electronic and structural characteristics are still the source of much discussion and in some cases controversy.

This introduction gives an overview of the electronic and structural characteristics of the metal oxide systems investigated in this thesis, with a particular focus on In_2O_3 and TiO_2, and gives an overview of their technological importance and possible applications. It concludes with a summary of the scope and organisation of the present work.

1.2 Electronic Structure of Metal Oxides

The general electronic structure of metal oxides can be understood at different levels using a variety of models. This introduction will focus on the simple ionic model and band theory, which can explain the behaviour of metal oxides in a transparent and practical fashion.

1.2.1 Ionic Model

The ionic model is based on the assumption that the metal-oxygen (M-O) bond is predominantly ionic and can be rationalised by the transfer of electrons from the metal ion to the oxygen. It predicts that for a main group metal oxide, the valence band (VB) will be made up by the highest occupied O level, and the conduction band (CB) will be made up by the lowest unoccupied metal level.

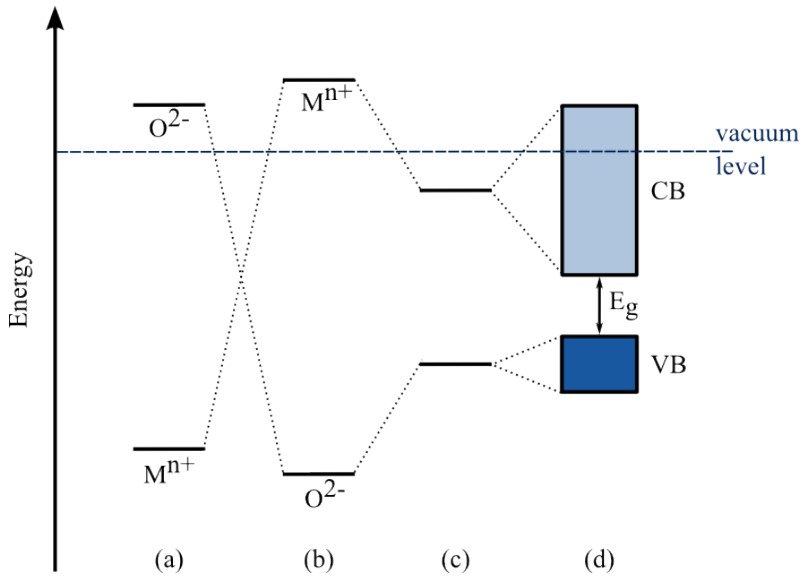


Figure 1.1: Ionic model for metal oxides, showing (a) the free ions and the successive corrections for (b) the Madelung potential, (c) the polarisation, and (d) the orbital overlap.

Starting from this premise, the free ion metal cation levels M^{n+} lie below the oxygen anion O^{2-} level, because O^{2-} is not stable in the gas phase (see figure 1.1(a)). This ordering of levels differs from that of the free atoms M and O because of the positive and negative charges. To correct this, the Madelung potential V_M is applied. It describes the electrostatic potential between an ion and its surrounding ions of opposite charge. As V_M stabilises the O^{2-} and destabilises the M^{n+} level, it changes the ordering of levels, see figure 1.1(b). In a next step polarisation is added,

which takes account of deviation from perfectly ionic behaviour. This increases the energy of the occupied O levels and decreases the energy of the unoccupied M levels (see figure 1.1(c)). In a last step interactions between metal and oxygen orbitals are taken into consideration, which gives rise to non-vanishing band widths (see figure 1.1(d)). Valence and conduction band are now separated by a band gap E_g.

In summary, the valence band in metal oxides is dominated by O $2p$ orbitals, and is separated by a band gap from a conduction band dominated by metal orbitals. In post-transition metal oxides, such as In_2O_3, the energy of the O $2p$ orbitals lies much closer to the metal s and p orbitals than in pre-transition metal main group oxides, leading to increased hybridization and deviation from a purely ionic description.

Transition metal oxides can be described by the ionic model, with the difference that in main group metals the lowest unoccupied metal level is usually an s orbital, whereas in transition metals the d orbitals are lower in energy. In addition, the d-band is split by ligand field effects, which have their origin in the interaction between the d-orbitals of the metal and its surrounding ligands. d orbitals that point directly at a ligand undergo σ interactions, which are much stronger than the π interactions experienced by d orbitals pointing between ligands. This difference represents the main contribution to the ligand field splitting. The form of the splitting depends on the geometry of the ligands around the metal centre. In octahedral coordination, which is found for TiO_2, two separate bands form. The band at lower energy consists of three d orbitals, xy, xz, yz, of t_{2g} symmetry, and the higher energy band consists of the remaining two d orbitals, $3z^2 - (x^2 + y^2 + z^2)$ (often called z^2) and $x^2 - y^2$, of e_g symmetry. Figure 1.2 shows a schematic of the ligand field splitting Δ for octahedral coordination.

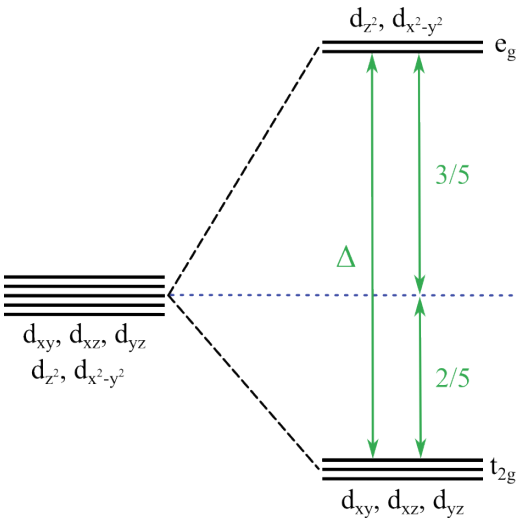


Figure 1.2: d orbital ligand field splitting Δ in case of octahedral coordination.

1.2.2 Band Theory of Crystalline Solids

The ionic model predicts a band like structure in oxides, with a valence and a conduction band separated by a band gap E_g. The highest occupied molecular orbital (HOMO) is situated at the top of the valence band (VB) and the lowest unoccupied molecular orbital (LUMO) is at the bottom of the conduction band (CB). In order to gain a deeper understanding of the band structure, one has to look at the orbitals in a crystal which form the different bands.

One of the most important characteristics of a crystal is its periodicity. Due to the ordering in crystalline solids, they can be described by simple Bloch functions $\psi(x)$ of the form:

$$\psi(x) = e^{ikx}u(x) \ , \tag{1.1}$$

where $u(x)$ is a periodic function describing the orbitals and e^{ikx} is a plane wave describing free electrons. k is called the wave vector and plots of energy versus k for the valence and conduction bands give the band structure diagram of a solid. The

region of k-space used in such plots for one dimension is usually $-\pi/a \leq k < \pi/a$, where a is the lattice parameter. This is known as the first Brillouin zone.

A linear combination of atomic orbitals (LCAO) approach can be used to extend the idea of Bloch functions from a general form to a band composed of overlapping orbitals. Consider the band structure in one dimension, starting from the assumption that each atom in a linear chain of atoms only has one s orbital in its valence band, Bloch sums of atomic orbitals can be formulated as follows. A crystal orbital $\psi(x)$ can be described by:

$$\psi(x) = \sum_n c_n \chi_n(x) \ , \tag{1.2}$$

where n is the number of an atom, χ_n is the wave function of an atomic orbital of one of the n atoms, and c_n are coefficients which, using Bloch's theorem, can be described by:

$$c_n = e^{ikna} \ , \tag{1.3}$$

where a is the lattice spacing.

This approach using Bloch sums can be extended to other orbitals in the valence band. In the case of p orbitals, σ and π interactions can take place depending on the orientation of the orbital relative to the wave vector k. Figure 1.3 shows groups of p orbitals oriented in bonding and anti-bonding fashion perpendicular or parallel to the wave vector k.

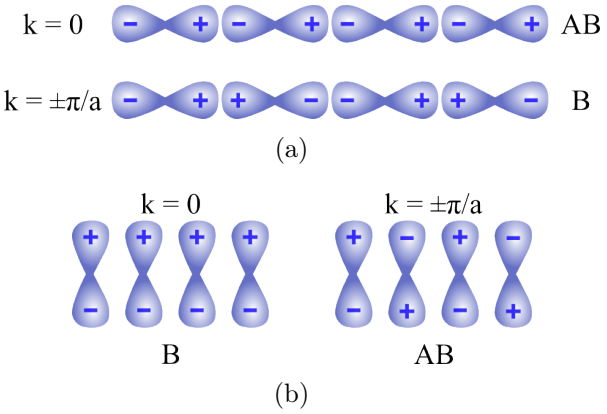


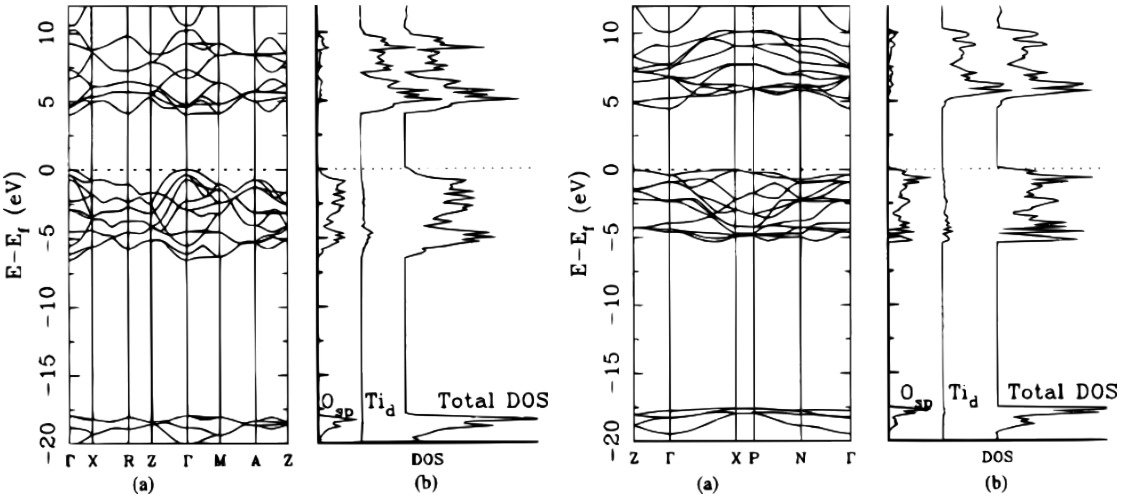
Figure 1.3: p orbitals oriented (a) parallel (σ-bonding) and (b) perpendicular (π-bonding) to the wave vector k. In both cases a bonding B and an antibonding AB state exist.

The situation in two- and three-dimensional crystals is more complicated than in the simple model presented here. Each orbital is still described by a Bloch function, but the Brillouin zone now extends over three dimensions. High symmetry points are indexed using Greek capitals, with the centre $k = (000)$ always being denoted as Γ. Instead of showing energy levels for all k, typical band structures show the change in energy along restricted high symmetry directions in the Brillouin zone.

The molecular orbitals forming bands in solids are very closely spaced with their density varying across the bands. This is expressed by the density of states (DOS). The DOS is defined as the number of allowed energy levels per unit volume over an energy range. The DOS is zero in the band gap.

In band theory the band gap E_g is a fundamental characteristic of a material. The gap is called direct if the valence band maximum (VBM) and conduction band minimum (CBM) are both found at the same point in reciprocal space, most usually the Γ point. The gap is indirect if the CBM and VBM are at different points in k space. Figure 1.4 shows the calculated band structures of rutile and anatase illustrating the difference between a direct and an indirect band gap. Rutile has a direct band gap with the VBM and CBM both being at the centre of the Brillouin

zone Γ. Anatase shows an indirect band gap with CBM and VBM being at different symmetry points. However, the band gap of anatase has been considered as approximately direct due to the energy levels at Γ being only less than 0.2 eV lower than the VBM.



(a) Rutile (b) Anatase

Figure 1.4: Band structures and density of states for (a) the rutile and (b) the anatase polymorph of TiO_2. Adapted from F. Labat *et al.*[1]

Table 1.1 summarises the band gaps of a number of polymorphs of the metal oxides investigated in this thesis.

Table 1.1: Band gaps E_g for the metal oxides investigated in this thesis.

oxide	polymorph	E_g / eV	type
In_2O_3	cubic bixbyite	2.93[2]	direct forbidden
	corundum	3.02[2]	direct forbidden
Ga_2O_3	α	5.08[3]	direct
	β	5.03[3]	indirect
Tl_2O_3	cubic bixbyite	0.33[4]	direct
TiO_2	rutile	3.03[5]	direct forbidden
	anatase	3.20[5]	indirect
SnO_2	rutile	3.60[6]	direct forbidden

A further important feature in a band diagram of a solid is the Fermi level E_F,

which for insulators and intrinsic semiconductors lies within the band gap between VB and CB. E_F is the energy level described in the Fermi-Dirac distribution $f(E)$:

$$f(E) = \frac{1}{1 + e^{\frac{E-E_F}{k_B T}}} , \tag{1.4}$$

where k_B is the Boltzmann constant and T is the temperature. At absolute zero, the Fermi-Dirac distribution shows a sharp cut-off between electron filled and unfilled levels at the Fermi energy. With increasing temperatures it is smeared out, meaning that most valence levels below E_F are partially empty, and a few electrons are thermally excited to conduction band states above E_F. Although the Fermi function has some intensity in the band gap due to the smearing out of E_F, this does not mean that electrons are present in the band gap since the occupation is the product of the Fermi function and the density of states. As mentioned above, the DOS is zero within the gap, meaning that there are no allowed energy levels available within E_g. Figure 1.5 shows a schematic drawing of the changes in the Fermi level at different temperatures for an intrinsic semiconductor.

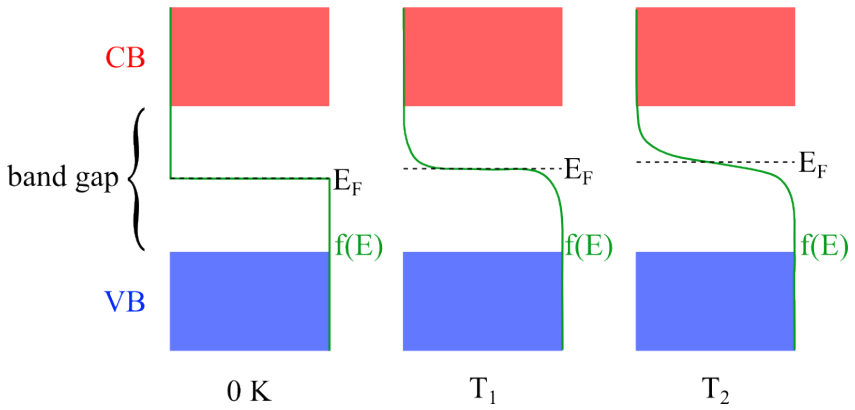


Figure 1.5: The Fermi function $f(E)$ at three different temperatures 0 K, T_1, and T_2, where 0 $K < T_1 < T_2$. $f(E)$ gets increasingly more smeared out the higher the temperature. The energy of the Fermi level E_F increases with increasing temperature and is in all three cases positioned inside the band gap E_g between the valence band (VB) and the conduction band (CB).

In extrinsic semiconductors the position of the Fermi level is determined by donor

or acceptor state densities. Donor levels are located close to the CBM giving an n-type semiconductor, whereas acceptor states are located just above the VBM giving a p-type semiconductor.

1.3 Crystal Structure of Metal Oxides

This section explores the fundamental structural properties of the metal oxides investigated in this thesis.

Oxides in general have more complicated crystal structures than many conventional semiconductors, which has a significant influence on possible fabrication techniques as well as their physical properties. Therefore, knowledge of the crystal structure is intrinsic to any further study of their behaviour and eventual use in technological applications. The images of crystal structures in this chapter were prepared using the CrystalMaker software package.

1.3.1 In_2O_3

In its crystalline state the thermodynamically stable phase of In_2O_3 has a body-centred cubic bixbyite structure with a unit cell containing 80 atoms, which is shown in figure 1.6.

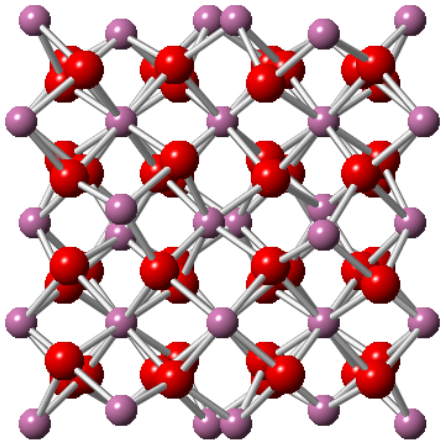
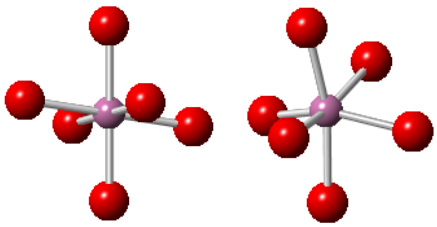


Figure 1.6: Unit cell of the bixbyite structure of In_2O_3. The pink spheres represent In, whilst the red spheres represent O.

The bixbyite structure of In_2O_3 is based upon that of fluorite. Its space group is $Ia\overline{3}$ and the lattice parameter is 1.0117 nm.[7] It represents a $2 \times 2 \times 2$ superstructure of fluorite, but with an ordered array of vacancies on a quarter of the anion sites and subsequent relaxation of atomic positions.[8,9] The unit cell contains 32 In atoms in two non-equivalent sites (Wyckoff positions 8a and 24d), and 48 oxygen atoms in one set of equivalent sites (Wyckoff position 48e). The oxygen atoms are in distorted tetrahedral sites, with four different In-O bonding lengths of 2.133, 2.161, 2.187, and 2.247 Å.



(a) (b)

Figure 1.7: In environments in the bixbyite phase of In_2O_3: (a) trigonally compressed octahedral site, (b) highly distorted octahedral coordination. The pink spheres represent In, whilst the red spheres represent O.

One quarter of the indium atoms (8a) are in trigonally compressed octahedral sites, with an In-O bond length of 2.161 Å (see figure 1.7(a)). The other three

quarters of the In atoms (24d) are in highly distorted octahedral coordination, with different In-O bonding lengths of 2.133, 2.187, and 2.247 Å respectively (see figure 1.7(b)).

In_2O_3 also has a second metastable corundum-type structure, which can be prepared through a high temperature - high pressure synthesis.[10] This structure is equivalent to that adopted by α-Al_2O_3. The In atoms are located in octahedral interstitial sites (Wyckoff position 12c) in a hexagonally close packed array of oxygen atoms (Wyckoff position 18e). Furthermore, a high pressure orthorhombic structure which remains metastable at ambient pressure and temperature has been prepared.[11] Table 1.2 summarises crystallographic information for the bixbyite-, corundum-type, and orthorhombic phases.

Table 1.2: Structural parameters of the bixbyite-type[7], corundum-type[10], and orthorhombic[12] phase of In_2O_3. a, b, and c are the lattice parameters, Z are the formula units per cell, and ρ is the theoretical density.

	Bixbyite	Corundum	Orthorhombic
a / Å	10.117	5.487	7.962
b / Å	10.117	5.487	5.477
c / Å	10.117	14.510	5.592
Crystal system	cubic	trigonal	orthorhombic
Space group	$Ia\overline{3}$	$R\overline{3}c$	$Pbcn$
Space group No.	206	167	60
Volume / Å^3	1035.51	378.33	243.86
Z	16	6	-
ρ / g cm^{-3}	7.12	7.31	-

1.3.2 Ga_2O_3

Five modifications of Ga_2O_3 are known, of which β-Ga_2O_3 is the most stable with 20 atoms per unit cell. This is a monoclinic system with the space group $C12/m1$ and $\beta = 103.7°$.[13] Figure 1.8 shows the unit cell of β-Ga_2O_3.

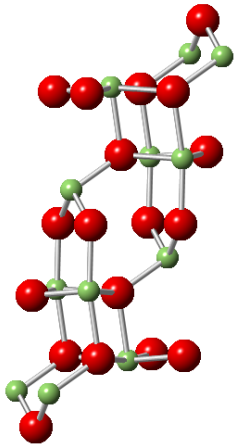
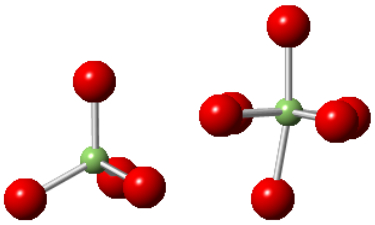


Figure 1.8: Unit cell of β-Ga_2O_3. The green spheres represent Ga, whilst the red spheres represent O.

The Ga atoms occupy two different sites, both with the Wyckoff position 4i. One site has a distorted tetrahedral coordination, with bond lengths of 1.803, 1.833, and 1.853 Å, the other has a distorted octahedral coordination, with bond lengths of 1.940, 1.978, 2.023, and 2.077 Å. Figure 1.9 shows the two different Ga environments. The oxygen ions are in three different sites, all with a Wyckoff position 4i. One is a slightly distorted trigonal planar site, with bond lengths of 1.833 and 1.940 Å, another is a distorted trigonal pyramidal site with bond lengths of 1.803 and 1.978 Å, and the third is a distorted tetrahedral site with bond lengths of 1.853, 2.023, and 2.077 Å respectively.



(a) (b)

Figure 1.9: Ga environments in β-Ga_2O_3: (a) distorted tetrahedral coordination, (b) distorted octahedral coordination. The green spheres represent Ga, whilst the red spheres represent O.

α-Ga_2O_3 can be obtained by heating the β form under pressure, whilst the γ[14], δ[15], and ϵ[15] phases of Ga_2O_3 are accessible through high temperature synthesis. Table 1.3 summarises crystallographic information for all five polymorphs.

Table 1.3: Structural parameters of the five polymorphs α[16], β[13], γ[14], δ[15], and ϵ[15] of Ga_2O_3. a, b, and c are the lattice parameters, Z are the formula units per cell, and ρ is the theoretical density.

	α	β	γ
a / Å	4.9285	12.230	8.2376
b / Å	4.9825	3.040	8.2376
c / Å	13.4330	5.800	8.2376
Crystal system	trigonal	monoclinic	cubic
Space group	$R\overline{3}c$	$C12/m1$	$Fd\overline{3}m$
Space group No.	167	12	227
Volume / Å^3	28.80	209.50	-
Z	6	4	-
ρ / g cm^{-3}	6.47	5.94	5.94
	δ	ϵ	
a / Å	9.401	5.120	
b / Å	9.401	8.792	
c / Å	9.401	9.410	
Crystal system	cubic	orthorhombic	
Space group	$Ia\overline{3}$	$Pna2_1$	
Space group No.	206	33	
Volume / Å^3	-	423.6	
Z	-	8	
ρ / g cm^{-3}	-	5.88	

1.3.3 Tl_2O_3

Tl_2O_3 has a cubic bixbyite structure with the space group $Ia\overline{3}$ and a lattice parameter of 1.0543 nm.[17] This structure is very similar to that of In_2O_3 but with a 4.21% larger lattice parameter due to the increase in ionic radius from In to Tl. Figure 1.10 shows the unit cell of Tl_2O_3.

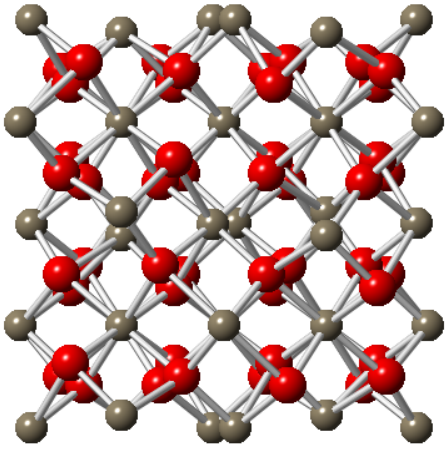


Figure 1.10: Unit cell of Tl_2O_3. The grey spheres represent Tl, whilst the red spheres represent O.

Analogous to In_2O_3, Tl_2O_3 is also based upon the fluorite structure. It represents a $2 \times 2 \times 2$ superstructure of fluorite, but with an ordered array of vacancies on a quarter of the anion sites. The unit cell contains 32 Tl atoms in two non-equivalent sites (Wyckoff positions 8a and 24d), and 48 oxygen atoms in one site (Wyckoff position 48e). Due to the difference in atomic radii between In and Tl, the bond lengths between the cation and O increase from In to Tl. The oxygen atoms are in distorted tetrahedral sites, with four different Tl-O bonding lengths of 2.140, 2.189, 2.271, and 2.475 Å.

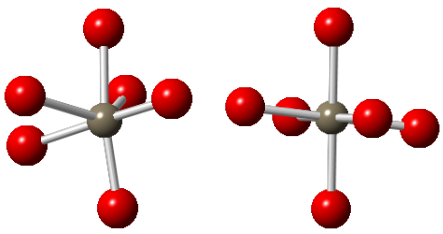


Figure 1.11: Tl environments in the bixbyite phase of Tl_2O_3: (a) trigonally compressed octahedral site, (b) distorted octahedral coordination. The grey spheres represent Tl, whilst the red spheres represent O.

One quarter of the Tl atoms (8a) are in trigonally compressed octahedral sites, with a Tl-O bond length of 2.271 Å (see figure 1.11(a)). The other three quarters of the Tl atoms (24d) are in highly distorted octahedral coordination, with Tl-O

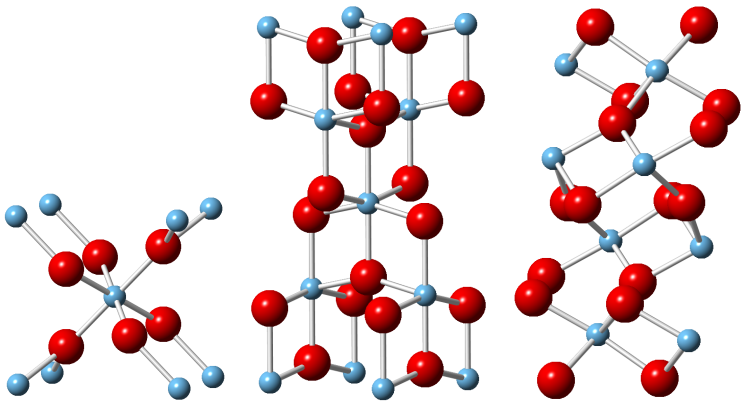
bonding lengths of 2.140, 2.189, and 2.475 Å respectively (see figure 1.11(b)). Table 1.4 summarises the relevant crystallographic information for bixbyite-type Tl_2O_3.

Table 1.4: Structural parameters of the bixbyite-type phase of Tl_2O_3.[17] a, b, and c are the lattice parameters, Z are the formula units per cell, and ρ is the theoretical density.

	Bixbyite
a / Å	10.543
b / Å	10.543
c / Å	10.543
Crystal system	cubic
Space group	$Ia\overline{3}$
Space group No.	206
Volume / Å^3	1171.91
Z	16
ρ / g cm^{-3}	10.35

1.3.4 TiO_2

TiO_2 has three main polymorphs, rutile, anatase, and brookite. Figure 1.12 shows the unit cells of these polymorphs. In addition, other high pressure phases such as cotunnite have been synthesised.[18] However, only rutile and anatase are of significant importance for technological applications.



(a) (b) (c)

Figure 1.12: Unit cells of the three polymorphs of TiO_2, (a) rutile, (b) anatase, and (c) brookite. The light blue spheres represent Ti, whilst the red spheres represent O.

Both rutile and anatase have a tetragonal unit cell with the Ti atoms in D_{2h} sites approximating to octahedral coordination and the O atoms in roughly trigonal planar coordination. The Ti-O bond lengths are 1.945 and 1.986 Å for rutile and 1.934 and 1.980 Å for anatase. The shorter bond lengths and different connectivities in anatase lead to a reduction in the a and b lattice parameters. The c parameter increases from 1.480 Å/Z in rutile to 2.379 Å/Z in anatase.

Brookite has an orthorhombic structure with the Ti atoms in a distorted octahedral coordination with six different bond lengths of 1.863, 1.923, 1.931, 1.990, 1.999, and 2.052 Å. The oxygen atoms are in two different trigonal planar coordinations, with bond lengths of 1.863, 1.990, and 1.999 Å in one environment, and 1.923, 1.931, and 2.052 Å in the other. Table 1.5 summarises important structural parameters for all three polymorphs of TiO_2.

Table 1.5: Structural parameters of the three polymorphs of TiO_2, rutile[19], anatase[20], and brookite[21]. a, b, and c are the lattice parameters, Z are the formula units per cell, and ρ is the theoretical density.

	Rutile	Anatase	Brookite
a / Å	4.594	3.784	5.138
b / Å	4.594	3.784	9.174
c / Å	2.959	9.515	5.449
Crystal system	tetragonal	tetragonal	orthorhombic
Space group	$P4_2/mnm$	$I4_1/amd$	$Pbca$
Space group No.	136	141	61
Volume / Å^3	62.45	136.25	256.84
Z	2	4	8
ρ / g cm^{-3}	4.25	3.90	4.13

Rutile is the most stable among the three polymorphs, with anatase and brookite converting into rutile upon heating. Figure 1.13 shows XRD patterns which chart the change from anatase into rutile upon heating a powder sample at temperatures from 400 to 1000°C.

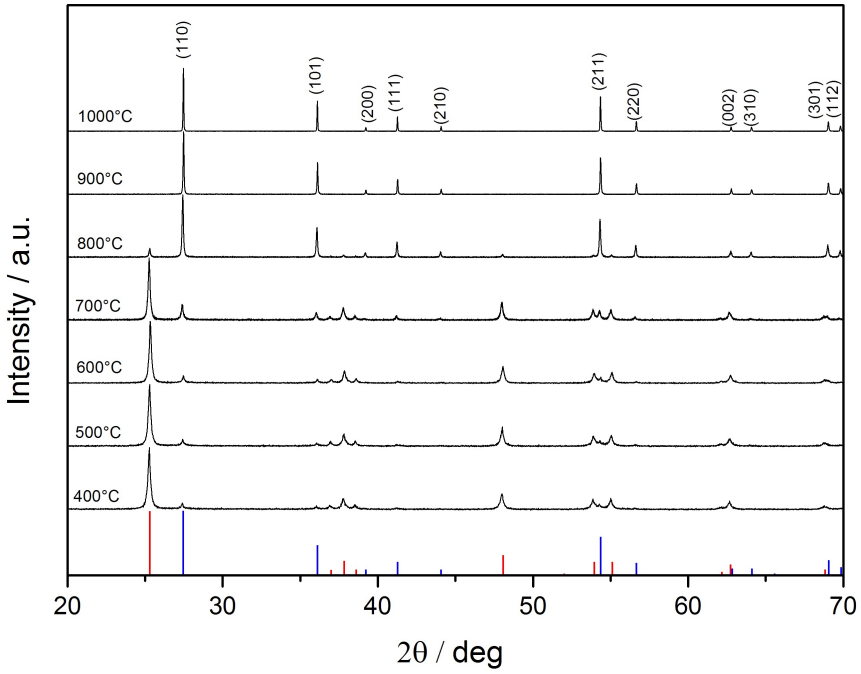


Figure 1.13: X-ray diffraction patterns of anatase TiO_2 after heating at different temperatures. The red reference corresponds to the anatase form, whereas the blue reference corresponds to the rutile form. This data was collected by K. M. Leong (Part II thesis, Oxford, 2013).

The transformation from anatase to rutile is reconstructive, meaning that it involves a major rearrangement of atoms including the breaking and reforming of bonds. As there is no phase equilibrium involved, it is not possible to experimentally define a clear transition temperature. Therefore, a temperature range across which the transformation takes place is observed, which leads to a range of transition temperatures from 400 to 1000°C being reported in the literature. A range of activation energies E_A and reaction enthalpies ΔH° have also been reported, which are summarised in table 1.6. As can be seen from the negative values for ΔH° the transformation is exothermic with necessary activation energies between 300 and 800 kJ/mol depending on the sample. The transformation is highly influenced by the method of sample preparation[22,23], impurities or additives[22,24–27], the atmosphere during sample preparation[22,26], deviations from the stoichiometry[28], particle size[23,29], and surface area[25]. This can explain the rather large variations in reported

values.

Table 1.6: Activation energy E_A and reaction enthalpy ΔH° for the anatase→rutile transformation from the literature.

Source	E_A / kJ/mol	Source	ΔH° / kJ/mol
Canderna 1958[30]	377 - 460	Rao 1961[31]	−0.42 (903.15K)
Yoganarasimhan 1962[25]	502	Vahldiek 1966[32]	−2.79 (1183K)
Shannon 1964[33]	418 - 753	Navrotsky 1967[34]	−6.57 (968K)
Shannon 1965[33]	418/481/795	Mitsuhashi 1979[35]	−3.26 (971K)
Borkar 2004[27]	328	Dassler 1988[36]	−1.12 to −1.4
Grzmil 2013[24]	500	Smith 2009[37]	−1.70 (298.15K)

1.3.5 SnO_2

SnO_2 crystallises in the tetragonal rutile structure, with the Sn atoms in octahedral coordination and the O atoms in trigonal planar coordination. The Sn-O bond lengths are 2.052 and 2.058 Å. Figure 1.14 shows the unit cell of SnO_2.

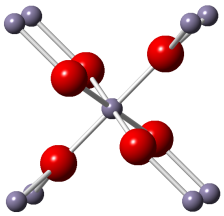


Figure 1.14: Unit cell of the SnO_2. The grey spheres represent Sn, whilst the red spheres represent O.

Table 1.7 summarises essential structural parameters of the rutile structure of SnO_2.

Table 1.7: Structural parameters of the rutile-type phase of SnO_2.[19] a, b, and c are the lattice parameters, Z are the formula units per cell, and ρ is the theoretical density.

	Rutile
a / Å	4.7380
b / Å	4.7380
c / Å	3.1865
Crystal system	tetragonal
Space group	$P4_2/mnm$
Space group No.	136
Volume / Å^3	71.53
Z	2
ρ / g cm^{-3}	7.00

1.4 Technological Importance of Metal Oxides

1.4.1 Transparent Conducting Oxides

Materials that combine optical transparency in the visible region with a high electrical conductivity have been extensively researched over recent decades and have found use in a variety of industrial applications. In general three classes of materials combine these two characteristics: very thin pure metals, highly doped conjugated polymers, and doped wide band gap oxide or nitride semiconductors.[38] Wide band gap oxides are of particular interest today and many different systems have been studied.

Bädeker[39] was the first to report a transparent conducting cadmium oxide CdO film and since then the interest in this group of materials has grown continuously. CdO is still of some interest today[40–46], although it has been widely replaced by other materials due to its relatively narrow fundamental band gap (2.31 eV at 0 K and 2.18 at 300 K[47]) and the high toxicity of Cd limit its use in practical devices.[48]

Although conductivity in post transition metal oxides has been well known for over half a century[49], there is still much controversy regarding the electrical and optical properties. The major cause of discussion is that the quality of samples varies immensely with the deposition parameters, the presence of impurities, post-deposition annealing, and the presence of oxygen during fabrication (see Dawar *et al.*[50] for further explanation of the influence of these parameters).

As pure post transition metal oxides in general are insulators at room temperature they have to be heavily doped to make them conducting. The oxides of the d^{10} cations may have high concentrations of intrinsic defects, with oxygen vacancies traditionally regarded as the most important.[51] They are generally presumed to be readily ionised to donate electrons to the CB, although this concept has been questioned.[52] Extrinsic dopants are generally required to achieve the necessary metallic conductivities. For example, In_2O_3 is an insulator, but doping with Sn leads to one of the most important of the TCOs. Tin-doped indium oxide is widely but somewhat misleadingly known as indium tin oxide or ITO. Doping leads to maximum conductivities of 10^4 $S{\cdot}cm^{-1}$ and transmittance above 80% in the visible region.[48,53,54] The optical window in which TCOs transmit light is defined by two boundaries: the near-UV cut off which is determined by the effective band gap, and the near-IR cut off which is determined by an increase in reflectance caused by the plasma resonance.[48]

Whilst p-type conducting oxides exist and are a focus of intense research[45,55–61], almost all well known TCOs today are n-type conducting oxides. The most widely used oxides at present are tin oxide SnO_2, zinc oxide ZnO, indium oxide In_2O_3, and their alloys. Together with cadmium oxide CdO and gallium oxide Ga_2O_3 they define the phase space of possible TCO combinations (see figure 1.15). As mentioned

before, tin doped indium oxide (ITO) is the most widely used material today, but In_2O_3 is also used with other dopants including Sn, Ge, Mo, Ti, Zr, Hf, Nb, Ta, W, Te and F.[48,62]

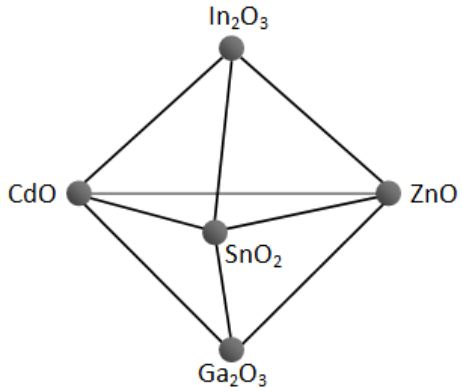


Figure 1.15: The five most important TCOs currently used individually and in their alloys.

A combination of n- and p-conducting TCOs could lead to active, rather than passive, applications for oxides. One possible application would be a "functional window", which would transmit light in the visible region, but could generate electricity using ultraviolet photons.[57]

The applications for TCOs are many; heat reflecting films, gas sensors, protective coatings for glass surfaces[50], heating layers protecting vehicle windscreens from freezing[63], laser-damage resistant coatings[64], photoelectrochemical cells[65], antistatic surface layers in satellites[66], surface layers in electroluminescent applications[67], flat panel displays, touch panels, LEDs[68,69], organic LEDs[70], low thermal emittance coatings[71], electrochromatic smart windows[53,72] and high performance transparent electronics[73–78]. An area that has received extensive attention is their use in solar cells.[54,79,80]

1.4.2 Photocatalysis in Transition Metal Oxides

When electrons in an oxide are excited from the VB into the CB, a redox electron/hole pair is formed. The electrons can act as a reducing agent, whilst the holes can act as an oxidising agent and react with molecules located on the oxide surface. This redox behaviour can be exploited for water splitting or the oxidation of organic pollutants.

TiO_2 is a relatively abundant compound, making up around 6,500 parts per Million of the earth's crust. Titanium and its oxides are produced on a massive scale of almost seven million tons per year, the majority from deposits in Australia and South Africa. Moreover TiO_2 is a benign material, even having use as a food additive. When Fujishima and Honda reported the photocatalytic splitting of water on a TiO_2 electrode in 1972[81], it sparked enormous interest in photocatalysis mediated by TiO_2.

As the excitation of electrons in TiO_2 is dependent on the ability to absorb light, the band gaps for both rutile and anatase being in excess of 3 eV presents a severe limitation of their usability and efficiency in solar-driven processes. The large band gaps mean that TiO_2 only absorbs UV radiation, which only represents a very small proportion of sun light. Doping of TiO_2 can be used to modify the electronic structure and increase the efficiency of TiO_2 as a potentially outstanding photocatalytic material.

Metal oxides with photocatalytic properties, mainly TiO_2, have been used in a range of applications (see the review by Fujishima *et al.*[82]); water purification, air purification, self-cleaning surfaces, self-sterilizing surfaces, anti-fogging surfaces, heat transfer and dissipation, anti-corrosion applications, photocatalytic lithogra-

phy, photochromism, and microchemical systems.

1.5 Scope and Organisation of this Thesis

This chapter has summarised electronic and structural characteristics, and possible applications of the metal oxides investigated in this thesis. The following two chapters describe the background and setup of the experimental techniques involved in the presented research, including molecular beam epitaxy (MBE), sol-gel dip-coating, laboratory- and synchrotron-based X-ray diffraction (XRD), laboratory- and synchrotron-based X-ray spectroscopy (XPS), diffuse reflectance spectroscopy (DRS), Raman spectroscopy, low energy ion scattering spectroscopy (LEIS), atomic force microscopy (AFM), and ellipsometry.

Chapter 4 introduces the concept of thin film growth of In_2O_3 and probes the strain leading to nanostructured samples by reciprocal space mapping. Chapters 5 and 6 use a solid-state approach to investigate structural and electronic changes upon isovalent doping of In_2O_3 with Ga and Tl. Sol-gel dip-coating as an alternative technique to other growth methods for the preparation of metal oxide thin films is explored in chapter 7, starting with the design of experiments setup for TiO_2, followed by an in-depth study of anatase and rutile thin films grown on single crystal substrates. Chapter 8 presents hard X-ray photoemission results for both undoped and Sn-doped anatase TiO_2.

Chapter 9 concludes the results chapters and draws on the preceding findings in an effort to grow In_2O_3 thin films via a sol-gel method.

The main concluding remarks of the here presented work are given in chapter 10.

1.6 References

[1] F. Labat, P. Baranek, C. Domain, C. Minot, and C. Adamo, The Journal of Chemical Physics **126**, 154703 (2007).

[2] P. D. C. King, T. D. Veal, F. Fuchs, C. Y. Wang, D. J. Payne, A. Bourlange, H. Zhang, G. R. Bell, V. Cimalla, O. Ambacher, R. G. Egdell, F. Bechstedt, and C. F. McConville, Physical Review B **79**, 205211 (2009).

[3] H. He, R. Orlando, M. A. Blanco, R. Pandey, E. Amzallag, I. Baraille, and M. Rérat, Physical Review B **74**, 195123 (2006).

[4] A. B. Kehoe, D. O. Scanlon, and G. W. Watson, Physical Review B **83**, 233202 (2011).

[5] D. O. Scanlon, C. W. Dunnill, J. Buckeridge, S. A. Shevlin, A. J. Logsdail, S. M. Woodley, C. R. A. Catlow, M. J. Powell, R. G. Palgrave, I. P. Parkin, G. W. Watson, T. W. Keal, P. Sherwood, A. Walsh, and A. A. Sokol, Nature Materials **12**, 798 (2013).

[6] J. Robertson, Journal of Physics C: Solid State Physics **12**, 4767 (1979).

[7] M. Marezio, Acta Crystallographica **20**, 723 (1966).

[8] S. Aldridge and A. J. Downs, editors, *The group 13 metals aluminium, galium, indium and thallium. Chemical patterns and peculiarities.* (John Wiley & Sons, Hoboken, 2011).

[9] D. Beena, K. J. Lethy, R. Vinodkumar, A. P. Detty, V. P. M. Pillai, and V. Ganesan, Journal of Alloys and Compounds **489**, 215 (2010).

[10] C. T. Prewitt, R. D. Shannon, D. B. Rogers, and W. W. Sleight, Inorganic Chemistry **8**, 1985 (1969).

[11] M. F. Bekheet, M. R. Schwarz, S. Lauterbach, H.-J. Kleebe, P. Kroll, R. Riedel, and A. Gurlo, Angewandte Chemie International Edition **52**, 6531 (2013).

[12] A. Walsh and D. O. Scanlon, Physical Review B **88**, 161201 (2013).

[13] S. Geller, The Journal of Chemical Physics **33**, 676 (1960).

[14] H. Y. Playford, A. C. Hannon, E. R. Barney, and R. I. Walton, Chemistry - A European Journal **19**, 2803 (2013).

[15] S. Yoshioka, H. Hayashi, A. Kuwabara, F. Oba, K. Matsunaga, and I. Tanaka, Journal of Physics: Condensed Matter **19**, 346211 (2007).

[16] M. Marezio and J. P. Remeika, Journal of Chemical Physics **46**, 1862 (1967).

[17] P. Papamantellos, Zeitschrift für Kristallographie, Kristallgeometrie, Kristallphysik, Kristallchemie **126**, 143 (1968).

[18] L. S. Dubrovinsky, N. A. Dubrovinskaia, V. Swamy, J. Muscat, N. M. Harrison, R. Ahuja, B. Holm, and B. Johansson, Nature **410**, 653 (2001).

[19] W. H. Baur and A. A. Khan, Acta Crystallographica B **27**, 2133 (1971).

[20] M. Horn, C. F. Schwerdtfeger, and E. P. Meagher, Zeitschrift für Kristallographie, Kristallgeometrie, Kristallphysik, Kristallchemie **136**, 273 (1972).

[21] E. P. Meagher and G. A. Lager, Canadian Mineralogist **17**, 77 (1979).

[22] Y. Iida and S. Ozaki, Journal of the American Ceramic Society **44**, 120 (1961).

[23] M. Fernandez-Garcia, X. Wang, C. Belver, J. C. Hanson, and J. A. Rodriguez, Journal of Physical Chemistry C **111**, 674 (2007).

[24] B. Grzmil, M. M. Glen, B. Kic, and K. Lubkowski, Polish Journal of Chemical Technology **15**, 73 (2013).

[25] S. R. Yoganarasimhan and C. N. R. Rao, Transactions of the Faraday Society **58**, 1579 (1962).

[26] F. C. Gennari and D. M. Pasquevich, Journal of Materials Science **33**, 1571 (1998).

[27] S. A. Borkar and S. R. Dharwadkar, Journal of Thermal Analysis and Calorimetry, **78**, 761 (2004).

[28] D. A. H. Hanaor and C. C. Sorrell, Journal of Materials Science **46**, 855 (2011).

[29] H. Zhang and J. F. Banfield, Journal of Physical Chemistry B **104**, 3481 (2000).

[30] A. W. Czanderna, C. N. R. Rao, and J. M. Honig, Transactions of the Faraday Society **54**, 1069 (1958).

[31] C. N. R. Rao, Canadian Journal of Chemistry **39**, 498 (1961).

[32] F. W. Vahldiek, Journal of Less-Common Metals **11**, 99 (1966).

[33] R. D. Shannon and J. A. Pask, The American Mineralogist **49**, 1707 (1964).

[34] A. Navrotsky and O. J. Kleppa, Journal of the American Ceramic Society **50**, 626 (1967).

[35] T. Mitsuhashi and O. J. Kleppa, Journal of the American Ceramic Society **62**, 356 (1979).

[36] A. Dassler, A. Feltz, J. Jung, W. Ludwig, and E. Kaisersberger, Journal of Thermal Analysis **33**, 803 (1988).

[37] S. J. Smith, R. Stevens, S. Liu, G. Li, A. Navrotsky, J. Boerio-Goates, and B. F. Woodfield, American Mineralogist, **94**, 236 (2009).

[38] G. P. Crawford, editor, *Flexible flat panel displays* (John Wiley & Sons, Chichester, 2005).

[39] K. Bädeker, Annalen der Physik **327**, 749 (1907).

[40] Q. Zhou, Z. Ji, B. Hu, C. Chen, L. Zhao, and C. Wang, Materials Letters **61**, 531 (2007).

[41] M. Kul, A. S. Aybek, E. Turan, M. Zor, and S. Irmak, Solar Energy Materials & Solar Cells **91**, 1927 (2007).

[42] F. C. Eze, Materials Chemistry and Physics **89**, 205 (2005).

[43] R. Cuscó, J. Ibáñez, N. Domenech-Amador, L. Artús, J. Zúñiga-Pérez, and V. Muñoz-Sanjosé, Journal of Applied Physics **107**, 063519 (2010).

[44] A. W. Metz, J. R. Ireland, J.-G. Zheng, R. P. S. M. Lobo, Y. Yang, J. Ni, C. L. Stern, V. P. Dravid, N. Bontemps, C. R. Kannewurf, K. Poeppelmeier, and T. J. Marks, Journal of the American Chemical Society **126**, 8477 (2004).

[45] K. Ueda, T. Hase, H. Yanagi, H. Kawazoe, and H. Hosono, Journal of Applied Physics **89**, 1790 (2001).

[46] K. M. Yu, M. A. Mayer, D. T. Speaks, H. He, R. Zhao, L. Hsu, S. S. Mao, E. E. Haller, and W. Walukiewicz, Journal of Applied Physics **111**, 123505 (2012).

[47] S. K. V. Farahani, V. Munoz-Sanjose, J. Zuniga-Perez, C. F. McConville, and T. D. Veal, Applied Physics Letters **102**, 022102 (2013).

[48] H. Liu, V. Avrutin, N. Izyumskaya, U. Özgür, and H. Morkoc, Superlattices and Microstructures **48**, 458 (2010).

[49] C. A. Hogarth, Nature **167**, 521 (1951).

[50] A. L. Dawar and J. C. Joshi, Journal of Materials Science **19**, 1 (1984).

[51] P. D. C. King and T. D. Veal, Journal of Physics: Condensed Matter **23**, 334214 (2011).

[52] S. Lany, A. Zakutayev, T. O. Mason, J. F. Wager, K. R. Poeppelmeier, J. D. Perkins, J. J. Berry, D. S. Ginley, and A. Zunger, Physical Review Letters **108**, 016802 (2012).

[53] C. G. Granqvist and A. Hultaker, Thin Solid Films **411**, 1 (2002).

[54] C. G. Granqvist, Solar Energy Materials & Solar Cells **91**, 1529 (2007).

[55] S.-H. Wei, X. Nie, and S. B. Zhang, Conference record of the twenty-ninth IEEE photovoltaic specialists conference , 496 (2002).

[56] S.-H. Wei and S. B. Zhang, Physical Review B **63**, 045112 (2001).

[57] H. Kawazoe, M. Yasukawa, H. Hyodo, M. Kurita, H. Yanagi, and H. Hosono, Nature **389**, 939 (1997).

[58] X. Nie, S.-H. Wei, and S. B. Zhang, Physical Review Letters **88**, 066405 (2002).

[59] X. Nie, S.-H. Wei, and S. B. Zhang, Physical Review B **65**, 075111 (2011).

[60] H. Yanagi, T. Hase, S. Ibuki, K. Ueda, and H. Hisono, Applied Physics Letters **78**, 1583 (2001).

[61] H. Yanagi, S. i. Inoue, K. Ueda, and H. Kawazoe, Journal of Applied Physics **88**, 4159 (2000).

[62] T. Minami, Thin Solid Films **516**, 5822 (2008).

[63] H. Yoshida, H. Furubayashi, Y. Inoue, and T. Tonomura, Journal of the Vacuum Society of Japan **19**, 13 (1976).

[64] W. T. Pawlewicz, I. B. Mann, W. H. Lowdermilk, and D. Milam, Applied Physics Letters **34**, 196 (1979).

[65] H. T. Tien and J. Higgins, Journal of the Electrochemical Society **127**, 1475 (1980).

[66] G. Hass, J. B. Heaney, and A. R. Toft, Applied Optics **18**, 1488 (1979).

[67] R. Tueta and M. Braguier, Thin Solid Films **80**, 143 (1981).

[68] A. Porch, D. V. Morgan, R. M. Perks, M. O. Jones, and P. P. Edwards, Journal of Applied Physics **96**, 4211 (2004).

[69] A. Porch, D. V. Morgan, R. M. Perks, M. O. Jones, and P. P. Edwards, Journal of Applied Physics **95**, 4734 (2004).

[70] P. K. Nayak, J. Yang, J. Kim, S. Chung, J. Jeong, C. Lee, and Y. Hong, Journal of Physics D: Applied Physics **42**, 035102 (2009).

[71] I. Hamberg and C. G. Granqvist, Journal of Applied Physics **60**, R123 (1986).

[72] A. Azens and C. G. Granqvist, Journal of Solid State Electrochemistry **7**, 64 (2002).

[73] G. Thomas, Nature **389**, 907 (1997).

[74] J. F. Wager, Science **300**, 1245 (2003).

[75] J. Heber, Nature **459**, 28 (2009).

[76] H. Takagi and H. Y. Hwang, Science **327**, 1601 (2010).

[77] J. Mannhart and D. G. Schlom, Science **327**, 1607 (2010).

[78] H. Ohta and H. Hosono, Materials Today **7**, 42 (2004).

[79] E. Fortunato, L. Raniero, L. Silva, A. Goncalves, A. Pimentel, P. Barquinha, H. Aguas, L. Pereira, G. Gonc-alves, I. Ferreira, E. Elangovan, and R. Martins, Solar Energy Materials & Solar Cells **92**, 1605 (2008).

[80] E. Fortunato, D. Ginley, H. Hosono, and D. C. Paine, MRS Bulletin **32**, 242 (2007).

[81] A. Fujishima and K. Honda, Nature **238**, 37 (1972).

[82] A. Fujishima, X. Zhang, and D. A. Tryk, Surface Science Reports **63**, 515 (2008).

2 Background to Experimental Techniques

This chapter presents a brief background to the experimental techniques used in this thesis. Three methods were employed to prepare the samples studied in this research. Ceramic samples were prepared using a solid state approach, whilst thin film samples were prepared using molecular beam epitaxy (MBE) and sol-gel dip-coating. The electronic and structural characteristics of the samples were analysed using laboratory- and synchrotron-based X-ray diffraction (XRD), laboratory- and synchrotron-based X-ray photoelectron spectroscopy (XPS), diffuse reflectance spectroscopy (DRS), Raman spectroscopy, low energy ion scattering spectroscopy (LEIS), atomic force microscopy (AFM), and ellipsometry.

2.1 Molecular Beam Epitaxy

Molecular beam epitaxy (MBE) is a method that was developed in the 1970s by John R. Arthur and Alfred Y. Cho[1] for the growth of GaAs. Today the technique is widely used for the epitaxial growth of thin films under ultra-high vacuum (UHV) conditions. Due to the slow growth rates, it allows for a highly precise control of film thickness and, under ideal conditions, layer-by-layer growth.

2.1.1 Principles

MBE uses Knudsen effusion cells (K-cells) to evaporate the elemental source materials. In an idealised K-cell the condensed phase and vapour are in equilibrium, and in this case the flux F at the substrate can be described by the following equation:

$$F = \frac{p_{\mathrm{eq}}(T)a}{\pi L^2 \sqrt{2\pi m k_{\mathrm{B}} T}} \ , \tag{2.1}$$

where $p_{\mathrm{eq}}(T)$ is the pressure at equilibrium as a function of the temperature T, a is the area of the cell aperture, L is the distance to the substrate, m is the mass of the effusion species, and k_{B} is the Boltzmann constant.

When the flux of gaseous atoms reaches the substrate surface and condenses, a variety of processes can occur, which are illustrated in figure 2.1.

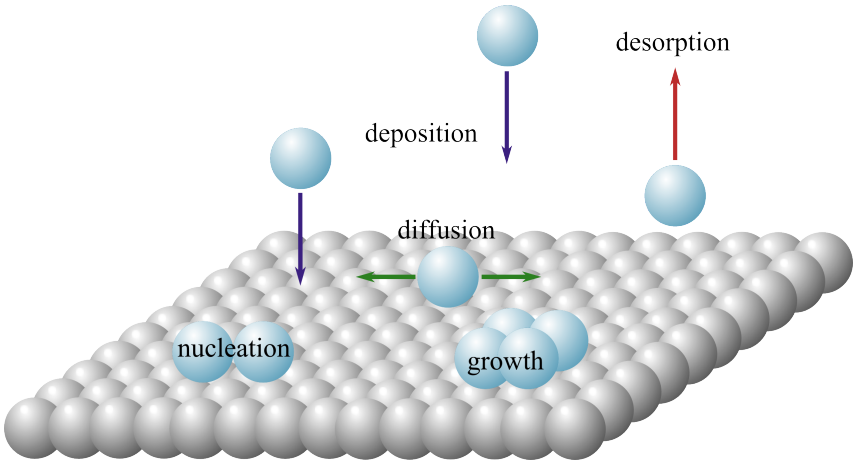


Figure 2.1: Atomic processes during film growth. A number of different processes occur, including deposition, diffusion, nucleation, growth, and desorption.

The atom can: (i) form a bond with the surface and stay in place (deposition), (ii) diffuse across the surface to a preferred location (diffusion), or (iii) evaporate

again and leave the surface (desorption). Both deposition and diffusion can lead to nucleation and ultimately to film growth.

2.1.2 Instrumentation

An MBE system usually consists of three separate UHV chambers; a load lock, a preparation and analysis chamber for sample cleaning and characterisation, and the main MBE chamber. Figure 2.2 shows a schematic diagram of the main chamber of an MBE system.

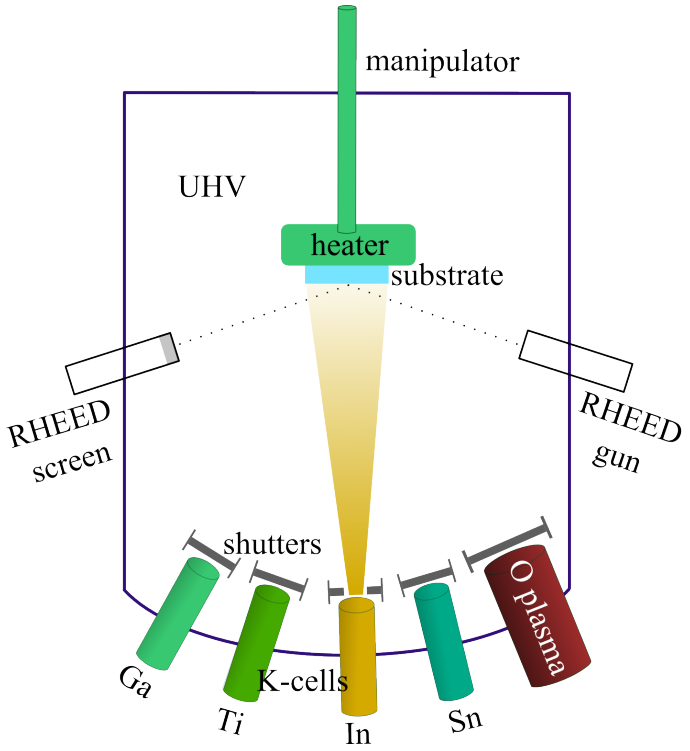


Figure 2.2: Schematic of a main MBE chamber. A range of different atomic beam sources (K-cells) is indicated, which can be used on their own, or in combination, to achieve film doping.

As the objective is to grow high purity films, MBE systems are operated under clean UHV conditions. Since the growth of monolayers is comparatively slow, unwanted residual gases in the chamber have time to adsorb on the surface. Therefore, the residual gas concentrations must be kept as low as possible, particularly

for highly adsorbing species like water.

Inside the main MBE chamber, a number of high purity elements are placed in K-cells and, under precise control, heated until they start to evaporate. In front of every effusion cell is a shutter which, in combination with the temperature regulation of the K-cells, allows the control of film composition and dopant concentration. The sample is placed on a heater to achieve epitaxial growth and the beam of gaseous atoms from the effusion cell is directed at it. When growing oxides, as opposed to pure metals or group IV or III-V semiconductors, an oxygen source is used in addition to the elemental cells. This may be a simple molecular source or a source with a significant fraction of O atoms produced in a radiofrequency (RF) or electron cyclotron resonance (ECR) plasma.

Monolayer growth is often monitored using a reflection high energy electron diffraction (RHEED) system.[2] In a RHEED system a high energy electron beam is scattered by the sample surface, and the resulting signal is projected onto a fluorescent screen. As the RHEED signal oscillates with the growth of a monolayer it can be used for in-situ film control.

2.2 Sol-Gel Dip-Coating

Sol-gel dip-coating is a chemical solution deposition method,[3] where typically alkoxides dissolved in alcohols are used as precursor solutions.

Although the first synthesis of a metal alkoxide which gelled in air was published in 1846 by J. J. Ebelman,[4] it was not until the 1930s that it was recognized as a method for preparing films.[5] Today sol-gel dip-coating offers several advantages

to classic thin film growth methods, including low cost, easy control of film composition, freedom from temperature restrictions, and no requirement for a vacuum environment.

2.2.1 Principles

Two main chemical steps are involved in the formation of a metal oxide film via the sol-gel technique: hydrolysis and condensation. Equations 2.2a and 2.2b show the chemical equations for both hydrolysis (a) and condensation (b) in the case of a Ti (IV) isopropoxide precursor.

$$\mathrm{Ti}\left[\mathrm{OCH(CH_3)_2}\right]_4 + 4\,\mathrm{H_2O} \rightarrow \mathrm{Ti(OH)_4} + 4\,\mathrm{(CH_3)_2CHOH} \tag{2.2a}$$

$$\mathrm{Ti(OH)_4} \xrightarrow{\Delta} \mathrm{TiO_2} + 2\,\mathrm{H_2O} \tag{2.2b}$$

The polarity of the M-OR bond in general is the main factor influencing the hydrolysis behaviour, with faster hydrolysis the more polar the bond. In addition, the larger the rest R, the slower the hydrolysis. Catalysts, like acids and bases, are frequently added to the alkoxide-alcohol solution to support an attack on the M-OR bond.

2.2.2 Instrumentation

Figure 2.3 outlines the principal steps of a sol-gel dip-coating process. First, a precursor solution is prepared in a glove box and placed in a suitable container. Following this, a clean substrate is brought into the precursor solution and held stationary for a period of time after which it is withdrawn at a constant speed. During the removal process, a wet layer is formed on the substrate, and the solvent begins

to evaporate in air. The substrate is then placed in a stream of wet nitrogen gas and the first chemical reaction, hydrolysis, occurs. These steps are repeated until the desired film thickness is achieved. Thereafter, the substrate is placed in a furnace at appropriate calcination temperatures, to allow condensation and crystallisation to take place.

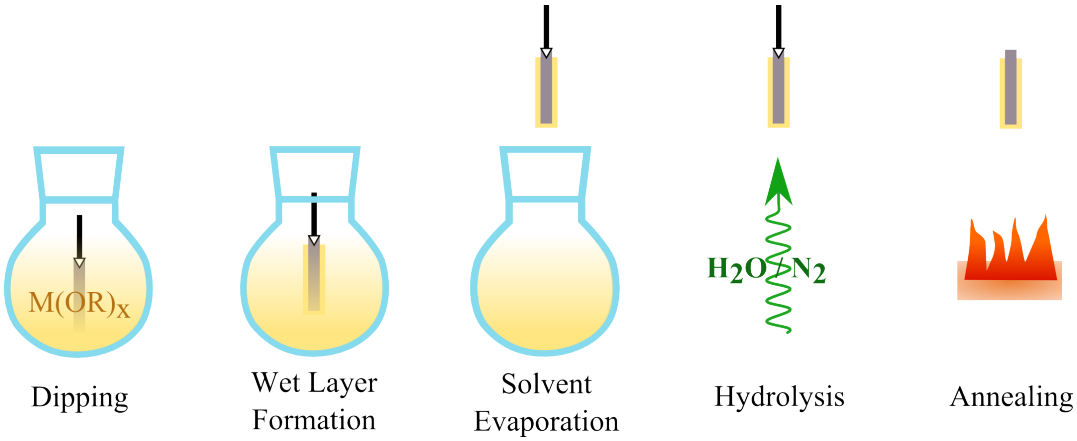


Figure 2.3: Principal steps of a sol-gel dip-coating process.

2.3 X-Ray Diffraction

X-ray diffraction (XRD) in crystals was discovered by Max von Laue, Walter Friedrich, and Paul Knipping in 1912 and the technique was developed by William Henry and William Lawrence Bragg.[6] It is a non-destructive technique used to investigate solid state phases. It can provide information about the crystal structure of the material, including lattice parameters and positions of atoms within the unit cell. In addition, it can also find film thicknesses, strain, and defect densities in thin films.

2.3.1 Principles and Theoretical Considerations

When X-rays are scattered from a crystalline solid, the contributions from each atom within the unit cell give an overall scattering pattern. Constructive and destructive interference occurs and is dependent upon the direction of the beam and the positions of the atoms. Diffraction from a crystal lattice leads to a diffraction pattern which is a map of the reciprocal lattice. The real space cell parameters $(a, b, c, \alpha, \beta, \gamma)$ change to $a^*, b^*, c^*, \alpha^*, \beta^*, \gamma^*$.

On combination of single unit cells with a crystal lattice a complete picture of a crystal can be obtained. The diffraction pattern is given by the product of the scattering from both the unit cell and the lattice.

The conditions under which constructive interference occurs in a specular geometry, and therefore a diffraction signal can be detected, can be described by Bragg's law:

$$2d_{hkl} \sin\theta = n\lambda \ , \tag{2.3}$$

where d_{hkl} is the lattice plane spacing, θ is the angle of the incident beam, n is an integer, and λ is the wavelength of the incident beam. Figure 2.4 illustrates this relationship.

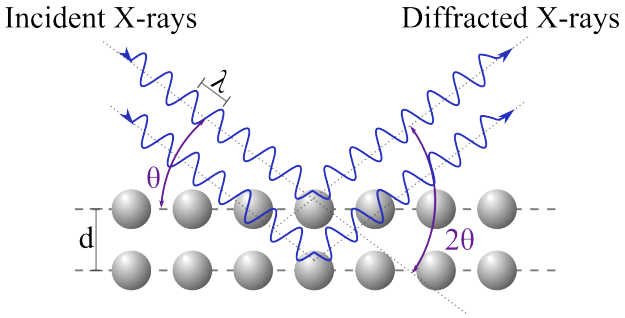


Figure 2.4: Illustration of Bragg's law and constructive interference on the lattice planes of a crystal.

2.3.1.1 Reciprocal Space

In real space the lattice vector $\mathbf{r_n}$ is defined as:

$$\mathbf{r_n} = n_1\mathbf{a} + n_2\mathbf{b} + n_3\mathbf{c} \ , \tag{2.4}$$

where n_i are integers, and $\mathbf{a}$, $\mathbf{b}$, and $\mathbf{c}$ are the unit cell vectors.

The reciprocal lattice vectors $\mathbf{a}^*$, $\mathbf{b}^*$, and $\mathbf{c}^*$ can be expressed through the unit cell vectors in real space:

$$\mathbf{a}^* = 2\pi\frac{\mathbf{b}\times\mathbf{c}}{\mathbf{a}\cdot(\mathbf{b}\times\mathbf{c})} \qquad \mathbf{b}^* = 2\pi\frac{\mathbf{c}\times\mathbf{a}}{\mathbf{a}\cdot(\mathbf{b}\times\mathbf{c})} \qquad \mathbf{c}^* = 2\pi\frac{\mathbf{a}\times\mathbf{b}}{\mathbf{a}\cdot(\mathbf{b}\times\mathbf{c})} \ , \tag{2.5}$$

where $\mathbf{a}\cdot(\mathbf{b}\times\mathbf{c}) = V^*$, the volume of the reciprocal unit cell. A similar relationship to equation 2.4 can be defined for the reciprocal space vector $\mathbf{Q_{hkl}}$:

$$\mathbf{Q_{hkl}} = h\mathbf{a}^* + k\mathbf{b}^* + l\mathbf{c}^* \ , \tag{2.6}$$

where h, k, and l are integers, and $\mathbf{a}^*$, $\mathbf{b}^*$, and $\mathbf{c}^*$ are the unit cell vectors in reciprocal space.

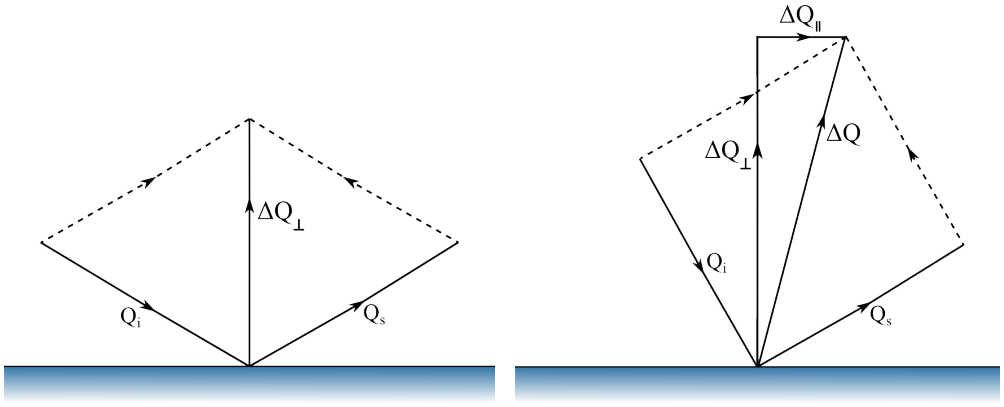
The diffraction condition can be expressed in terms of the reciprocal lattice. A photon of wavelength λ has a wavevector $\mathbf{Q} = \frac{2\pi}{\lambda}$ and in general diffraction involves a change in wavevector $\mathbf{\Delta Q}$:

$$\mathbf{Q} + \mathbf{\Delta Q} = \mathbf{Q'} \ , \tag{2.7}$$

where $\mathbf{Q}$ is the initial wavevector, and $\mathbf{Q'}$ is the scattered wavevector. The diffraction condition is:

$$\Delta\mathbf{Q} = \mathbf{Q_{hkl}} \ . \tag{2.8}$$

In a specular θ-2θ scattering geometry it can be seen that only wavevector changes normal to the surface $\Delta Q_\perp$ can be sampled (see figure 2.5(a)). In an off specular geometry $\Delta Q_\parallel$ transfer within the scattering plane can also be achieved (see figure 2.5(b)). Alternatively, $\Delta Q_\parallel$ transfer orthogonal to the scattering plane can be achieved with a four-circle diffractometer in a specular scattering geometry by rotating the crystal to take the surface normal out of the scattering plane.



(a) Specular scattering geometry (b) Off specular scattering geometry

Figure 2.5: Schematic drawings of wavevector changes for two scattering geometries. Q_i and Q_s are incident and scattered wavevectors and ΔQ is a change in wavevector, with $\Delta Q_\perp$ and $\Delta Q_\parallel$ being the wavevector changes normal and parallel to the surface.

2.3.1.2 Absences and the Structure Factor

The structure factor F_{hkl} can be seen as a mathematical way of representing the interaction between atoms and X-rays. It is given by:

$$F_{hkl} = \sum_{n=1}^{n=N} f_n \exp 2\pi i(hx_n + ky_n + lz_n) \ , \tag{2.9}$$

where hkl are the Miller indices, N is the number of atoms in a unit cell, f_n is the atomic scattering factor (or form factor) and x_n, y_n, z_n are the fractional coordinates of the atoms. f_n represents the amplitude of a wave scattered by an atom, and is influenced by the scattering from both the core and valence electrons of the atom.

The observed intensities I_{hkl} in a diffraction pattern are proportional to the product of the structure factor F_{hkl} with its complex conjugate F^*_{hkl}:

$$I_{hkl} \propto F_{hkl} \cdot F^*_{hkl} \ . \tag{2.10}$$

Systematic absences in a diffraction pattern arise when structure factors are zero due to face or body centering within the unit cell. In particular, for face-centred cubic systems reflections are absent unless h, k, and l are either all odd or all even, while for body-centred cubic cells reflections are absent unless $h + k + l$ is even. Further absences can arise in different space groups due to more specific symmetries. Calculated structure factors for different reflections give their intensities and can therefore be used to predict these absences.

2.3.2 Instrumentation

An X-ray diffractometer typically consists of an X-ray source, a monochromator, a sample holder, and a detector. Figure 2.6 shows the general outline of a powder diffractometer operating in the so called θ-2θ, or Bragg-Brentano, scattering geometry. θ is defined as the angle between the incident beam and the sample surface and 2θ is the angle between the scattered beam and the incident beam.

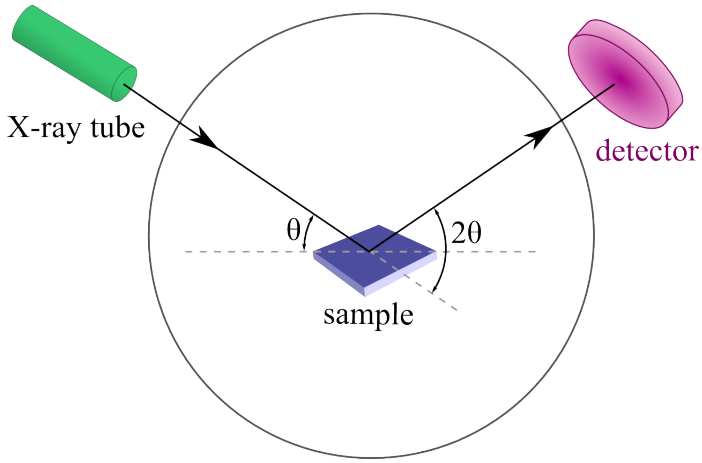


Figure 2.6: Schematic of the general outline of an X-ray diffractometer in θ-2θ scattering geometry.

The most widely used X-ray source for laboratory applications is an X-ray tube, with Cu $K\alpha$ with a wavelength of 1.54056 Å being a common anode material. In addition to laboratory based diffractometers, synchrotron radiation is also employed as an X-ray source. Detectors are often charge coupled devices (CCDs).

2.3.2.1 Four-Circle Diffractometers

Four-circle diffractometers allow the automatic measurement of intensities of all accessible reflections with a single setup of the sample. A schematic drawing of a typical laboratory four-circle diffractometer is shown in figure 2.7. The diffraction plane is formed by the centre of the X-ray source, the sample, and the detector and in most laboratory based diffractometers the so called scattering plane is horizontal. The sample is mounted on a goniometer head itself attached to a Eulerian cradle. The axis perpendicular to the sample surface is called the principal axis.

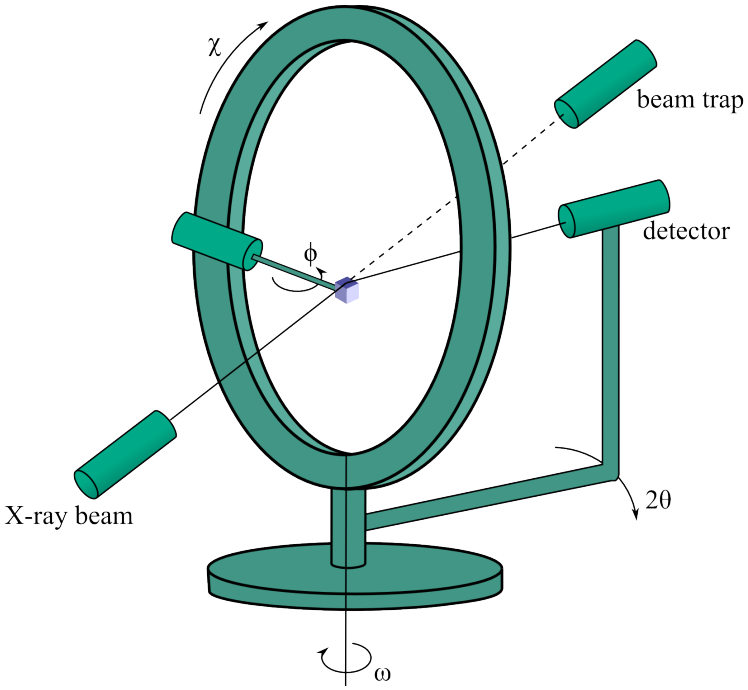


Figure 2.7: Schematic drawing of a typical laboratory based four-circle diffractometer with a horizontal scattering geometry.

There are four axes of rotation which give the spectrometer its name:

- 2θ axis: The detector rotates around the principal axis.
- ω axis: Rotation of the Eulerian cradle to produce sample rocking with the vector normal to the surface in the scattering plane.
- ϕ axis: Azimuthal rotation of the goniometer head, where the sample always stays at the centre of the χ ring. ϕ is usually mounted on the χ ring, so that the ϕ axis moves with χ.
- χ axis: Sample rotation around the Eulerian cradle to take the surface normal out of the scattering plane.

2.4 X-Ray Photoelectron Spectroscopy

X-ray Photoelectron Spectroscopy (XPS) is a widely used technique for qualitative and quantitative analysis of surfaces. It it used to provide information regarding the chemical composition and electronic structure of a material.

2.4.1 Principles and Theoretical Considerations

XPS has its origin in the discovery of the photoelectric effect by Heinrich Hertz in 1887, which involves the interaction between light and matter.[7] When a photon with the energy $h\nu$ interacts with a sample surface, electrons which have a binding energy E_B may be ejected from the sample with a kinetic energy E_k. Ernest Rutherford stated the basic equation describing this process, and XPS, for the first time in 1914.[8] It is presently formulated as the following:

$$E_k = h\nu - E_B - \phi \ , \tag{2.11}$$

where ϕ is the work function of the sample, which gives the minimal energy required to eject an electron. This is nowadays widely known as the Einstein equation. The early experiments concentrated on electrons at the Fermi level where by definition $E_B = 0$. However, provided the photon energy is sufficiently high, both valence and conduction electrons, and core electrons may be emitted. Figure 2.8 shows an energy schematic of photoemission, including the energy levels of a solid state sample and a spectrometer, and the core levels and the valence band of the sample.

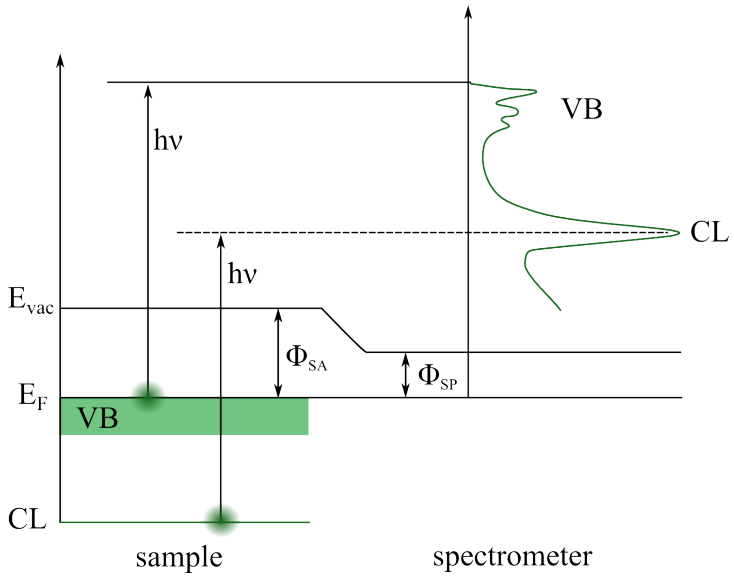


Figure 2.8: Energy schematic of photoemission. Electrons are excited from core levels, CL, and the valence band, VB, above the vacuum level E_{vac} by photons with energy $h\nu$. The work functions of the sample ϕ_{SA} and the spectrometer ϕ_{SP} are also shown.

2.4.1.1 Inelastic Mean Free Path

X-rays are able to penetrate the first few hundred nanometres of a sample. However, due to inelastic scattering within the sample, only electrons from the first few monolayers of atoms are detected. This makes XPS sensitive to the chemical and electronic state of a sample surface. The inelastic mean free path $\lambda_m(E)$ was given by Seah and Dench[9] as:

$$\lambda_m(E) = \frac{A_m}{E^2} + B_m E^{1/2} \ , \tag{2.12}$$

where $\lambda_m(E)$ is the path length in mono layers, A_m and B_m are empirical parameters, and E is the energy. A more complete analysis suggests a pathlength λ of the form:

$$\lambda = \frac{E}{E_p^2[\beta \ln(\gamma E) - \frac{C}{E} + \frac{D^*}{E^2}]} \ , \tag{2.13}$$

where E is the electron energy, E_p is the valence electron plasmon energy, and

β, γ, C, and D are parameters characteristic of the material.[10] An $E^{0.63}$ power law has also been suggested more recently.[11] Figure 2.9 shows the correlation between $\lambda_m(E)$ and E. A minimum can be observed at energies around 40 eV. The dominant mechanism for inelastic electron scattering involves excitation of volume plasmons with energies of around 10 - 30 eV. There is thus a threshold for inelastic scattering but beyond this the scattering probability decreases. This accounts for the minimum in pathlength.

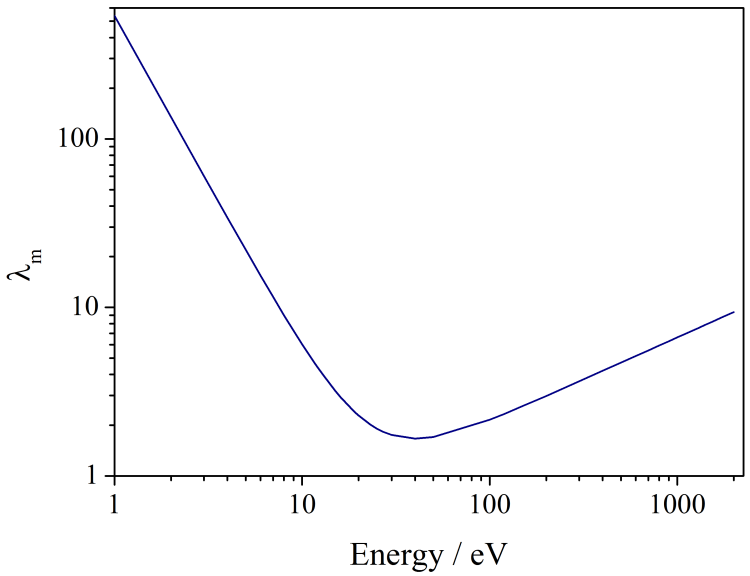


Figure 2.9: Schematic variation of the inelastic mean free path with the kinetic energy of the emerging electron as derived from equation 2.12. The pathlength λ_m is in monolayers.

2.4.1.2 Chemical Shift

Every element has a set of characteristic core lines, with binding energies E_B characteristic of the element. For example, the $3d$ levels of indium metal are $3d_{3/2}$ = 451.4 eV and $3d_{5/2}$ = 443.9 eV, whereas the $3d$ levels of tin are $3d_{3/2}$ = 493.2 eV and $3d_{5/2}$ = 484.9 eV. Figure 2.10 shows an XPS spectrum indicating the core line features for In_2O_3. In addition to core photoelectron peaks, Auger peaks are also observed arising from the decay of a core hole and emission of a third electron.

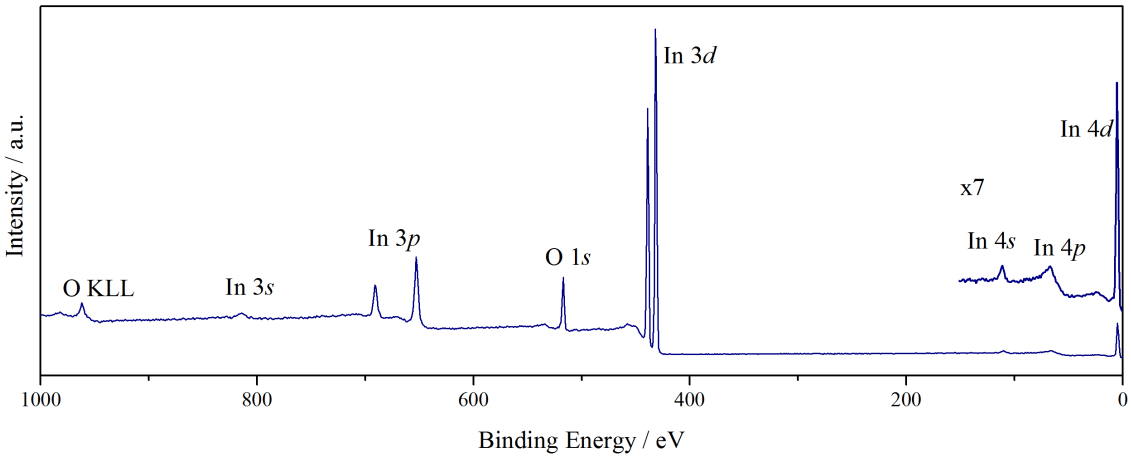


Figure 2.10: X-ray photoelectron spectrum of In_2O_3. The core levels of indium and oxygen as well as an oxygen Auger line are shown.

The level from which the photoemission is occuring is not the only influence on the binding energy of core levels in XPS. Oxidation state and local chemical environment can also have an influence on E_B which can lead to shifts of up to 5 eV. These small shifts are referred to as *chemical shift*, and the ability of XPS to show these is a major strength of the technique. Table 2.1 summarises values for Ti atoms in different oxidation states from the literature. The binding energy BE increases with the oxidation number of Ti.

Table 2.1: Values for binding energy maxima BE_{max}, minima BE_{min}, and averages BE_{av} for the Ti $2p_{3/2}$ core line for different oxidation states of Ti. The values are taken from the NIST X-ray Photoelectron Spectroscopy Database, online version.[12] n_{ref} is the number of available references for a specific core line on the database.

ox. state (compound)	BE_{min} / eV	BE_{max} / eV	BE_{av} / eV	n_{ref}
Ti (0) (metal)	453.2	454.3	453.9	13
Ti (II) (TiO)	454.6	455.9	455.2	3
Ti (III) (Ti_2O_3)	456.8	457.8	457.2	3
Ti (IV) (TiO_2)	458.0	459.6	458.7	91

2.4.1.3 Spin-orbit Splitting

Core level signals in XPS are split into doublets for all orbitals except s orbitals. This is due to spin-orbit splitting between the electron spin and the angular momentum

vector of the orbital. The total angular momentum J is the summation of the spin angular momentum s and the orbital angular momentum l:

$$J = \sum_i j_i = \sum_i (l_i + s_i) \ . \tag{2.14}$$

Core level peaks also show specific intensity ratios that arise from the degeneracy of the two states of the doublet. The degeneracy g is defined as:

$$g = 2j + 1 \ . \tag{2.15}$$

Values for the aforementioned variables for selected orbitals are given in table 2.2.

Table 2.2: Principal quantum numbers n and l, spin-orbit splitting values j, and degeneracy g for selected orbitals.

notation	n	l	j	g
$1s$	1	0	$1/2$	2
$2p_{1/2}$	2	1	$1/2$	2
$2p_{3/2}$	2	1	$3/2$	4
$3d_{3/2}$	3	2	$3/2$	4
$3d_{5/2}$	3	2	$5/2$	6
$4f_{5/2}$	4	3	$5/2$	6
$4f_{7/2}$	4	3	$7/2$	8

2.4.2 Photoionisation Cross Section

Sets of partial ionisation cross sections σ_{IF} can be used to express the rate of photoemission. Given that the dipole approximation is assumed to be valid, meaning that the vector potential of the radiation field is independent of the electron coordinates, the cross sections are given by:

$$\sigma_{IF} = \frac{4\pi\alpha a_0^2}{3h\nu} | \left\langle I | \sum_{j=1}^{N} \widehat{p} | F \right\rangle |^2 \ , \tag{2.16}$$

where α is the fine structure constant, a_0 is the Bohr radius, and $\widehat{p_j}$ are momentum operators.

Continuum wavefunctions and the related atomic ionisation cross sections for the entire periodic table have been calculated using the Hartree-Fock and relativistic Dirac-Fock methods. These methods give reasonable estimates of the one-electron atomic orbital ionisation cross sections except in the case of regions of core thresholds, where resonance enhancements of photoionisation cross sections occur. Here, ionisation of an orbital with angular momentum l can lead to excitation into $l+1$ or $l-1$ continuum states, where the $l \rightarrow l+1$ excitation is dominating in most cases. Valence orbital cross sections in general are largest close to the threshold, in which case the wavelength of the free electron final state matches the "size" of the wavefunction for the atomic orbital that is being ionised.

Cooper minima are a simple matrix element effect, where a change in the sign of the photoionization matrix element occurs as the dominant contribution to the matrix element moves between two protrusions in the radial wavefunction.[13] In the case of very high photon energies the free electron wave oscillates rapidly, and positive and negative contributions to the matrix element almost cancel each other out completely. In comparison, at moderately high photon energies the inner radial extrema in $4s$, $5s$, or $6s$ orbital wavefunctions contribute significantly to the cross section, which therefore decays less rapidly than the cross section for smoothly varying O $2p$ orbitals.

The Gelius model provides a comparatively simple way of calculating molecular valence level cross section at high photon energies of typically around 1 keV and higher. It can be quantified using the cross sections of the constituent atomic or-

bitals of a molecule, where the cross section σ_j^{MO} for the j^{th} molecular orbital is given by:

$$\sigma_j^{MO} = \sum_{A,i} P_{j,i,A} \sigma_i^A \ , \tag{2.17}$$

where σ_i^A are one electron atomic cross sections. i indicates different atomic orbitals and A indicates different atomic centres, so that the $P_{j,i,A}$ factors describe the net atomic population and therefore the contribution of the atomic orbitals to the molecular orbitals. If the basis set is orthonormalised for different atomic centres A, it follows that

$$P_{j,i,A} = (c_{j,i,A})^2 \ . \tag{2.18}$$

When moving from the above model for a molecule to a model for a solid, the total density of states $N_{\text{tot}}(E)$ at an energy E can be broken down into contributions from the atomic orbitals i on the different atoms A present in a solid. This results in the following sum of partial densities of states:

$$N_{\text{tot}}(E) = \sum_{i,A} N_i^A(E) \ . \tag{2.19}$$

The Gelius model for a solid is now as follows:

$$N_{\text{tot}}^W(E) = \sum_{i,A} N_i^A(E) \sigma_i^A \ , \tag{2.20}$$

where $N_{\text{tot}}^W(E)$ is the cross section weighted density of states which can be measured in photoemission experiments at high energies of 10 keV and higher.

2.4.3 Instrumentation

Although the fundamental theoretical concepts of XPS were discovered around the beginning of the 20$^{\text{th}}$ century, it took another 50 years until Kai Siegbahn's ground breaking work led to the construction of the first spectrometers using X-Ray excitation.[14] Siegbahn also coined the term ESCA (Electron Spectroscopy for Chemical Analysis) to emphasise the scope of XPS as a technique.

A major influence on the development of photoemission techniques was the advancement of vacuum technology, as XPS experiments usually take place under ultra high vacuum (UHV) conditions. Figure 2.11 shows the design principle of a spectrometer. A sample is irradiated with a focused beam of X-rays, which have a specific energy $h\nu$. The most widely used X-ray sources for laboratory-based systems are X-ray tubes, which generate X-rays by bombardment of a suitable material with electrons, e.g. aluminium or magnesium. In addition, synchrotron radiation sources can also be used for XPS measurements. The resulting photoelectrons are analysed according to their kinetic energy E_k, multiplied, and detected to give a spectrum.

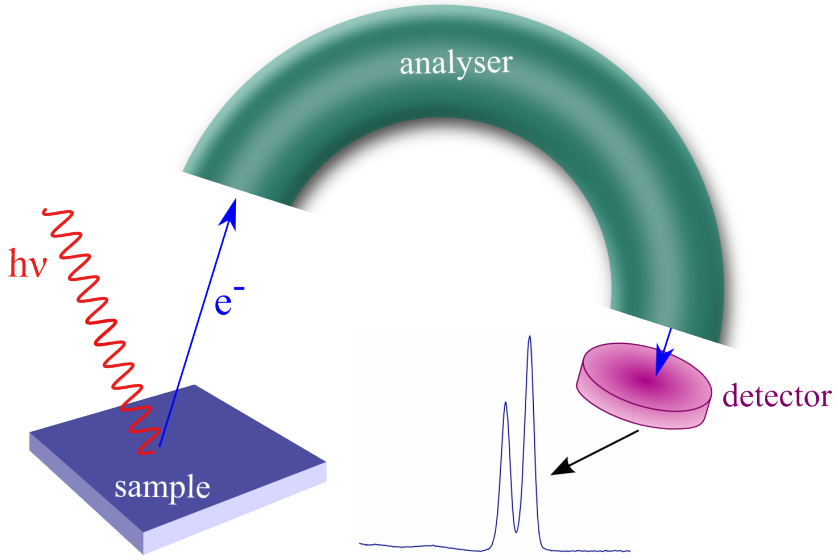


Figure 2.11: Schematic illustration of an X-ray photoelectron spectrometer.

2.4.4 Hard X-ray Photoemission Spectroscopy (HAXPES)

Standard XPS measurements are conducted at energies of 1-2 keV, for example 1253.6 eV for Mg $K\alpha$ or 1486.6 eV for Al $K\alpha$, which are considered soft X-rays. In HAXPES hard X-rays with energies between 2 keV and 15 keV are used. Although experiments with hard X-ray sources, such as Mo $K\alpha$, were conducted early in the development of XPS,[15] and Lindau *et al.* reported the detection of photoelectrons with a kinetic energy E_{kin} of up to 8 keV,[16] valence band HAXPES only started to become a feasible experimental method with the development of third generation synchrotron sources during the 1990s. The main reason is that HAXPES, compared to XPS, suffers from a dramatic decrease in photoemission cross sections, and this must be compensated for with a higher primary photon flux. A consequence is that the higher photon energy ensures a greater sampling depth, of up to 100 Å when looking at relatively shallow core levels.

The reduction of photoemission cross sections is not uniform for the different atomic subshells, but varies for different principal and angular momentum quantum

numbers. For example, the reduction is more pronounced for subshells with high l values, like f and d. This influences the spectral weights of core levels as well as the structure of the valence band.

2.4.4.1 Polarisation Dependent Cross Sections

The photoemission cross sections for different orbitals do not only vary with photon energy, but also change depending on the angle θ between the polarization vector **E** and the wave vector of the emitted photoelectrons **Q**. The cross sections are not symmetric, and this fact can be described by the asymmetry parameter β. Figure 2.12 shows a schematic illustration of the angular dependence of the cross sections with varying β values.

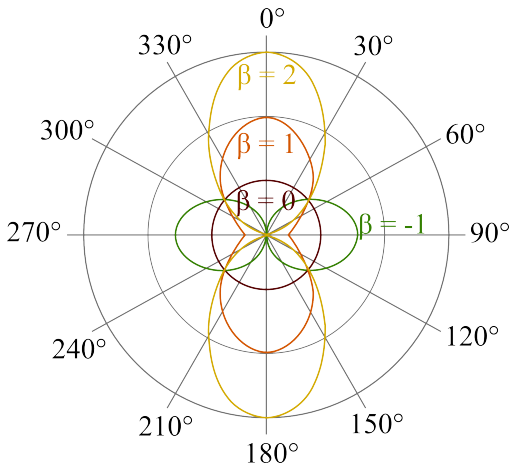


Figure 2.12: Schematic illustration of the angular dependence of the cross sections with varying β values.

The differential cross section, i.e. the cross section in a particular direction, is given by:

$$\frac{d\sigma_i}{d\Omega} = \frac{\sigma_i}{4\pi}\left[1 + \frac{\beta}{2}(3\cos^2\theta - 1) + (\delta + \gamma\cos^2\theta)\sin\theta\cos\varphi\right] , \qquad (2.21)$$

where σ_i is the relativistic photoelectric cross section for the i^{th} atomic subshell,

β, γ, and δ are the asymmetry parameters, θ is the angle between the electric vector of the incident radiation and the electron direction, and φ is the angle between the direction of photon propagation and the plane containing the electron direction and the polarisation vector. γ and δ only appear when quadrupolar terms in the radiation field are important. This is only the case when the wavelength of the radiation is comparable to the size of the orbital. For this to be the case the energy would have to be very high and therefore in most experiments the γ and δ terms can be neglected.

In general β for s orbitals is 2. From figure 2.12 it can be seen that this leads to higher intensity for electron emission parallel to **E**, which translates to a horizontal geometry $\mathbf{E}\|\mathbf{Q}$ with $\theta = 0°$. However, it leads to a very low intensity for electron emission perpendicular to **E**, which translates to a vertical geometry $\mathbf{E}\perp\mathbf{Q}$ with $\theta = 90°$.

2.5 Diffuse Reflectance Spectroscopy (DRS)

Diffuse reflectance of an incident beam from a rough surface gives reflection across a range of directions, not only one specular reflection. The measurement of diffuse reflectance with an ultraviolet (UV) - visible spectrometer can be used to study the optical properties of solids, including ceramic pellets and thin films.

2.5.1 The Kubelka-Munk Theory

In 1931 Paul Kubelka and Franz Munk[17] proposed a set of differential equations describing diffuse reflectance:

$$-di = -(r+s)idx + rjdx \ , \tag{2.22a}$$

$$dj = -(r+s)jdx + ridx \ . \tag{2.22b}$$

These equations describe the processes that occur upon light with the intensity I_0 hitting the surface of an infinitely thick sample (see figure 2.13 for a schematic drawing of the processes). The Kubelka-Munk theory uses a two-flux model where the light is split in two, one part propagating downward i and the other going upward j. If one considers a small layer of the sample x, parts of i and j will be absorbed and scattered. This is expressed by the terms $(r+s)idx$ and $(r+s)jdx$. The light leaving the sample J_0 has lost intensity compared to I_0 due to scattering or absorption.

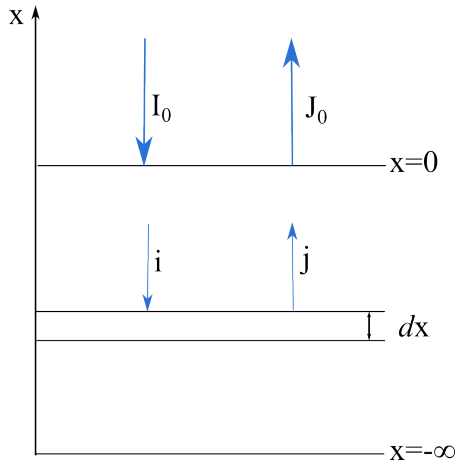


Figure 2.13: Schematic of the Kubelka-Munk two-flux model of diffuse reflectance.

Although there have been many more sophisticated models postulated since the 1930s, the Kubelka-Munk model is still the most common approach to diffuse reflectance spectroscopy.

From the original set of differential equations a Kubelka-Munk formula was derived (see Myrick *et al.*[18] for a complete derivation):

$$\frac{K}{S} = \frac{(R_\infty - 1)^2}{2R_\infty} = F_R \ , \tag{2.23}$$

where K is the effective absorption coefficient, S is the effective scattering coefficient, R_∞ is the reflectance for an infinitely thick sample, and F_R is the Kubelka-Munk function.

To derive a band gap from diffuse reflectance data a Tauc plot is used, plotting $(F_R h\nu)^n$ against $h\nu$, where n is a power dependent on the nature of the transition at the band edge. The band gap can be obtained by extrapolating a linear fit to this plot.

2.5.2 Instrumentation

Figure 2.14 shows the schematics of a Diffuse Reflectance Spectrometer (DRS) with an integrating sphere. A radiation source is monochromated to produce photons of a specific energy $h\nu_i$ in the ultraviolet-visible (UV-vis) region and irradiates the sample, upon which specular and diffuse reflection occurs. The main specular reflection is scattered back along the direction on the incoming beam and leaves the sphere. However, the resulting diffusely reflected light reaches the detector, which is located at the bottom of the integrating sphere.

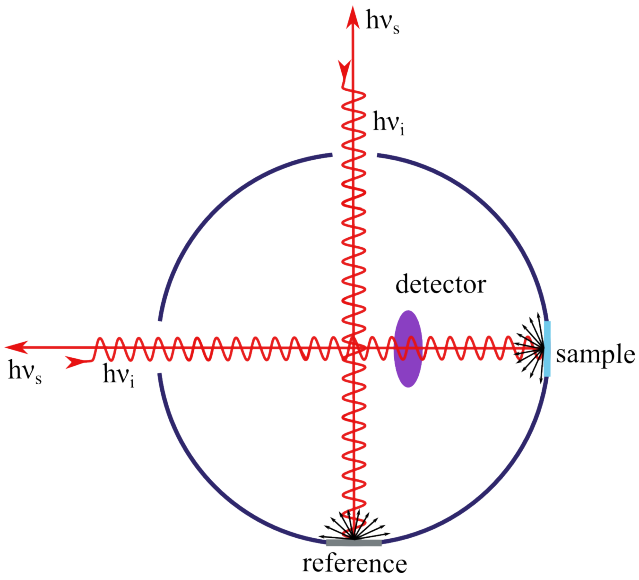


Figure 2.14: Schematic illustration of a diffuse reflectance spectrometer with an integrating sphere. The sample and reference beams enter at mid-point height whereas the detector sits at the bottom of the sphere.

2.6 Raman Spectroscopy

Raman spectroscopy and its underlying physics were discovered in 1928 by Sir Chandrasekra Venkata Raman.[19] This method uses vibrational frequencies to characterise molecules and solids.

2.6.1 Principles and Theoretical Considerations

The underlying process of Raman spectroscopy is a two-photon process involving inelastic light-scattering. The first photon with frequency ν_0, causes a virtual excitation in the sample. The sample then emits a second photon whose energy may differ from that of the incident photon by an energy $\pm h\nu$, where $h\nu$ is a characteristic excitation energy usually in the vibrational regime.

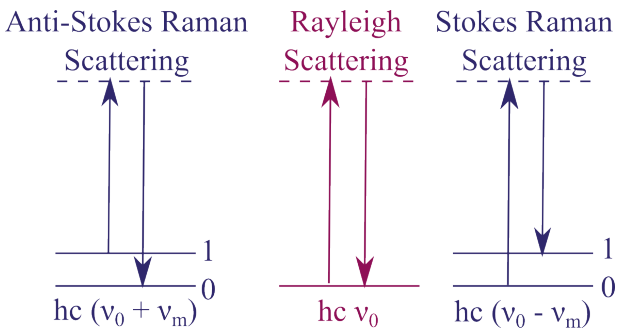


Figure 2.15: Schematic illustration of the different scattering processes occurring in Raman spectroscopy.

Energy gain to give anti-Stokes Raman scattering arises due to thermal population of vibrational energy levels. The electric field E associated with the incident electromagnetic radiation causes a redistribution of the valence electron density relative to the positively charged atomic cores. This induces a dipole μ given by:

$$\mu = \alpha E \ , \tag{2.24}$$

where α is the polarizability. A vibration is Raman active if the polarizability α is changed during the vibration.

As μ and E both have three components in x, y and z directions, the tensor form of equation 2.24 can be written as

$$\begin{bmatrix} \mu_x \\ \mu_y \\ \mu_z \end{bmatrix} = \begin{bmatrix} \alpha_{xx} & \alpha_{xy} & \alpha_{xz} \\ \alpha_{yx} & \alpha_{yy} & \alpha_{yz} \\ \alpha_{zx} & \alpha_{zy} & \alpha_{zz} \end{bmatrix} \begin{bmatrix} E_x \\ E_y \\ E_z \end{bmatrix} \ . \tag{2.25}$$

Using this equation, it can be seen that a vibration is Raman active if one of the parts of the polarizability tensor change during the vibration.[19] This requires that the vibration belongs to the same irreducible representation as one component of the polarizability tensor in the relevant molecular point group or solid state space

group. Since $x \rightarrow -x$, but $x^2 \rightarrow x^2$ etc. under inversion, in groups with inversion symmetry only *gerade* g modes are Raman active and there is mutual exclusion from infrared active *ungerade* u modes.

Although a large number of vibrations are present in crystal lattices, Raman spectra of crystals are often comparatively simple.

2.6.2 Instrumentation

Figure 2.16 shows a schematic illustration of a Raman spectrometer. A laser beam is directed at the sample and the resulting backscattered radiation is filtered to remove elastically scattered light, so that only Raman scattering can reach the spectrometer. The radiation is then detected and the resulting spectrum is recorded.

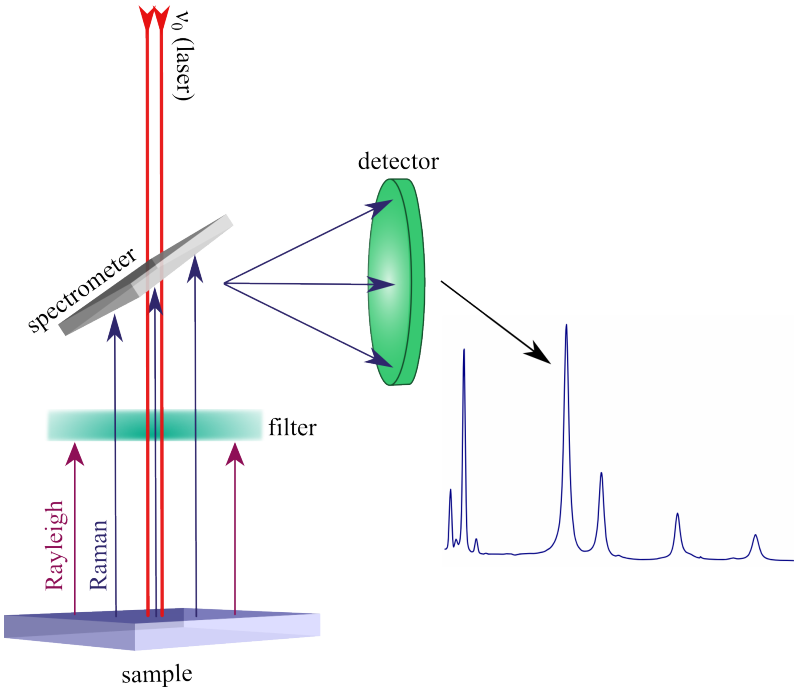


Figure 2.16: Schematic illustration showing a Raman spectrometer.

2.7 Low Energy Ion Scattering

The potential of Low Energy Ion Scattering (LEIS) to provide the atomic composition of the surface layers of a sample was discovered by David Smith during the 1960s.[20]

2.7.1 Principles

During LEIS a sample is bombarded with noble gas ions, such as He^+ and Ne^+, that have a fixed energy E_0 of the order of a few keV. When these ions collide with the atoms on the sample surface, they are backscattered and detected at a fixed angle. The scattering of the ions can be described as elastic binary scattering events.

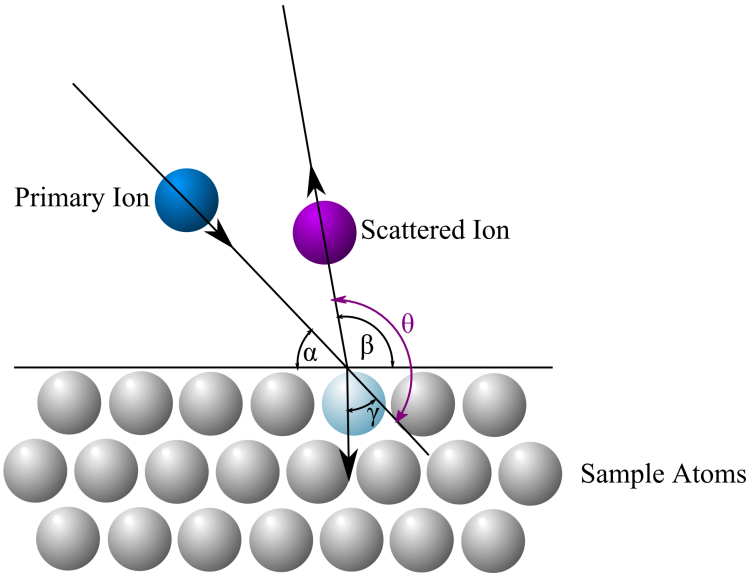


Figure 2.17: Binary scattering of a noble gas ion. The following angles are indicated: scattering θ, incident α, exit β, and recoiling γ.

Figure 2.17 shows binary scattering of an ion on the surface of a sample. The primary ion with mass m_1 and energy E_0 collides with a sample atom of mass m_2. After the collision the scattered ion has a reduced energy E_1 and the sample atom has recoiled with energy E_2. The energy ratio between the initial and final energy

of the scattered ion is given by:

$$\frac{E_2}{E_1} = \left(\frac{\cos\theta \pm \sqrt{\frac{m_2}{m_1} - \sin^2\theta}}{1 + \frac{m_2}{m_1}} \right)^2 , \tag{2.26}$$

where θ is the scattering angle.

The backscattered ions have discrete energies that are closely related to their collision with the surface atoms of the sample. In broad terms, the higher the mass of the surface atom involved in a collision, the higher the energy of the scattered ion. Therefore, information about the sample, including the identity of surface atoms and their concentration, can be obtained. At the same time the ion beam may be used to sputter away surface atoms so that depth profiles may be obtained.

2.7.2 Instrumentation

Conventional hemispherical analysers, as used in XPS, can be used to carry out LEIS measurements using reversed polarities in the electron optics. However, greater detection efficiency is achieved using toroidal electrostatic analysers developed by Brongersma and co-workers.[21] Figure 2.18 shows a widely used layout for dedicated LEIS instruments. A beam of noble gas ions is produced by an ion gun and focused through optics onto the sample. The resulting backscattered ions are collected by an energy analyser and detected.

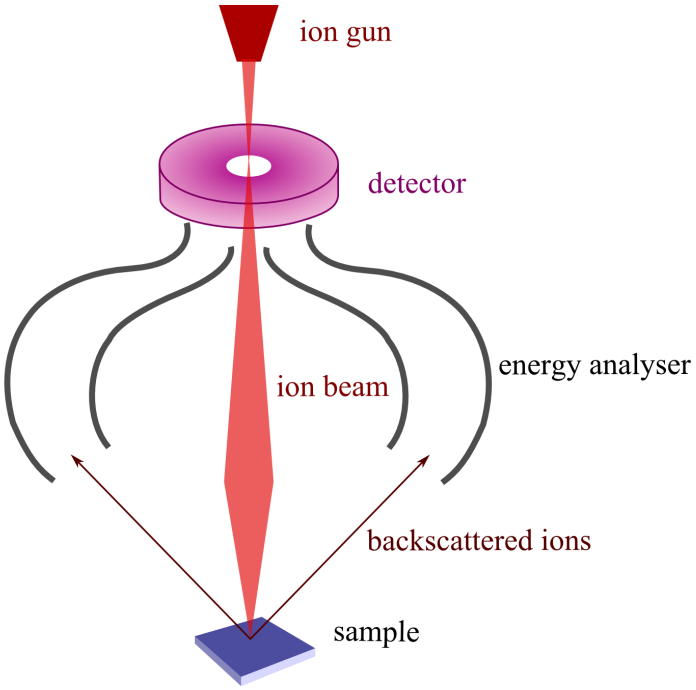


Figure 2.18: Schematic illustration of a LEIS instrument incorporating a toroidal electrostatic analyser.

2.8 Atomic Force Microscopy

Atomic Force Microscopy (AFM) is a scanning probe microscopy technique invented in 1986 by Gerd Binnig, Calvin Quate, and Christoph Gerber.[22] It utilises a small force between the AFM tip and the surface atoms of a sample to create an image of the surface. These forces are in the range of 10^{-11} to 10^{-6} N,[23] which allows non-destructive imaging.

2.8.1 Principles

Figure 2.19 shows a simplified image of the AFM tip tracing the sample surface. AFM records height profiles of the sample that can then be converted into an AFM image, giving a view of surface morphology and structure.

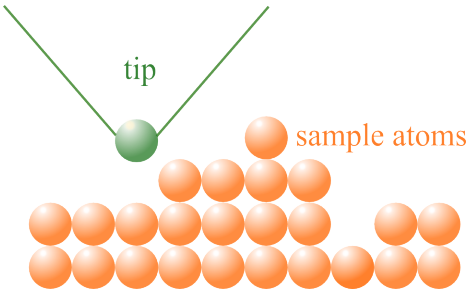


Figure 2.19: Representation of the interaction between the AFM tip and the sample surface.

AFM offers an array of experimental modes suitable for a wide range of samples,[24] the most common of which is contact mode. In contact mode the AFM tip is always touching the surface of the sample and ionic repulsion forces allow the generation of an image of the sample surface. These forces originate from the Pauli exclusion principle, and from Coulombic repulsion between nuclei.

The sum of all forces affecting the deflection of the cantilever can be described by Hooke's law:

$$F = -k \times D \ , \tag{2.27}$$

where F is the force, k is the probe force constant, and D is the deflection distance. In order to measure the small forces occurring in AFM measurements, k has to be as small as possible and the resonance frequency must be kept high.

There are two variations of contact mode: constant force and constant height mode. In constant force mode the deflection of the cantilever is kept constant, while the height of the sample varies. In constant height mode, the change in deflection of the cantilever is monitored whilst the height of the sample is kept constant. Constant force mode is the most common topographic mode of AFM.[25]

2.8.2 Instrumentation

Figure 2.20 shows the basic principle of AFM. The AFM tip, which should ideally consist of only one imaging atom, is mounted on a silicon or silicon nitride cantilever spring. Using a piezoelectric tube, often a PZT scanner based on lead zirconate titanate, the sample can be moved under the tip. When the tip approaches the sample, forces between the main tip atom and the sample atoms deflect it sightly. This deflection is measured by a laser beam, which is reflected from the back of the cantilever and, using mirrors, directed at a photo detector.

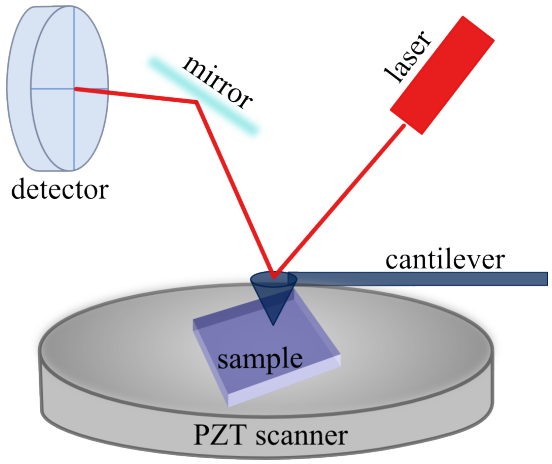


Figure 2.20: Schematic drawing of the principle setup of an AFM system.

2.9 Ellipsometry

Ellipsometry began to be recognised as an analytical method for thin film characterisation in the 1960s following developments in integrated circuits and computational power. It measures the polarisation of light after reflection off a sample. The most general state of polarisation is elliptic, hence the technique's name.[26]

2.9.1 Principles

Ellipsometers are setup in specular geometry, meaning that the angle of incidence and reflection are the same, forming the plane of incidence. When polarised light is reflected by a surface, the change in polarisation can be quantified using the parallel (p-polarisation) and perpendicular (s-polarisation) components, in respect to the plane of incidence. These polarisation components correlate to the reflectivities r_p and r_s. The complex reflectance ratio ρ is defined as

$$\rho = \frac{r_p}{r_s} = \tan\psi e^{i\Delta} \ , \tag{2.28}$$

where $\tan\psi$ is the relative amplitude and Δ is the phase shift. In broad terms ellipsometry data may be modelled in terms of the thickness, roughness, and refractive index of the material in a thin film and the substrate. Data analysis for multilayer samples is more complicated.

2.9.2 Instrumentation

Figure 2.21 shows the setup for phase modulated ellipsometry. A laser, usually a HeNe laser, is used as a light source. The light is then linearly polarised by the polariser and passes through a birefringence modulator before it is reflected off the sample surface. It then passes through the analyser (a second polariser) before it reaches the detector.

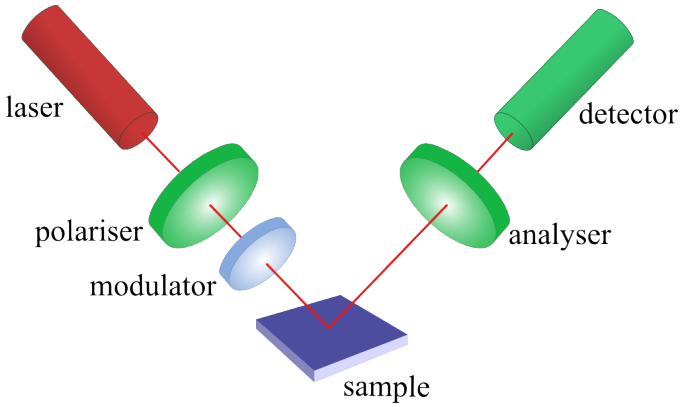


Figure 2.21: Schematic illustration of an ellipsometer.

The main parameters that may be varied in the experiment are the wavelength of the light (spectroscopic ellipsometry) and/or the angle of incidence. In the current work only the angle was varied.

2.10 References

[1] A. Y. Cho and J. R. Arthur, Progress in Solid-State Chemistry **10**, 157 (1975).

[2] P. K. Larsen and P. J. Dobson, editors, *Reflection High Energy Electron Diffraction and Reflection Electron Imaging of Surfaces*, NATO ASI Vol. 188 (Plenum Press, New York, 1988).

[3] D. Mitzi, *Solution Processing of Inorganic Materials* (Wiley, 2009).

[4] J. J. Ebelmen, Justus Liebigs Annalen der Chemie **57**, 319 (1846).

[5] C. J. Brinker and G. W. Scherer, *Sol-Gel Science. The Physics and Chemistry of Sol-Gel Processing* (Academic Press, 1990).

[6] C. Hammond, *The Basics of Crystallography and Diffraction* (International Union of Crystallography/Oxford University Press, 2009).

[7] H. Hertz, Annalen der Physik **267**, 983 (1887).

[8] E. Rutherford, Philosophical Magazine Series 6 **28**, 305 (1914).

[9] M. P. Seah and W. A. Dench, Surface and Interface Analysis **1**, 2 (1979).

[10] C. J. Powell and A. Jablonski, Nuclear Instruments and Methods in Physics Research A **601**, 54 (2009).

[11] J. Rubio-Zuazo and G. R. Castro, Journal of Electron Spectroscopy and Related Phenomena **184**, 384 (2011).

[12] A. V. Naumkin, A. Kraut-Vass, S. W. Gaarenstroom, and C. J. Powell, NIST X-ray Photoelectron Spectroscopy Database, Version 4.1.

[13] J. W. Cooper, Physical Review **128**, 681 (1962).

[14] K. Siegbahn, Nobel Lecture (1981).

[15] E. Sokolowski, C. Nordling, and K. Siegbahn, Physical Review **110**, 776 (1985).

[16] I. Lindau, P. Pianetta, S. Doniach, and W. E. Spicer, Nature **250**, 214 (1974).

[17] P. Kubelka and F. Munk, Zeitschrift für Technische Physik **12**, 593 (1931).

[18] M. L. Myrick *et al.*, Applied Spectroscopy Reviews **46**, 140 (2011).

[19] J. R. Ferraro, K. Nakamoto, and C. W. Brown, *Introductory Raman Spectroscopy* (Academic Press, 2003).

[20] D. P. Smith, Journal of Applied Physics **38**, 340 (1967).

[21] H. H. Brongersma, P. A. C. Groenen, and J. P. Jacobs, Application of low energy ion scattering to oxidic surfaces, in *Science of Ceramic Interfaces*, edited by J. Nowotny, Elsevier, 1994.

[22] G. Binnig, C. Quate, and C. Gerber, Physical Review Letters **56**, 930 (1986).

[23] E. Meyer, Progress in Surface Science **41**, 3 (1992).

[24] F. J. Giessibl, Reviews of Modern Physics **75**, 949 (2003).

[25] P. Eaton and P. West, *Atomic Force Microscopy* (Oxford University Press, 2010).

[26] I. Ohlídal and D. Franta, Ellipsometry of thin film systems, in *Progress in Optics*, pp. 181–282, Elsevier, 2000.

3 Experimental Apparatus and Techniques

This chapter presents the methods and apparatus used in this thesis.

3.1 Molecular Beam Epitaxy

Indium oxide films were grown in an oxide molecular beam epitaxy (MBE) system (SVT, USA) located in the Chemistry Research Laboratory at the University of Oxford. The system is shown in figure 3.1.

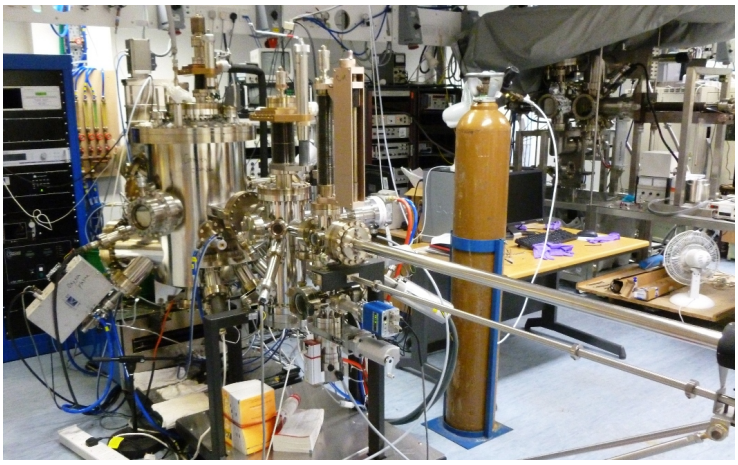


Figure 3.1: The oxide MBE system at the Chemistry Research Laboratory, University of Oxford.

All MBE samples studied in this thesis were prepared by Dr. Kelvin Hongliang

Zhang. The MBE system is operated at a base pressure of 5×10^{-9} mbar and the substrates were heated radiatively using a graphite filament. The substrates were held in place by gravity in a recessed Mo mounting plate. In order to clean the substrates, they were annealed at 900°C for one hour in the oxygen atom beam, and films were grown at a range of temperatures up to 1000°C. The indium effusion cell was set at a temperature of 780°C, and a radio frequency (RF) plasma operating at 200 W with an oxygen background pressure of 3×10^{-5} mbar was used.

3.2 Sol-Gel Dip-Coating

The precursor solutions for sol-gel experiments were prepared in a glove box under a constant flow of dry nitrogen. The solutions were removed from the glove box and transferred into a wide-necked (B29) 50 mL round bottom flask for the dip-coating process. A small motor manufactured by B. Braun was used as the main building block of a custom built dip-coater, shown in figure 3.2.

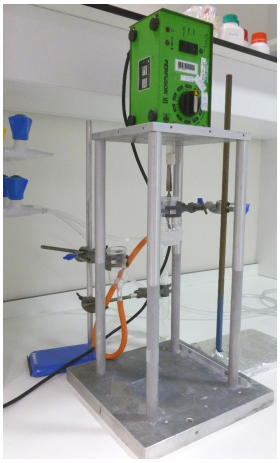


Figure 3.2: Custom build dip-coating apparatus at the Chemistry Research Laboratory, University of Oxford.

The samples were mounted using stainless steel cross-over tweezers and the motor was set at a withdrawal speed of 0.35 cm/min. For the hydrolysis of the films,

nitrogen gas was bubbled through deionised water. Further details of the sample preparations are given in the relevant chapters.

3.3 X-Ray Diffraction

X-ray diffraction patterns were measured using the Phillips PANanalytical X'Pert PRO diffractometer located in the Inorganic Chemistry Laboratory at the University of Oxford. The X-ray source and detector are arranged in a Bragg-Brentano (θ-2θ) geometry. The diffractometer is equipped with a Cu Kα_1 X-ray source, which is monochromated using a curved Ge (111) crystal. The operating conditions included an anode voltage of 40 kV and an emission current of 45 mA. The slit for the incident beam was programmed to always irradiate the entire sample, whereas the slit for the diffracted X-rays was fixed at 0.25 mm. The step size for all measurements was set at 0.0042°, which was interpolated to 0.004° using X'Pert software.

Samples were mounted on a stainless steel holder with a circular recess which measured 10 mm diameter and 2 mm depth. The samples were fixed in the centre of the recess with a small amount of adhesive and the surface was levelled to match the level of the sample holder.

Thin film samples were aligned using a rocking curve scan. Using a fast θ-2θ scan the peak centre of the most intense Bragg reflections was determined. This information was used to set up a rocking curve around the diffraction angle of this reflection. A rocking curve, or ω plot, is a plot of X-ray intensity vs. the incident angle, here called ω, which is equivalent to the angle θ. From the ω-scan a more accurate peak maximum can be obtained and used to compensate for any offset in

the alignment.

This diffractometer has two known sources of impurity radiation:

1. Most of the Cu Kα_2 radiation from the X-ray source is removed by the monochromator. However, a small percentage is reflected, which causes weak shoulders on the higher diffraction angle side of intense Bragg peaks.
2. High energy Bremsstrahlung radiation can ionise $1s$ Ge core electrons of the germanium monochromator leading to Ge Kα radiation with a wavelength λ = 1.2541 Å. This can produce diffraction peaks, especially from high intensity Bragg reflections from single crystal substrates.

3.3.1 XMaS, Beam Line BM28, European Synchrotron Radiation Facility (ESRF), Grenoble, France

Diffraction measurements were conducted on XMaS, a bending magnet beam line at the ESRF.[1] The ESRF is a third-generation synchrotron with an energy of 6 GeV and a current of 200 mA. The storage ring has a circumference of 844 m and hosts more than 40 beamlines, including undulators, multipole wigglers, and dipole magnets.

XMaS is a beam line dedicated to diffraction experiments over an energy range of 2.5 to 15 keV. It is situated on dipole 28, which has a critical energy in the photon beam of 9.8 keV. A photon energy of 12.3984 keV, corresponding to a wavelength λ = 1.0000 Å, was used for all experiments conducted on XMaS which are presented in this thesis.

The optics of the beam line include a Si (111) double-crystal monochromator and a single crystal Si toroidal mirror with a reflective layer of rhodium. The beam

size measured less than 0.5 x 0.5 mm. An 11-axis Huber diffractometer is installed. Whilst it can be operated in both vertical and horizontal scattering geometries, only vertical scattering geometry was used for the measurements presented here.

Two different detectors were used: (i) diffraction from In_2O_3 samples was measured using an avalanche photodiode (APD) with a linear response of up to 2×10^6 counts/s, whilst (ii) diffraction from TiO_2 samples was measured using a Dectris Pilatus 300K-W area detector with a size of 1465 x 195 pixels.

For diffraction experiments at elevated temperatures a ceramic heater custom build for the XMaS beamline was used which covers a temperature range of 298 to 1300 K.[2]

3.3.2 Beam Line I16, Diamond Light Source (DLS), Rutherford-Appleton Laboratory, Harwell, UK

In addition to measurements undertaken at XMaS further diffraction experiments were conducted on beam line I16 at the DLS.[3] The DLS is a third-generation medium energy synchrotron with an energy of 3 GeV. The storage ring has a circumference of 561 m and currently houses 20 beamlines with more to be installed during the next phase of construction.

I16 is an undulator beamline with an energy range from 3.3 keV to 15 - 25 keV depending on the optical configuration. A photon energy of 12.3984 keV, corresponding to a wavelength $\lambda = 1$ Å, was used for the experiments presented in this thesis.

The beamline incorporates a large six-circle kappa diffractometer which allows flexible access to reciprocal space. A Dectris Pilatus 100K area detector with a size of 487 x 195 pixel was used.

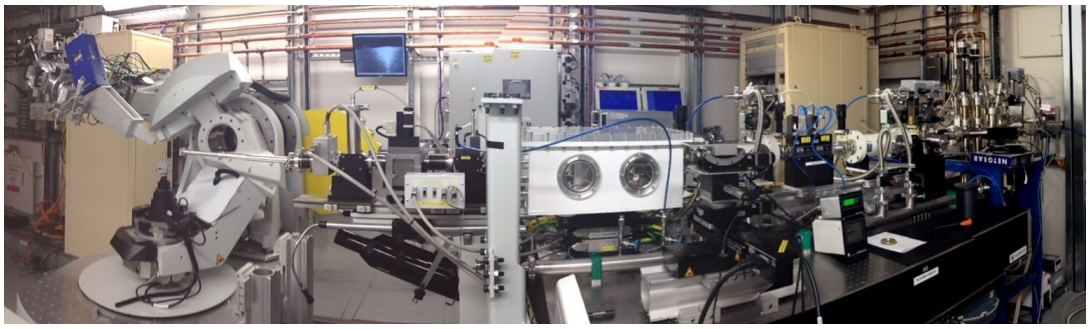


Figure 3.3: Photograph of the experimental hutch at the I16 beam line at the Diamond Light Source including the six-circle kappa diffractometer on the left.

3.4 X-Ray Photoelectron Spectroscopy

3.4.1 Scienta ESCA 300 Spectrometer, Daresbury Laboratory, UK

High resolution X-ray Photoemission Spectra (XPS) of ceramic samples were recorded using the Scienta ESCA 300 spectrometer at the National Centre for Electron Spectroscopy and Surface Analysis (NCESS), Daresbury Laboratory.[4,5]

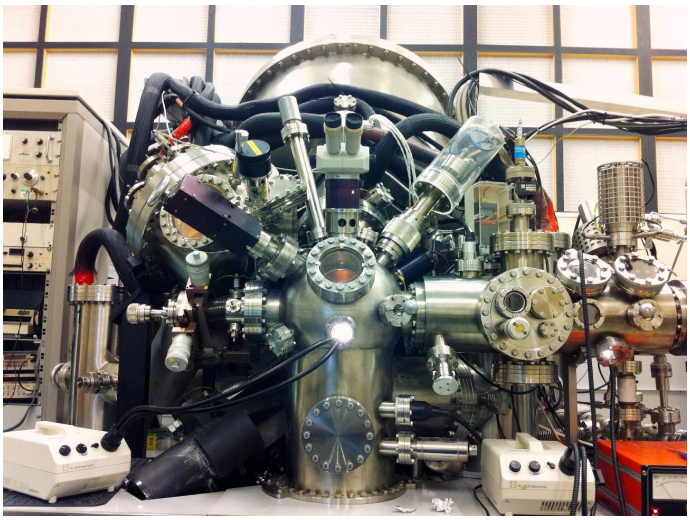


Figure 3.4: Photograph of the Scienta ESCA 300 spectrometer at the National Centre for Electron Spectroscopy and Surface Analysis (NCESS), Daresbury Laboratory.

This system uses a high power rotating anode producing monochromatised Al K_α (1486.7 eV) or Cr K_β (5946.7 eV) radiation. The rotating anode is a 300 mm diameter water-cooled Ti alloy disc spinning at speeds of up to 10,000 rpm. An electron beam with a maximum power of 8 kW from a two-stage fine-focus gun is directed onto Al or Cr bands on the edge of the anode. The electron gun was operated at 14 keV, 200 mA, and 2800 W. X-rays from the anode are collected by the monochromator, a seven quartz crystal system, and focused into a line with a width of 0.5 mm and a length of 6 mm. The base pressure in the analysis chamber is approximately 5×10^{-10} mbar. The photoelectrons emitted from the sample are focused onto the entrance of a 300 mm radius hemispherical analyser. Using this equipment a minimum overall resolution of 0.3 eV is possible, but in the experiments conducted here we used an analyser pass energy of 150 eV and 0.8 mm slits giving a resolution of 0.4 eV. The system employs a detector system consisting of two channel plates, a phosphor screen, and a TV camera. The data collected was analysed using CasaXPS software.

3.4.2 Kratos Axis Ultra-DLD, Cardiff University, UK

Additional high resolution XPS was conducted on the Kratos Axis Ultra-DLD system located in the Wolfson Nanoscience Laboratory of the Cardiff Catalysis Institute at Cardiff University. Figure 3.5 shows the Kratos system at Cardiff, which operates at a base pressure of approximately 1×10^{-9} mbar.

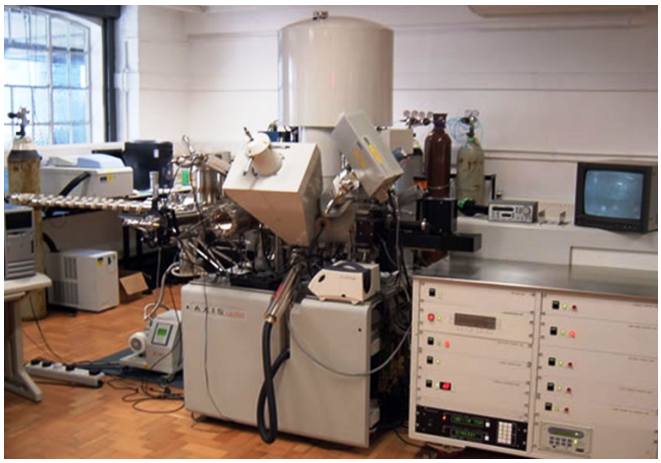


Figure 3.5: The Kratos Axis Ultra-DLD system in the Wolfson Nanoscience Laboratory of the Cardiff Catalysis Institute at Cardiff University (photo taken by Dr. David Morgan).

This system has a resolution better than 0.5 eV and can either use a dual anode with unmonochromatised Mg and Al K_α radiation or monochromatised Al K_α radiation. It is equipped with a 165 mm mean radius 180° hemispherical analyser and a delay-line detector (DLD), comprising a multi-channel plate stack above a delay-line anode. The latter was used in all experiments described here with the anode running at 10 mA emission current and 15 kV anode voltage. Although the power input into the X-ray gun of the Kratos system is only 150 W and therefore a factor of almost 20 lower than in the Scienta spectrometer, the analyser is coupled to a magnetic immersion lens and collects electrons over an angular range of ±30°, as compared to about ±10° in the Scienta spectrometer. This recovers a factor of 10 in the intensity, which coupled with the greater efficiency of the DLD detector means count rates are comparable in the two instruments. In addition the Kratos system

incorporates a charge neutralisation system coupled into the magnetic immersion lens giving superior performance on highly insulating materials. CasaXPS software was used to analyse the collected data.

Sputtering experiments were conducted using a rastered Kratos minibeam-I ion source for argon etching. An area of 5 x 5 mm was etched with the ion gun operating at 4 keV and 15 mA, and an argon pressure of 1×10^{-6} mbar.

3.4.3 Thermo Scientific K-Alpha, University College London, UK

Further XPS measurements were conducted on a Thermo Scientific K-Alpha spectrometer located at University College London. This system employs a monochromated Al K_α X-ray source, a 180° double focussing hemispherical analyser, and a 128 channel position sensitive detector.

3.4.4 Beam Line BL12XU, SPring-8, Hyogo, Japan

Hard X-ray PhotoElectron Spectroscopy (HAXPES) was conducted at the Taiwan beam line BL12XU at the Super Photon Ring - 8 GeV (SPring-8) located in the Harima Science Garden City in the Hyogo prefecture, Japan. SPring-8 is a large third-generation synchrotron operating with an energy of 8 GeV, and it currently delivers the most powerful synchrotron radiation available. The circumference of the storage ring is 1436 m, currently accommodating 62 operational beamlines, based on undulators, bending magnets, and wigglers. Beamline BL12XU is based on an undulator and a diamond (111) monochromator, and can deliver photon energies of

between 4.5 and 25 keV. Since 2006 this beamline has had a sideline dedicated to HAXPES. A photon energy of 6472 eV was chosen for the experiments presented in this thesis.

The unique feature of the beamline is that it involves two separate analysers allowing two electron optical geometries, referred to as horizontal and vertical. Synchrotron radiation from an undulator is strongly polarized in the horizontal plane. In horizontal geometry, the angle between electron emission and the polarization vector of the synchrotron beam θ is therefore 0°, whereas in vertical geometry θ is 90°.[6] Figure 3.6 shows the end station of the beam line with both analysers.

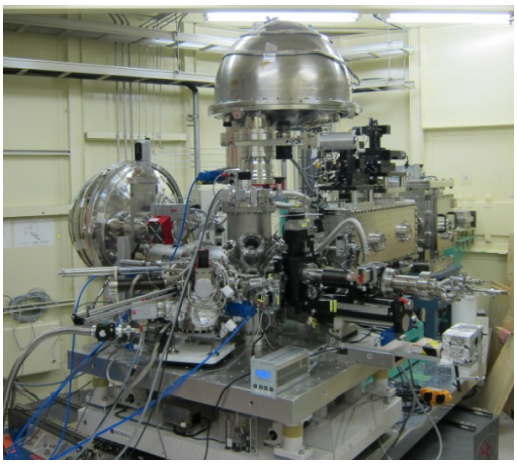


Figure 3.6: Endstation of beam line BL12XU at SPring-8 showing the two analysers which allow measurements in both horizontal and vertical geometry.

3.5 Diffuse Reflectance Spectroscopy (DRS)

Diffuse reflectance measurements were conducted on a PerkinElmer Lambda 750S instrument located in the Inorganic Chemistry Laboratory at the University of Oxford. This system incorporates deuterium and tungsten halogen light sources, double holographic grating monochromators, and a 60 mm integrating sphere coated in Teflon. It can operate at wavelengths from 200 - 2500 nm, with an ultraviolet -

visible (UV-vis) resolution of 0.17 - 5.00 nm and a near infrared (NIR) resolution of 0.20 - 20.00 nm.[7]

Ceramic pellets were studied in reflection, with Teflon discs in the reference beam. Thin film samples were studied in transmission.

3.6 Raman Spectroscopy

Raman spectra were recorded using a PerkinElmer RamanStation 400F dispersive Raman spectrometer located in the Inorganic Chemistry Laboratory at the University of Oxford. It uses a near infrared laser with a wavelength of 785 nm which delivers a maximum of 100 mW at the sample, with a laser spot size of 100 μm. It has a spectral range of 95 - 3500 cm^{-1} Raman shift with a pixel resolution of 1 cm^{-1} across the entire range.[8]

This system has a high sensitivity open electrode CCD detector with a 1024 x 256 pixel sensor, which is air-cooled to -50°C during operation.

The samples were mounted on microscope slides and aligned with the help of a CCD camera.

3.7 Low Energy Ion Scattering (LEIS)

A Qtac^{100} instrument by ION-TOF GmbH, located at Imperial College, London, was used to conduct LEIS measurements on ceramic pellets. The base pressure was 3×10^{-10} mbar, with a working pressure in the region of 10^{-8} mbar. This instrument is fitted with a double toroidal energy analyser which collects backscattered ions at

an angle of 145° from all azimuth angles.[9]

The sample surfaces were cleaned using Ar^+ sputtering with 500 eV ions incident at 60° to the surface normal. The sputtered area was 2000 x 2000 μm^2. The Ar^+ beam was also used for depth profiling. For the analysis Ne^+ ions at 5 keV or He^+ at 3 keV and normal incidence were used with the sputtered area being 1000 x 1000 μm^2. Electron charge compensation was employed to counteract the accumulated charge during the analysis.

3.8 Atomic Force Miscroscopy

Atomic Force Microscopy (AFM) was employed to examine the surfaces of the thin films produced by sol-gel dip-coating, using a Digital Instruments Multimode SPM instrument located in the University of Oxford Surface Analysis Facility.[10] Two scanners with lateral ranges of 100 μm and 10 μm were operated in contact mode using silicon nitride probes (Nascatec GmbH model NST NCHFR).

Image processing, including the flattening of the images, was performed using the Nanoscope software.

3.9 Ellipsometry

The Beaglehole Instruments Picometer Ellipsometer used during this work is located in the University of Oxford Surface Analysis Facility. It uses a technique known as phase modulated ellipsometry (PME) which results in the ellipsometer being faster, more sensitive, and easier to use than conventional ellipsometers. It employs a pho-

toelastic birefringence modulator to analyse the polarisation of light that is reflected by the sample.

This system uses a HeNe laser with a wavelength λ of 632.8 nm. The light passes through a fixed polariser oriented at 45° to the plane of incidence, followed by the modulator. After being reflected by the sample, the phase modulation of the light beam is converted to an intensity modulation by the analyser and the resulting intensity is measured by the detector.

3.10 References

[1] S. D. Brown *et al.*, Journal of Synchrotron Radiation **8**, 1172 (2001).

[2] D. Bellet *et al.*, Journal of Applied Crystallography **36**, 366 (2003).

[3] S. Collins *et al.*, AIP Conference Proceedings **1234**, 303 (2010).

[4] U. Gelius *et al.*, Journal of Electron Spectroscopy and Related Phenomena **52**, 747 (1990).

[5] G. Beamson *et al.*, Surface and Interface Analysis **15**, 541 (1990).

[6] J. Weinen *et al.*, Hard x-ray photoelectron spectroscopy: New opportunities for chemical and physical analysis, in *Max-Planck-Institut für Chemische Physik fester Stoffe Research Reports*, pp. 99–102, 2009-2010.

[7] PerkinElmer, the new LAMBDA™ 750 UV/Vis/NIR spectrophotometer from PerkinElmer, 2007.

[8] PerkinElmer, RamanStation 400 and 400F Technical Specifications, 2007.

[9] H. H. Brongersma, T. Grehl, E. R. Schofield, R. A. P. Smith, and H. R. J. ter Veen, Platinum Metals Review **54**, 81 (2010).

[10] Digital Instruments, *MultiMode™ SPM Instruction Manual*, 1997.

4 Reciprocal Space Mapping of In_2O_3 on Y-doped ZrO_2 (111) and (110)

4.1 Introduction

Due to the renewed interest in the basic physical properties of In_2O_3, the need for high quality samples has led to attempts to grow single crystal thin films by oxygen-plasma assisted molecular beam epitaxy (MBE).[1–4] The body-centred cubic bixbyite structure of In_2O_3 is closely related to the fluorite structure. Due to this relationship oxygen deficient fluorite Y-stabilised cubic zirconia, $Zr_{1-x}Y_xO_{2-x/2}$ or YSZ, which belongs to the space group $Fm\bar{3}m$, has become widely used as a substrate for epitaxial growth of indium oxide thin films.

The lattice parameter of YSZ increases with the Y doping level and is measured to be 5.1447 Å at the 17% doping level used in the here presented work. The mismatch m between $2a_s$ for YSZ and a_e for In_2O_3 can be determined using the following equation:

$$m = \frac{a_e - 2a_s}{2a_s} \ . \tag{4.1}$$

A value of -0.017, i.e. a mismatch of -1.7%, can be derived for the presented case, where the negative value indicates that the epilayer is under tensile stress.

The orientation of the YSZ substrate has a critical influence on the growth morphology of the In_2O_3. Continuous or near continuous films are obtained on (111) oriented substrates.[4,5] In contrast, on (110) substrates rod-like growth is observed with the long axis of the rods lying along the $\left[1\bar{1}0\right]$ direction,[6] while on (001) substrates square islands with edges aligned along $\langle 110 \rangle$ directions are obtained.[1,7] For both In_2O_3 and YSZ, the surface energies γ for the low index terminations follow the sequence $\gamma(001) > \gamma(110) > \gamma(111)$.[6,8,9] Table 4.1 lists the values for the surface energies.

Table 4.1: Surface energies for the low index surface terminations of In_2O_3.[8]

Surface	Bulk-terminated surface energy / Jm^{-2}	Relaxed surface energy / Jm^{-2}	Relaxation energy / Jm^{-2}
(100) In terminated	2.721	2.088	0.633
(100) O terminated	2.449	1.759	0.690
(110)	1.595	1.070	0.525
(111)	1.522	0.891	0.631

In this chapter reciprocal space mapping using synchrotron-based X-ray diffraction (XRD) is used to investigate two types of MBE-grown samples.

To begin with, In_2O_3 thin films on Y-doped ZrO_2 (111) are investigated, with a focus on strain and strain relaxation. Recent interest in the influence of strain on indium oxide has been stimulated by the finding that epitaxial tensile strain may be used to tune the band gap of In_2O_3 thin films.[10,11] The growth of epitaxial films was confirmed using X-ray diffraction (XRD) and transmission electron microscopy (TEM). The obtained results from reciprocal space mapping are discussed in rela-

tion to the morphologies of the films revealed by atomic force microscopy (AFM).

Subsequently, the growth of In_2O_3 nanorods on Y-doped ZrO_2 (110) is investigated. The growth of one-dimensional (1D) nanowires and nanoribbons of semiconducting materials has received growing attention due to potential uses in field effect transistors and gas sensors.[12–19] However, most of the well-established vapour deposition techniques lead to a tangled mass of interpenetrating structures.[15,18,20,21] Epitaxial growth of 1D nanostructured materials on single crystal substrates provides a general approach to precise control over the alignment and morphology of the epilayer. In order to achieve an effective control over the epilayer, it is necessary to develop a clear understanding of the mechanisms which drive the formation of the nanorods. Here we use reciprocal space maps in combination with AFM results to study the evolution of the nanorods with substrate temperature and investigate their strain and tilt.

4.2 Experimental

In_2O_3 thin films and nanorods were grown on 1 x 1 cm (111) and (110) oriented Y-stabilized ZrO_2 substrates with a nominal Y doping level of 17% in an ultrahigh vacuum oxide MBE system. All samples were prepared by Dr. K. H. L. Zhang, who also conducted TEM and AFM characterisation of the samples. XRD for these samples was measured on the Phillips PANanalytical X'Pert PRO diffractometer.

Thin films were grown at a substrate temperature of 700 °C in growth runs with a duration of between 10^3 and 12×10^3 s. The nominal growth rate was 0.035 nm/s as determined by HRTEM measurements.[11] The thickness of the three samples studied

here varied between 35 and 420 nm.

Nano rod samples were grown at a range of substrate temperatures between 500 and 1000 °C. Most of the data presented in this chapter relates to samples with a deposition time of 3000 s which corresponds to a film thickness of 100 nm assuming a layer growth mode.

Reciprocal space mapping of all samples was conducted on the XMaS beam line (BM28) at the ESRF, Grenoble, France. See section 3.3.1 for more details on the experimental setup. Reciprocal space maps were built up from a series of line scans along a chosen transverse direction for an incrementing series of fixed longitudinal wave vector transfers.

4.3 Thin films of In_2O_3 on Y-doped ZrO_2 (111)

To confirm epitaxial growth of the In_2O_3 thin films, θ-2θ diffraction profiles were measured on the Phillips diffractometer. The pattern for the 420 nm thick sample is shown in figure 4.1(a). (222) and (444) epilayer peaks are found at diffraction angles slightly above the substrate (111) and (222) Bragg reflections. In expanded scans of the substrate (111) and the film (222) reflection, shown in figure 4.1(b), a shift of the epilayer peak to smaller diffraction angles with increasing thickness can be observed. This is discussed further below.

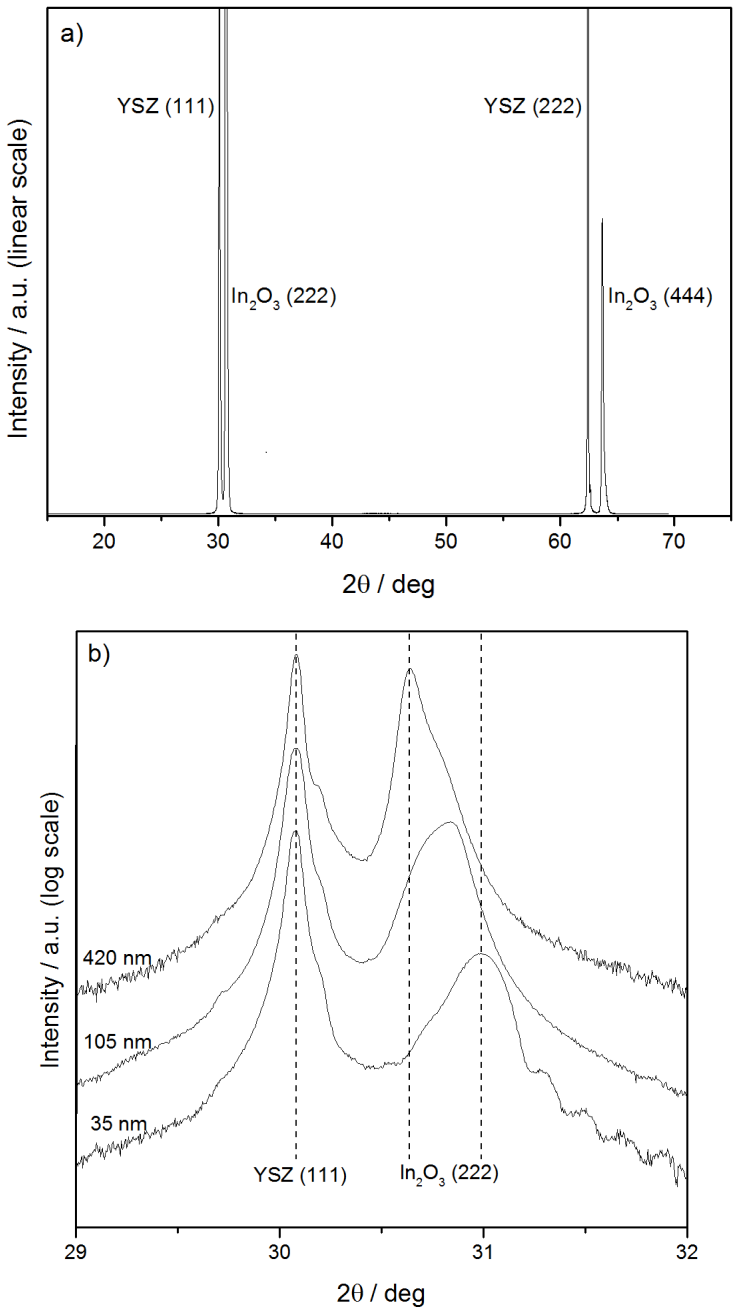


Figure 4.1: θ-2θ diffraction patterns for the three samples used in reciprocal space mapping. (a) Wide scan for the sample with thickness 420 nm showing (111) and (222) reflections of the substrate and (222) and (444) reflections for the thin film on a linear scale. (b) Expanded scan of the substrate (111) and film (222) Bragg reflections for all three samples on a logarithmic scale.

Epitaxial growth was further confirmed by high resolution TEM (HRTEM), which was conducted by Dr. K. H. L. Zhang. Figure 4.2 shows an HRTEM image of a

section of 70 nm thick In_2O_3 film grown on Y-stabilized ZrO_2. The thickness of this film lies between the two thinner samples used for reciprocal space mapping here. A well defined interface between film and substrate can be observed, and in atomic-scale images the excellent quality of the epitaxial thin film is apparent.

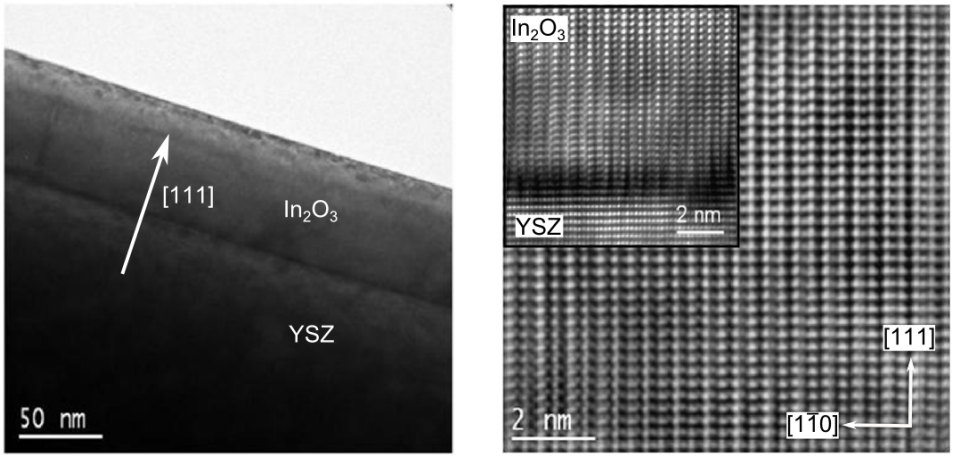


Figure 4.2: Cross-sectional HRTEM images of an In_2O_3 (111) sample with a thickness of 70 nm. Left panel: low-resolution image showing sample morphology. Right panel: Atomic-scale resolution image with the inset showing the interface region. All images are viewed down the $[11\bar{2}]$ direction.

AFM images of the three samples with thicknesses of 35, 105, and 420 nm, also collected by Dr. K. H. L. Zhang, are shown in figure 4.3. The thinnest film shows characteristic crosshatch ridges running across the sample. The ridges have a typical height of 1.8 nm, giving an overall root mean square (RMS) roughness of 1.4 nm. They are preferentially aligned along the $\langle 110 \rangle$ directions with a crosshatch angle of 60°, reflecting the 3-fold rotational symmetry of the (111) surface of the substrate. This pattern has previously been attributed to an array of dislocations at the interface, especially in systems with a lattice mismatch below 2% before, e.g. $Si_{1-x}Ge_x/Si$.[22–24] The 105 nm thick sample shows pinholes caused by a dewetting process, increasing the RMS roughness to 5.2 nm. In the 420 nm thick sample the coverage is sufficient to fill in the pinholes and protruding triangular islands form, which leads to a further increase in RMS roughness to 11.0 nm.

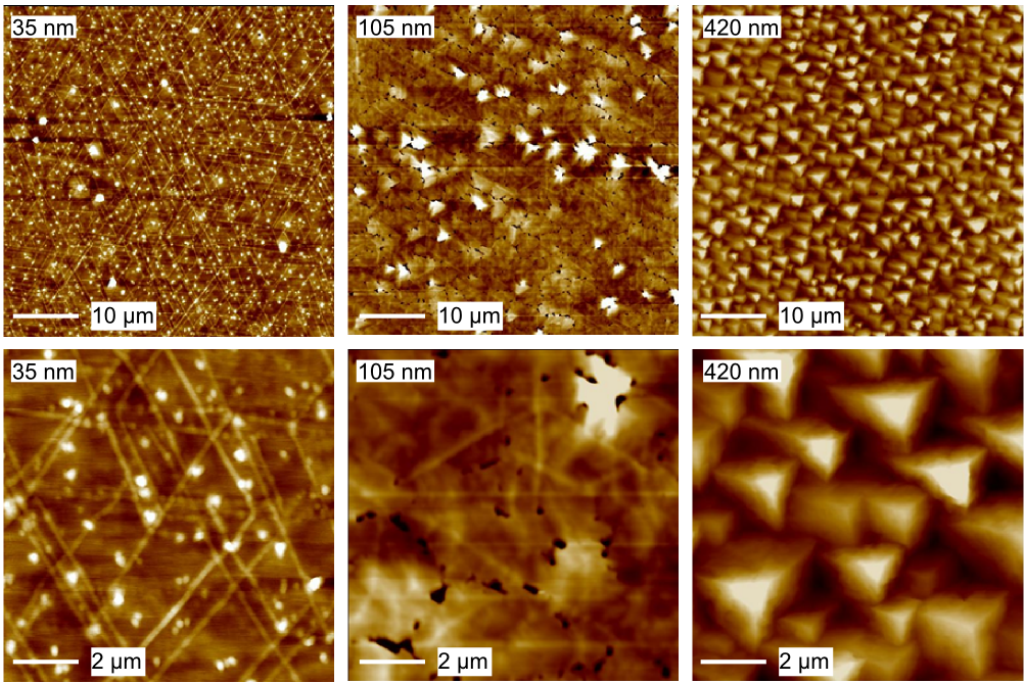


Figure 4.3: AFM images of samples with thickness 35, 105, and 420 nm. The top row shows images with a dimension of 50 × 50 μm and the bottom row shows images with a dimension of 10 × 10 μm. The RMS (root mean square) roughness for the three samples was calculated from the 50 μm images, giving the following values: 1.4, 5.2, and 11.0 nm, with vertical ranges of 30, 80, and 100 nm.

Reciprocal space maps taken around the epilayer (666) reflection are shown for three samples with thicknesses of 35, 105, and 420 nm in figure 4.4. The transverse wave vector transfer is along the $[1\bar{1}0]$ direction in figure 4.4(a) and along the alternative high symmetry $[11\bar{2}]$ direction in figure 4.4(b). In both cases, the longitudinal wave vector transfer is along the [111] direction. It is apparent in all shown reciprocal space maps that the scattered intensity is at a maximum at zero transverse wave vector transfer. This is in contrast to the situation found on (001) oriented YSZ substrates where the scattering intensity is displaced from zero due to tilting of the epilayer through an angle of about 0.7° along <110> directions.[25] From the lack of shift in the samples presented here, it can be concluded that epilayers of In_2O_3 grow on (111) oriented YSZ substrates without any tilt of this sort.

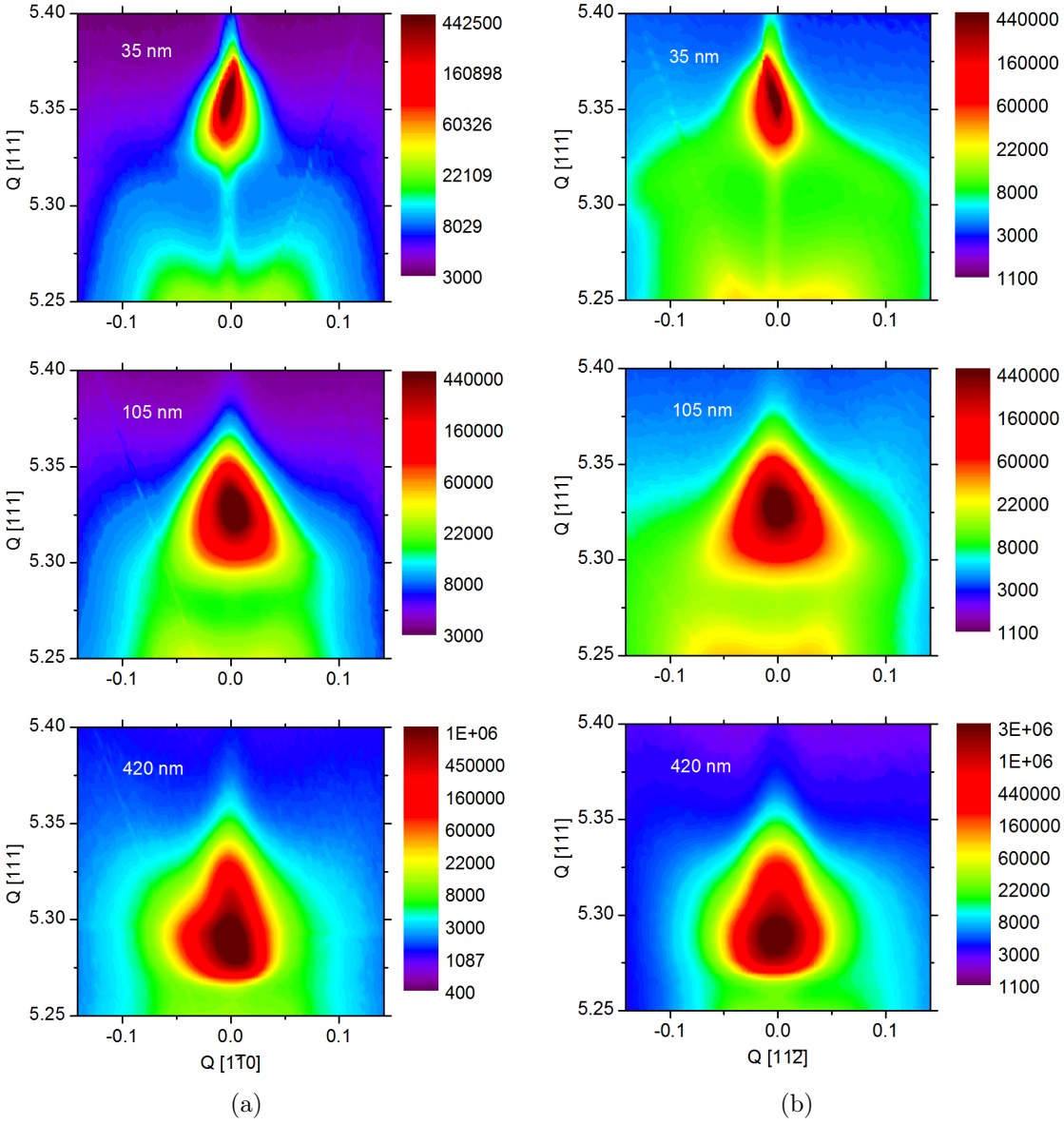


Figure 4.4: Reciprocal intensity space maps for the three samples studied taken around the epilayer (666) reflection. The horizontal axis gives transverse wave vector transfer along the (a) $[1\bar{1}0]$ direction and (b) $[11\bar{2}]$ direction and the vertical axis gives longitudinal transfer along the [111] direction in reciprocal lattice units of the substrate.

Two important trends are observed in both sets of maps shown in figure 4.4.

1. The position of maximum intensity moves to progressively lower $Q[111]$ with increasing sample thickness, approaching the value of $Q[111] = 5.284$ substrate reciprocal lattice units characteristic for bulk In_2O_3. The pronounced shift to higher $Q[111]$ found for the thinnest 35 nm thick film arises from

epitaxial strain, which leads to an expansion in the in-plane lattice spacings and a corresponding contraction normal to the surface via the Poisson effect. Progressive strain relaxation with increasing film thickness allows the films to relax back toward the bulk lattice spacing of In_2O_3.

2. The full width at half maximum height ΔQ for line profiles running through the position of maximum scattering intensity in a transverse direction increases with increasing film thickness, as shown in figure 4.5.

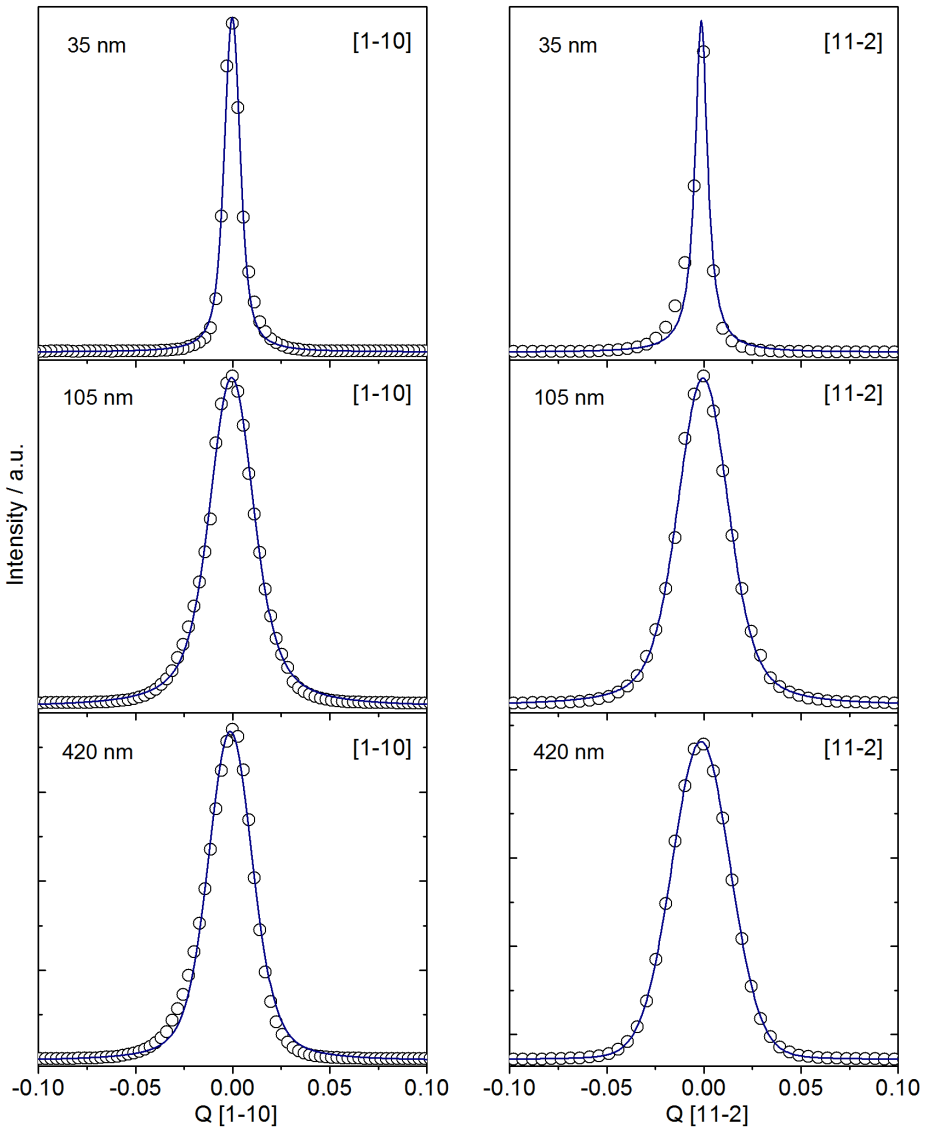


Figure 4.5: Line profiles on a linear scale for transverse cuts through the maps in figure 4.4(a) and figure 4.4(b) at the longitudinal wave vector corresponding to maximum intensity. The Q transfer is given in terms of reciprocal lattice units of the substrate.

Values for the full widths at half maximum height ΔQ were derived from fitting transverse scans through (666) Bragg peaks to a Voigt function, which are summarised in table 4.2. Values for the (444) reflection are also included for transverse scans along $[1\bar{1}0]$. Because the (444) reflection has a much higher intensity than the (666) reflection, attenuators had to be inserted into the beam. However, the calibration factors on the attenuators were incorrect. Unfortunately this led to discontinuities in the individual line scans used to build up the maps around the (444) reflection. These artefacts can be seen in the reciprocal space maps around the epilayer (444) reflection, which are shown for two samples with thicknesses of 35 and 105 nm in figure 4.6. The full width at half maximum height given in table 4.2 were estimated by Dr. D. Wermeille after manually resetting the attenuator corrections.

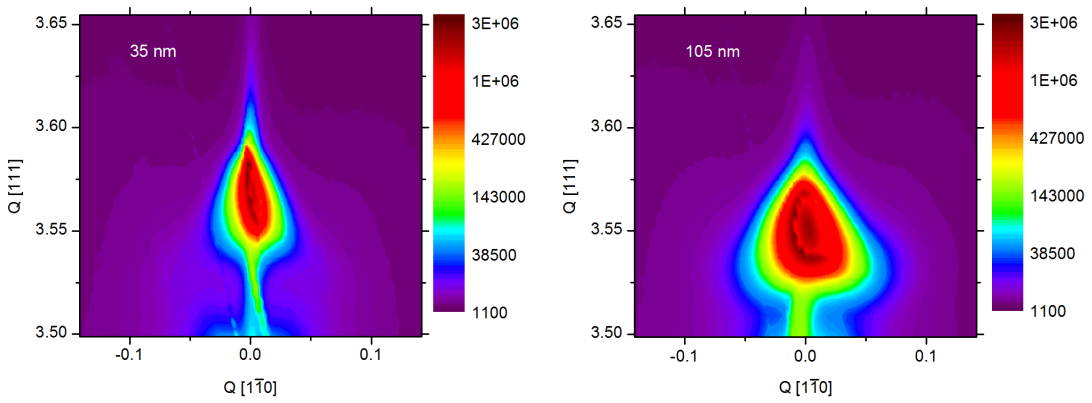


Figure 4.6: Reciprocal intensity space maps for the 35 and 105 nm thick samples studied, taken around the epilayer (444) reflection. The horizontal axis gives transverse wave vector transfer along the $[1\bar{1}0]$ direction and the vertical axis gives longitudinal transfer along the [111] direction in reciprocal lattice units of the substrate.

ΔQ is larger for the (666) than for the (444) reflection and it increases roughly in proportion to the longitudinal wave vector transfer. The observed peak widths can be interpreted in terms of mosaic spread. Mosaic spread or mosaicity arises when ions within small perfect crystal domains are aligned in a parallel fashion, but where domains are slightly misoriented relative to each other (see figure 4.7).

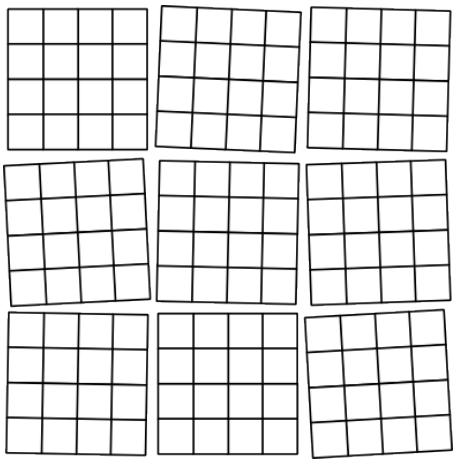


Figure 4.7: Exaggerated illustration of the mosaic spread. Individually perfect, small crystal domains are slightly disoriented to each other. The mosaic spread τ can range from tenths of a degree to a few degrees depending on the sample.

This mosaic spread leads to an increase of the width of transverse scans through Bragg reflections. The misorientation of the crystallites usually follows a Gaussian distribution, within which the full width at half maximum (FWHM) τ is considered the mosaic spread. The mosaic spread may be derived from the full width ΔQ at half maximum height in a transverse scan using the equation:

$$\tau = \tan^{-1} \frac{\Delta Q}{Q_\perp} \,, \tag{4.2}$$

where $Q_\perp$ is the corresponding longitudinal wave vector transfer. Flat epitaxial films usually exhibit values of τ of a few tenth of a degree, but higher values of up to a few degrees can be observed. For all the samples presented here the mosaic spread is below 0.5°. Values calculated using equation 4.3 are given in table 4.2.

Table 4.2: ΔQ and the corresponding values for Mosaic spread τ for transverse scans through the epilayer [666] and [444] reflections. Values for the [444] reflection were estimated by Dr. D. Wermeille due to attenuator problems.

Sample thickness	Reflection	Transverse direction	ΔQ / nm^{-1}	Mosaic spread FWHM τ
35 nm	[666]	$[1\bar{1}0]$	0.132	0.12±0.02°
	[444]	$[1\bar{1}0]$	0.086	0.11±0.02°
		$[11\bar{2}]$	0.093	0.08±0.02°
105 nm	[666]	$[1\bar{1}0]$	0.372	0.33±0.02°
	[444]	$[1\bar{1}0]$	0.240	0.31±0.02°
		$[11\bar{2}]$	0.434	0.38±0.02°
420 nm	[666]	$[1\bar{1}0]$	0.378	0.34±0.02°
		$[11\bar{2}]$	0.508	0.45±0.02°

Figure 4.8 shows reciprocal space maps for the nonspecular ($\underline{10}26$) Bragg peak. A $[4\bar{4}0]$ transverse wave vector transfer along the $[1\bar{1}0]$ direction is added to [666] longitudinal wave vector transfer along the [111] direction. In each map the circular dot represents the coordinates for unstrained In_2O_3 (assuming the bulk lattice parameter to be $a = 10.117$ Å). In the thinnest film, with a thickness of 35 nm, the maxima Q_I in the scattering from the epilayer are found at $Q_I[1\bar{1}0] = 2.8324$ and $Q_I[111] = 5.3950$. Both are strongly displaced from the values Q_0 for bulk In_2O_3 of $Q_0[1\bar{1}0] = 2.8765$ and $Q_0[111] = 5.2845$ (marked by a dot in the reciprocal space map). In-plane, the epilayer comes close to matching the substrate, for which $Q[1\bar{1}0] = 2.8284$. This mismatch between the lattice parameters of the film and substrate of 1.7% is almost completely compensated by in-plane strain. At the same time there is a large increase in $Q[111]$ due to the Poisson contraction normal to the surface. On the other hand the 420 nm thick film is almost completely relaxed, which results in the coordinates for unstrained In_2O_3 being located in the centre of the map of scattering intensity. For the intermediate 105 nm thick film, the reciprocal space map shows an elongated ovoid shape. This is visualised by showing the principal axis as a superimposed line, which slopes in a downward diagonal direction. The diagonal line links points of maximum intensity in transverse cuts through the map

and extrapolates toward the coordinates for bulk In_2O_3. This suggests an only partially relaxed thin film. Close to the interface the film is under tensile strain to bring the lateral periodicity toward that of the substrate, but moving away from the interface the strain relaxes and $Q_I[1\bar{1}0]$ moves toward the value for bulk In_2O_3. Parallel to this variation, $Q_I[111]$ decreases as $Q_I[1\bar{1}0]$ increases due to the Poisson effect.

As mentioned above, the Poisson effect can be observed in the data presented here. The Poisson ratio ν is defined by the following equation:

$$\frac{\epsilon^{\perp}}{\epsilon^{\parallel}} = \frac{\frac{a^{\perp}-a_0^{\perp}}{a_0^{\perp}}}{\frac{a^{\parallel}-a_0^{\parallel}}{a_0^{\parallel}}} = -\frac{2\nu}{1-\nu} \ , \tag{4.3}$$

where $\epsilon^{\perp}$ and $\epsilon^{\parallel}$ are the strains normal and parallel to the surface, $a^{\perp}$ and $a^{\parallel}$ are the corresponding separations between atomic planes in the strained layer, and $a_0^{\perp}$ and $a_0^{\parallel}$ are the values for the unstrained system. This equation can be formulated for the reciprocal space coordinates for the ($\underline{10}26$) reflection of bulk In_2O_3 and the thin film as follows:

$$\frac{Q_I[111]^{-1} - Q_o[111]^{-1}}{Q_I[1\bar{1}0]^{-1} - Q_0[1\bar{1}0]^{-1}} \times \frac{Q_0[111]}{Q_0[1\bar{1}0]} = -\frac{2\nu}{1-\nu} \ , \tag{4.4}$$

where

$$\frac{Q_0[111]}{Q_0[1\bar{1}0]} = \frac{3\sqrt{3}}{2\sqrt{2}} \ , \tag{4.5}$$

and the reciprocal lattice coordinates are expressed in terms of reciprocal lattice vectors of the substrate. This calculation gives a Poisson ratio of $\nu = 0.31 \pm 0.02$. This value is higher than for (001) oriented film, where $\nu = 0.27 \pm 0.04$.[26]

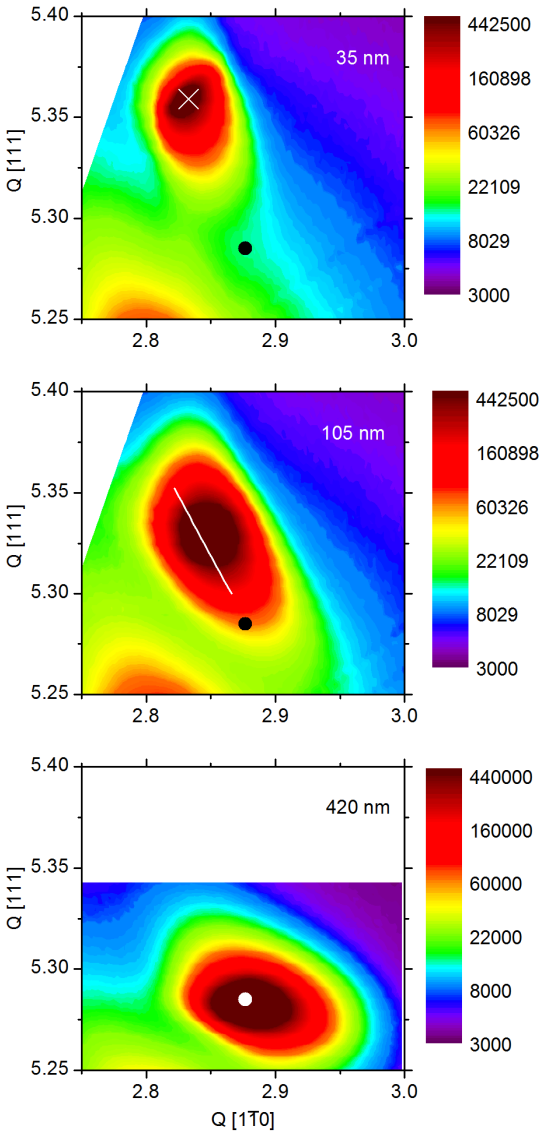


Figure 4.8: Reciprocal space maps for the three samples studied taken around the epilayer ($10\underline{2}6$) reflection. The horizontal axis gives transverse wave vector transfer along the $[1\bar{1}0]$ direction and the vertical axis gives longitudinal wave vector transfer along the $[111]$ direction in reciprocal lattice units of the substrate. The circular spots in the lower part of each figure marks the position of the ($10\underline{2}6$) reflection for unstrained In_2O_3, while the cross for the sample with thickness of 35 nm identifies the position of maximum intensity in the map. The white line in the map for the sample with a thickness of 105 nm was derived from a linear least squares fit to a plot of $Q_I\,[111]^{-1}$ versus $Q_I\,[1\bar{1}0]^{-1}$, where the subscript I signifies the coordinates of maximum scattering in successive transverse scans used to build up the map.

This experimental value can be compared to the value derived from atomistic

simulations. The Poisson ratio for the [111] direction in a cubic crystal is:[27]

$$\frac{2\nu[111]}{1-\nu[111]} = \frac{2C_{12} - 2C_0/3}{2C_{11} + 2C_0/3} \ , \tag{4.6}$$

where

$$C_0 = 2C_{44} - C_{11} + C_{12} \ . \tag{4.7}$$

Walsh *et al.*[28] have computed elastic constants, which are as follows: C_{11} = 297.75 GPa, C_{12} = 141.78 GPa, and C_{44} = 76.42 GPa. The derived value for C_0 is only −3.13 GPa. From this a value of 0.33 for $\nu[111]$ is calculated, which is comparable to that of 0.31±0.02 found experimentally.

Table 4.3 summarises data for the Poisson ratio from previous experimental work. The value for Sn-doped In_2O_3 is considerably higher than the value determined here. The values for the structurally related Y-doped ZrO_2 however, agree with our experimental result. A value for undoped In_2O_3 could not be found.

Table 4.3: Poisson ratios ν for In_2O_3 related systems from the literature including the technique used to determine ν.

	ν	Material	Technique
Neerinck[29]	0.35	10% Sn-doped In_2O_3	X-ray diffraction
Ingel[30]	0.30	7% Y-doped ZrO_2	acoustic wave pulse overlap technique
	0.32	17% Y-doped ZrO_2	
Atkinson[31]	0.308	8% Y-doped ZrO_2	impulse excitation resonance technique

4.4 In_2O_3 Nanorods on Y-doped ZrO_2 (110)

Figure 4.9 shows a θ-2θ diffraction pattern for the sample grown at 900 °C showing the (220) and (440) reflections of the YSZ substrate and the (220), (440), (660), and

(880) reflections for In_2O_3. The In_2O_3 reflections have been magnified by the factors given in the figure. The presented pattern is representative for all three samples used for reciprocal space mapping presented here. The epilayer peaks (440) and (880) are observed close to the substrate peaks. Only $(hk0)$ reflections for $h = k$ from the epilayer, where $h = 2n$ and n is an integer, can be seen for the space group $Ia\overline{3}$, to which In_2O_3 belongs. (220) and (660) Bragg reflections are observed at 2θ angles of $2\theta_{220} = 25.025°$ and $2\theta_{660} = 80.840°$ respectively, but these are very weak indeed. The structure factors for these reflections arise purely from the (2 x 2) supercell associated with ordering of the oxygen positions missing from the fluorite structure.

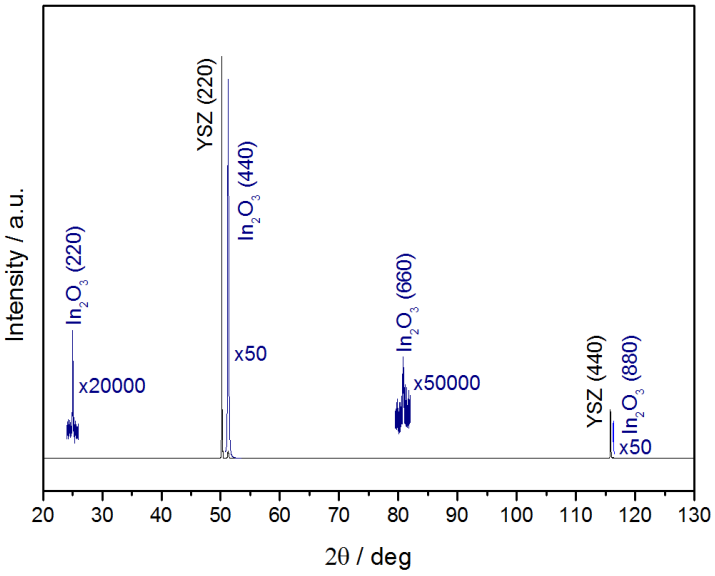


Figure 4.9: θ-2θ diffraction pattern for the sample grown at 900 °C showing the (220) and (440) reflections of the YSZ substrate and the (220), (440), (660), and (880) reflections for the In_2O_3.

LEED patterns for the sample grown at 900 °C, which were measured *in situ* in the MBE growth chamber, show a 2-fold rotational symmetry (see figure 4.10). The spots are not circular, but show streaking and spot splitting, which varies strongly with the beam energy. This suggests that the surface is extensively faceted. Both the LEED and XRD patterns confirm the epitaxial growth of In_2O_3 on YSZ (110). This is further confirmed by high resolution transmission electron microscopy im-

ages measured by Dr. K. H. L. Zhang.[6]

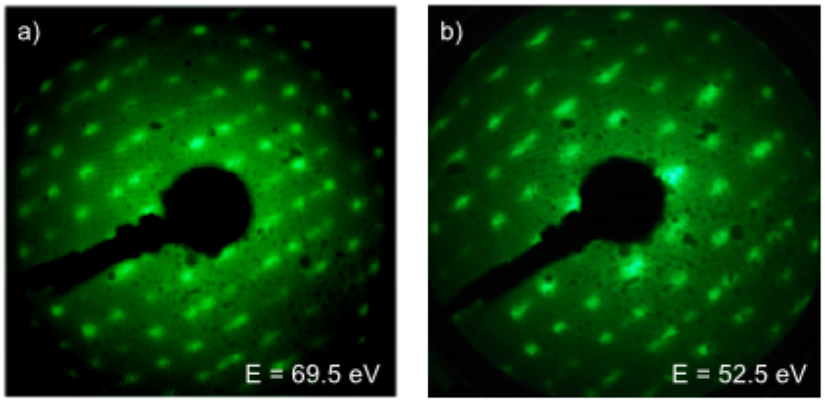


Figure 4.10: LEED patterns of a representative sample measured *in situ* in the MBE growth chamber at a beam energy of (a) 69.5 eV and (b) 52.5 eV.

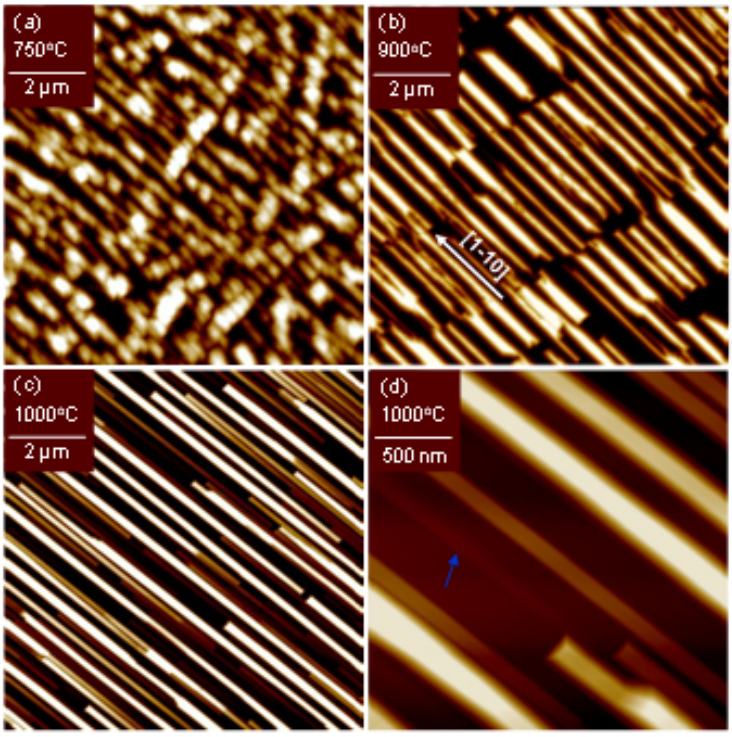


Figure 4.11: AFM images of the three samples. (a) - (c) 10 × 10 μm images of the samples grown at substrate temperatures of 750 °C, 900 °C, and 1000 °C. (d) Expanded image of the sample grown at substrate temperatures of 1000 °C. The arrow indicates a nanorod with a height of 6 nm.

In order to examine the morphology of the samples, AFM images were collected, which are shown in figure 4.11. All four images show rod-like nanostructures. From the synchrotron-based XRD results discussed later in this chapter, it could be seen

that the long axis of the nanorods lies along the $[1\bar{1}0]$ direction of the YSZ substrate.

The aspect ratio of the rods, which is defined as length/width $= l/w$, increases with increasing substrate temperature, and the rods become more defined. The most well defined nanorods, grown at a substrate temperature of 1000 °C, have an average length of 15 μm, a height of approximately 100 nm and a width of close to 200 nm.

To explain why such highly aligned 1D nanorods are formed, a simple thermodynamic model can be used. Although the shape of a nanostructure is in principle determined by the interplay between the surface and interface energies and strain energy, a reduced model based only on surface and interface energies can qualitatively explain the observed results.

Figure 4.12(a) shows a false 3D AFM image of a nanorod. The side facet along the long axis of the rod is determined to be {111} and the end facet is {001}. Consider an idealised nanorod with a rectangular shape with height h, length l, and width w, where $l > w$, as shown in figure 4.12(b). The sum E of surface and interface energies can be formulated as follows:

$$E = 2\Gamma_1 lh + 2\Gamma_2 wh + \Gamma_3 lw \ . \tag{4.8}$$

With the side facets as described above, with {111} along the long axis and {001} along the short axis, we can write:

$$\Gamma_1 = \gamma_e(111)\mathrm{cosec}\theta_1 - \frac{1}{2}(\gamma_s(110) + \gamma_e(110) - \gamma_i(110))\cot\theta_1 \tag{4.9}$$

$$\Gamma_2 = \gamma_e(001)\mathrm{cosec}\theta_2 - \frac{1}{2}(\gamma_s(110) + \gamma_e(110) - \gamma_i(110))\cot\theta_2 \tag{4.10}$$

$$\Gamma_3 = (\gamma_i(110) + \gamma_e(110) - \gamma_s(110)) \ , \tag{4.11}$$

where the contact angles are $\theta_1 = 35.3°$ and $\theta_2 = 45°$, γ_s and γ_e are surface energies for the substrate and epilayer respectively and γ_i is an interface energy. Minimising E subject to the constraint of constant area using Lagrangian multipliers, the aspect ratio l/w is found to be given by:

$$\frac{l}{w} = \frac{\Gamma_2}{\Gamma_1} \ . \tag{4.12}$$

Figure 4.12(c) shows the aspect ratio l/w as a function of the interface energy $\gamma_i(110)$ assuming the surface energies given in table 4.1. The aspect ratio diverges toward infinity for an interface energy of approximately 0.4 Jm^{-2}, because Γ_2 is always positive due to the large surface energy of (001). The sum of terms $\gamma_e(111)\mathrm{cosec}\theta_1 - \frac{1}{2}(\gamma_s(110) + \gamma_e(110))\cot\theta_1$ in Γ_1 has a negative value of -0.29 Jm^{-2}, due to the small value in the surface energy of (111). This quantitative analysis indicates that 1D nanorods spontaneously grow due to the minimisation of the total surface and interface energies by development of {111} side facets. The figure also includes the aspect ratio as a function of the interface energy for rods with {110} facets. This truncation is in fact energetically favoured due to the (110) surface energy being lower than the (100) surface energy. However, the influence of this term is small for nanorods with a high aspect ratio, as its fraction of the total surface area is small.

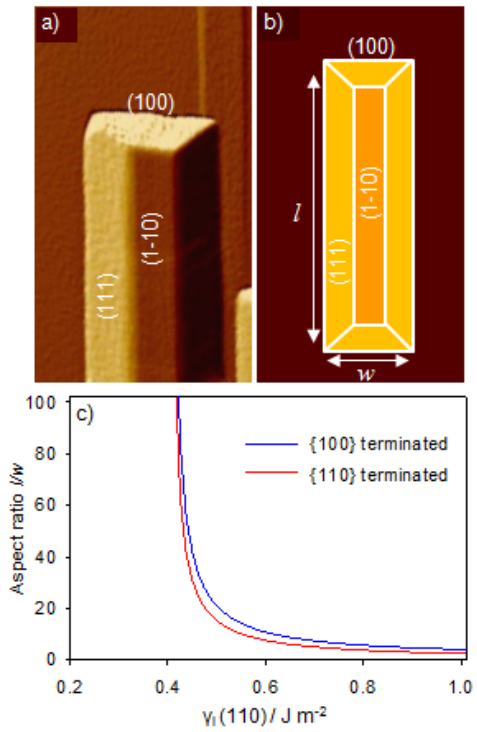


Figure 4.12: (a) False 3D AFM image of a nanorod showing 110 side facets collected by Dr. H. K. L. Zhang. (b) Schematic drawing of a nanorod. (c) Aspect ratio length/width $= l/w$ for In_2O_3 nanorods as a function of the interface energy γ_i for different termination facets.

Reciprocal space mapping using synchrotron-based X-ray scattering was used to probe strain in the nanorods. The (444) reflection has a high intensity and in order to avoid saturation of the detector, as was observed for the (111) thin film samples presented earlier in this chapter, the weaker (880) reflection was chosen. The transverse wave vector transfer is along the $[1\bar{1}0]$ or [001] directions and the longitudinal wave vector transfer is along the [110] direction. In each map the circular dot represents the coordinates for unstrained bulk In_2O_3 (assuming the bulk lattice parameter to be $a = 10.117$ Å).

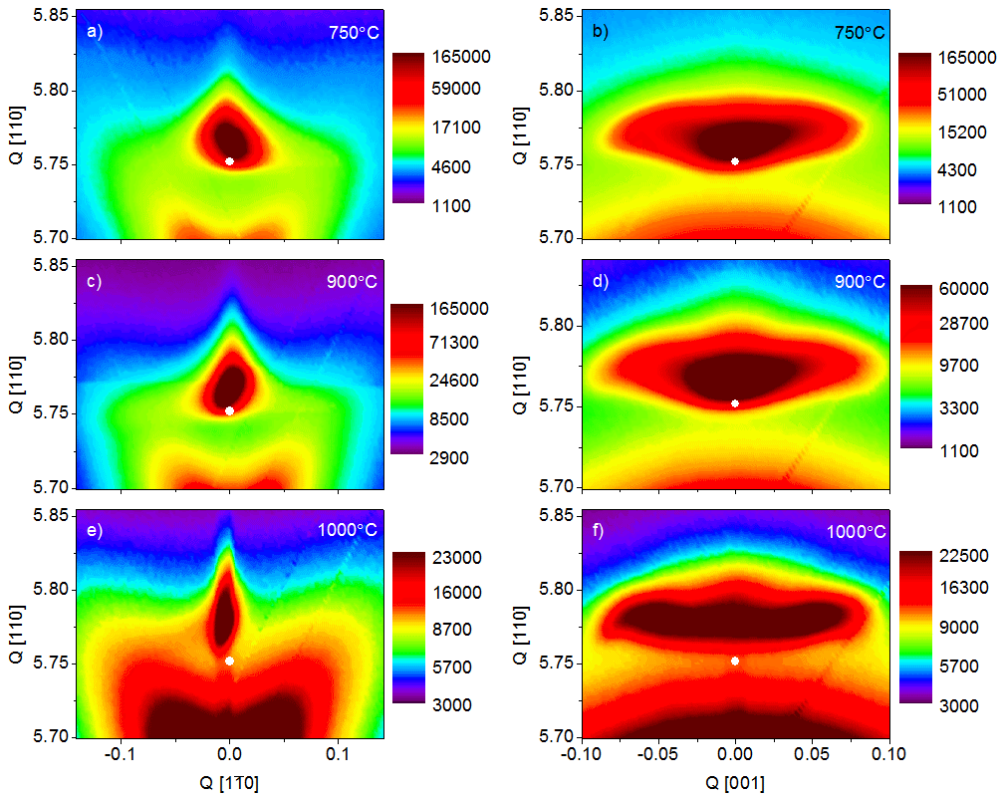


Figure 4.13: Reciprocal intensity space maps for the three samples studied taken around the epilayer (880) reflection. The horizontal axis gives transverse wave vector transfer along the $[1\bar{1}0]$ direction in (a), (c), and (e), and along the [001] direction in (b), (d), and (f). The vertical axis is the longitudinal transfer along the [110] direction in reciprocal lattice units of the substrate. The position of scattering from unstrained bulk In_2O_3 is indicated by a circular dot. Intensity at the lower edge of the maps originates from the close (440) substrate peak.

Transverse cuts through the reciprocal space maps in figure 4.13 at the longitudinal wave vector transfer with maximum scattering intensity are shown in figure 4.14. The transverse line profiles show that the maximum scattering intensity is moved to higher longitudinal wave vector transfers compared to bulk In_2O_3. This behaviour indicates an in-plane tensile strain, where in-plane expansion leads to out-of-plane contraction, as described by the Poisson effect. Comparing line profiles of scans along the $[1\bar{1}0]$ and the [001] directions, major differences become apparent. Whilst $[1\bar{1}0]$ profiles are mostly narrow, symmetric, and can be fitted with a single Voigt profile, [001] profiles are much broader and show additional peaks on either side of the central peak. Whilst these peaks are of low intensity in the samples grown

at 750 °C and 900 °C, the sample grown at 1000 °C shows two peaks with comparable intensity to the central peak, which are displaced by about 0.05 reciprocal lattice unit from $Q[1\bar{1}0] = 0$. In addition, the relative intensity of the central and side peaks varies strongly with the value of the longitudinal wave vector transfer $Q[110]$, as shown in figure 4.15. The most obvious dependence is that the central peak becomes relatively stronger the higher the value of $Q[110]$, i.e. the higher the contraction of the out-of-plane lattice parameter.

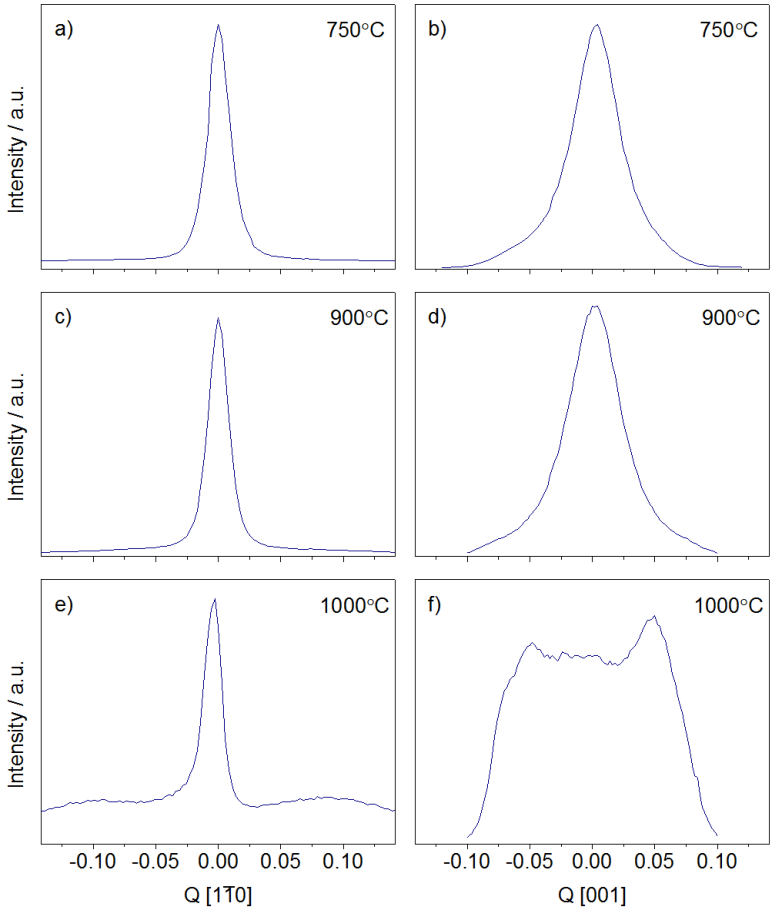


Figure 4.14: Transverse line profiles through the (880) epilayer reflection at the longitudinal wave vector transfer with highest scattering intensity. The corresponding reciprocal space maps are shown in figure 4.13. The Q values are given in reciprocal lattice units of the substrate.

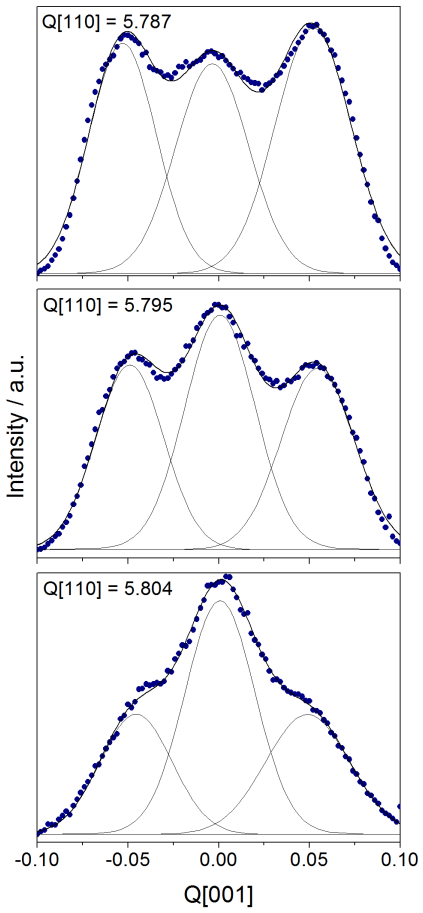


Figure 4.15: Transverse line profiles through the (880) epilayer reflection along the [001] direction of the sample grown at 1000 °C. The line profiles are taken at different longitudinal wave vector transfer along [110] from the reciprocal space map f) in figure 4.13. The Q values are given in reciprocal lattice units of the substrate.

An interpretation for the observed line profiles is based on AFM images of the samples, where all samples show rods of different widths and heights. The tilting of an epilayer relative to the surface can partially accommodate a mismatch between substrate and epilayer. Tilting has been observed in square islands grown on YSZ (001), where a transition between tilted and non-tilted islands could be observed, which was dependent on the island volume.[32] Smaller islands will accommodate the mismatch purely by strain, not by tilting. In addition, some samples with a bimodal distribution of tilted and non-tilted islands were prepared and these exhibited a three peak structure similar to that found here. Extending the conclusions drawn for square islands to the rods investigated here, the outer peaks in the nanorod line

profiles correspond to thicker rods which tilt or roll around the $[1\bar{1}0]$ direction, and the central peak corresponds to untilted rods. The increase in intensity of the central peak with higher values of $Q[110]$, which corresponds to an increasing predominance of untilted rods, can be explained by recognising that highly strained rods are less likely to tilt. The tilt angle ψ can be estimated using the following equation:

$$\tan\psi = \frac{Q[001]}{Q[110]} \ . \tag{4.13}$$

This gives a value of 0.5° for the nanorods, which is similar to the value of 0.7° reported for square islands.[25]

Tilting of nanorods around the $[1\bar{1}0]$ direction can only accommodate mismatch between substrate and epilayer in the [001] direction. Along the $[1\bar{1}0]$ direction the mismatch is still compensated by strain or misfit dislocations. Walsh *et al.* derived elastic parameters for In_2O_3 by an atomistic modelling procedure, giving C_{11} = 297.8 GPa, C_{12} = 141.8 GPa, and C_{44} = 76.4 GPa.[28] As noted earlier, the energy density associated with the strain along the <100> directions is determined by C_{11} = 297.8 GPa, whereas strain along the <110> directions is dependent on $2C_{11}+2C_{12}+C_{44}/4$ = 238.9 GPa. The latter is smaller than C_{11}.[25] The difference in elastic parameters favours strain along the $[1\bar{1}0]$ direction and augments the effects of surface energies by favouring elongated growth along the $[1\bar{1}0]$ direction.

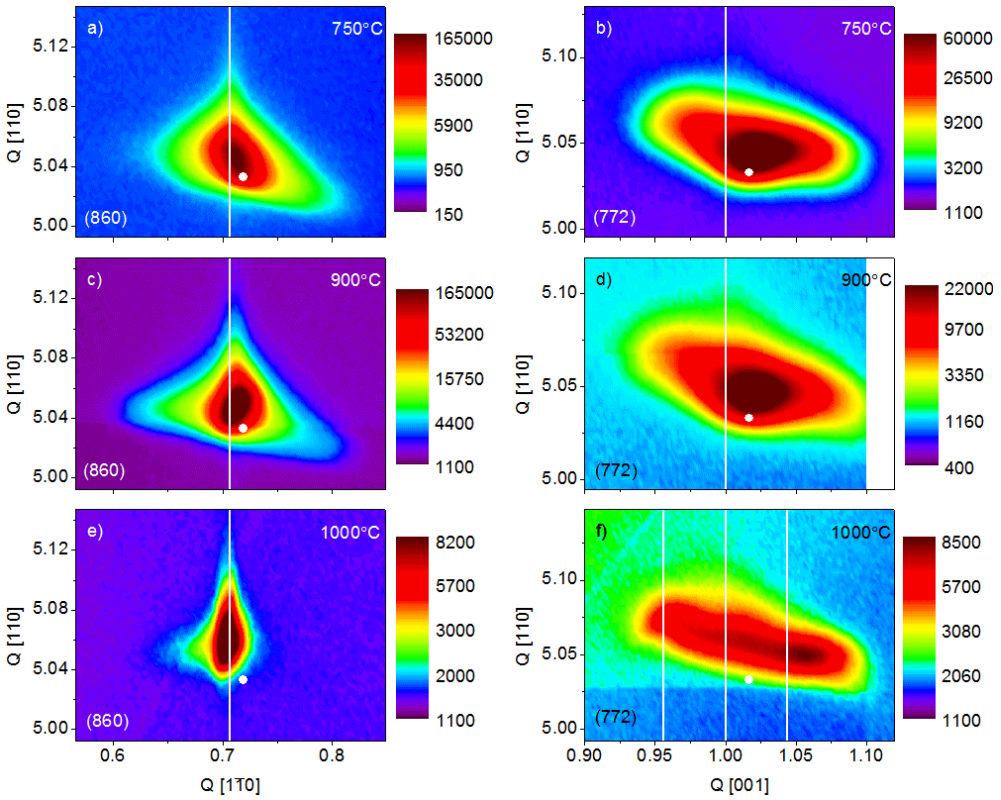


Figure 4.16: Reciprocal intensity space maps for the three samples studied taken around the epilayer (860) and (772) reflections. The horizontal axis gives transverse wave vector transfer along the $[1\bar{1}0]$ direction in (a), (c), and (e), and along the [001] direction in (b), (d), and (f). The vertical axis is the longitudinal transfer along the [110] direction in reciprocal lattice units of the substrate. The position of scattering from unstrained bulk In_2O_3 is indicated by a circular dot, whilst the vertical lines indicate the transverse wave vector transfer for a film strained to match the substrate in-plane.

Figure 4.16 shows reciprocal space maps for non-specular Bragg reflections. Maps were taken around the epilayer (860) reflection with transverse wave vector transfer along the $[1\bar{1}0]$ direction and around the (772) reflection with transverse wave vector transfer along the [001] direction. The vertical axis gives the longitudinal wave vector transfer along the [110] direction. In each map the circular dot represents the coordinates for unstrained bulk In_2O_3 (assuming the bulk lattice parameter to be $a = 10.117$ Å). The vertical lines indicate the transverse wave vector transfer for a film strained to match the substrate in-plane. Corresponding line profiles derived from reciprocal space maps are shown in figure 4.17.

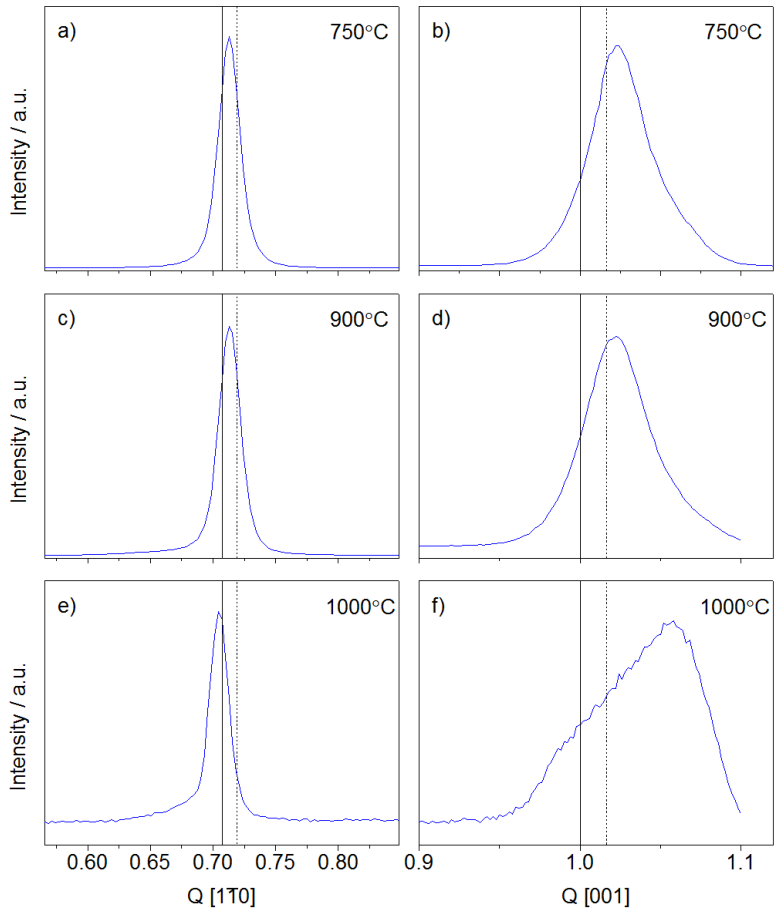


Figure 4.17: Transverse line profiles through the (860) and (772) epilayer reflection at the longitudinal wave vector transfer where maximum scattering occurs from the maps in figure 4.16. The solid line corresponds to the transverse wave vector transfer of the substrate and the dashed line corresponds to the same for the epilayer. Q is given in reciprocal lattice units of the substrate.

In the (860) maps it is apparent that the scattering intensity maximum moves towards the transverse wave vector transfer of the substrate, which is most pronounced in the sample grown at 1000 °C. This is indicative of strain coherent with the substrate in the epilayer along the $[1\bar{1}0]$ direction as shown in figure 4.18. In the (772) maps for the samples grown at 750 °C and 900 °C the scattering intensity maximum is close to the position of bulk In_2O_3, indicating only very little strain in the epilayer in the [001] direction. If anything there is in fact a small increase in Q[001] relative to the value for bulk In_2O_3. Of course the epilayer is under tensile stress in both [001] and $[1\bar{1}0]$ directions so that the decrease in lattice parameter

along the [001] direction must be a second order Poisson effect arising from expansion along $[1\bar{1}0]$. The contraction is, however, less pronounced than the contraction in interplanar spacings normal to the surface.

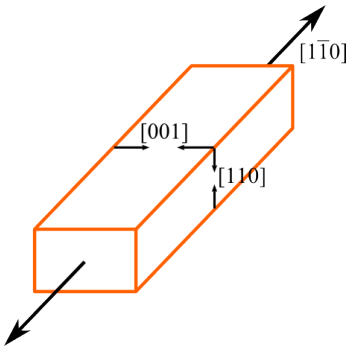


Figure 4.18: Schematic of the first and second order Poisson effects in the nano rods.

The (772) map for the sample grown at 1000 °C is complicated by the pronounced tilt discussed above. The tilting causes pronounced elongation along the (001) direction, which makes it very difficult to assess strain in this map. The range of displacement in $Q[001]$ produced by a tilt of $\pm 0.5°$ is indicated in the reciprocal space map in figure 4.16. Similar to the results from line profiles through the specular (880) epilayer reflection, we can conclude that the nanorods are coherently strained along the long-axis direction, but remain relaxed across the rods. This means that the main growth direction of the rods is along the direction with higher strain. This is an unexpected result when considering previous findings where the self-assembly of 1D silicide nanowires on Si (001) is driven by anisotropic lattice mismatch.[33] In this case the preferential growth is along the less strain affected direction. However, in the present cubic based system the percentage of mismatch is isotropic, but there is anisotropy in the elastic constants of the epilayer. In addition, there is large anisotropy in the surface energies of the {111} and {110} facets. The overall reduction in surface and interface energies by rods growing along the $[1\bar{1}0]$ direction outweighs any penalty arising from strain.

4.5 Concluding Remarks

Both In_2O_3 thin film and nanorod samples grown respectively on (111) and (110) YSZ substrates were investigated using reciprocal space mapping in conjunction with AFM. In both systems, epitaxial growth was confirmed by laboratory-based XRD and TEM.

Three thin film samples of In_2O_3 on Y-stabilised ZrO_2 (111) were probed to investigate strain. The thinnest film (35 nm) is highly strained to match the substrate laterally with an out-of-plane contraction due to the Poisson effect. Measurements on the strained sample allowed us to derive a value for the Poisson ratio in excellent agreement with values derived by atomistic simulation. The sample shows a crosshatch morphology with low roughness. Upon increase of the film thickness, strain is released and the sample surface roughness increases with pinholes appearing in the 105 nm sample, which are completely filled in in the 420 nm sample. The widths in transverse scans through (444) and (666) specular Bragg reflection increase with increasing film thickness and longitudinal wave vector transfer. Peak widths are interpreted in terms of mosaic spread within the epilayer.

The growth of In_2O_3 nanorods on Y-stabilised ZrO_2 (110) at different substrate temperatures was rationalised using a simple thermodynamic model with minimisation of surface and interface energies, The nanorods grow preferentially along the $[1\bar{1}0]$ direction, which is driven by development of lowest surface energy {111} facets. The lattice mismatch between substrate and epilayer is accommodated by strain along the $[1\bar{1}0]$ direction coupled with tilting along the [001] and $[00\bar{1}]$ directions and contraction in the [110] direction.

4.6 References

[1] A. Bourlange *et al.*, Thin Solid Films **517**, 4286 (2009).

[2] A. Bourlange *et al.*, Chemistry of Materials **20**, 4551 (2008).

[3] O. Bierwagen and J. S. Speck, Journal of Applied Physics **107**, 113159 (2010).

[4] E. H. Morales, Y. B. He, M. Vinnichenko, B. Delley, and U. Diebold, New Journal of Physics **10**, 125030 (2008).

[5] K. H. L. Zhang *et al.*, Chemistry of Materials **21**, 4353 (2009).

[6] K. H. L. Zhang *et al.*, Nano Letters **10**, 3740 (2010).

[7] A. Bourlange *et al.*, Chemistry of Materials **20**, 4551 (2008).

[8] A. Walsh and C. R. A. Catlow, Journal of Materials Chemistry **20**, 10438 (2010).

[9] P. Agoston and K. Albe, Physical Review B **84**, 045311 (2011).

[10] A. Walsh, C. R. A. Catlow, K. H. L. Zhang, and R. G. Egdell, Physical Review B **83**, 161202 (2011).

[11] K. H. L. Zhang *et al.*, Journal of Physics: Condensed Matter **23**, 334211 (2011).

[12] L. J. Lauhon, M. S. Gudiksen, C. L. Wang, and C. M. Lieber, Nature **420**, 57 (2002).

[13] N. Mathews *et al.*, Nanoscale **2**, 1984 (2010).

[14] H. A. Nilsson *et al.*, Applied Physics Letters **96**, 153505 (2010).

[15] Z. W. Pan, Z. R. Dai, and Z. L. Wang, Science **291**, 1947 (2001).

[16] Y. Cui, Q. Q. Wei, H. K. Park, and C. M. Lieber, Science **293**, 1289 (2001).

[17] A. Kolmakov, Y. X. Zhang, G. S. Cheng, and M. Moskovits, Advanced Materials **15**, 997 (2003).

[18] Q. Wan *et al.*, Applied Physics Letters **84**, 3654 (2004).

[19] Z. R. Dai, Z. W. Pan, and Z. L. Wang, Advanced Functional Materials **13**, 9 (2003).

[20] C. O'Dwyer *et al.*, Nature Nanotechnology **4**, 239 (2009).

[21] R. Noriega *et al.*, Journal of Applied Physics **107**, 074312 (2010).

[22] H. Chen *et al.*, Physical Review B **65**, 233303 (2002).

[23] M. A. Lutz, R. M. Feenstra, F. K. Legoues, P. M. Mooney, and J. O. Chu, Applied Physics Letters **66**, 724 (1995).

[24] M. Albrecht *et al.*, Applied Physics Letters **67**, 1232 (1995).

[25] R. A. Cowley *et al.*, Physical Review B **82**, 165312 (2010).

[26] K. H. L. Zhang *et al.*, Physical Review B **84**, 233301 (2011).

[27] A. Segmuller, Journal of Vacuum Science and Technology A **9**, 2477 (1991).

[28] A. Walsh, C. R. A. Catlow, A. A. Sokol, and S. M. Woodley, Chemistry of Materials **21**, 4962 (2009).

[29] D. G. Neerinck and T. J. Vink, Thin Solid Films **278**, 12 (1996).

[30] R. P. Ingel and D. Lewis, Journal of the American Ceramic Society **71**, 265 (1988).

[31] A. Atkinson and A. Selcuk, Mechanical properties of ceramic materials for solid oxide fuel cells, in *Solid Oxide Fuel Cells V*, edited by U. Stimming, S. C. Singhal, H. Tagawa, and W. Lehnert, pp. 671–680, 1997.

[32] K. H. L. Zhang *et al.*, ACS Nano **6**, 6717 (2012).

[33] Y. Chen, D. A. A. Ohlberg, and R. S. Williams, Journal of Applied Physics **91**, 3213 (2002).

5 Electronic and Surface Properties of Ga-doped In_2O_3 Ceramics

5.1 Introduction

In 1925 V. M. Goldschmidt published his investigations of the Ga_2O_3-In_2O_3 system, for which he prepared samples by precipitation of the hydroxides from ammonia. This was the first account of the Ga_2O_3-In_2O_3 system, and in his work Goldschmidt also observed the expected decrease of the lattice parameter of In_2O_3 upon Ga doping.[1] In the 1960s interest in this system re-emerged and publications by Schneider *et al.* (1961)[2], MacDonald *et al.* (1967)[3], and Shannon and Prewitt (1968)[4], attempted to construct a phase diagram for the system. A ternary compound $GaInO_3$ was identified in these early publications, which adopted the β-Ga_2O_3 structure. In addition, Shannon and Prewitt also observed a high pressure phase with a structure similar to $YAlO_3$. Additional investigations of the phase diagram by Edwards *et al.* (1961)[5], and Patzke and Binnewies (2000)[6] established that the β-Ga_2O_3 structure only extends to limiting dopant concentrations of up to 48%. Table 5.1 shows a summary of the published dopant maxima on both sides of the phase diagram.

Table 5.1: Solubility of In_2O_3 in β-Ga_2O_3 and of Ga_2O_3 in In_2O_3 from the literature.[5,6]

	In:β-Ga_2O_3		Ga:In_2O_3	
	T / °C	mol% In	T / °C	mol% Ga
Edwards	1000	44.0	1000	4.8
	1250	42.4	1250	7.4
	1400	41.4	1400	10.5
Patzke	800	48		
	900	46		

In-between these two doping limits, bulk samples are biphasic, consisting of monoclinic In-doped β-Ga_2O_3 and cubic Ga-doped In_2O_3.

$(Ga_xIn_{1-x})_2O_3$ thin films have been prepared using a range of methods including direct current magnetron sputtering onto glass substrates ($0 < x < 0.4$);[7] oxygen plasma-assisted molecular beam epitaxy on Al_2O_3 (0001) substrates ($0.0 < x < 1.0$)[8] and on β-Ga_2O_3 substrates (x=1.00);[9] metallo-organic chemical vapour deposition on Y-stabilised ZrO_2 (100) ($0.1 < x < 0.9$)[10] and on MgO (100) ($0.63 < x < 1.00$);[11] combinatorial aerosol-assisted chemical vapour deposition on glass substrates ($0.2 < x < 0.8$);[12] and sol-gel spin-coating on Al_2O_3 (0001) ($0 < x < 1.0$).[13] It becomes apparent that the main focus lies on the Ga_2O_3 side of the phase diagram, where it is clear that the band gap decreases with increasing In concentration.[8,10,11,13] However, the change in band gap upon In-doping is not linear.[13]

Less is known about the effect of Ga-doping on the cubic bixbyite phase of In_2O_3, especially with respect to the low energy forbidden absorption onset.

One of the motivations to investigate the properties of Ga-doped In_2O_3 is a recent observation by the Egdell group on Sn-doped rutile TiO_2 where "alloying" the narrower gap TiO_2 with the wider gap SnO_2 leads to a small but significant reduction

in the band gap at low Sn doping levels.[14,15] This effect, usually referred to as band gap bowing, is well established in III-V semiconductor systems,[16] but has been less well studied in oxides. There are a few cases of alloys of ZnO with Ca, Cd, Mg, Se and Be, where small band gap bowing is observed,[17–20] and a case of SiO_2 alloyed with Hf and Zr showing band bowing.[21]

The second motivation is the Egdell group's recent interest in the growth of In_2O_3 thin films on cubic Y-stabilised ZrO_2 by oxygen assisted molecular beam epitaxy.[22,23] Here, a difference in lattice parameters between substrate and In_2O_3 leads to tensile strain, which in turn leads to changes in the band gap on (111) oriented substrates and to the formation of nanostructures on (001) and (110) substrates.

The anticipated reduction in lattice parameter upon Ga-doping of In_2O_3, as observed by Goldschmidt,[1] provides a simple means of increasing the mismatch in lattice parameter, where the strain at the interface would be enhanced and the possibility to tune the size of the nanostructures would become available.

A high temperature solid state route was used to prepare $(In_{1-x}Ga_x)_2O_3$ ceramics with Ga doping levels of up to x = 0.1. The solubility limit of Ga in In_2O_3 is investigated by X-ray diffraction and Raman spectroscopy. The band gaps of doped samples are studied by diffuse reflectance spectroscopy and X-ray photoelectron spectroscopy (XPS). XPS shows pronounced surface segregation which is further studied by low energy ion scattering. Finally, the mechanism for segregation is studied with reference to XPS measurements for pure β-Ga_2O_3.

5.2 Experimental

Ga-doped In_2O_3 ceramic samples were prepared using a high temperature solid state approach. The starting materials were Ga_2O_3 (99.999%, supplied by Strem Chemicals Inc.) and In_2O_3 (99.99%, supplied by Sigma-Aldrich Inc.). The method described by Edwards *et al.*[5] was adapted for the research presented in this thesis. A series of mixed oxide powders with the composition $(In_{1-x}Ga_x)_2O_3$ (with Ga-doping levels between x = 0.01 and x = 0.10) were prepared by grinding stoichiometric amounts of the oxide powders in an agate mortar for 30 minutes until the mixture was homogeneous. The powder mixtures were pressed into pellets with a diameter of 1 cm and a thickness of approximately 1 mm at 5 tonnes, for 5 minutes, and placed in ceramic crucibles. The samples were then sintered in a muffle furnace (base temperature of 600 °C) at 1250 °C for 72 h, and cooled at a rate of 5 °C per minute. The resulting pellets had a pale yellow colour, much like boiled egg yolk, and some showed hints of green. Ceramics discs of Ga_2O_3 and In_2O_3 were prepared by the same procedure.

All ceramic samples were analysed in pelletised form using the Phillips PANanalytical X'Pert PRO diffractometer. XPS was mainly performed on the Scienta ESCA 300 spectrometer, with sputtering experiments being conducted on the Kratos Axis Ultra-DLD. The Kratos system offers a superior flood gun charge neutralisation system which makes analysis of a highly insulating material, as is Ga_2O_3, possible. An area of 5 x 5 mm was etched with an Ar ion gun operating at 4 keV and 15 mA, and an argon pressure of 1×10^{-6} mbar for 20 minutes at a time. Raman spectroscopy and diffuse reflectance measurements were conducted on the in-house apparatus, whilst LEIS was performed on the Qtac^{100} instrument at Imperial College, London.

5.3 Computational Methods

Density functional theory (DFT) calculations were performed by Dr. D. O. Scanlon using the VASP code,[24] with interactions between the cores (In:[Kr], Ga:[Ar] and O:[He]) and the valence electrons described using the projector augmented wave (PAW) method.[25] The calculations were performed using the HSE06 (Heyd-Scuseria-Ernzerhof) hybrid functional as proposed by Krukau *et al.*[26] In the HSE06 approach, a value of exact nonlocal exchange α of 25%, and screening parameter of $\omega = 0.11$ bohr^{-1} are added to the Perdew-Burke-Ernzerhof (PBE) formalism. The HSE approach has been proven to result in structural and band gap data which is in better agreement with experimental data than standard DFT functionals.[27–30] Furthermore, it has been proven to provide an excellent description of the electronic structure of In_2O_3.[31] A planewave cutoff of 400 eV and a k-point sampling of Gamma-centred $3 \times 3 \times 3$ for the primitive cell of In_2O_3 was used, with the structure deemed to be converged when the forces on all the atoms were less than 0.01 eV Å^{-1}. The optical transition matrix elements and the optical absorption spectrum were calculated within the transversal approximation.[32] Within this methodology, the absorption spectra is summed over all direct VB to CB transitions and therefore ignores indirect and intraband adsorptions.[33]

5.4 Results and Discussion

5.4.1 Solubility Limit of Ga in In_2O_3 and Changes in Crystal Structure

The θ-2θ X-ray diffraction pattern for 6% Ga-doped In_2O_3, shown in figure 5.1, is representative for all doping levels up to 7% Ga. The diffraction pattern is combined with a In_2O_3 reference pattern from Marezio.[34] All reflections can be attributed to

the cubic bixbyite phase of In_2O_3, and the reference was in perfect agreement with an In_2O_3 pellet prepared using the above method.

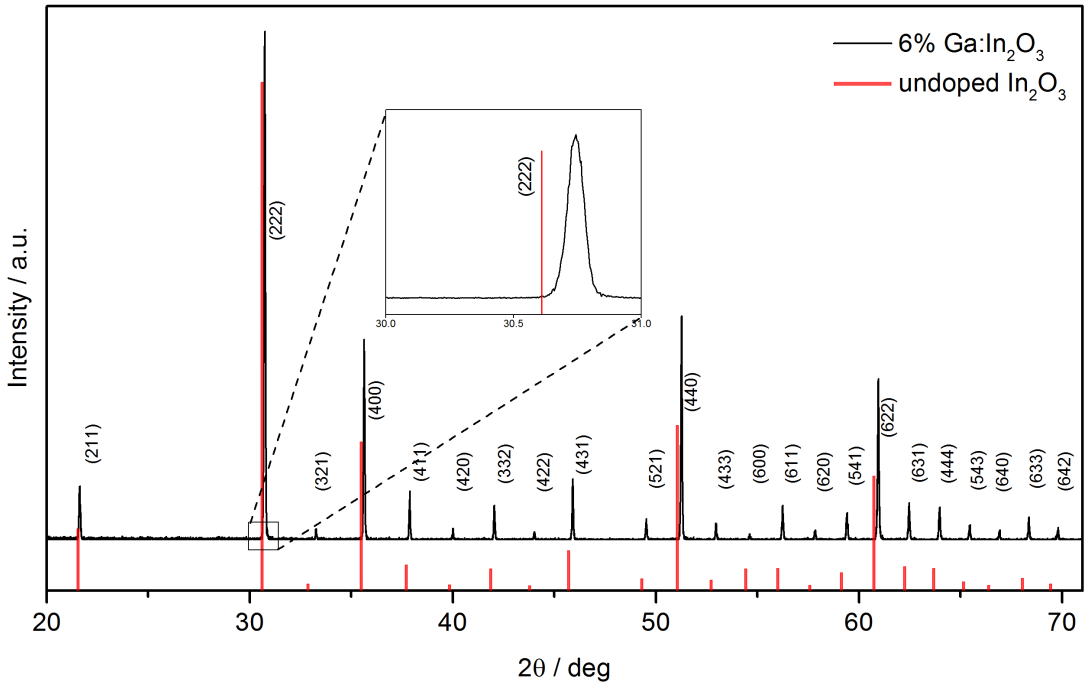


Figure 5.1: XRD pattern for a 6% Ga-doped In_2O_3 pellet and reference data for undoped In_2O_3.[34]

The inset in figure 5.1 shows the (222) diffraction peak in more detail. A shift in the doped sample to a higher diffraction angle can be observed, originating from a contraction in lattice parameters. This is as expected from the difference in ionic radii for Ga^{3+} ($r_{Ga^{3+}} = 0.620$ Å) in comparison to In^{3+} ($r_{In^{3+}} = 0.790$ Å) in oxides.[35] When the smaller Ga^{3+} replaces In^{3+}, the crystal contracts, leading to a reduction in lattice parameters.

In order to compensate for any diffractometer related shifts in diffraction angles, Si powder was used as an internal standard. Equal amounts of Si powder and calcined sample were ground together under acetone, dried, and pelletised. The diffraction patterns were aligned using the Si (111) peak at 28.4427°.[36] The corrected In_2O_3 (222) peaks for four samples, 3%, 5%, and 7% Ga-doped and undoped In_2O_3, are

shown in figure 5.2.

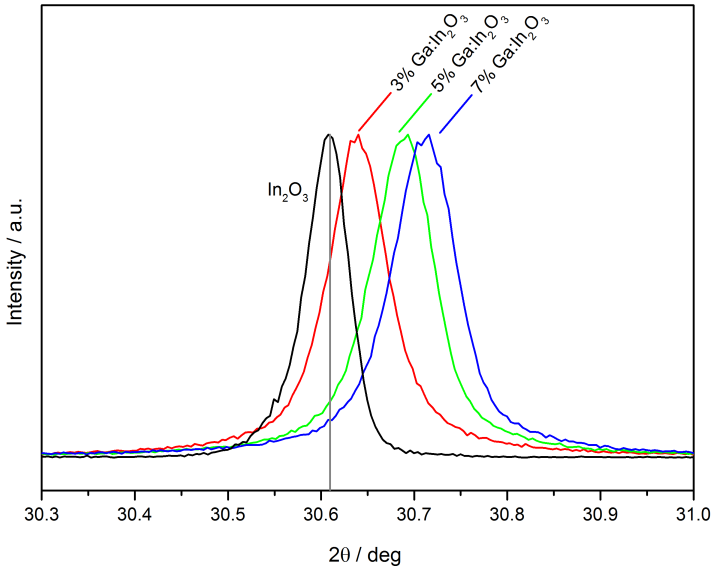


Figure 5.2: Si-corrected XRD signal of the In_2O_3 (222) peak for undoped In_2O_3 and three Ga-doped samples. The grey vertical bar indicates the position of the (222) peak from the reference.[34]

The Si (111) peak shows no significant shift between different samples and repeat measurements. The Si-corrected diffraction patterns establish that the shifts in the diffraction angle upon doping are due to changes in the lattice parameter of Ga-doped samples, rather than being artefacts from the diffractometer.

To investigate the changes in more detail, cubic lattice parameters a for pure In_2O_3 and samples with Ga-doping levels of up to 7% were obtained from Rietveld refinements of the diffraction patterns using GSAS software. Figure 5.3 shows the decrease in the lattice parameter with increasing Ga-doping. The variation can be compared with a Vegard plot based on unit cell volumes for In_2O_3 and Ga_2O_3. Vegard's law states that there is a linear relation between the crystal lattice parameters of an alloy and the concentrations of its constituents.[37] As In_2O_3 and Ga_2O_3 do not have the same structure unit cell volumes rather than lattice parameters were used. Alternatively we can use values for cell parameters for In_2O_3 and Ga_2O_3 from

calculations by Dr. D. O. Scanlon. The observed variation in lattice parameter is intermediate between that derived from computed values for lattice parameters and the variation from experimental unit cell volumes.

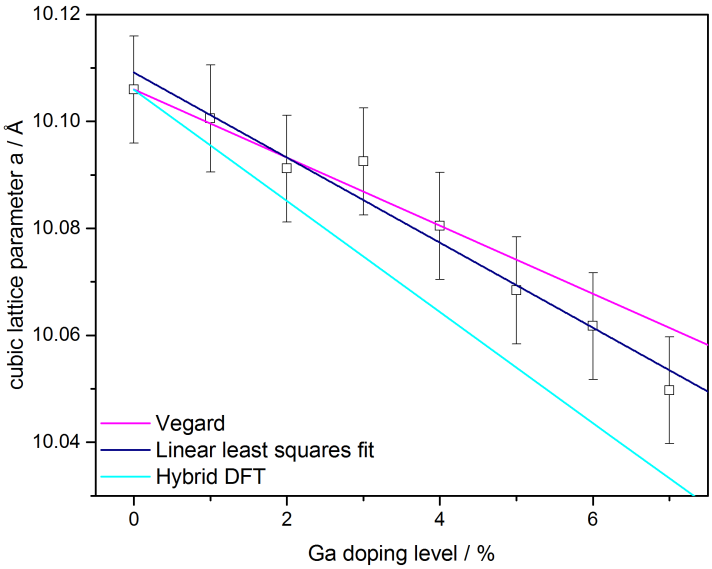


Figure 5.3: Cubic lattice parameters a from Rietveld refinements for undoped and 1-7% Ga-doped In_2O_3.The magenta line is a linear least squares fit to the experimental data points whilst the blue line is a Vegard plot derived from the experimental unit cell volumes of In_2O_3 (as determined here) and monoclinic Ga_2O_3. The turquoise line is fitted to the unit cell parameters for In_2O_3 and 6.25% Ga-doped In_2O_3 as calculated by Dr. D. O. Scanlon, which was scaled to fit the experimental data for undoped In_2O_3.

For a doping level of 7% Ga and beyond a second phase was identified in diffraction data, as shown in figure 5.4. This second phase does not match the d-spacings for any of the reported polymorphs of Ga_2O_3.[38–40]

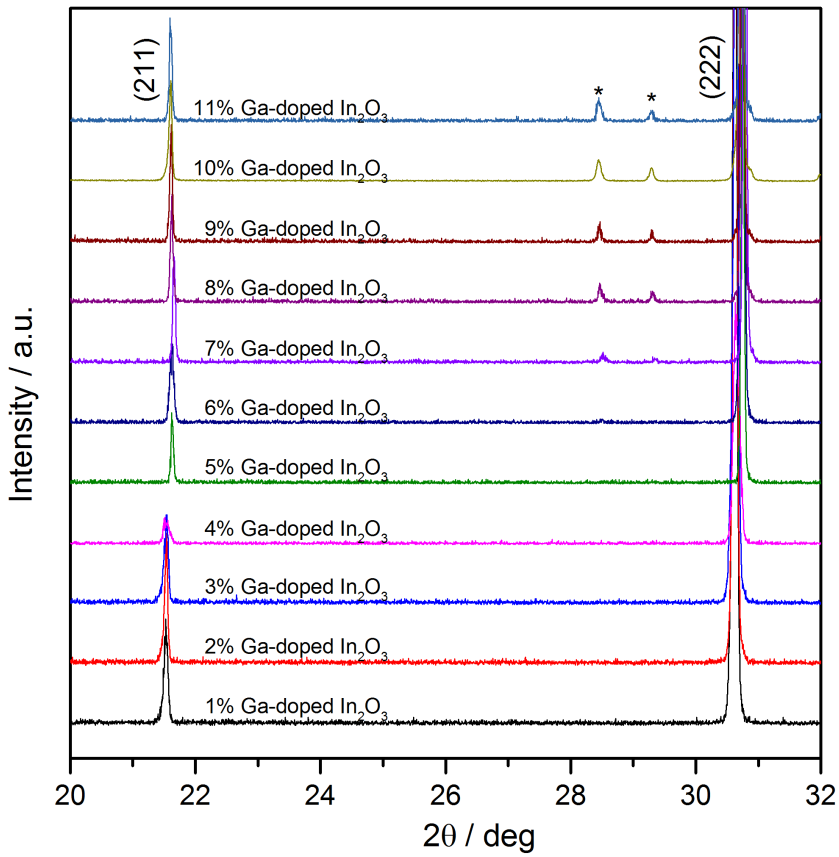


Figure 5.4: Partial diffraction profile for Ga-doped In_2O_3 for doping levels from 1 to 11%. Reflections (211) and (222) of the bixbyite phase of In_2O_3 are indicated. The second β-$GaInO_3$ like phase is indicated by *.

Raman spectroscopy confirms the observations from the X-ray diffraction. The body-centred cubic structure of In_2O_3 belongs to the space group $Ia\bar{3}$ with Z=16 and the primitive cell contains eight formula units amounting to 40 atoms. The 120 vibrational modes span irreducible representations Γ in the T_h factor group as follows:

$$\Gamma = 4A_g + 5A_u + 4E_g + 5E_u + 14T_g + 17T_u \ , \tag{5.1}$$

where the 22 *gerade* g modes are Raman active.[41] Figure 5.5 shows a reference spectrum for bulk In_2O_3 in pelletised form, where a total of 17 modes could be identified.

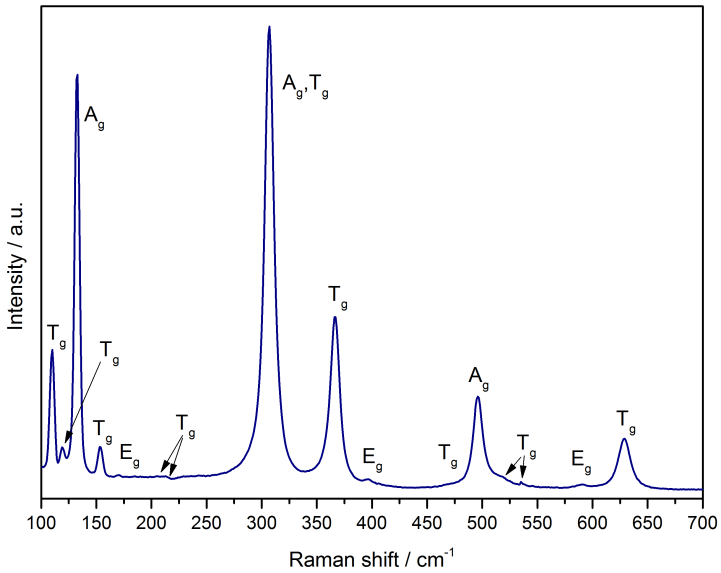


Figure 5.5: Raman spectrum for an In_2O_3 pellet with the 17 detectable modes indicated.

Table 5.2: Observed Raman modes in cm^{-1} for bulk In_2O_3 and comparison with experimental data from Garcia *et al.*[41]

Mode (sym)	this work	Garcia *et al.*
T_g	109±3	108
T_g	118±3	118
A_g	132±3	131
T_g	153±3	152
E_g	170±3	169
T_g	206±3	205
T_g	213±3	213
A_g, T_g	307±3	306
T_g	366±3	365
E_g	396±3	396
T_g	466±3	467
A_g	496±3	495
T_g	519±3	513
T_g	535±3	-
E_g	591±3	590
T_g	629±3	628

Table 5.2 shows all observed Raman modes of In_2O_3 and compares the data presented here with experimental results by Garcia *et al.*[41] The experimentally determined frequencies are in excellent agreement with those from the literature reported here.

Raman spectra for Ga-doped In_2O_3 are very similar to that of pure In_2O_3. Consistent with the XRD data, a second phase can be identified for Ga-doping levels above 7%, with additional vibrational modes at 171 cm^{-1} and 429 cm^{-1} (see figure 5.6).

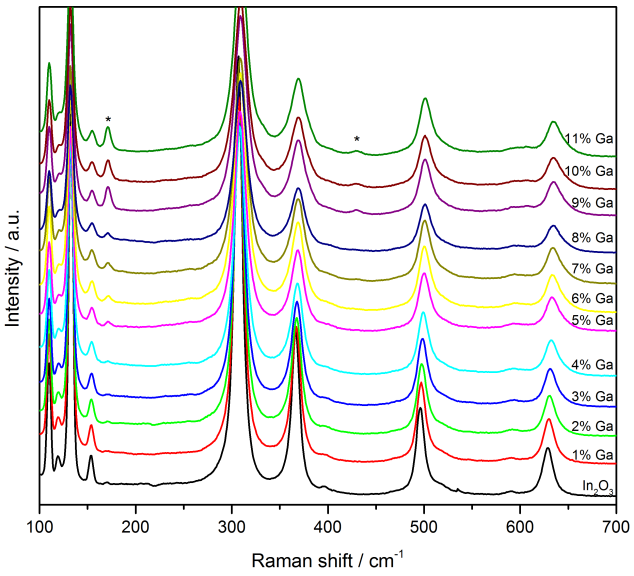


Figure 5.6: Raman spectra for Ga-doped In_2O_3 with Ga-doping levels from 1 to 11%. An increase in Raman shifts can be observed upon doping. In addition for all samples with a Ga-doping level above 7% a second phase can be identified (indicated with *).

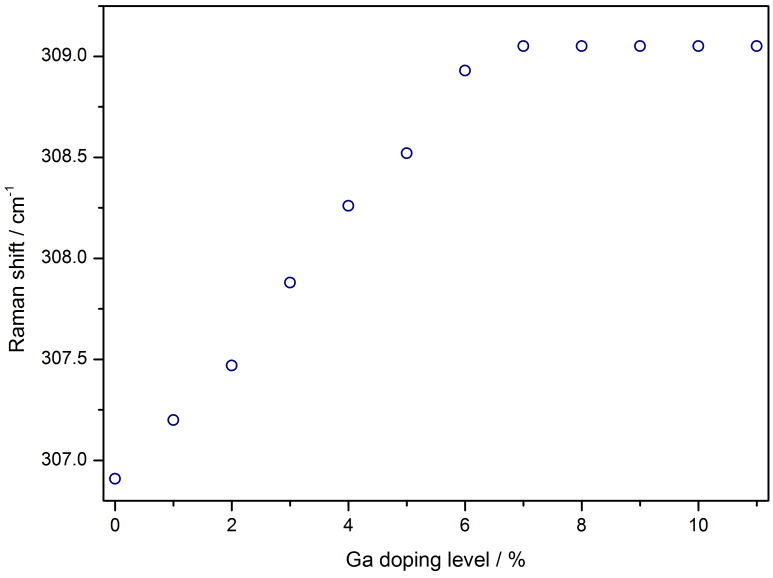


Figure 5.7: Raman shift of the A_g vibrational mode close to 307 cm^{-1} for pure and Ga-doped In_2O_3.

An increase in Raman shift is observed up to a doping level of 7% after which the

shift remains constant. Figure 5.7 shows the increase in shift for the most intense A_g vibrational mode at 307 cm^{-1}. The shift of the vibrational mode shown in figure 5.7 is representative for the shifts observed in other modes, including T_g at 365 cm^{-1}, A_g at 495 cm^{-1}, and T_g at 629 cm^{-1}.

For comparison a β-Ga_2O_3 reference spectrum was collected.

The monoclinic structure of β-Ga_2O_3 belongs to the space group $C2/m$ with two formula units per cell. The 30 vibrational modes span the following irreducible representation Γ in the C_{2h} factor group:

$$\Gamma = 10A_g + 4A_u + 5B_g + 8B_u \ , \tag{5.2}$$

where the 15 *gerade* g modes are Raman active.[42] Figure 5.8 shows a reference Raman spectrum for bulk Ga_2O_3, where all modes could be identified.

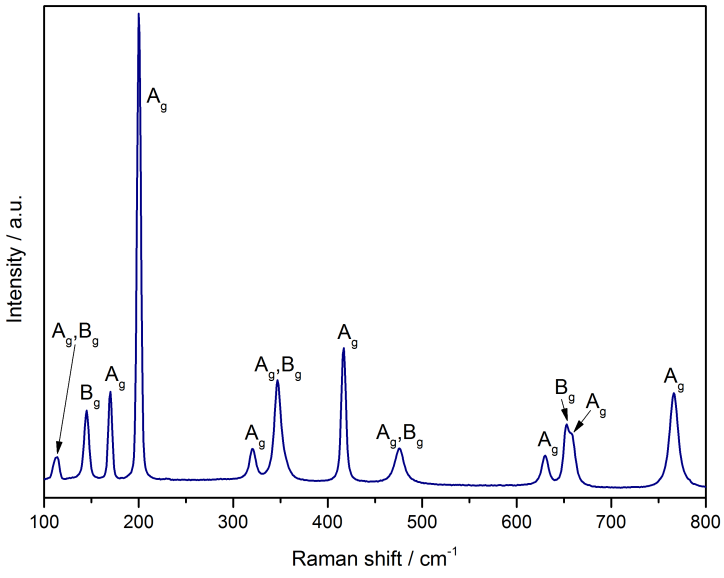


Figure 5.8: Raman spectrum for an Ga_2O_3 pellet with 15 detectable modes indicated.

Table 5.3 gives all observed vibrational modes and compares them to data from

Dohy *et al.*[42] The experimentally determined frequencies are consistent with those from the literature reported here.

Table 5.3: Observed Raman modes in cm^{-1} for bulk Ga_2O_3 and comparison with experimental data from Dohy *et al.*[42]

Mode (sym)	this work	Dohy *et al.*
A_g	767±3	763
A_g	657±3	657
B_g	653±3	651
A_g	629±3	628
A_g, B_g	476±3	475
A_g	417±3	415
B_g, A_g	354±3, 347±3	353, 346
A_g	320±3	318
A_g	200±3	199
A_g	170±3	169
B_g	145±3	147
B_g, A_g	114±3, 110±3	114, 111

As is evident from figure 5.8, the most intense peak for β-Ga_2O_3 can be observed at 200 cm^{-1}. The absence of a detectable mode at 200 cm^{-1} in the Ga-doped In_2O_3, verifies that the second phase, which appears beyond the solubility limit of Ga, is not Ga_2O_3, as has been suggested elsewhere.[5,6]

5.4.2 Band Gaps from Diffuse Reflectance Spectroscopy

Figure 5.9 shows the Tauc plot for pellets of In_2O_3 and Ga_2O_3, where the Kubelka-Munk function F is derived from diffuse reflectance data. Linear fits to the absorption edge give band gaps of 2.95 eV for In_2O_3 and 4.60 eV for Ga_2O_3. The former value corresponds to the direct but dipole forbidden absorption onset for In_2O_3, as discussed in recent publications, for example Walsh *et al.*[43] The larger band gap for Ga_2O_3 is in agreement with values determined elsewhere.[44]

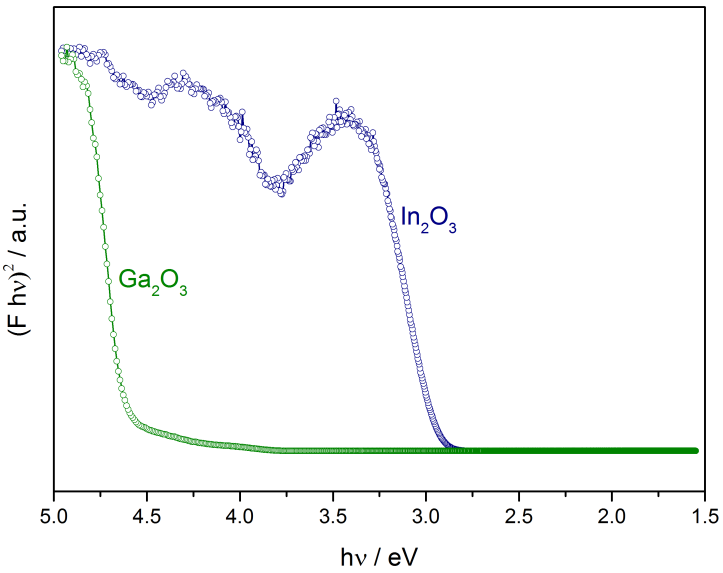


Figure 5.9: Tauc plot for pure In_2O_3 and Ga_2O_3 pellets, both showing clear absorption edges.

Figure 5.10 shows DRS data for 1%, 6%, and 9% Ga-doped In_2O_3 samples in comparison with an expanded scan for pure In_2O_3. The band gap decreases with 1% and 6% Ga-doping, although at higher levels, such as 9% shown here, this trend does not continue.

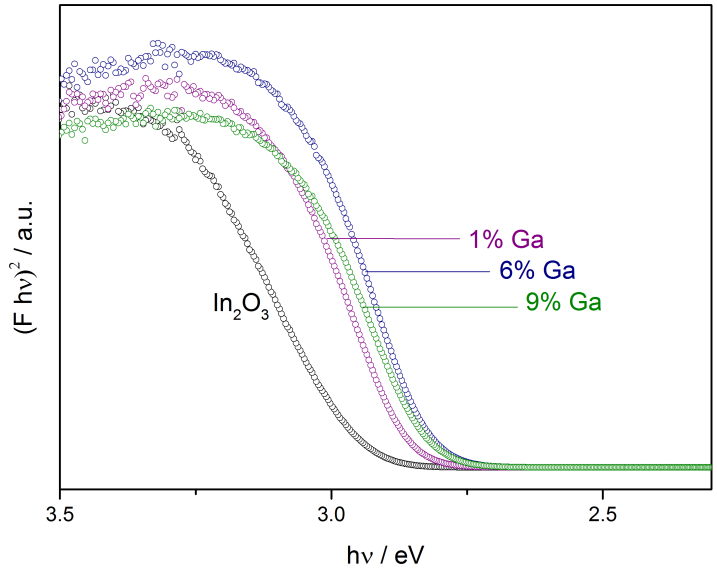


Figure 5.10: Tauc plot for pure In_2O_3 and three Ga-doped samples.

The band gap values derived from diffuse reflectance spectra for undoped In_2O_3 and for the complete series of Ga-doped samples are shown in figure 5.11. The decrease in band gap does, as expected, level off at approximately 6% Ga-doping.

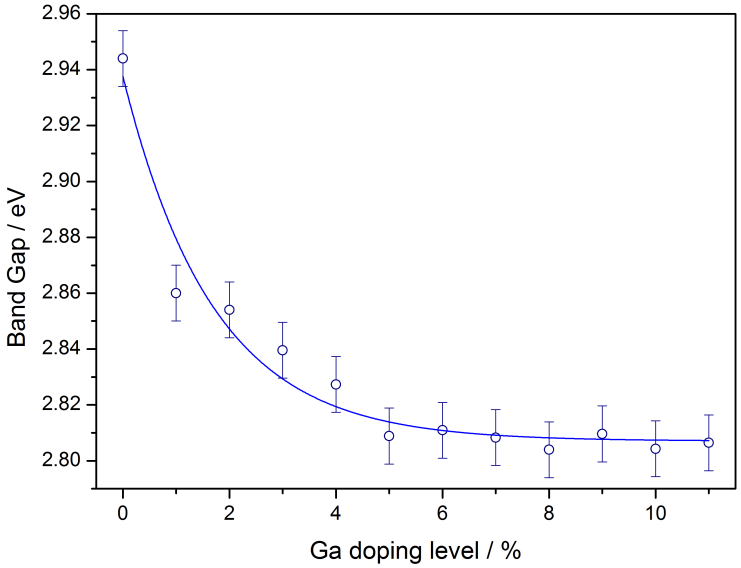


Figure 5.11: Band gap values for In_2O_3 and Ga-doping levels of up to 11%.

The decrease in band gap at lower doping levels does not simply follow an interpolation between narrower gap In_2O_3 and wider gap Ga_2O_3. This behaviour is not expected considering previous work on $(Ga_xIn_{1-x})_2O_3$ thin films, although most previous work investigates rather coarse doping steps of x = 0.1. The results imply that there is pronounced band bowing as has been observed in many "alloy" semiconductor systems as well as Sn-doped TiO_2 (see the introduction of this chapter for a more in-depth discussion).

The following equation was used to calculate band gap bowing coefficients B from the experimentally derived band gaps:[45]

$$E_g(x) = xE_g(Ga_2O_3) + (1-x)E_g(In_2O_3) - x(1-x)B \ , \tag{5.3}$$

where $E_g(x)$ is the band gap of the doped sample, x is the doping level, and $E_g(Ga_2O_3)$ and $E_g(In_2O_3)$ are the band gaps for the pure oxides. High band gap bowing coefficients B are derived for very small dopant concentration, but they quickly become smaller with higher doping levels. Whilst at 1% doping level a value

of B greater than 10 eV is calculated, the band gap bowing for $x = 0.1$ decreases to 3.32 eV. This shows that for the case of $(In_{1-x}Ga_x)_2O_3$ the band gap bowing coefficient is strongly concentration dependant. Figure 5.12 shows the trend in B for doped samples up to 7% Ga-content for $(Ga_xIn_{1-x})_2O_3$. However, it has to be noted that this procedure has severe limitations due to the end member oxides having different structures.

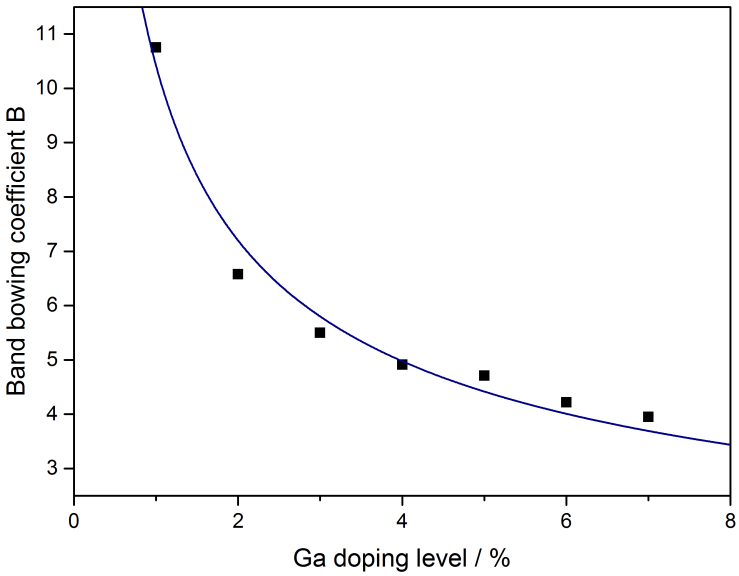


Figure 5.12: Band gap bowing coefficients B for Ga-doped In_2O_3. The solid line is for guidance only.

5.4.3 Band Gaps from Valence Band X-ray Photoemission Spectroscopy

Valence band spectra for pure In_2O_3 and Ga_2O_3 are shown in figure 5.13. The In_2O_3 spectrum was calibrated using the Fermi edge, and the Ga_2O_3 spectrum was calibrated assuming the C 1s binding energy was 285.0 eV.

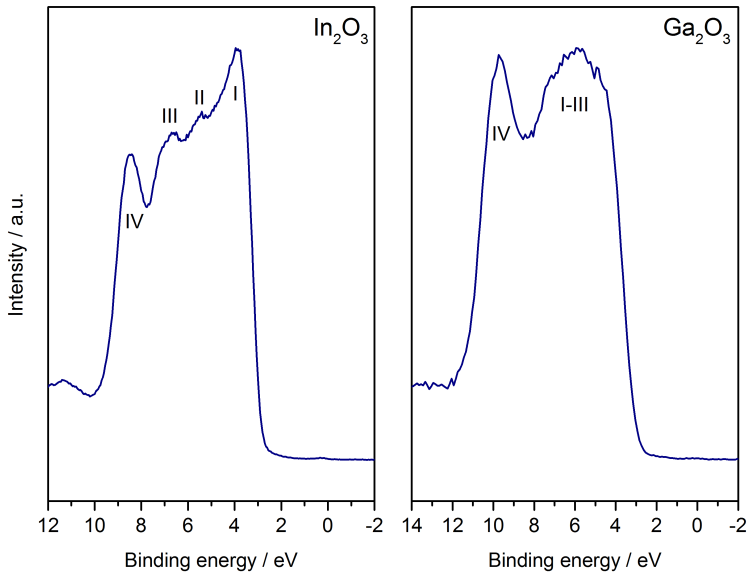


Figure 5.13: Valence band spectra for In_2O_3 and Ga_2O_3.

The valence band of In_2O_3 has four main features, labelled IV, III, II, and I in figure 5.13. They appear at binding energies of 8.5, 6.6, 5.4, and 3.9 eV respectively. Feature IV stems from states of mixed character In $5s$ and O $2p$, III and II arise from states of mixed O $2p$ and In $5p$ states, whilst I is mainly dominated by O $2p$ with some contribution from In $4d$.[46] In the spectrum of Ga_2O_3 the first three features overlap to give a broad band. II and III are a hybrid of Ga $4p$ and O $2p$. At the top of the valence band, feature I is dominated by states of more purely O $2p$ character with some interaction with shallow Ga $3d$ states. Feature IV remains distinct at a binding energy of 9.7 eV. This peak arises from states of mixed Ga $4s$ and O $2p$ character.

Valence band spectra for undoped In_2O_3 and 1% and 6% Ga-doped samples are shown in figure 5.14. The binding energies were referenced to the Fermi energy associated with the occupation of conduction band states.

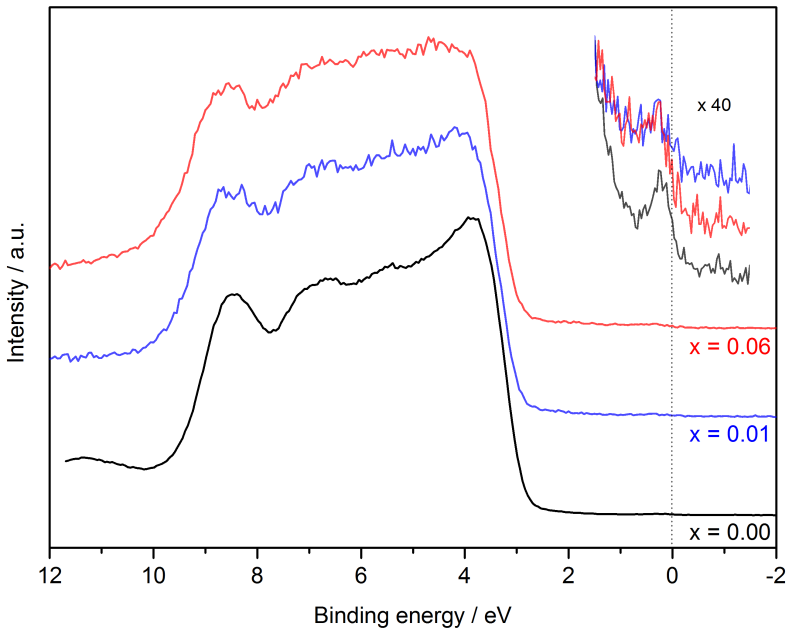


Figure 5.14: Valence band spectra for undoped In_2O_3 and 1% and 6% Ga-doped samples.

Apparent band gaps were derived by linear extrapolation of the lower binding energy side of the valence band from the valence band spectra. The extrapolations are indicated in figure 5.15.

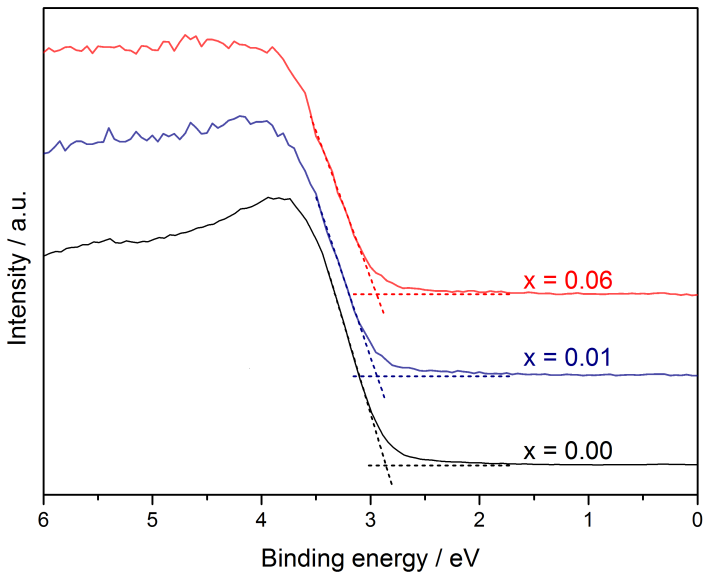


Figure 5.15: Expanded valence band spectra for undoped In_2O_3 and 1% and 6% Ga-doped samples showing the linear extrapolations to derive band gaps.

Figure 5.16 shows estimated band gap values from XPS data for Ga-doping levels

from 1% to 10%. It has to be noted that the procedure used here does not give a reliable estimate of the absolute value of the band gap for two reasons. First, downward band bending leads to carrier accumulation at the surface with partial occupation of the conduction band which leads to the valence band edge lying further below the Fermi level than in the bulk.[47,48] This band bending accounts for the appearance of the conduction band feature which can be seen in figure 5.14. Second, experimental and phonon broadening of the valence band edge, which is very sharp in the DFT calculated density of states, shifts the apparent valence band onset to lower binding energy. These two effects mutually cancel to some extent so that the band gaps from XPS are quite close to those from diffuse reflectance. *If* band bending is the same for all samples these effects should not influence estimated variations in band gap. Finally, it should be mentioned that there is recent evidence from angle resolved photoemission that there may be pronounced shrinkage of the band gap at the surface due to many body effects.[49]

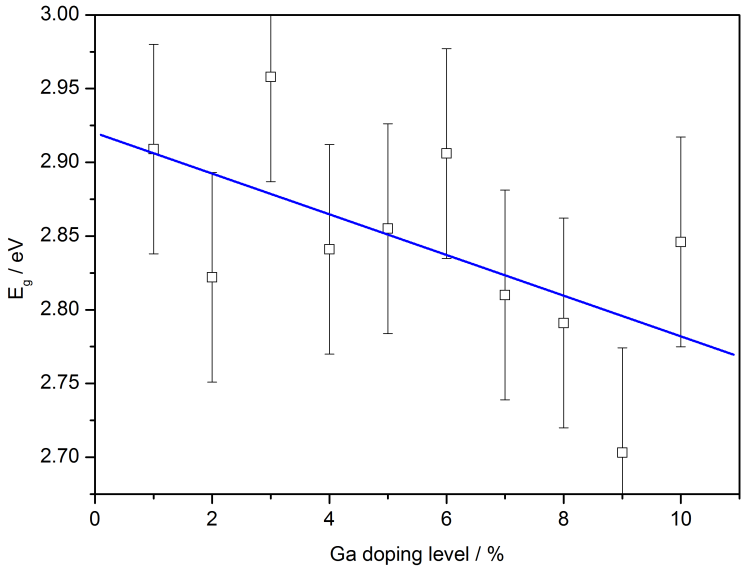


Figure 5.16: Estimated band gap values from valence band edges for In_2O_3 with Ga-doping levels from 1% to 10%.

The experimental results derived from the diffuse reflectance data were compared with calculations performed by Dr. D. O. Scanlon. The incorporation of one Ga

atom into a 40 atom primitive cell of In_2O_3 on both the 8b and 24d sites was tested. Ga is 0.096 eV more stable on the 8b site, indicating that it will have a strong preference at room temperature for taking up this site. The HSE06 calculated fundamental band gap and optical band gaps for In_2O_3 and $In_{1.875}Ga_{0.125}O_3$ are shown in Figure 5.17. It is immediately obvious that the incorporation of Ga causes the fundamental band gap, as well as the optical band gap, to increase slightly from 2.75 eV to 2.81 eV, which is not in agreement with the experimental results presented here. Clearly, the incorporation of the much smaller Ga onto an In site is not sufficient to break the symmetry of the disallowed VB to CB transitions, and so does not significantly alter the optical properties. Many symmetry distortions were trialled, with the Ga ion placed off-centre from both distinct In sites, and, without fail, the Ga returns to the In lattice site.

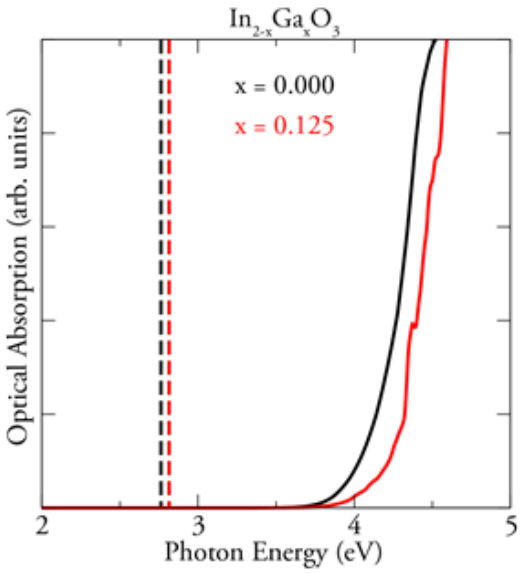


Figure 5.17: HSE06 calculated optical absorption spectra for $In_{2-x}Ga_xO_3$ for x = 0.000 and 0.125. Dashed lines indicate fundamental band gap, full lines indicate optical absorption.

5.4.4 Core-level X-ray Photoemission Spectroscopy and Gallium Surface Segregation

XPS wide scans of 1% and 10% Ga-doped In_2O_3 are shown in figure 5.18. The presence of gallium dopant results in a number of Ga signatures appearing. The most pronounced are the Ga $2p$ core lines and the Ga LMM Auger lines. The weaker Ga $3p$ core levels are observed between the In $4p$ and $4s$ structures, whilst the Ga $3s$ core level can be observed in higher doped samples. However, the Ga 3d core line overlaps the In $4d$ and O $2s$ peaks of the host material.

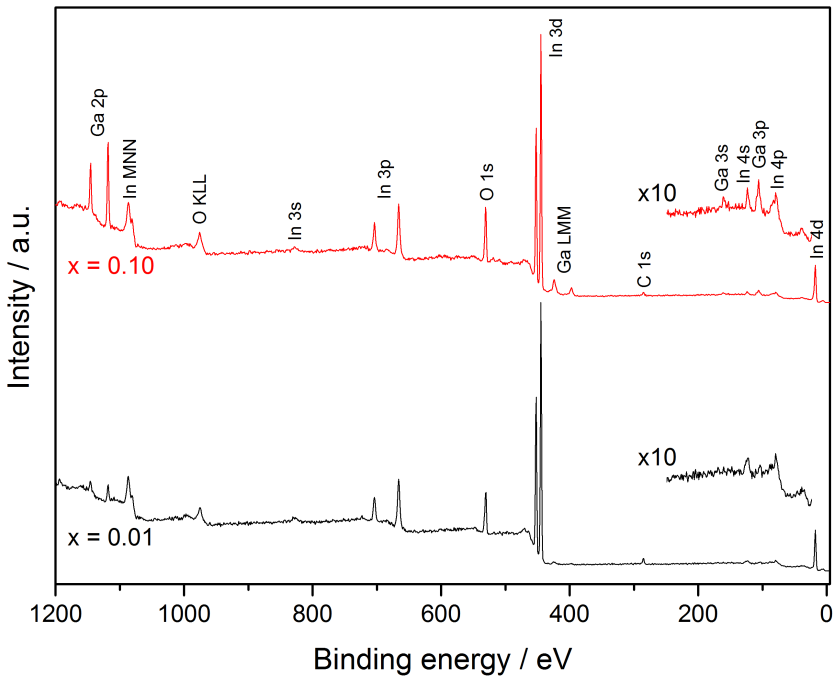


Figure 5.18: Widescan XPS of 1% and 10% Ga-doped In_2O_3.

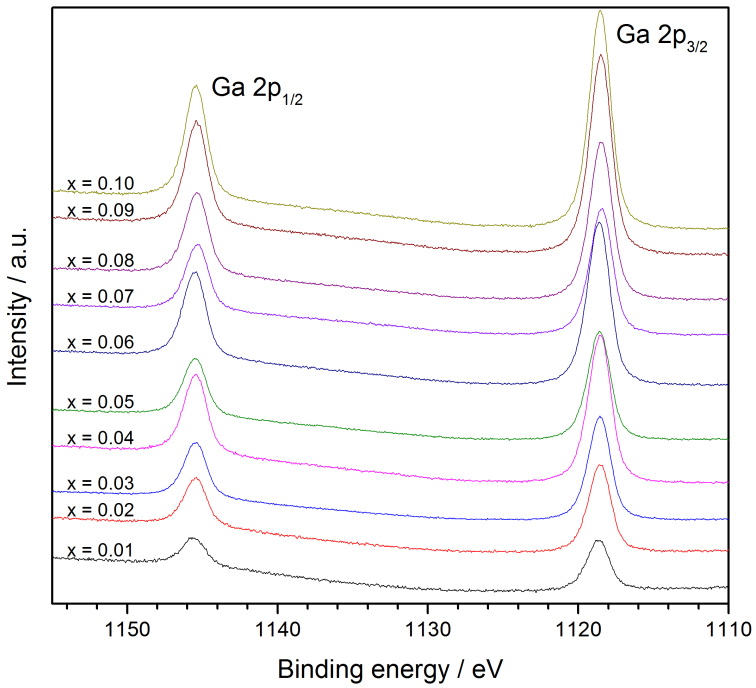


Figure 5.19: Ga $2p$ core level spectra of Ga-doped In_2O_3. The intensities have been normalised to the In $3d$ intensity.

Figure 5.19 shows the Ga $2p$ core level in greater detail, with intensities normalised to the In $3d$ intensity of In_2O_3.

From these data the Ga content on the surface of the samples could be obtained. In order to achieve this, the peak areas of the Ga $2p_{3/2}$ and the In $3d_{5/2}$ core levels were corrected with the relevant atomic sensitivity factors of 5.4 for Ga $2p_{3/2}$ and 3.9 for In $3d_{5/2}$.[50] The apparent surface Ga content ratios for samples with doping levels of 1% to 10% and for pure In_2O_3 are shown in figure 5.20. Pronounced surface enrichment of Ga is observed for all doped samples, especially for low Ga concentrations.

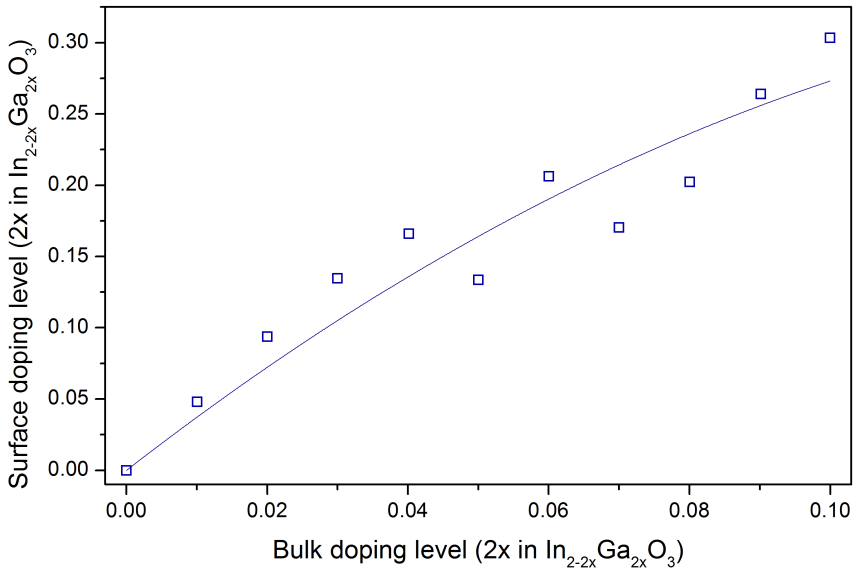


Figure 5.20: Surface Ga-doping levels as a function of the bulk doping level from Ga $2p_{3/2}$ and In $3d_{5/2}$ core level intensities. The solid line is for guidance only.

There are two possible driving forces for the surface segregation of Ga. Firstly, this surface segregation can be understood in terms of strain. The mismatch in ionic radii upon doping will lead to strain around the dopant. This strain is lowered if the dopant leaves its position in the regular crystal lattice and segregates on the surface. Friedel proposed the use of the calculation of an elastic energy for this purpose in 1954,[51] and here a derived equation from Battaile *et al.* is used.[52] The elastic energy E_{el} can be calculated using the following equation:

$$E_{el} = \frac{24\pi K_A G_B r_B^3 r_A (\frac{r_A}{r_B} - 1)^2}{3K_A r_A + 4G_B r_B} \ , \tag{5.4}$$

where index A denotes the solute and index B denotes the solvent, and K is the bulk modulus, G is the shear modulus, and r is the ionic radius. A value of 228 GPa for the bulk modulus of Ga_2O_3 was used.[53] A shear modulus of 84 GPa was calculated for In_2O_3 from equation 5.5 using the Poisson ratio ν determined before to be 0.31[54,55] and a bulk modulus of 194 GPa calculated by Walsh *et al.*[56]

$$G = \frac{3K(1-2\nu)}{2(1+\nu)} \ . \tag{5.5}$$

A value of 0.185 eV per Ga ion for the elastic strain energy could be derived for Ga-doped In_2O_3. This is sufficient to drive pronounced surface segregation.

Secondly, segregation in post transition metal dopants can be driven by a change in the valence state of the surface. This has previously been found in systems such as Sn-doped TiO_2,[14,15] Sb-doped SnO_2,[57,58] and Sn-doped In_2O_3.[59] In these systems the dopant substitutes bulk ions with a group of oxidation state of N, and has an electronic configuration $5s^0 5p^0$. However, segregated ions have an oxidation state of $N-2$, with an electronic configuration $5s^2 5p^0$. At surface sites, mixing between $5s$ and $5p$ states mediated by interaction with O $2p$ valence states leads to a lowering of the internal electronic energy of the segregated ions, and thus provides a driving force for segregation.[60]

Extending these findings to the $(In_{1-x}Ga_x)_2O_3$ system, segregation could be understood in terms of occupation of surface sites by Ga^+ ions. For this case, one might expect a chemical shift between bulk and surface Ga ions. As the segregation is more pronounced at lower Ga-doping levels, one would expect a greater contribution from surface segregated ions in this case.

However, a chemical shift could not be observed. Figure 5.21 shows Ga $2p_{3/2}$ core lines for 1% and 10% Ga-doped In_2O_3, which can be well fitted with single pseudo-Voigt functions possessing the characteristics summerised in table 5.4.

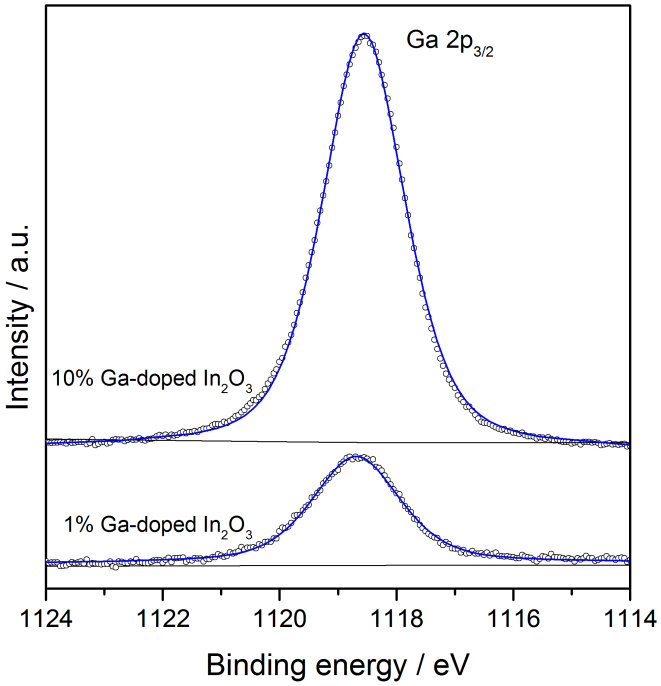


Figure 5.21: Curve fits to the Ga $2p_{3/2}$ core line for 1% and 10% Ga-doped In_2O_3.

Table 5.4: Curve parameters from fits to the Ga $2p_{3/2}$ core line for 1% and 10% Ga-doped In_2O_3. Binding energy BE, full width at half maximum FWHM, and the lorentzian part of the function are given.

Sample	BE / eV	FWHM / eV	% Lorentzian
1% Ga-doped In_2O_3	1118.69±0.4	1.78±0.05	0.58±0.05
10% Ga-doped In_2O_3	1118.56±0.4	1.70±0.05	0.60±0.05

It is concluded that either there is no shift between bulk Ga^{3+} and surface Ga^{+} or that this mechanism does not pertain. The next section will explore this topic further.

5.4.5 Influence of Ion Bombardment on Valence and Core Level XPS of Ga_2O_3

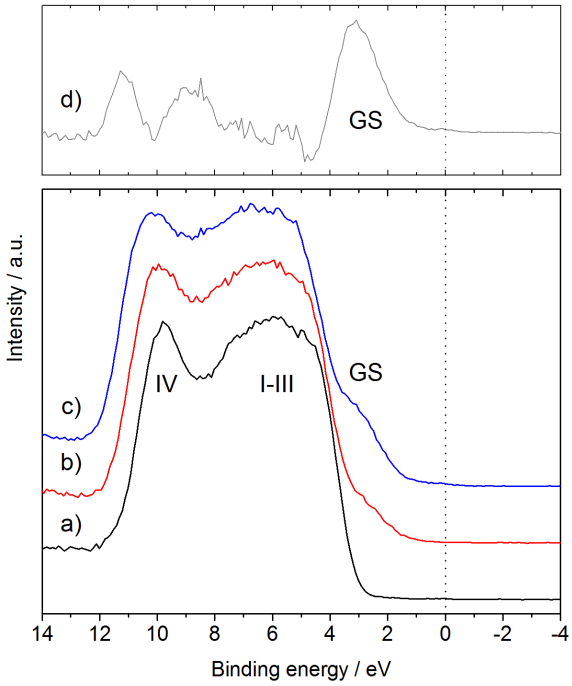


Figure 5.22: Sputtering results for pure Ga_2O_3. (a) Valence band of as-presented β-Ga_2O_3, (b) valence band spectrum after ion bombardment for 20 minutes, and (c) after 40 minutes. (d) presents the difference between (c) and (a) to illustrate the growth of a gap-state (GS) structure above the valence band edge as a consequence of ion bombardment.

Figure 5.22 shows the valence band of "as-presented" β-Ga_2O_3, along with spectra obtained after two consecutive 20 minute sputtering cycles as described in the experimental section of this chapter. The spectrum of the sample before bombardment shows the features described in section 5.4.3. The spectra were aligned assuming that the C 1s core line is at 285.0 eV. With this correction, the Fermi edge is pinned in the middle of the band gap which is a known behaviour for insulators and the valence band onset appears at around 2.5 eV.[61]

After ion bombardment an additional feature appears above the top of the O 2p valence band. A gap state structure, labelled GS in the figure, increases in intensity upon ion bombardment. The observed structure is very similar to that found in va-

lence band XPS of ion bombarded SnO_2[62] or indeed in the valence band spectrum of SnO.[63] In the case of SnO_2 the structure is assigned to Sn^{2+} states arising from new occupied antibonding states of mixed O $2p$ - Sn $5s$ character above the top of the valence band, which further hybridise with Sn $5p$ states to give a directional lone pair.[60,64] By analogy with this earlier work we take the appearance of the gap state structure to be the definitive signature of reduction of Ga_2O_3 under ion bombardment by preferential sputtering of oxygen to give reduced Ga^+.

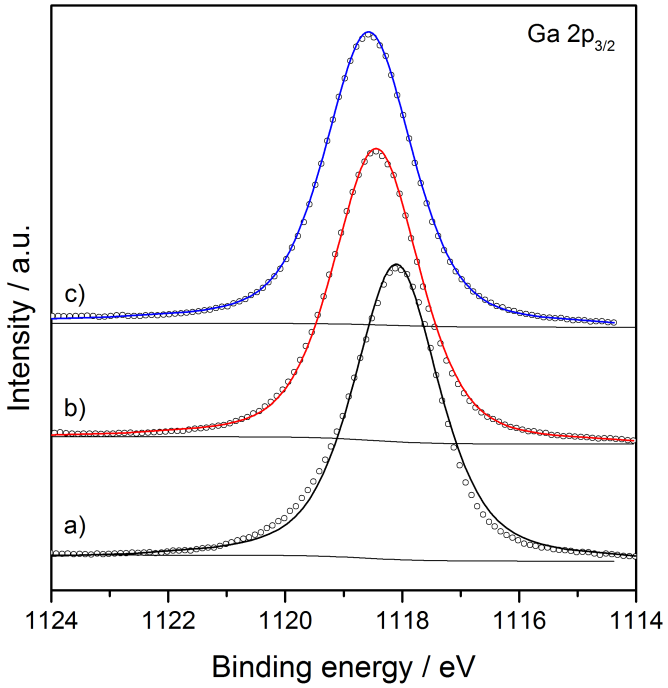


Figure 5.23: Curve fits to the Ga $2p_{3/2}$ core line for β-Ga_2O_3 (a) "as-presented", (b) after ion bombardment for 20 minutes, and (c) after ion bombardment for 40 minutes.

Although there is a noticeable change in the valence band with the emergence of the gap state structure, no significant changes to the Ga $2p_{3/2}$ core level are observed. Figure 5.23 shows Ga $2p_{3/2}$ core lines for β-Ga_2O_3, which can be well fitted with single pseudo-Voigt functions with the characteristics summarised in table 5.5. The peak for "as-presented" Ga_2O_3 is slightly asymmetric, which is most probably due to surface contamination.

Table 5.5: Curve parameters from fits to the Ga $2p_{3/2}$ core line for "as-presented" and ion bombarded β-Ga_2O_3. Binding energy BE, full width at half maximum (FWHM), and the Lorentzian part of the function are given.

Sample	BE / eV	FWHM / eV	% Lorentzian
"as-presented"	1118.10±0.4	1.74±0.05	0.68±0.05
20 min	1118.44±0.4	1.75±0.05	0.56±0.05
40 min	1118.57±0.4	1.77±0.05	0.57±0.05

It retains very similar widths and Gaussian-Lorentzian mixes as for the "as-presented" β-Ga_2O_3. Therefore, it can be concluded that there is no significant chemical shift between bulk Ga^{3+} and surface Ga^{+}, which is responsible for the gap state.

It should be noted, that a pronounced chemical shift of around 1.5 eV between Ga_2O_3 and Ga_2O has been suggested.[65] This shift is not consistent with the results presented here and is out of line with other $N/N-2$ systems, as discussed below.

The behaviour observed here is analogous to that found for tin oxides, where a chemical shift in Sn $3d$ core levels between SnO and SnO_2 is below 0.08 eV; and for the mixed valence oxide Pb_3O_4, where unsplit and symmetric Pb $4f$ core levels are observed despite the presence of Pb^{4+} and Pb^{2+}.[66]

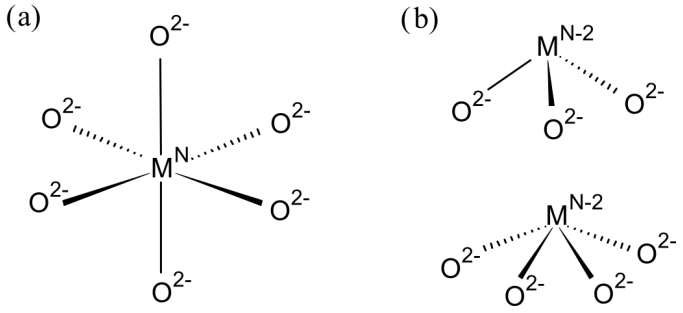


Figure 5.24: Schematic environments of metal cations in metal oxides. (a) cation with oxidation state N in a 6-coordinate centrosymmetric site, (b) cation with oxidation state $N-2$ occupying asymmetric 3- or 4-coordinate sites.

To understand the absence of a chemical shift between N and $N-2$ oxidation

states, one has to take the coordination symmetry of the two states into account. Figure 5.24 shows that ions with oxidation state N occupy 6-coordinate centrosymmetric sites, whereas $N-2$ ions occupy asymmetric 3- or 4-coordinate sites. This leads to a change in the Madelung site potentials which can cancel out the changes in the free ion potentials.[66–68]

5.4.6 Surface Atomic Composition from Low Energy Ion Scattering (LEIS)

Ceramic $(In_{1-x}Ga_x)_2O_3$ samples show pronounced surface segregation in XPS. LEIS was used to investigate this further and to create a depth profile of selected samples.

Ion scattering spectra were measured with a Ne^+ probe beam with Ar^+ depth profiling in between scans. The sputtering yields were estimated by Dr. H. Tellez-Lozano using "Stopping and Range of Ions in Matter" (SRIM) software and are given in table 5.6. The sputter yields for both In_2O_3 and Ga_2O_3 are very similar. The In_2O_3 sputter yield is equivalent to an etch depth of 0.327±0.05 nm during a 5 seconds sputter cycle. However, SRIM overestimates sputtering yields for oxides by a factor of 3 to 5, meaning that the actual sputter rate could be closer to 0.10 nm.

Table 5.6: Sputtering yields estimated using SRIM for Ar^+ at 500 eV and 59°. For In_2O_3 a cubic structure with a density of 7.179 g/cm^3 and for Ga_2O_3 the β-phase with a density of 5.88 g/cm^3 were assumed.

	atoms/ion	eV/atom
In	1.68	17.79
O	2.73	13.87
total	4.41	31.66
Ga	1.66	18.84
O	2.95	12.64
total	4.61	31.48

Ion scattering spectra excited with 3 keV Ne^+ ions for 1% and 10% Ga-doped In_2O_3 are shown in figure 5.25. Both spectra were taken after mild Ar ion bombardment followed by 10 seconds exposure to the Ne^+ probe ion beam, which is sufficient to remove surface carbon contamination. The scattering peak associated with collision with the lighter Ga is found to lower energy of the scattering peak associated with scattering from In.

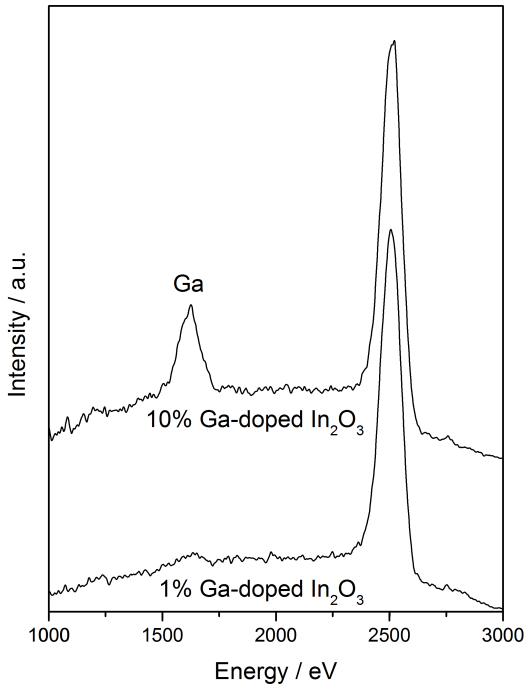


Figure 5.25: Low energy ion scattering spectra of 1% and 10% Ga-doped In_2O_3 measured with 3 keV Ne ions after removal of the initial carbon contamination layer by Ar^+ sputtering for 10 seconds.

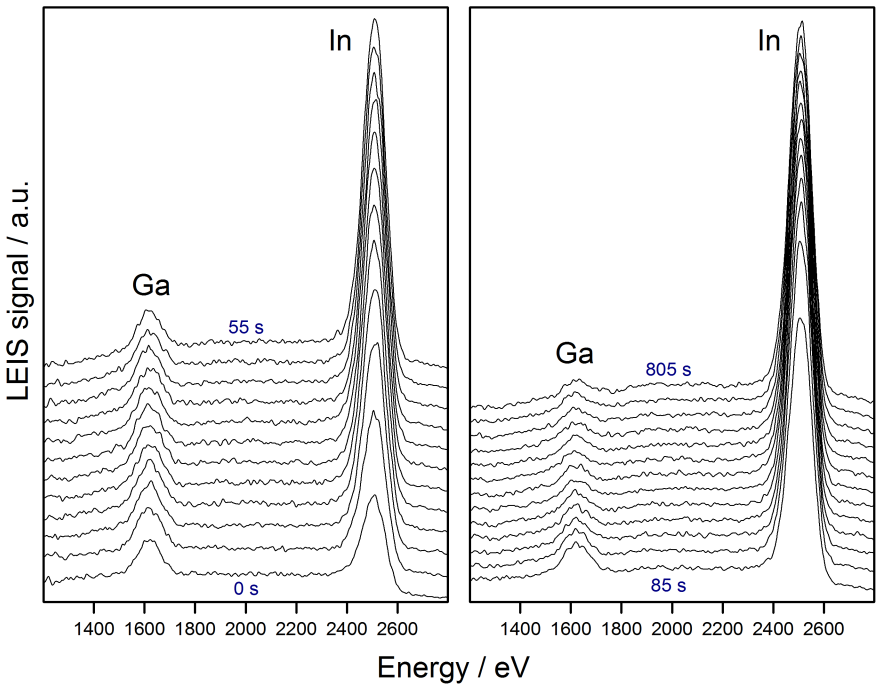


Figure 5.26: Low energy ion scattering spectra for 5 keV Ne^+ scattered over 145° by a 10% Ga-doped In_2O_3 sample. The left hand panel shows spectra measured at 5 s sputtering intervals between 0 s and 55 s. The right hand panel shows spectra measures at 60 s intervals between 85 s and 805 s.

Figure 5.26 shows a series of spectra for 10% Ga-doped In_2O_3 over a total sputtering time of 805 s. The Ga peak is continuously getting smaller, indicating a difference between surface and bulk concentration. A progressive decrease in the Ga peak is observed.

Depth profiles for 1%, 6%, and 10% doped samples, were recorded and quantified (see figure 5.27). Spectra were taken in intervals of 5 s until the change in concentration slowed down and spectra were measured every 60 s from that point. Sputtering was continued until the Ga concentration stabilised.

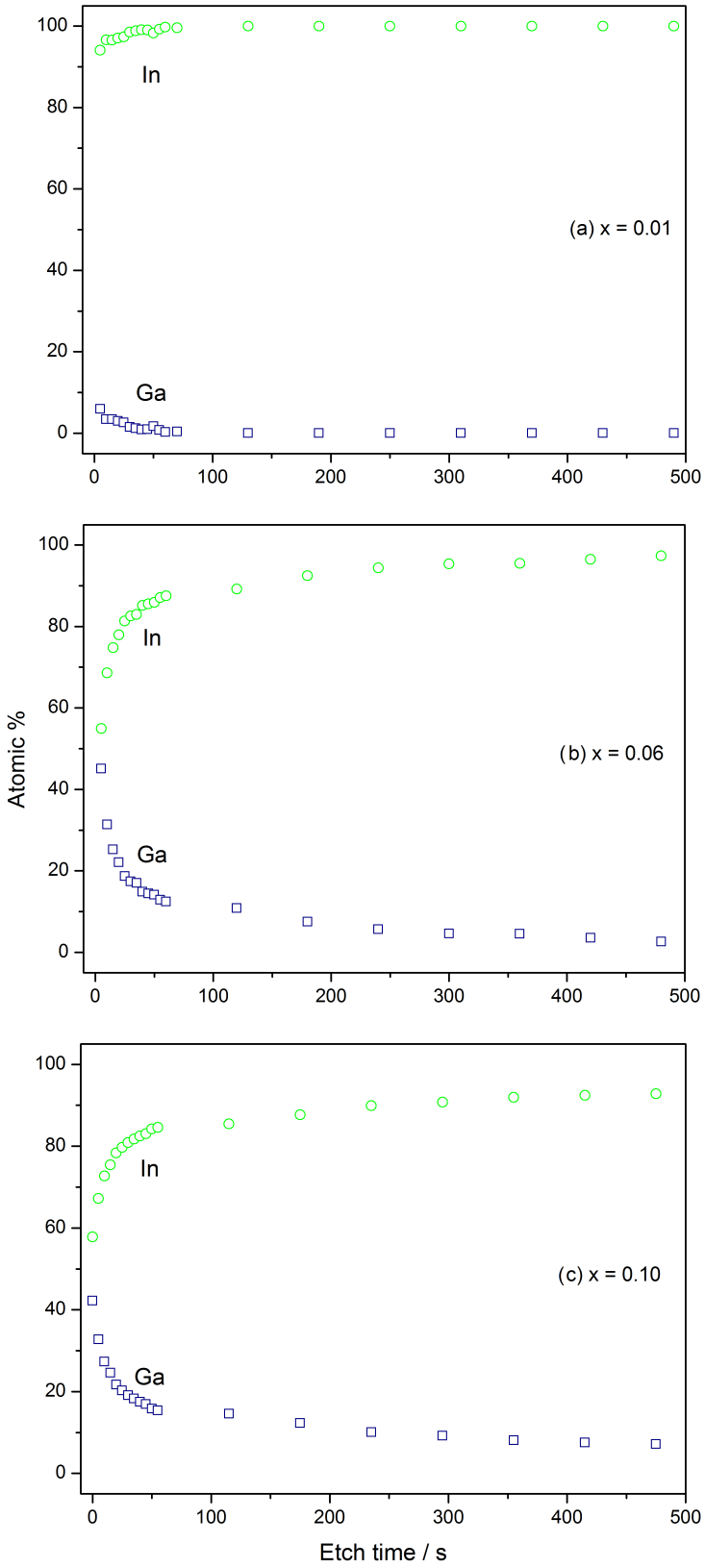


Figure 5.27: Atomic percentages of Ga and In for three samples, (a) 1%, (b) 6% and (c) 10% Ga-doped In_2O_3 upon sputtering.

Pronounced surface segregation can be seen for all three samples and table 5.7 gives the surface c_{surf} and bulk c_{bulk} concentrations for all three samples. The segregation is more pronounced for lower doping levels, for example $c_{bulk} = 15 \times c_{surf}$ for the 6% doped sample and $c_{bulk} = 9 \times c_{surf}$ for the 10% doped sample.

Table 5.7: Surface c_{surf} and bulk c_{bulk} concentrations of Ga in %.

Sample	c_{surf}	c_{bulk}
x = 0.01	5.03	<0.0001
x = 0.06	22.11	1.44
x = 0.10	28.95	3.09

The equilibrium surface Ga concentration was, in all cases, significantly lower than the bulk doping level suggesting that in the steady state during a LEIS experiment the surface is depleted of the lighter Ga dopant atoms as compared to the bulk In.

5.5 Concluding Remarks

This chapter shows structural and electronic changes upon Ga-doping of In_2O_3. In the prepared ceramic samples a solubility limit for Ga in In_2O_3 of 7% was confirmed with X-ray diffraction and Raman spectroscopy. The increase in dopant concentration goes hand in hand with a decrease in lattice parameters and above 7% Ga-doping a second phase could be identified. $(Ga_xIn_{1-x})_2O_3$ samples show apparent narrowing of the band gap in both diffuse reflectance spectroscopy and X-ray photoemission spectroscopy. Taken at face value the results suggest an unusually large band bowing effect. Calculations by Dr. D. O. Scanlon on bulk Ga-doped In_2O_3 fail to reproduce the observed narrowing of the bandgap with doping and instead predict a monotonic increase of gap with increasing Ga content.

In XPS spectra a pronounced surface segregation of Ga is apparent which sug-

gests that the effects observed could be attributed to surface segregated Ga^+. There was no direct evidence for Ga^+ in core level XPS. Contrary to this observation, the experiments on ion bombarded Ga_2O_3 show a clear indication for a reduced Ga^+ species with a lone pair state above the valence band edge in valence band XPS, without the simultaneous appearance of a chemically shifted Ga $2p$ component.

This leads to the conclusion that the chemical shift between surface Ga^+ and bulk Ga^{3+} in this system is negligibly small, as in related systems such as SnO_2/SnO. This allows for the possibility that the apparent band gap narrowing arises from surface segregated Ga^+. It is noted that the shape of structure at the valence band edge is somewhat different between ion bombarded Ga_2O_3 and Ga-doped In_2O_3 with segregated Ga, but the surface sites in these two systems could be very different.

5.6 References

[1] V. M. Goldschmidt, T. Barth, and G. Lunde, *Geochemische Verteilungsgesetze Der Elemente. V. Isomorphie und Polymorphie der Sesquioxyde, die Lanthaniden-Kontraktion und ihre Konsequenzen.*, Skrifter (Norske videnskaps-akademi i Oslo. I - Mat.-naturv. klasse) No. 7 (Kristiania, 1925).

[2] S. J. Schneider, R. S. Roth, and J. L. Waring, Journal of Research of the National Bureau of Standards **65A**, 345 (1961).

[3] J. MacDonald, J. A. Gard, and F. P. Glasser, Journal of Inorganic and Nuclear Chemistry **29**, 661 (1967).

[4] R. D. Shannon and C. T. Prewitt, Journal of Inorganic and Nuclear Chemistry **30**, 1389 (1968).

[5] D. D. Edwards, P. E. Folkins, and T. O. Mason, Journal of the American Ceramic Society **80**, 253 (1997).

[6] G. Patzke and M. Binnewies, Solid State Sciences **2**, 689 (2000).

[7] T. Minami, Y. Takeda, T. Kakumu, S. Takata, and I. Fukuda, Journal of Vacuum Science and Technology A **15**, 958 (1997).

[8] T. Oshima and S. Fujita, Physica Status Solidi C **5**, 3113 (2008).

[9] T. Oshima, N. Arai, N. Suzuki, S. Ohira, and S. Fujita, Thin Solid Films **516**, 5768 (2008).

[10] L. Kong, J. Ma, F. Yang, C. Luan, and Z. Zhu, Journal of Alloys and Compounds **499**, 75 (2010).

[11] L. Kong, J. Ma, C. Luan, and Z. Zhu, Journal of Solid State Chemistry **184**, 1946 (2011).

[12] C. E. Knapp, A. Kafizas, I. P. Parkin, and C. J. Carmalt, Journal of Materials Chemistry **21**, 12644 (2011).

[13] Y. Kokubun, T. Abe, and S. Nakagomi, Physica Status Solidi A **207**, 1741 (2010).

[14] M. H. Harunsani, F. E. Oropeza, R. G. Palgrave, and R. G. Egdell, Chemistry of Materials **22**, 1551 (2010).

[15] F. E. Oropeza, B. Davies, R. G. Palgrave, and R. G. Egdell, Physical Chemistry Chemical Physics **13**, 7882 (2011).

[16] I. Vurgaftman, J. R. Meyer, and L. R. Ram-Mohan, Journal of Applied Physics **89**, 5815 (2001).

[17] X. F. Fan, H. D. Sun, Z. X. Shen, J.-L. Kuo, and Y. M. Lu, Journal of Physics: Condensed Matter **20**, 235221 (2008).

[18] K. Iwata, P. Fons, A. Yamada, H. Shibata, K. Matsubara, K. Nakahara, H. Takasu, and S. Niki, Physica Status Solidi B **229**, 887 (2002).

[19] A. Schleife, C. Rödl, J. Furthmüller, and F. Bechstedt, New Journal of Physics **13**, 085012 (2011).

[20] L. Dong and S. P. Alpay, Physical Review B **84**, 035315 (2011).

[21] E. P. Nakhmedov, E. Nadimi, M. Bouhassoune, C. Radehaus, and K. Wieczorek, Physical Review B **75**, 115204 (2007).

[22] A. Bourlange, D. J. Payne, R. G. Palgrave, J. S. Foord, R. G. Egdell, R. M. J. Jacobs, A. Schertel, J. L. Hutchison, and P. J. Dobson, Thin Solid Films **517**, 4286 (2009).

[23] A. Bourlange, D. J. Payne, R. M. J. Jacobs, R. G. Egdell, J. S. Foord, A. Schertel, P. J. Dobson, and J. L. Hutchison, Chemistry of Materials **20**, 4551 (2008).

[24] G. Kresse and J. Hafner, Physical Review B **49**, 14251 (1994).

[25] G. Kresse and D. Joubert, Physical Review B **59**, 1758 (1999).

[26] A. V. Krukau, O. A. Vydrov, A. F. Izmaylov, and G. E. Scuseria, Journal of Chemical Physics **125**, 224106 (2006).

[27] M. Burbano, D. O. Scanlon, and G. W. Watson, Journal of The American Chemical Society **133**, 15065 (2011).

[28] D. O. Scanlon, A. B. Kehoe, G. W. Watson, M. O. Jones, W. I. F. David, D. J. D. J. Payne, R. G. Egdell, P. P. Edwards, and A. Walsh, Physical Review Letters **107**, 246402 (2011).

[29] J. P. Allen, D. O. Scanlon, and G. W. Watson, Physical Review B **81**, 161103(R) (2010).

[30] D. O. Scanlon and G. W. Watson, Journal of Materials Chemistry **21**, 3655 (2011).

[31] P. Agoston, K. Albe, R. M. Nieminen, and M. J. Puska, Physical Review Letters **103**, 245501 (2009).

[32] M. Gajdos, K. Hummer, G. Kresse, J. Furthmuller, and F. Bechstedt, Physical Review B **73**, 045112 (2006).

[33] B. Adolph, J. Furthmuller, and F. Bechstedt, Physical Review B **63**, 125108 (2001).

[34] M. Marezio, Acta Crystallographica **20**, 723 (1966).

[35] R. D. Shannon and C. T. Prewitt, Acta Crystallographica B **25**, 925 (1969).

[36] D. M. Toebbens, N. Stuesser, K. Knorr, H. M. Mayer, and G. Lampert, Materials Science Forum **378**, 288 (2001).

[37] A. R. Denton and N. W. Ashcroft, Physical Review A **43**, 3161 (1991).

[38] R. Roy, V. G. Hill, and E. F. Osborn, Journal of the American Chemical Society **74**, 719 (1952).

[39] S. Yoshioka, H. Hayashi, A. Kuwabara, F. Oba, K. Matsunaga, and I. Tanaka, Journal of Physics: Condensed Matter **19**, 346211 (2007).

[40] H. Y. Playford, A. C. Hannon, E. R. Barney, and R. I. Walton, Chemistry - A European Journal **19**, 2803 (2013).

[41] B. Garcia-Domene, H. M. Ortiz, O. Gomis, J. A. Sans, F. J. Manjon, A. Munoz, P. Rodriguez-Hernandez, S. N. Achary, D. Errandonea, D. Martinez-Garcia, A. H. Romero, A. Singhal, and A. K. Tyagi, Journal of Applied Physics **112**, 123511 (2012).

[42] D. Dohy and G. Lucazeau, Journal of Molecular Structure **79**, 419 (1982).

[43] A. Walsh, J. L. F. D. Silva, S.-H. Wei, C. Korber, A. Klein, L. F. J. Piper, A. DeMasi, K. E. Smith, G. Panaccione, P. Torelli, D. J. Payne, A. Bourlange, and R. G. Egdell, Physical Review Letters **100**, 167402(4) (2008).

[44] M. Orita, H. Ohta, M. Hirano, and H. Hisono, Applied Physics Letters **77**, 4166 (2000).

[45] C.-Y. Moon, S.-H. Wei, Y. Z. Zhu, and G. D. Chen, Physical Review B **74**, 233202 (2006).

[46] C. Körber, V. Krishnakumar, A. Klein, G. Panaccione, P. Torelli, A. Walsh, J. L. F. D. Silva, S. H. Wei, R. G. Egdell, and D. J. Payne, Physical Review B **81**, 165207 (2010).

[47] P. D. C. King, T. D. Veal, D. J. Payne, A. Bourlange, R. G. Egdell, and C. F. McConville, Physical Review Letters **101**, 116808 (2008).

[48] P. D. C. King, T. D. Veal, F. Fuchs, C. Y. Wang, D. J. Payne, A. Bourlange, H. Zhang, G. R. Bell, V. Cimalla, O. Ambacher, R. G. Egdell, F. Bechstedt, and C. F. McConville, Physical Review B **79**, 205211 (2009).

[49] K. H. L. Zhang, R. G. Egdell, F. Offi, S. Iacobucci, L. Petaccia, S. Gorovikov, and P. D. C. King, Physical Review Letters **110**, 056803 (2013).

[50] C. D. Wagner, L. E. Davis, M. V. Zeller, J. A. Taylor, R. H. Raymond, and L. H. Gale, Surface and Interface Analysis **3**, 211 (1981).

[51] J. Friedel, Advances in Physics **3**, 446 (1954).

[52] C. C. Battaile, R. Najafabadi, and D. J. Srolovitz, Journal of the American Ceramic Society **78**, 3195 (1995).

[53] H. Wang, Y. He, W. Chen, Y. W. Zeng, K. Stahl, T. Kikegawa, and J. Z. Jiang, Journal of Applied Physics **107**, 033520 (2010).

[54] K. H. L. Zhang, A. Regoutz, R. G. Palgrave, D. J. Payne, R. G. Egdell, A. Walsh, S. P. Collins, D. Wermeille, and R. Cowley, Physical Review B **84**, 233301 (2011).

[55] A. Regoutz, K. H. L. Zhang, R. G. Egdell, D. Wermeille, and R. Cowley, Journal of Materials Research **27**, 2257 (2012).

[56] A. Walsh, C. R. A. Catlow, A. A. Sokol, and S. M. Woodley, Chemistry of Materials **21**, 4962 (2009).

[57] P. Cox, R. Egdell, C. Harding, A. Orchard, W. Patterson, and P. Tavener, Solid State Communications **44**, 837 (1982).

[58] P. Cox, R. Egdell, C. Harding, W. Patterson, and P. Tavener, Surface Science **123**, 179 (1982).

[59] P. Cox, W. R. Flavell, and R. G. Egdell, Journal of Solid State Chemistry **68**, 340 (1987).

[60] A. Walsh, D. J. Payne, R. G. Egdell, and G. W. Watson, Chemical Society Reviews **40**, 4455 (2011).

[61] R. G. Egdell, V. E. Henrich, R. Bowdler, and T. Sekine, Journal of Applied Physics **94**, 6611 (2003).

[62] R. G. Egdell, J. Rebane, T. J. Walker, and D. S. L. Law, Physical Review B **59**, 1792 (1999).

[63] C. L. Lau and G. K. Wertheim, Journal of Vacuum Science and Technology **15**, 622 (1978).

[64] A. Walsh and G. W. Watson, Physical Review B **70**, 235114 (2004).

[65] R. Carli and C. L. Binanchi, Applied Surface Science **74**, 99 (1994).

[66] J. M. Thomas and M. J. Tricker, Journal of the Chemical Society Faraday Transactions II **71**, 329 (1975).

[67] J. Q. Broughton and P. S. Bagus, Journal of Electron Spectroscopy and Related Phenomena **20**, 261 (1980).

[68] D. E. Parry, Journal of the Chemical Society Faraday Transactions II **71**, 337 (1975).

6 Electronic and Surface Properties of Tl-doped In_2O_3 Ceramics

6.1 Introduction

Following the experimental work on Ga-doped In_2O_3, Tl-doping of In_2O_3 was investigated. Tl_2O_3 has a very low band gap of only 0.33 eV.[1] This low value suggests there should be a pronounced reduction of the gap of In_2O_3 upon Tl doping.

No literature could be found on Tl-doping of In_2O_3, most possibly as a result of the complex safety issues regarding Tl_2O_3. Thallium and its compounds, including Tl_2O_3, are highly toxic. The main risks are easy absorption through the skin and high volatility, which leads to an associated risk of inhalation upon heating. Tl accumulates in the body and ultimately leads to irreparable damage to the nervous system.[2] Despite these concerns, calculations on Tl-doped In_2O_3 performed by Dr. D. O. Scanlon acted as a catalyst for the interest in Tl as a possible dopant.

In this chapter the calculated values of the band gap are compared with results from high resolution X-ray photoelectron spectroscopy (XPS) on ceramic $(In_{1-x}Tl_x)_2O_3$

samples. In addition, the pronounced surface segregation of Tl by means of ion bombardment depth profiling in XPS is investigated.

6.2 Experimental

Tl-doped In_2O_3 ceramic samples were prepared using a high temperature solid state approach. The starting materials were Tl_2O_3 (99.99%, supplied by Sigma-Aldrich Inc.) and In_2O_3 (99.99%, supplied by Sigma-Aldrich Inc.). Two types of mixed oxide powders with the composition $(In_{1-x}Tl_x)_2O_3$ with Tl doping levels of x = 0.01 and x = 0.06 were prepared by grinding stoichiometric amounts of the oxide powders initially under acetone in an agate mortar for 30 minutes until the mixture was homogeneous and carefully dried. The powder mixtures were pressed into pellets with a diameter of 1 cm and a thickness of approximately 1 mm at 5 tonnes, for 5 minutes, and placed in ceramic crucibles. The pellets were enclosed in a blanket of powder of the same composition to prevent the loss of volatile Tl_2O_3 during calcination. The samples were sintered in a tube furnace at 600 °C for 24 h, and cooled at a rate of 5 °C per minute. Due to the toxicity of thallium and its compounds, all work was conducted in fume hoods and additional precautions, including the wearing of face masks and special gloves, were taken.

All ceramic samples were analysed in pelletised form using the Phillips PANanalytical X'Pert PRO diffractometer. XPS was undertaken on the Kratos Axis Ultra-DLD at Cardiff University. For ion bombardment experiments an area of 5 x 5 mm was etched with an Ar ion gun operating at 4 keV and 15 mA, and an argon pressure of 1×10^{-6} mbar, for 20 minutes at a time.

6.3 Results and Discussion

6.3.1 Calculations

Density functional theory (DFT) calculations were performed by Dr. D. O. Scanlon using the Vienna ab-initio simulation package (VASP).[3] The full Heyd-Scuseria-Ernzerhof hybrid functional (HSE06) as proposed by Krukau *et al.*[4] was used, which has previously been shown to provide an excellent description of the electronic structure of Tl_2O_3[1] and In_2O_3[5].

Figure 6.1 shows the calculated band structures for In_2O_3, Tl_2O_3, $In_{1.875}Tl_{0.125}O_3$, and $In_{1.75}Tl_{0.25}O_3$. The two Tl-doped samples correspond to doping levels of approximately 6 and 12 %. A reduction in band gap is apparent upon doping with a limiting band gap of only 0.33 eV for Tl_2O_3 itself.

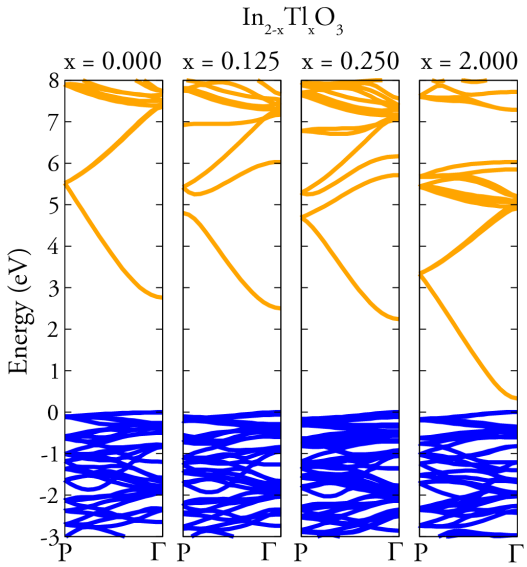
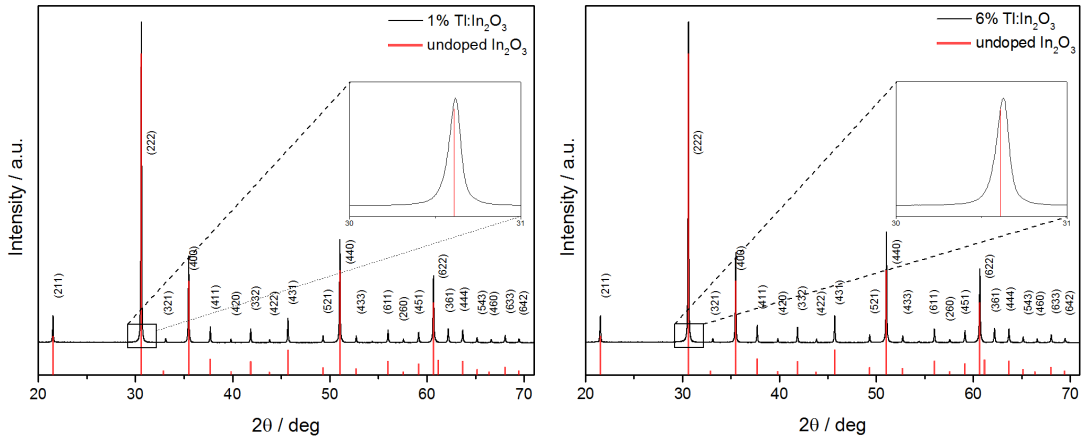


Figure 6.1: Band structure of $In_{2-x}Tl_xO_3$ for x = 0.000, 0.125, 0.250, and 2.000. Blue and orange denote valence bands and conduction bands. The valence band maximum is set to 0 eV in each case.

6.3.2 Surface versus Bulk Incorporation of Thallium

XRD patterns were recorded for the two Tl-doped In_2O_3 samples, which showed only minimal shifts to higher diffraction angles. Incorporation of the larger Tl^{3+} cation into In^{3+} sites would be expected to lead to an increase in lattice parameter and a shift of diffraction peaks to lower angles. The failure to find a shift of this sort suggests that Tl is not being incorporated as a bulk dopant, but is confined to a highly enriched surface layer.



(a) (b)

Figure 6.2: XRD patterns for (a) 1% and (b) 6% Tl-doped In_2O_3 pellets and reference data for undoped In_2O_3.[6]

This was confirmed using high resolution XPS. Binding energies in all XPS spectra presented here were referenced to the Fermi energy associated with the occupation of conduction band states for the 1% Tl sample and In_2O_3. As no intensity at the Fermi level could be observed in the 6% Tl sample, it was referenced assuming the C 1*s* core line to be 285.0 eV. This procedure placed the Fermi level at the correct position for the other two samples. Figure 6.3 shows survey scans for the 1 and 6% Tl-doped samples. Strong thallium core lines can be observed in both spectra confirming that a high Tl concentration is present at the sample surface compared to the nominal bulk concentration.

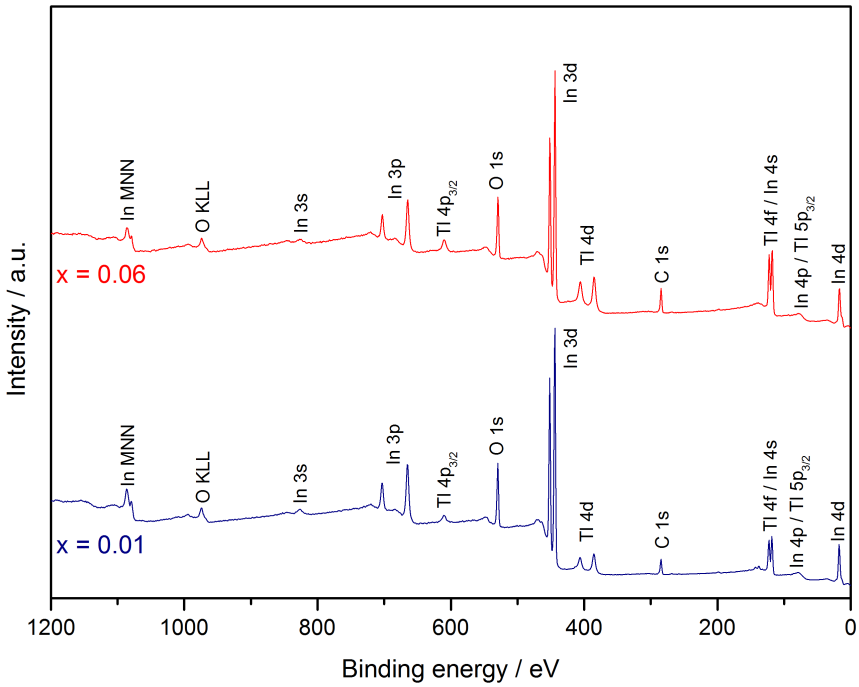


Figure 6.3: Widescan XPS spectra for $(In_{1-x}Tl_x)_2O_3$ with x = 0.01 and x = 0.06.

Figure 6.4 shows the observed Tl 4*f* core lines for both Tl-doped samples. From pseudo-Voigt fits to the XPS data the surface concentration of Tl could be calculated to be 0.19 for x = 0.01 and 0.36 for x = 0.06.

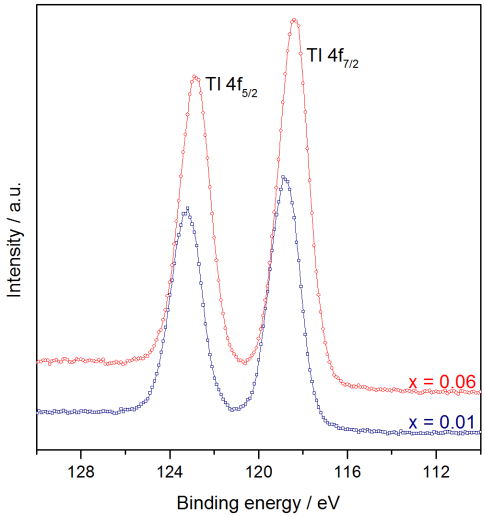


Figure 6.4: XPS spectra of the Tl 4*f* core level for $(In_{1-x}Tl_x)_2O_3$ with x = 0.01 and x = 0.06.

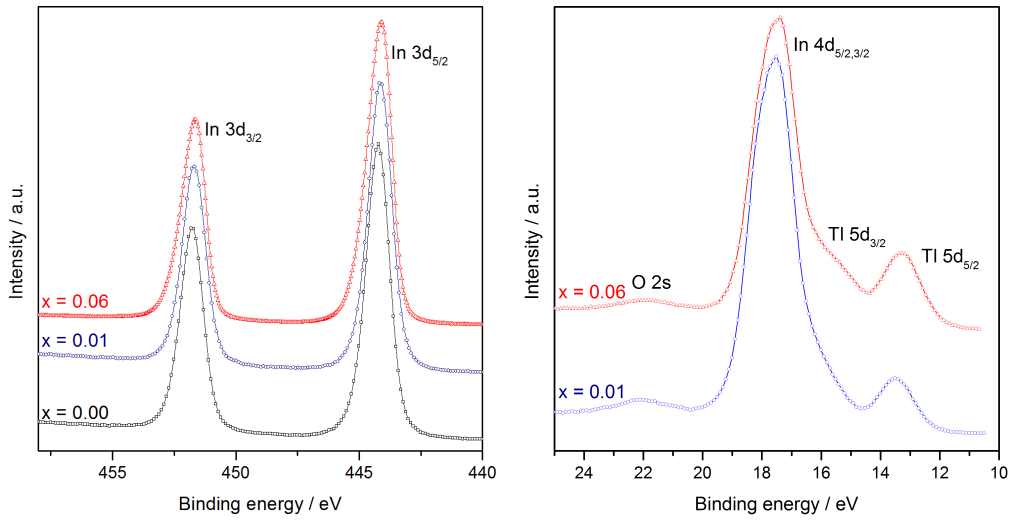


Figure 6.5: In $3d$ and $4d$ core levels for $(In_{1-x}Tl_x)_2O_3$ with x = 0.01 and x = 0.06.

Figure 6.5 shows the In $3d$ and $4d$ core levels for the Tl-doped samples compared to undoped In_2O_3. All core lines shown here exhibit a shift to lower binding energies with increased Tl doping level. Table 6.1 summarises the binding energies and shifts, as well as the spin-orbit splitting (SOS) of the core levels upon Tl doping.

Table 6.1: Binding energies BE of the Tl $4f$, In $3d$, and In $4d$ core levels upon Tl-doping. The column on the very right shows shifts in BE between the two doping levels. Spin-orbit splitting SOS is also included.

Core level	In_2O_3	$(In_{0.99}Tl_{0.01})_2O_3$	$(In_{0.94}Tl_{0.06})_2O_3$	
BE In $3d_{5/2}$	444.19	444.14	444.11	$\Delta BE = 0.03$ eV
BE In $3d_{3/2}$	451.73	451.7	451.67	
BE In $4d$		17.63	17.52	$\Delta BE = 0.11$ eV
BE Tl $4f_{7/2}$	-	118.82	118.43	$\Delta BE = 0.39$ eV
BE Tl $4f_{5/2}$	-	123.23	122.84	
SOS In $3d$	7.54	7.56	7.56	
SOS Tl $4f$	-	4.41	4.41	

6.3.3 Valence Band X-ray Photoemission Spectroscopy

Valence band spectra for undoped In_2O_3 and 1% and 6% Tl-doped samples are shown in figure 6.6. With increasing Tl doping level, the valence band edge shifts to lower binding energy. As the binding energies are referenced relative to the Fermi edge, which lies close to the conduction band minimum, this points towards a narrowing of the band gap. However, the intensity from conduction band states close to the Fermi edge decreases with Tl doping. It decreases so far that for the 6% Tl-doped sample the Fermi edge could no longer be observed with any confidence. As mentioned before, this led to all spectra for this sample to be aligned using the C 1*s* core level.

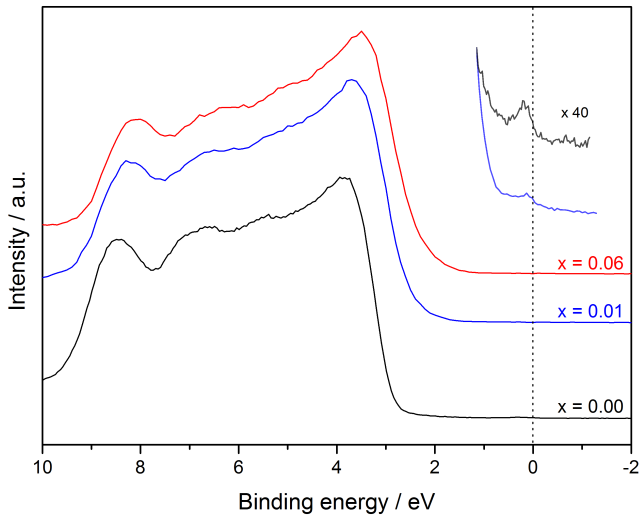


Figure 6.6: Valence band spectra for undoped In_2O_3 and 1% and 6% Tl-doped samples.

The decrease in the intensity around the Fermi edge, combined with the pronounced Tl surface segregation observed, suggests that part of the thallium located at the sample surface may be present as Tl^+. Lone pair cations like this are well known to segregate to surface sites.[7–9] Tl^+ would act like a two electron acceptor, which would lead to a partial compensation of the charge carriers arising from oxygen vacancies and native donor defects. Bi-doped PbO_2 exhibits a similar compensation, as Bi acts as an acceptor rather than a donor. In the formally related

system Sb-doped SnO_2 Sb acts as a donor as expected from simple electron counting considerations.[9,10] The Tl^+ idea is supported by the observation that the photoemission intensity in the band gap region immediately above the extrapolated valence band edge is stronger in the Tl-doped samples compared to undoped In_2O_3. Antibonding lone pair states are expected in this region. Figure 6.7 shows the linear extrapolation of the lower binding energy side of the valence band with the shaded area being attributed to the existence of antibonding lone pair states.

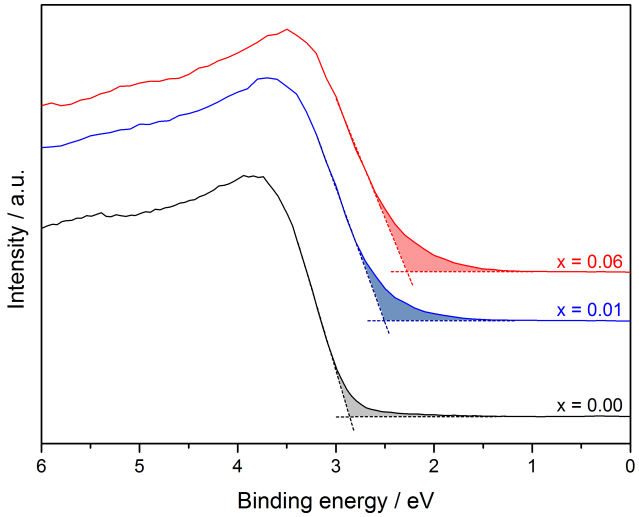


Figure 6.7: Expanded valence band spectra for undoped In_2O_3 and 1% and 6% Tl-doped samples showing the linear extrapolations to derive band gaps.

Table 6.2 shows the apparent band gaps derived from the linear fits to experimental data and from theoretical calculations. The calculated values for undoped In_2O_3 are consistent with the experimental results presented here. All the caveats discussed in relation to Ga-doped In_2O_3 apply to the experimentally values presented here and analysis of the data is further complicated by the fact that the intensity of the conduction band feature decreases with thallium doping.

Table 6.2: Band gaps for In_2O_3 and 1%, 6%, and 12% Tl-doped In_2O_3 derived from XPS data $E_g(exp)$ and theoretical calculations $E_g(calc)$. Both the nominal bulk concentration $c_{Tl}(nom)$ and the experimentally derived surface concentration $c_{Tl}(surf)$ are given.

$c_{Tl}(nom)$ / %	$c_{Tl}(surf)$ / %	$E_g(exp)$ / eV	$E_g(calc)$ / eV
0%	0%	2.78	2.75
1%	19%	2.41	-
6%	36%	2.27	2.51
12%	-	-	2.23

Both experimental and calculated data show a significant decrease in the band gap of In_2O_3 upon Tl doping. Due to the highly Tl-enriched surface a direct comparison for specific doping levels is complicated. The nominally 6% Tl-doped sample, with a surface concentration of 36% Tl, shows a band gap close to the calculated band gap for a 12% doped sample. It can be concluded that both calculated and experimental data show a significant decrease in the band gap compared to undoped In_2O_3.

6.3.4 Influence of Ion Bombardment on Valence and Core Levels XPS of Tl-doped In_2O_3

Figure 6.8 shows the valence band of 6% Tl-doped In_2O_3, along with spectra obtained after three consecutive 15 minute sputtering cycles as described in the experimental section of this chapter. The valence band shows the features typical of In_2O_3, which are described in section 5.4.3.

After ion bombardment an additional feature appears above the top of the O $2p$ valence band, similar to that observed in Ga-doped In_2O_3 previously. A gap state structure, labelled GS in the figure, is increasing in intensity upon ion bombardment. In analogy to the conclusions drawn for the Ga-In-O system, the gap state structure is attributed to the reduction of thallium under ion bombardment to give

reduced Tl^+.

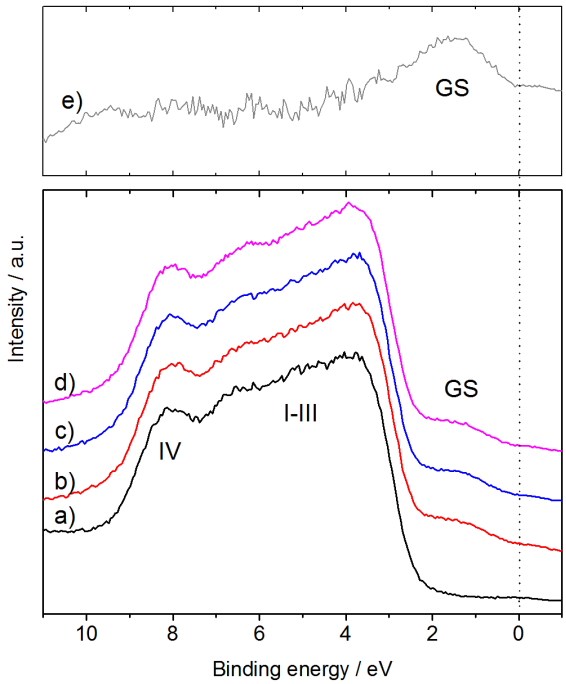


Figure 6.8: Sputtering results for 6% Tl-doped In_2O_3. (a) Valence band of as-presented Tl-doped In_2O_3, (b) valence band spectrum after ion bombardment for 15 minutes, (b) after 30 minutes, and (d) after 45 minutes. (e) presents the difference between (d) and (a) to illustrate the growth of a gap-state (GS) structure above the valence band edge as a consequence of ion bombardment.

In addition to changes in the valence band, the results of the ion bombardment were used to further investigate the segregation of thallium. The overall area of the Tl $4f$ core level decreases significantly upon ion bombardment. Figure 6.9 shows the Tl $4f$ core level for the sample before and after 2700 s sputtering. It should be noted that the Tl $4f_{5/2}$ core line overlaps with the In $4s$ core level. Therefore, only the Tl $4f_{7/2}$ core line was used for quantification of the decrease in thallium intensity.

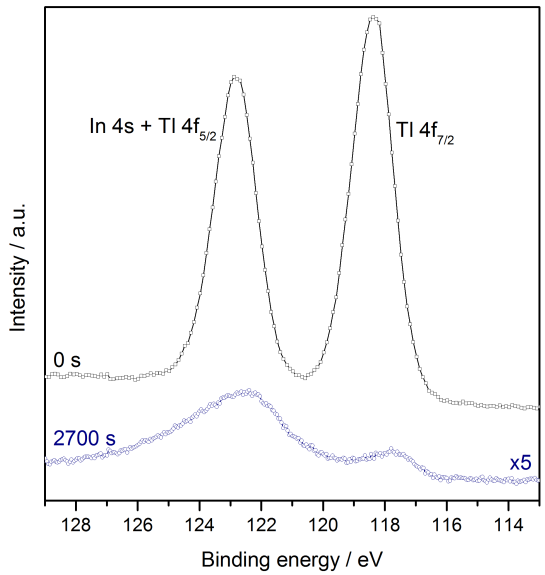


Figure 6.9: XPS core level spectra of Tl $4f$ and In $4s$ of the 6% Tl-doped In_2O_3 sample before and after 2700 s ion bombardment. The spectrum after 2700 s bombardment is dominated by the In $4s$ signal.

An immediate decrease in Tl intensity is observed with the surface Tl concentration dropping from 36% to 2.89% after 900 s. Upon further sputtering only a small further decrease to 2.73% after 1800 s and 2.65% after 2700 s, is observed. This further provides evidence for the pronounced surface segregation of Tl, with a remaining bulk concentration of approximately 2.7%.

6.3.5 Concluding Remarks

High resolution XPS was employed successfully to confirm calculations for the $(In_{1-x}Tl_x)_2O_3$ system. Ceramic samples with thallium doping levels of nominally 1 and 6% were investigated. The samples showed pronounced surface segregation leading to surface concentrations of 19% and 36% respectively. Upon doping a decrease in the band gap of In_2O_3 was observed, which was predicted by calculation beforehand.

6.4 References

[1] A. B. Kehoe, D. O. Scanlon, and G. W. Watson, Physical Review B **83**, 233202 (2011).

[2] A. L. J. Petera and T. Viraraghavan, Environment International **31**, 493 (2005).

[3] G. Kresse and J. Hafner, Physical Review B **49**, 14251 (1994).

[4] A. V. Krukau, O. A. Vydrov, A. F. Izmaylov, and G. E. Scuseria, Journal of Chemical Physics **125**, 224106 (2006).

[5] P. Agoston, K. Albe, R. M. Nieminen, and M. J. Puska, Physical Review Letters **103**, 245501 (2009).

[6] M. Marezio, Acta Crystallographica **20**, 723 (1966).

[7] P. A. Cox, R. Egdell, C. Harding, W. R. Patterson, and P. J. Tavener, Surface Science **123**, 179 (1982).

[8] A. Gulino, A. E. Taverner, S. Warren, P. Harris, and R. G. Egdell, Surface Science **315**, 351 (1994).

[9] S. Rothenberg, D. J. Payne, A. Bourlange, and R. G. Egdell, Journal of Applied Physics **102**, 113717 (2007).

[10] P. A. Cox *et al.*, Solid State Communications **44**, 837 (1982).

7 A Sol-Gel Approach to Growth of High Quality TiO_2 Thin Films

7.1 Introduction

Of the three polymorphs of TiO_2, anatase is the best photocatalyst.[1–3] This is mainly due to the indirect nature of the band gap in anatase and an electron mobility of $\approx$10 cm^2/Vs that is ten times greater than the value of $\approx$1 cm^2/Vs found for rutile.[4] These effects ultimately lead to a better separation of electron-hole pairs. Because rutile is the most stable phase thermodynamically, the synthesis of anatase is not possible via high temperature solid state routes, but anatase has been synthesised using precipitation from solution followed by calcination at very low temperatures. However, it will transform irreversibly into rutile upon heating above 600 °C or lower, depending on purity and morphology (see chapter 1).

Epitaxial thin films of anatase have been grown by a variety of techniques including oxygen plasma assisted molecular beam epitaxy (OPA-MBE), laser molecular beam epitaxy (L-MBE), pulsed laser deposition (PLD), reactive sputtering, atomic layer deposition (ALD), solution based synthesis, and radio frequency magnetron

sputtering (RFMS). Table 7.1 gives an overview over the different thin films grown by these techniques as reported in the literature.

Table 7.1: Summary of techniques used to grow doped and undoped epitaxial thin films of anatase TiO_2 as reported in the literature.

dopant	method	substrate
-	OPA-MBE	$LaAlO_3$ (001) [5–7]
-	OPA-MBE	$SrTiO_3$ (001) [5–7]
Co	OPA-MBE	$SrTiO_3$ (001) [7,8]
Co	OPA-MBE	$LaAlO_3$ (001) [7]
Mn	OPA-MBE	Nb:$SrTiO_3$ (001) [9]
-	L-MBE	$LaAlO_3$ (001) [10]
-	L-MBE	$SrTiO_3$ (001) [10]
Co	L-MBE	$LaAlO_3$ (001), $SrTiO_3$ (001) [11]
-	PLD	$LaAlO_3$ (001) [12]
-	PLD	$LaAlO_3$ (001), $SrTiO_3$ (001) [13]
Co	PLD	$LaAlO_3$ (001), $SrTiO_3$ (001) [14]
Nb	PLD	$LaAlO_3$ (100) [15]
-	reactive sputtering	$LaAlO_3$ (001) [16]
-	ALD	MgO (001) [17]
-	sol-gel	$LaAlO_3$ (001) [18]
-	RFMS	$SrTiO_3$ (001) [19]

Epitaxial thin films of anatase grown on $SrTiO_3$ (STO) or $LaAlO_3$ (LAO) can be stabilised to much higher temperatures of up to 1000 °C making them accessible to in depth characterisation. The reason for the stabilisation of anatase lies in the difference in mismatch between the anatase thin film and the single crystal substrate it is grown on, as compared to the corresponding mismatch for rutile.

Table 7.2: Lattice parameters a, b, and c of rutile R,[20] anatase A,[21] $SrTiO_3$ Sr,[22] and $LaAlO_3$ La,[23] and mismatches between thin film and substrate materials Δ_{R-STO}, Δ_{A-STO}, Δ_{R-LAO}, and Δ_{A-LAO}.

	Rutile	Anatase	$SrTiO_3$	$LaAlO_3$
a / Å	4.594	3.784	3.901	3.791
b / Å	4.594	3.784	3.901	3.791
c / Å	2.959	9.515	3.901	3.791
	Δ_{R-STO}	Δ_{A-STO}	Δ_{R-LAO}	Δ_{A-LAO}
	17.76%	2.99%	21.17%	0.19%

In the case of a $SrTiO_3$ substrate the mismatch between the lattice parameters is 17.8% for rutile and only 3% for anatase, which favours growth of anatase over rutile (see table 7.2). However, the 3% mismatch is expected, nonetheless, to lead to strain in the film.

The Egdell group has recently developed a simple and inexpensive sol-gel method to grow anatase TiO_2 thin films. Initially, samples made using this method showed stress induced de-wetting and the formation of square islands, rather than continuous thin films. Figure 7.1 shows AFM images of samples prepared by Dr. F. Oropeza at different annealing temperatures.[24]

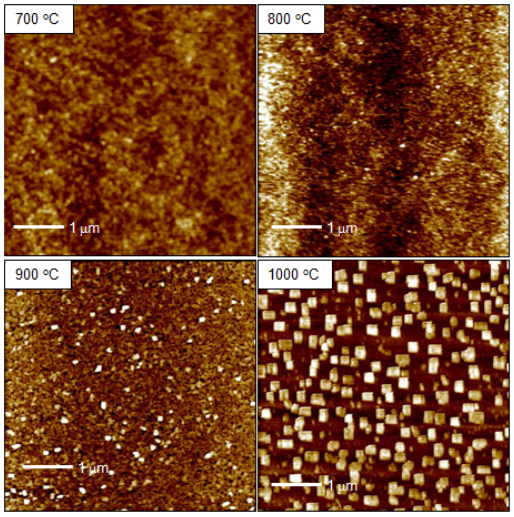


Figure 7.1: AFM images of TiO_2 samples grown on $SrTiO_3$ at four different annealing temperatures. All samples show de-wetting and ultimately the formation of square islands. Samples were prepared by Dr. F. Oropeza (DPhil Thesis, Oxford, 2011).

In the work presented here the sol-gel dip-coating method was refined starting from a Design of Experiments (DoE)[25] approach and it is shown that epitaxial anatase thin films grown are stable up to temperatures of 1000 °C. The high quality films allowed for extensive characterisation using XRD, Raman, UV-Vis, AFM, ellipsometry, and synchrotron based reciprocal space mapping. The influence of temperature on the thin films was investigated by synchrotron based diffraction. In addition, we prepared epitaxial rutile films and Sn-doped anatase films and investigated crystallographic changes.

7.2 Experimental

Thin films of TiO_2 were grown via sol-gel dip-coating using a Ti isopropoxide precursor in 2-propanol, acidified with nitric acid. For the initial DoE setup quartz substrates were used. A Plackett-Burman design[26] was chosen, which is ideal for screening a larger number of factors influencing the sample quality. It is a highly efficient setup reducing the number of necessary initial runs. All influencing factors

are set to have a minimum and maximum value with one additional run located at the centre points of all factors. The precursor concentration $c_{\text{precursor}}$, volume of nitric acid V_{acid}, number of dips n_{dips}, and annealing temperature T_{anneal} were identified as the main factors to be included in the DoE. Table 7.3 summarises the 13 runs included in the DoE and the settings for the different factors. The order of runs was randomised.

Table 7.3: Plackett-Burman design for sol-gel dip-coating of TiO_2 thin films on quartz substrates.

run	$c_{\text{precursor}}$ $[mol/L]$	V_{acid} $[\mu L]$	n_{dips}	T_{anneal} $[°C]$
1	0.45	90	12	1000
2	0.35	120	10	800
3	0.25	90	12	1000
4	0.45	90	12	600
5	0.25	90	8	600
6	0.25	90	8	1000
7	0.45	90	8	600
8	0.45	150	8	1000
9	0.25	150	12	1000
10	0.45	150	8	1000
11	0.45	150	12	600
12	0.25	150	8	600
13	0.25	150	12	600

From this design and the preliminary characterisation of the resulting films, the following final setup was chosen. 30 mL of the precursor solutions were prepared under an N_2 atmosphere in a glove box to prevent premature hydrolysis of the precursor. A precursor solution of Ti(IV)isopropoxide (99.999% trace metals basis, supplied by Sigma-Aldrich Inc.) in 2-propanol with a propoxide concentration of 0.25 mol/L was prepared, and 150 μL HNO_3 were added to promote gelling. After the precursor solution was prepared, it was removed from the glove box and transferred into a wide necked round bottom flask for the dip-coating.

Quartz substrates for the preliminary DoE setup as well as single crystal substrates

of $SrTiO_3$ (001) and R-plane Al_2O_3 ($1\bar{1}02$) for the preparation of high quality epitaxial thin films were cleaned with 2-propanol and dried under N_2 flow.

Substrates were dipped into the precursor solution and held stationary for one minute, after which they were withdrawn from the solution at a removal speed of 0.35 cm/min. Thereafter, they were hydrolysed in a stream of wet nitrogen gas for five minutes. This process was repeated until the desired number of dips was reached. The number of dips was varied between one and eight in order to prepare samples with different thicknesses.

Dip-coated samples were placed in recrystallised alumina boats and annealed at 600 - 1000 °C in a muffle oven for five hours. The cooling rate for all experiments was set at 5 °C per minute.

The preparation of Sn-doped TiO_2 samples only differed in that a mixed alkoxide solution of Ti(IV)isopropoxide (99.999% trace metals basis, supplied by Sigma-Aldrich Inc.) and Sn(IV)isopropoxide (10 % (w/v) in isopropanol/toluene, 99.99% trace metals basis, supplied by Sigma-Aldrich Inc.) in 2-propanol with an overall concentration of 0.25 mol/L was prepared for the Sn:TiO_2 sample. The nominal molar ratio between the Sn- and Ti-precursor was 0.1 to 0.9. The resulting Sn-doping level is 1%.

7.3 Results and Discussion

7.3.1 Exploratory Setup

Thirteen samples of TiO_2 prepared on quartz, prepared as described in table 7.3, were investigated to identify the ideal experimental conditions for the growth of TiO_2 thin films. Quartz was an ideal starting substrate as it is comparatively cheap and easy to handle. However, due to the broad and strong background from the quartz substrate, X-ray diffraction could not be employed to assess the quality of the films. Therefore, Raman spectroscopy and AFM were chosen to investigate the samples.

The tetragonal structure of anatase TiO_2 belongs to the space group $I4_1/amd$. The 15 vibrational modes span the following irreducible representation Γ in the D_{4h} factor group:

$$\Gamma = 1A_{1g} + 1A_{2u} + 2B_{1g} + 1B_{2u} + 3E_g + 2E_u \ , \tag{7.1}$$

where the six *gerade g* modes are Raman active. Table 7.4 summarises the Raman peaks observed in the here presented work and compares them to values from the literature.

Table 7.4: Observed Raman modes in cm^{-1} for TiO_2 on quartz and comparison with experimental data from Frank *et al.*[27]

Mode (sym)	this work	Frank *et al.*
E_g	144±3	144
E_g	196±3	196
B_{1g}	395±3	394
B_{1g}, A_{1g}	-	516
E_g	640±3	638

The B_{1g}, A_{1g} peaks could not be observed as they are masked by a quartz signal. The E_g reflection at 196 cm^{-1} is very weak and could only be observed in the thickest samples. Figure 7.2 shows the four observed modes in such a sample compared to a reference spectrum for a pristine quartz substrate.

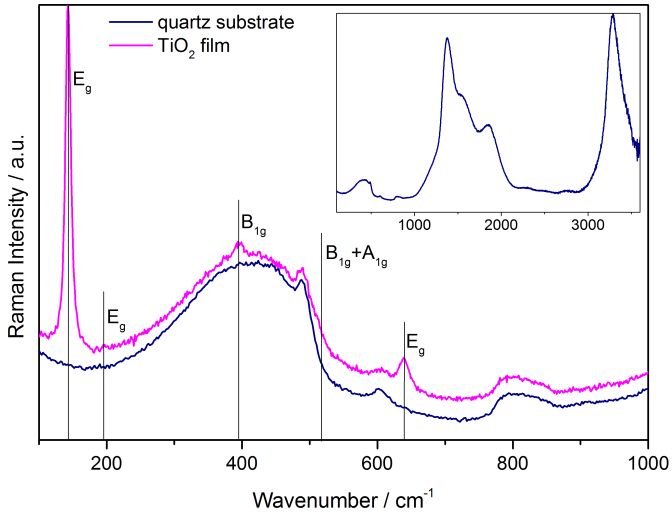


Figure 7.2: Raman spectra for a TiO_2 film on quartz and a pristine quartz substrate with the position of the Raman active modes for TiO_2 anatase indicated. The inset shows a wide spectrum of the pristine quartz substrate.

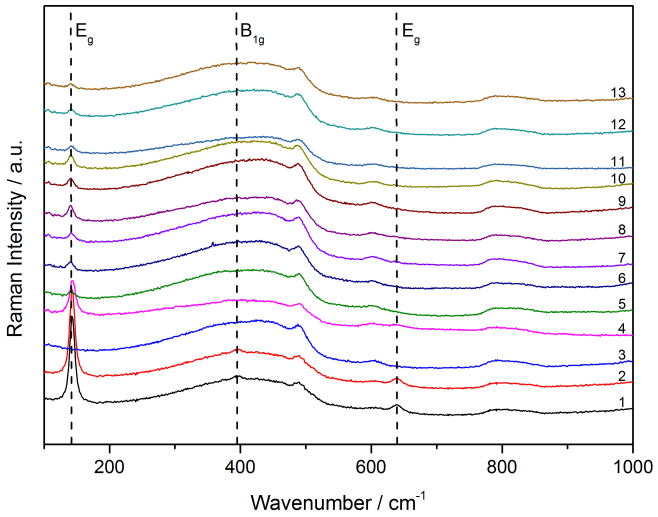
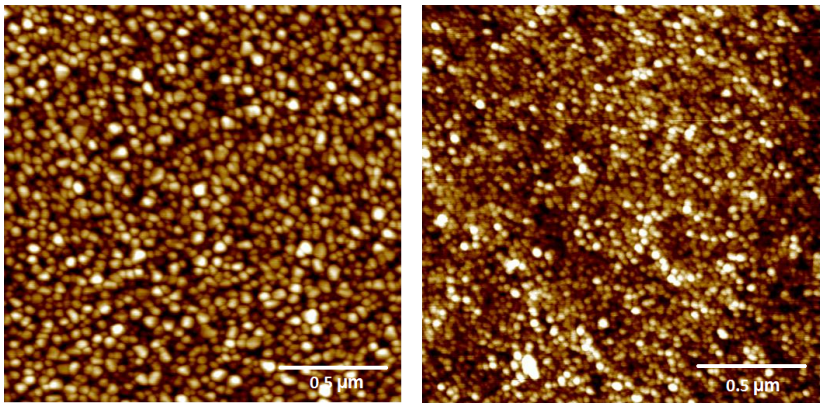


Figure 7.3: Raman spectra for all 13 TiO_2 films on quartz substrates from the DoE setup. The most intense modes observed are indicated.

The Raman E_g mode at 144 cm^{-1} shows the highest intensity and could be observed in all the samples prepared (see figure 7.3), therefore confirming the presence

of anatase TiO_2 on the entire series of samples deposited on quartz.

After confirming the growth of TiO_2 on all quartz substrates, the samples were characterised using atomic force microscopy (AFM). All samples showed a continuous layer of TiO_2 with different sized spherical crystallites. Figure 7.4 shows two exemplary images which are typical of the surface morphology for all samples.



(a) (b)

Figure 7.4: AFM images of two samples from the DoE setup, (a) sample number 6, and (b) sample number 12.

From the combination of Raman and AFM results for all 13 samples an optimised experimental setup was chosen. The precursor and acid concentrations were fixed for all further work to a concentration of 0.25 mol/L for the precursor and an acid volume of 150 μL. Due to the strong influence of the temperature and the number of dips on the quality and characteristics of the films, these two parameters were investigated further using single crystal substrates.

In addition to the general optimisation of the experimental setup, a change in the substrate cleaning procedure used for single crystals led to major improvements of the film quality. Previously, substrates were cleaned using acetone, water, and 2-propanol in an ultrasonic bath. The substrates for the samples prepared in the

current work were only cleaned using 2-propanol and without the aid of ultrasonic baths, as it is believed that the acetone introduces surface nucleation sites and the ultrasonic cleaning induces microscale cracking, especially at the edges of the substrates, leading to de-wetting and non-uniform film growth.

7.3.2 High Quality Thin Films of TiO_2 on $SrTiO_3$ (001)

To investigate the influence of the annealing temperature in more detail, two- and four-dip samples were annealed at 700, 800, 900, and 1000 °C. In the first instance they were investigated using X-ray diffraction. Figure 7.5 shows scans from 20 to 50 ° of a two and a four dip sample annealed at 1000 °C.

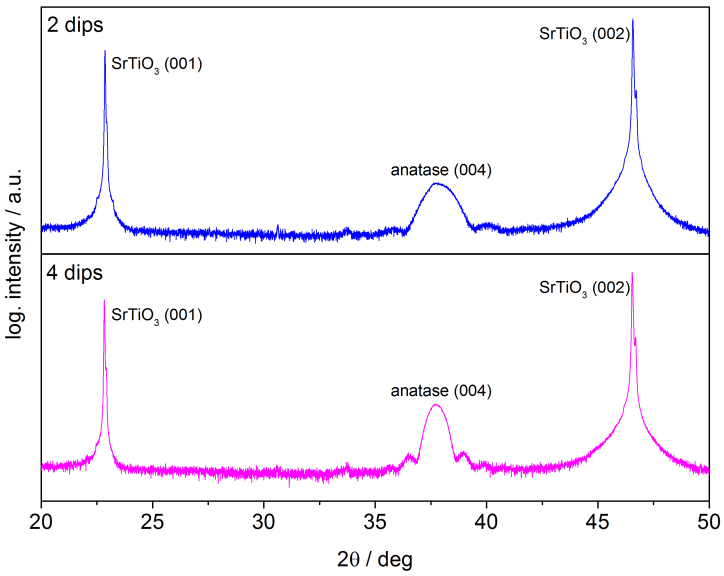
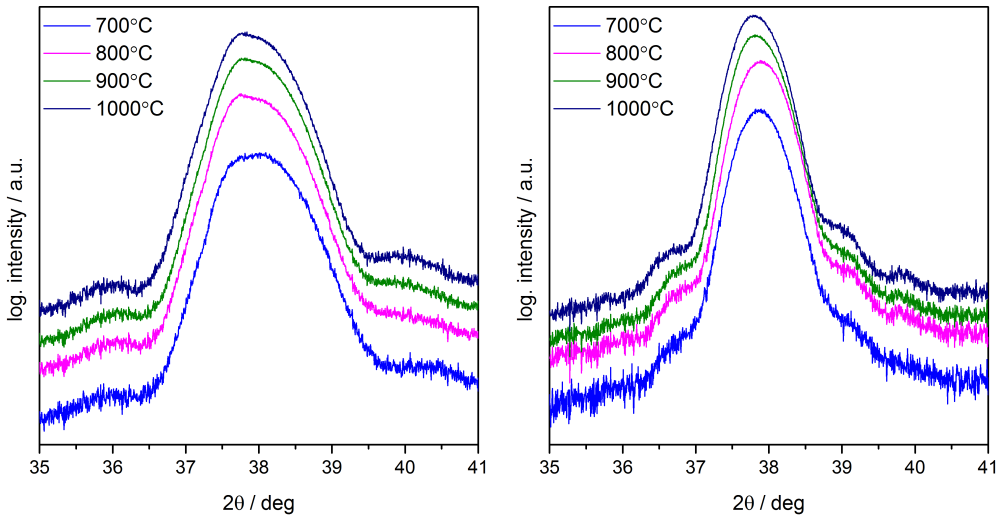


Figure 7.5: XRD scans of a two and a four dip sample annealed at 1000 °C.

The (004) anatase Bragg peak lies between the (001) and (002) reflections of the $SrTiO_3$ substrate. Figure 7.6 shows an expanded view of the anatase TiO_2 (004) reflection for all eight samples. All samples show broad specular Bragg peaks for anatase (004) with well-defined Pendellösung fringes on either side.



(a) 2 dips (b) 4 dips

Figure 7.6: Expanded view of the TiO_2 (004) reflection for two dip and four dip samples at annealing temperatures of 700 - 1000 °C.

To determine the *d*-spacing of the anatase thin films, the angle of the anatase (004) Bragg peak $2\theta_{An}$ was calibrated using the $SrTiO_3$ (100) and (200) reflections. The (100) and (200) reflections are expected to be at an angle of $2\theta_{STO(100)} = 22.7514°$ and $2\theta_{STO(200)} = 46.4674°$ respectively. The following equation was used to determine the corrected angle $2\theta_{An}$:

$$2\theta_{An} = 2\theta_{STO(100)} + \frac{(2\theta_{An}^{obs} - 2\theta_{STO(100)}^{obs}) \cdot \Delta 2\theta_{STO}}{\Delta 2\theta_{STO}^{obs}} , \tag{7.2}$$

where the index *obs* refers to the measured diffraction angle, and $\Delta 2\theta_{STO}$ is the difference between the angles of the (100) and (200) $SrTiO_3$ reflections.

Using the Bragg equation the d_{hkl}-spacing was calculated:

$$d_{hkl} = \frac{n\lambda}{2\sin\theta} , \tag{7.3}$$

where n is an integer, λ is the wavelength of the incident beam (1.54056 Å for Cu Kα_1), and θ is the angle of the incident beam. Table 7.5 gives the observed and

calculated angles, as well as the derived *d*-spacing values.

Table 7.5: Observed angles for the $SrTiO_3$ substrate and the anatase thin film, corrected diffraction angles of anatase, and the resulting *d*-spacing. All angles are given in degrees and the experimentally observed angles are subject to an uncertainty of ±0.004. 2d and 4d refer to two dip and four dip samples, respectively.

sample	$2\theta^{obs}_{STO(100)}$	$2\theta^{obs}_{STO(200)}$	$2\theta^{obs}_{An}$	$2\theta_{An}$	θ_{An}	d_{hkl} / Å
700 °C, 2d	22.833	46.567	37.964	37.971	18.934	2.373
700 °C, 4d	22.822	46.545	37.872	37.876	18.901	2.378
800 °C, 2d	22.853	46.539	37.739	37.933	18.925	2.375
800 °C, 4d	22.941	46.639	37.929	37.930	18.876	2.381
900 °C, 2d	22.956	46.664	37.895	37.973	18.887	2.380
900 °C, 4d	22.853	46.539	37.724	37.735	18.826	2.387
1000 °C, 2d	22.841	46.557	37.847	37.865	18.888	2.380
1000 °C, 4d	22.840	46.533	37.705	37.741	18.833	2.386

From the corrected angles the derived *d*-spacings for four dip samples are higher compared to those from two dip samples, and both show an increase in *d*-spacing with annealing temperature.

The Bragg reflections showed characteristic oscillations on either side of the Bragg peak, which is unexpected considering the comparatively low intensity of the film reflections in laboratory-based XRD. The oscillations were further investigated on samples grown at 1000 °C with a varying number of dips using laboratory- and synchrotron based XRD. The oscillations are extremely well defined in the synchrotron diffraction patterns.

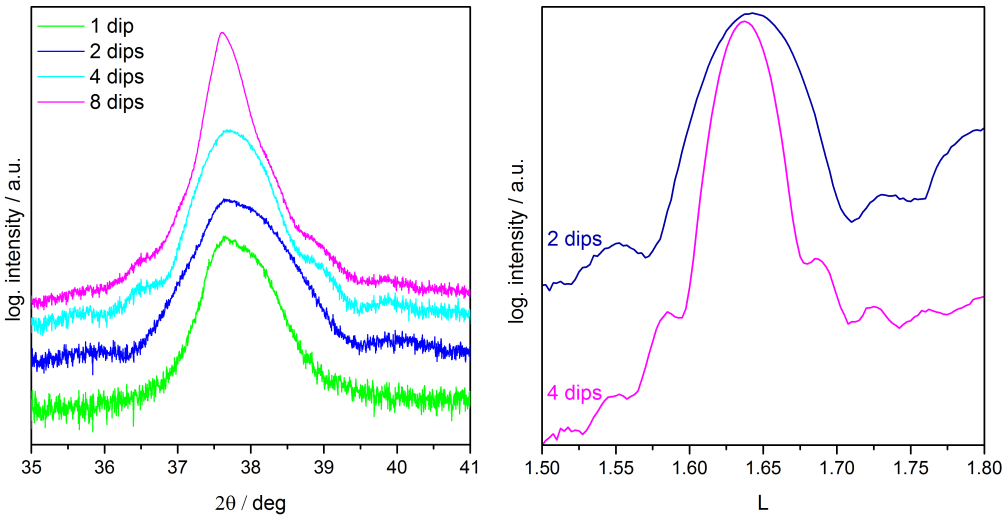


Figure 7.7: Expanded view of the TiO_2 (004) reflection of samples annealed at 1000 °C with varying numbers of dips from (a) laboratory based XRD, and (b) synchrotron based XRD. The horizontal scale in (b) is in reciprocal lattice units of the substrate.

The observed oscillations are known as Laue or Pendellösung fringes and arise from coherent scattering from a film of finite thickness.[28,29] The presence of the fringes is a good indication of the quality of the film as a long range structural coherence and uniform thickness is required to show these fringes. The spacing of the fringes is directly related to the thickness, with the fringes being closer together, the thicker the film. In one dimension the intensity oscillations as a function of wavevector transfer Q are given by:

$$I(Q) = \left[\frac{\sin((Na)/2 \times Q)}{sin((a/2) \times Q)}\right]^2 , \tag{7.4}$$

where a is the unit cell size normal to the surface and N is the number of cells. Na is therefore the film thickness t.

The Laue function has a maximum of intensity proportional to N^2 at the position given by the Bragg condition and a series of minima separated by a period $\Delta Q_p = 1/t$ from the Bragg peaks. The first intensity maxima in the fringes occur

at $\pm 3/2\Delta Q_p$. The splitting between the first two fringe maxima is $3\Delta Q_p$. This allows the evaluation of the film thickness. The film thickness of the two- and four-dip samples annealed at 1000 °C was calculated to be 6.31 nm and 11.24 nm respectively.

For the laboratory based data the intensities are measured as a function of angle rather than wavevector transfer, and the formula for the film thickness becomes:

$$t = \frac{\lambda}{2(\sin(\theta_{K-1} + \frac{\theta_{K+1}-\theta_{K-1}}{3}) - \sin\theta_{K-1})} , \tag{7.5}$$

where λ is the wavelength of the incoming X-rays, and θ_{K-1} and θ_{K+1} are the angles of the fringe maxima on either side of the Bragg reflection. The estimated film thicknesses are given in table 7.6.

Table 7.6: Estimation of the film thickness t from Laue fringes around the (004) anatase Bragg reflection. All angles are given in degrees. 2d and 4d refer to two dip and four dip samples, respectively.

sample	$2\theta_{K-1}$	$2\theta_{K+1}$	t / nm
800 °C, 2d	36.04±0.05	39.94±0.05	7.16±0.25
800 °C, 4d	36.78±0.05	39.15±0.05	11.80±0.25
700 °C, 2d	35.88±0.05	40.36±0.05	6.23±0.25
700 °C, 4d	36.66±0.05	39.15±0.05	11.23±0.25
900 °C, 2d	36.10±0.05	39.92±0.05	7.31±0.25
900 °C, 4d	36.69±0.05	38.92±0.05	12.53±0.25
1000 °C, 2d	35.82±0.05	40.06±0.05	6.58±0.25
1000 °C, 4d	36.49±0.05	38.98±0.05	11.22±0.25
1000 °C, 8d	36.99±0.05	38.35±0.05	20.56±0.25

The thicknesses derived from laboratory XRD data are consistent with results from synchrotron XRD given above and ellipsometry measurements (on samples on quartz substrates), where thicknesses of 4.57 nm (1 dip), 8.72 nm (2 dip), and 15.9 nm (4 dip) where found for samples annealed at 1000 °C.

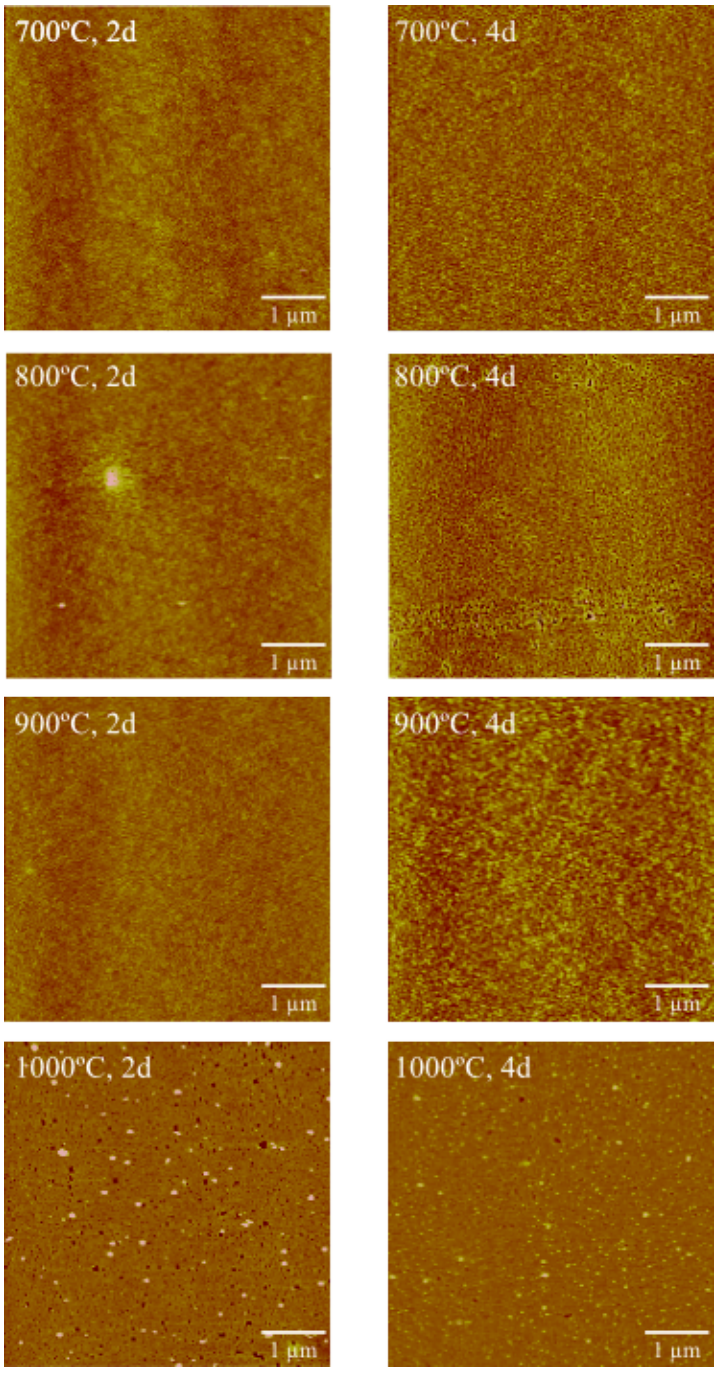


Figure 7.8: AFM images of TiO_2 thin films with varying dip numbers and annealing temperatures grown on $SrTiO_3$.

The XRD results suggest the presence of highly uniform thin films. The surface morphology was investigated using AFM. The samples increased in quality with increasing annealing temperature and film thickness. Figure 7.8 shows AFM images of two- and four-dip samples annealed at 700 - 1000 °C. The samples annealed at

1000 °C show the formation of pinholes.

7.3.3 Reciprocal Space Mapping of TiO_2 Thin Films

As well as recording line profiles using the central pixels on the Pilatus detector, the complete detector images were downloaded and stored as digital files of intensity versus pixel coordinates. The 2D detector surface gives a slightly curved surface in 3D reciprocal space, but software was developed by Dr. D. Wermeille to transform a series of detector images into a uniform mesh of intensity versus reciprocal space coordinates (h, k, l). These datasets were converted into .vtk format required for input into the Paraview 3D visualisation software suite using a short Fortran programme written by J. Paddison. The data could then be presented as a series of nested 3D isosurfaces of varying transparency sitting on a 2D contour map in an appropriate flat plane in reciprocal space. Maps around the specular (004) and the off-specular (013) reflection were produced in this way.

Figure 7.9 shows the 3D maps for a four dip sample annealed at 1000 °C. Maps around the (004) reflection show the previously mentioned Laue or Pendellösung fringes around the main Bragg peak along the l direction. In the l-scan map around the (004) reflection the scan did not reach far enough in h, leading to the contours not being entirely closed. In comparison the dimension of h is large enough in the h scan to show the contours fully closed. The l scan also shows a truncation rod coming from the substrate (002) reflection and spears through the thin film reflection.

The l-scan around the (013) reflection shows Laue or Pendellösung fringes as well. In addition the substrate (011) reflection can be seen on the right hand side, from which a truncation rod is extending in the l direction. This does not pass through

the centre of the epilayer reflection.

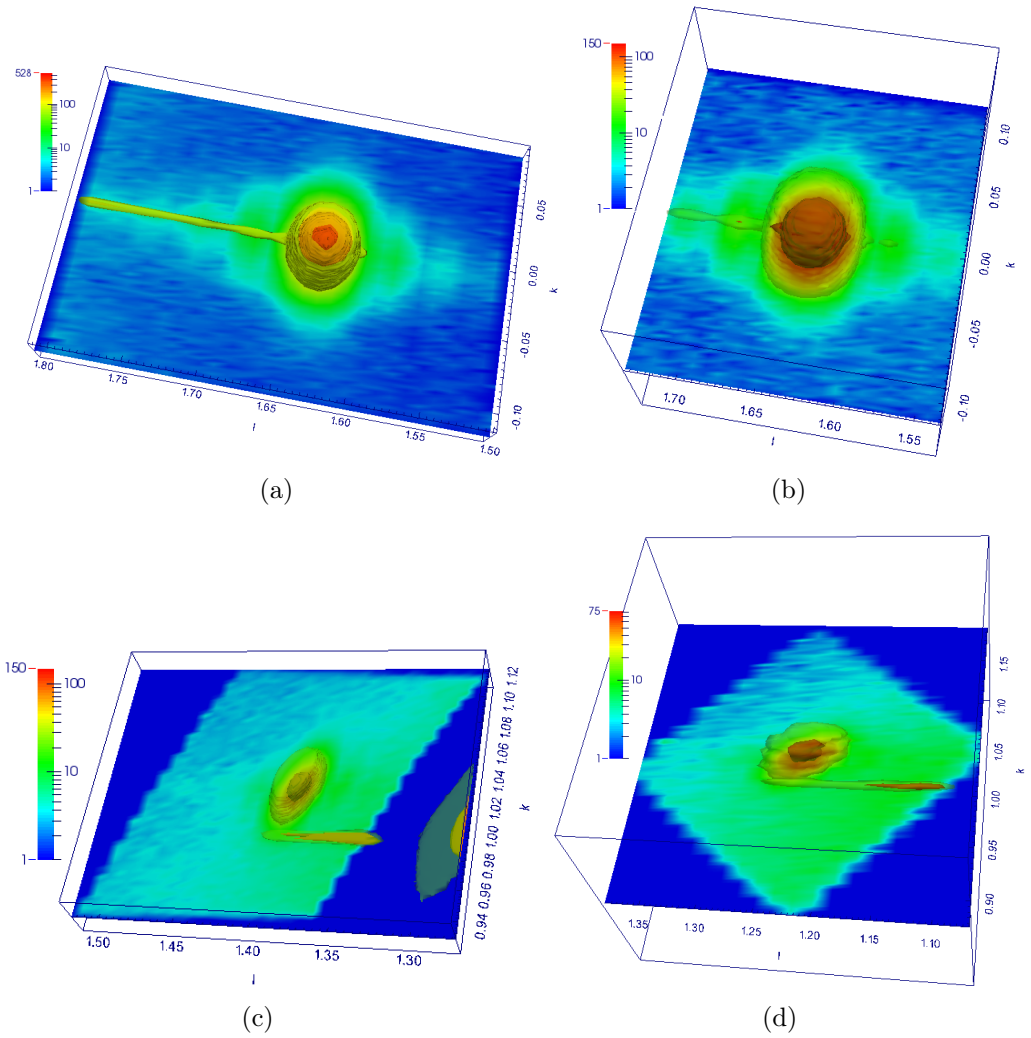


Figure 7.9: 3D reciprocal space maps of a four dip anatase TiO_2 thin film annealed at 1000 °C for (a) l-scan around the (004) reflection, (b) h-scan around the (004) reflection, (c) l-scan around the (013) off-specular reflection, and (d) h-scan around the (013) reflection. The scan range in h is (a) -0.023 to +0.018, (b) -0.074 to +0.062, (c) ±0.02, and (d) -0.127 to +0.11. h, k, and l values are specified in reciprocal lattice units of the substrate.

Figure 7.10 shows the 3D maps for a four dip sample annealed at 700 °C. The lower annealing temperature compared to the previous sample leads to a less uniform thin film (see AFM images in figure 7.8), which in turn results in less well pronounced Laue or Pendellösung fringes around the (004) reflection. As before, a truncation rod coming from the substrate reflection spears through the Bragg peak

along l. In this case, the h range for both samples shows completely closed contours of the Bragg peak.

Due to the low intensity of the l-scan and the lower annealing temperature the Laue or Pendellösung fringes of the (013) reflection are no longer well pronounced, although there is still some intensity present to either side of the main Bragg reflection. As before, the substrate (011) reflection can be seen on the right hand side, from which a truncation rod is extending in the l direction. The h-scan around the (013) reflection is very low in intensity, but still shows the main Bragg reflection and the truncation rod.

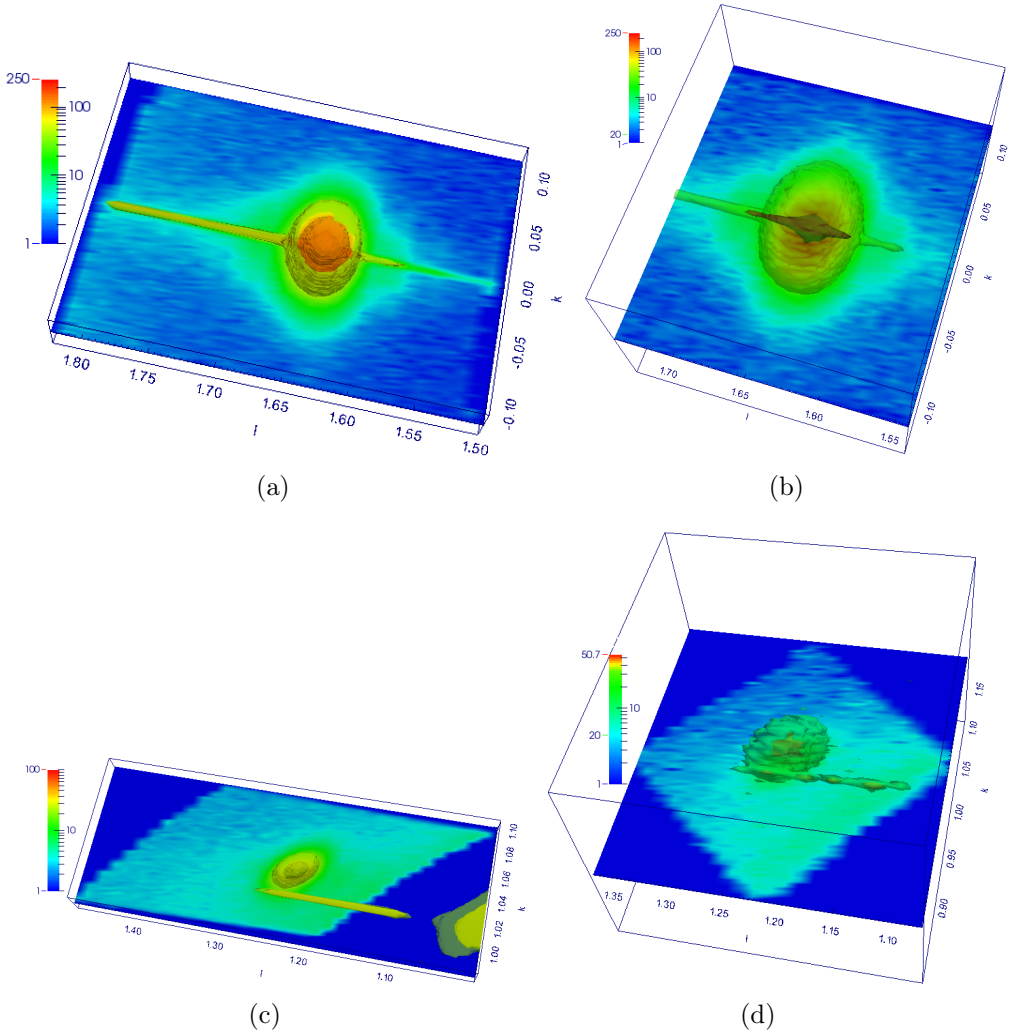


Figure 7.10: 3D reciprocal space maps of a four dip anatase TiO_2 thin film annealed at 700 °C for (a) l-scan around the (004) reflection, (b) h-scan around the (004) reflection, (c) l-scan around the (013) off-specular reflection, and (d) h-scan around the (013) reflection. The scan range in h is (a) -0.025 to +0.019, (b) -0.076 to +0.063, (c) -0.024 to +0.018, and (d) -0.129 to +0.108. h, k, and l values are specified in reciprocal lattice units of the substrate.

Figure 7.11 shows the 3D reciprocal space maps for a two dip sample annealed at 1000 °C. This very thin film shows a broadening of the (004) Bragg reflection. Laue or Pendellösung fringes are observed along the l direction around the main Bragg peak in both the l- and h-scan of the (004) reflection. As in the four dip sample, a truncation rod is observed, and in this case, fully closed contours are shown in both maps.

The off-specular (013) reflection is dominated by the truncation rod coming from the substrate (011) reflection, which can be seen on the right hand side in the l-scan. The truncation rod is also visible in the k scan.

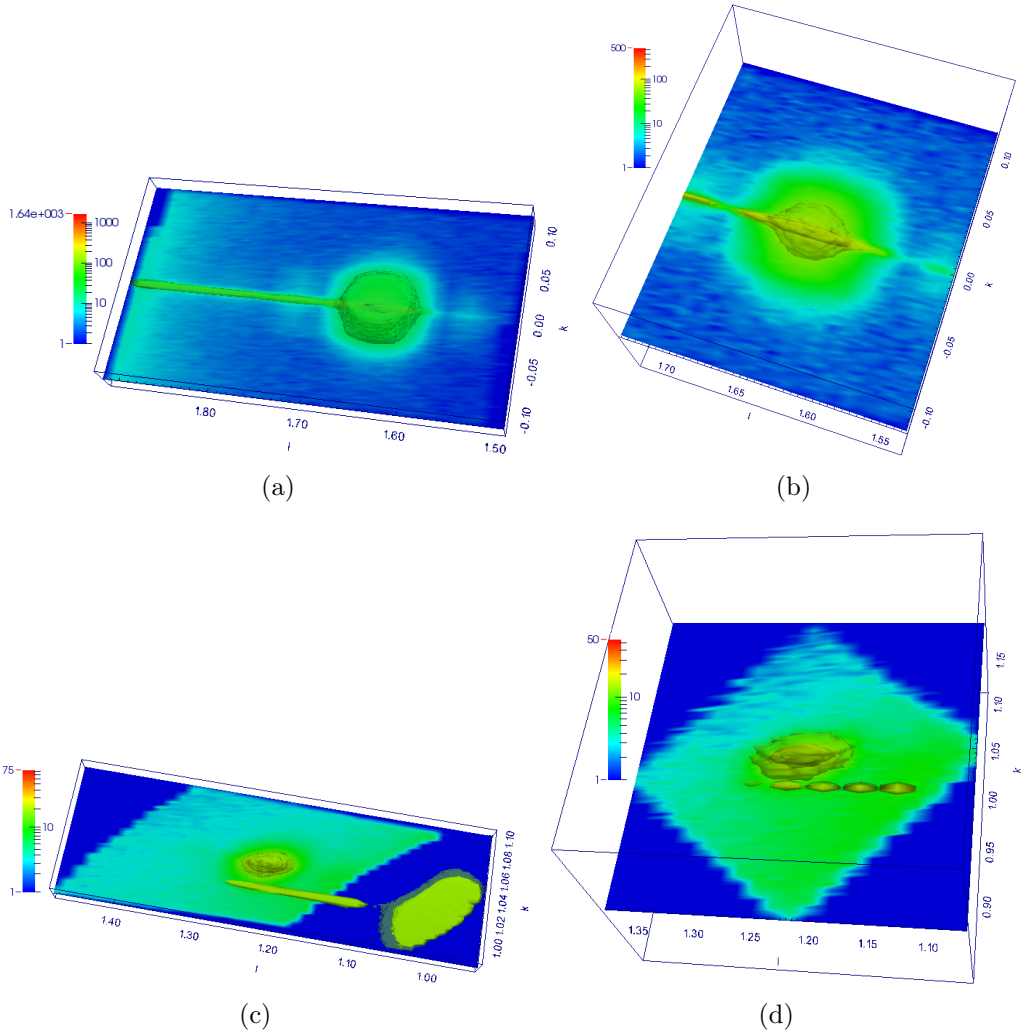


Figure 7.11: 3D reciprocal space maps of a two dip anatase TiO_2 thin film annealed at 1000 °C for (a) l-scan around the (004) reflection, (b) h-scan around the (004) reflection, (c) l-scan around the (013) off-specular reflection, and (d) h-scan around the (013) reflection. The scan range in h is (a) -0.026 to +0.02, (b) -0.076 to +0.063, (c) -0.024 to +0.018, and (d) -0.129 to +0.11. h, k, and l values are specified in reciprocal lattice units of the substrate.

7.3.4 Influence of Temperature on Thin Films Probed by Synchrotron Based Diffraction

The influence of temperature on thin films of TiO_2 on $SrTiO_3$ was studied using two- and four-dip samples, which where both annealed at 1000 °C. A heater was mounted on the diffractometer sample stage, which allowed heating of the samples to 600 °C. Complete 3D data sets were collected for (004) and (013) reflections of the epilayer, with what were essentially "line scans" extracted by integrating intensity in the 25 central pixels of the detector. For the (004) reflection h and l scans were performed and for the (013) reflection h, k, and l scans. In both cases h scans were only performed at room temperature. The l scan is essentially equivalent to a $\theta - 2\theta$ scan while the h scan is very close to an in-plane rocking curve.

Figure 7.12 shows line scans along l through the intensity maxima of reciprocal space maps around the (004) reflection for the two samples. The expected Bragg reflection shift was not observed along the l direction, with the two dip sample having a slightly higher l value than the four dip sample (1.644 compared to 1.638). The temperature dependence of the coefficients of thermal expansion of bulk anatase are given by the following two equations:

$$\alpha_{\parallel} = 7.380 \cdot 10^{-6} + 6.620 \cdot 10^{-9} T + 1.771 \cdot 10^{-11} T^2 \tag{7.6}$$

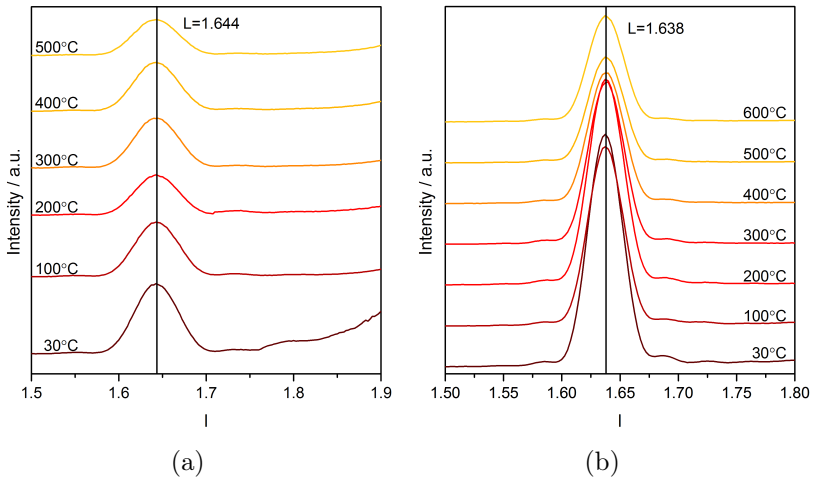
$$\alpha_{\perp} = 3.533 \cdot 10^{-6} + 5.610 \cdot 10^{-9} T + 4.315 \cdot 10^{-12} T^2 \ , \tag{7.7}$$

where $\alpha_{\parallel}$ and $\alpha_{\perp}$ are the thermal expansion coefficients parallel and perpendicular to the principal axis, and T is the temperature in °C.[30] Using the experimental values from Rao *et al.*[30], listed in table 7.7, values for 600 °C were interpolated. For the a and c lattice parameters, expansions of 0.326% and 0.675% respectively, were derived.

Table 7.7: Lattice parameters a and c of anatase TiO_2 at 28, 571, and 608 °C from Rao *et al.*[30] and at 600 °C interpolated from these data.

Temp. / °C	a / Å	c / Å
28	3.7845	9.5143
571	3.7962	9.5754
608	3.7970	9.5794
600	3.7968	9.5785

The expected increase of 0.675% in the c lattice parameter over the investigated temperature range should result in an observable shift, which is in contrast to the results in figure 7.12(a) and 7.12(b), where no shift could be observed.



(a) (b)

Figure 7.12: Line scans along l through the maximum intensity of the reciprocal space maps for the (004) reflection of (a) a two and (b) a four dip sample annealed at 1000 °C. l is in substrate reciprocal space units. l values are specified in reciprocal lattice units of the substrate.

Scans along h for the (004) and (013) reflections were collected at room temperature for both samples and are shown in figure 7.13. The peak sitting on top of the broad peak for h scans of the (004) reflection is due to the truncation rod from the substrate. This is apparent in the (004) h scan as the scan in this direction cuts through the rod, whereas in the l scan one is moving along the direction of the rod.

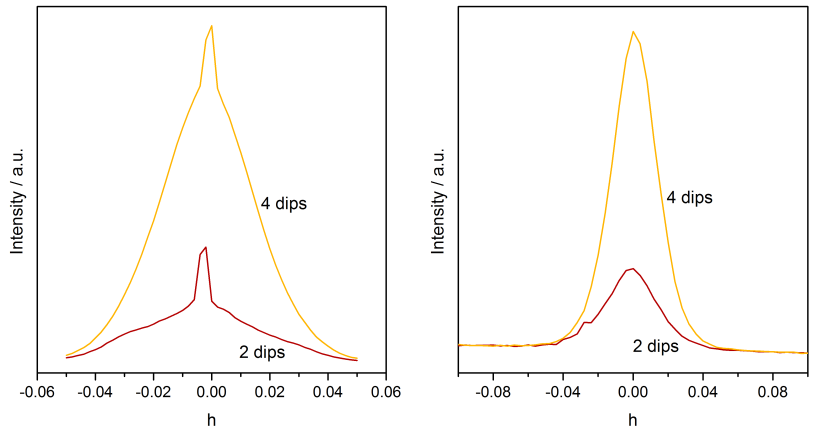


Figure 7.13: Line scans collected at room temperature along h through the maximum intensity of the reciprocal space maps for (a) the (004) and (b) the (013) reflection of samples annealed at 1000 °C. h is in substrate reciprocal space units. The sharp feature in (a) at $h = 0$ arises from a crystal truncation rod. A truncation rod is also evident in (b) for the 2-dip sample.

For the (013) reflection scans along l showed no shift, or only very small shifts, while scans along k showed large shifts to smaller Q values as shown in figure 7.14. The observed shift indicates an expansion of 1.16%, which is much greater than the value of 0.326% expected from the bulk thermal expansion data.

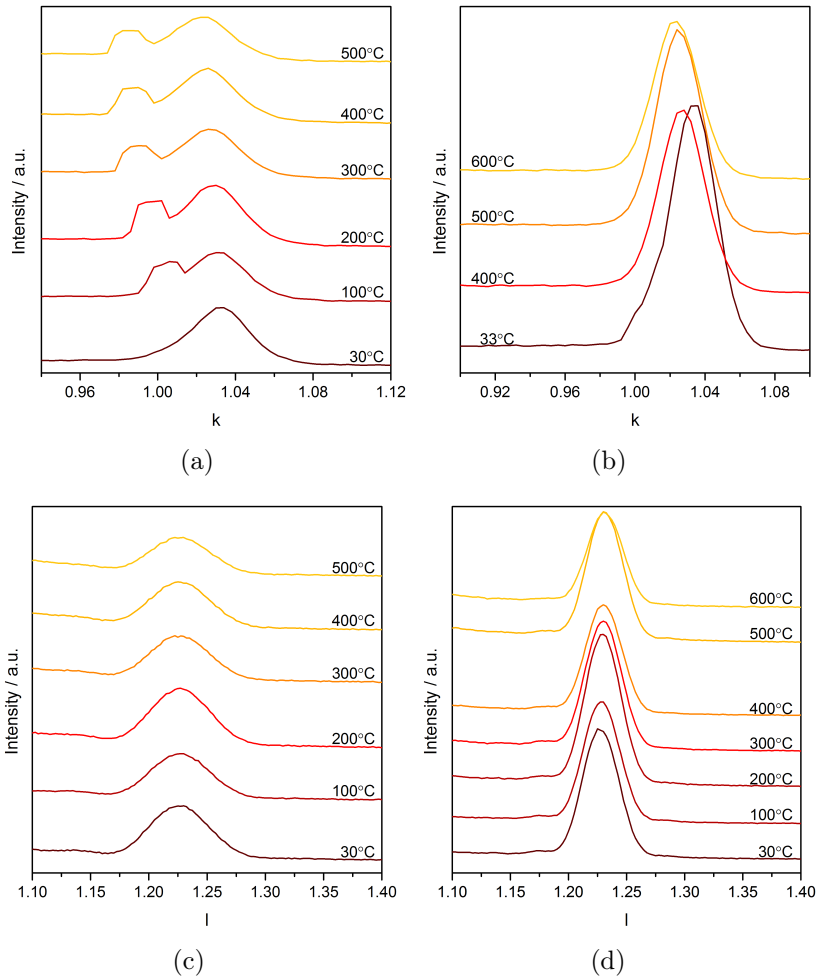


Figure 7.14: Line scans along k and l through the maximum intensity of the reciprocal space maps for the (013) reflection of (a), (c) two and (b), (d) four dip samples annealed at 1000 °C. k and l are in substrate reciprocal space units. The truncation rod in (a) moves to lower k values as the substrate crystal expands with increasing temperature.

To understand this rather unusual behaviour one must consider the $SrTiO_3$ substrate, as the investigated films are very thin and therefore greatly influenced by the characteristics of the substrate. $SrTiO_3$ has a much higher thermal expansion coefficient than TiO_2.[31] This leads to a 1.70% in-plane expansion upon heating to 600 °C. Due to this expansion, the anatase epilayer is placed under an increased tensile stress and an expansion above the value for bulk anatase is observed. The tensile strain leads to a contraction in the orthogonal direction via the Poisson effect.

To quantify this hypothesis we recall that strain in the longitudinal direction $\varepsilon_\perp$ is linked to strain in the transverse direction $\varepsilon_\parallel$ by:

$$\frac{\varepsilon_\perp}{\varepsilon_\parallel} = -\frac{2\nu}{1-\nu} \ , \tag{7.8}$$

where ν is the Poisson ratio. The transverse strain may be derived from the difference between the observed expansion of 1.16% and the expected thermal expansion of 0.326% leading to $\varepsilon_\parallel = 8.34\times10^{-3}$. The Poisson ratio for anatase has been estimated as 0.35 from theoretical calculations, while an experimental value of 0.27 was measured for thin films deposited by atomic layer deposition.[32,33] These two estimates lead to expected $\varepsilon_\perp$ values of -8.98×10^{-3} and -6.17×10^{-3} respectively. It can be seen that the latter Poisson contraction almost exactly cancels out the expected thermal expansion of 6.75×10^{-3} derived from thermal expansion coefficients.

7.3.5 Influence of the Substrate on Thin Films of TiO_2

In the work presented so far in this chapter, $SrTiO_3$ was chosen as a substrate to exploit the small mismatch between it and anatase which stabilises anatase even at high temperatures. Using the same experimental setup as for the samples described previously, an R-plane Al_2O_3 substrate was dip-coated. Table 7.8 summarises the lattice parameters for anatase, rutile, and the two substrates.

Table 7.8: Lattice parameters a, b, and c of rutile R,[20] anatase A,[21] $SrTiO_3$ Sr,[22] and Al_2O_3 Al.[34]

	Rutile	Anatase	$SrTiO_3$	Al_2O_3
a / Å	4.594	3.784	3.901	4.754
b / Å	4.594	3.784	3.901	4.754
c / Å	2.959	9.515	3.901	12.990

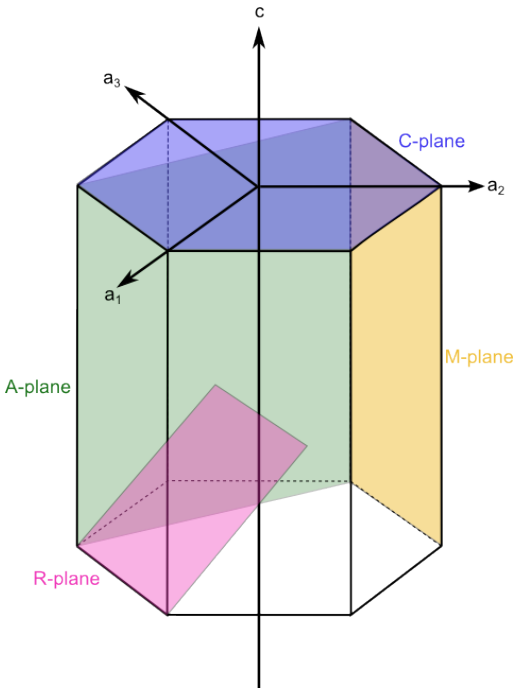


Figure 7.15: Schematic of the unit cell of sapphire Al_2O_3 indicating the different planes including the R-plane.

Al_2O_3 has a hexagonal unit cell with the lattice parameters listed above. For the current investigations, an R-plane Al_2O_3 $(01\bar{1}2)$ substrate was used. Figure 7.15 indicates the different planes in sapphire, including the R-plane. The rectangular surface unit cell of R-plane sapphire has dimensions $a_0(Al_2O_3) \times c_0'(Al_2O_3)$ where $c_0'(Al_2O_3) = \sqrt{3a_0^2(Al_2O_3) + c_0^2(Al_2O_3)} = 15.34$ Å.[35] The (101) surface unit cell of rutile has dimensions $a_0(\text{rutile}) \times c_0'(\text{rutile})$ where $c_0'(\text{rutile}) = \sqrt{a_0^2(\text{rutile}) + c_0^2(\text{rutile})}$ = 5.46 Å. There is thus a mismatch of $\frac{4.594-4.754}{4.754} \times 100\%$ = -3.36% between a_0 values in the short direction, and of $\frac{5.46-15.34/3}{15.34/3} \times 100\% = 6.78\%$ in the long c_0' direction between $c_0'(\text{rutile})$ and $c_0'/3(Al_2O_3)$. Figure 7.16 shows a schematic drawing of the dimensions of both the rutile and Al_2O_3 surface unit cells. The mismatch with anatase is much greater, thus favouring growth of the thermodynamically stable rutile phase.

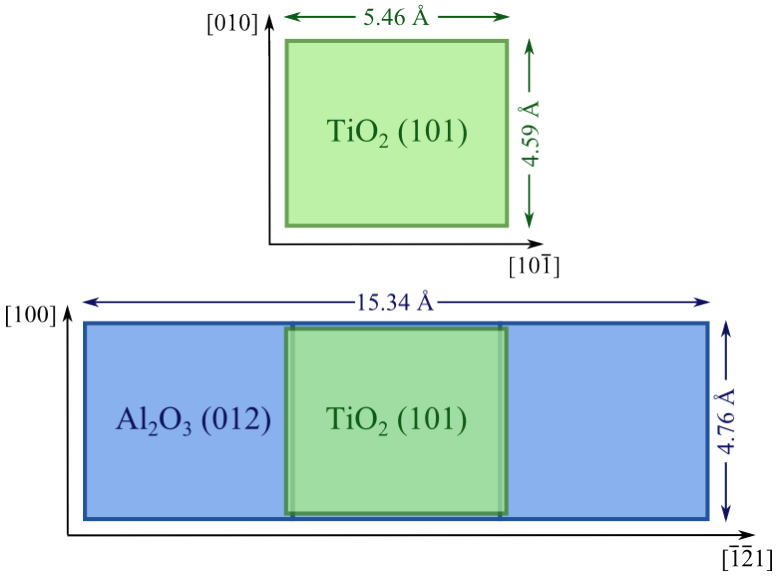


Figure 7.16: Schematic of the surface unit cells of rutile TiO_2 (top) and R-plane Al_2O_3 (012) (bottom).

X-ray diffraction was used to identify the crystal structure of the TiO_2 thin film. Figure 7.17 shows the XRD pattern of one of the thin films grown on Al_2O_3. The (101) Bragg reflection of rutile lies in between the substrate (012) and (024) reflections.

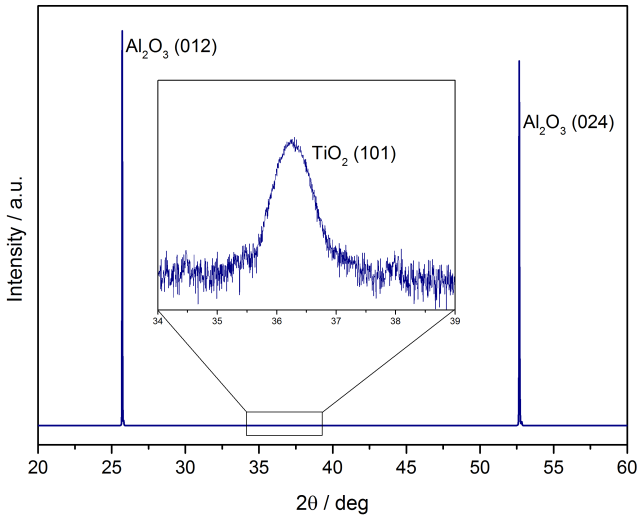


Figure 7.17: X-ray diffraction pattern of a rutile thin film on Al_2O_3. The inlay shows an expanded view (magnification of 3000) of the TiO_2 (101) reflection.

The (101) reflection of rutile appears at a lower diffraction angle compared to the anatase (004) reflection, as can be seen in figure 7.18.

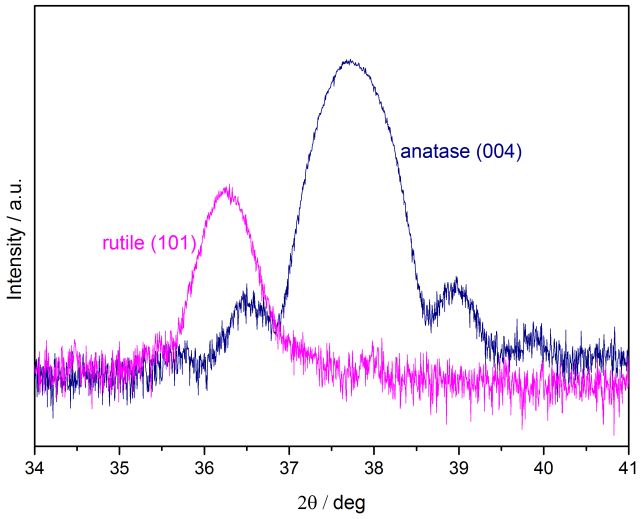
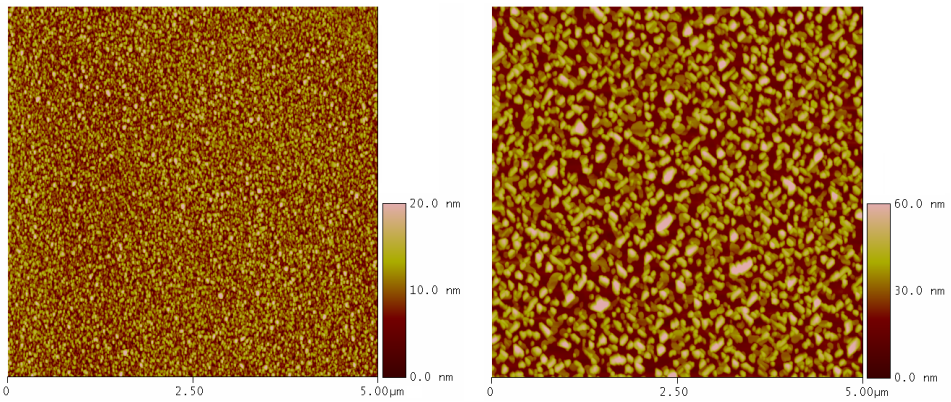


Figure 7.18: Expanded view of the rutile (101) and anatase (004) Bragg peaks from thin films grown on Al_2O_3 and $SrTiO_3$.

The surface morphology of the rutile samples was investigated using AFM. AFM images of two four-dip rutile samples annealed at 800 and 1000 °C are shown in figure 7.19. Both films show complete coverage of the substrate with TiO_2, with the lower annealing temperature appearing more favourable to achieve smooth thin films, whilst the higher annealing temperature lead to the formation of 100 - 300 nm large crystallites.



(a) (b)

Figure 7.19: AFM images of two four-dip samples of a thin film of rutile on Al_2O_3 annealed at (a) 800 °C and (b) 1000 °C.

7.3.6 The Effect of Sn-Doping on TiO_2 Thin Films

The comparatively wide band gap of anatase is one of the main factors restricting its use in solar applications as only UV radiation can be utilised, which presents a small percentage of the solar spectrum. Sn-doping can be used to narrow the band gap of TiO_2 and therefore increase the absorption into the visible region. Upon doping with Sn, the crystal structure of anatase changes, which was investigated by XRD (see figure 7.20). The (004) reflection shifts to a slightly lower diffraction angle upon Sn-doping, originating from an expansion in lattice parameters. This is as expected from the difference in ionic radii for Ti^{4+} ($r_{Ti^{4+}} = 0.68$ Å) in comparison to Sn^{4+} ($r_{Sn^{4+}} = 0.71$ Å) in oxides.[36] When the larger Sn^{4+} replaces Ti^{4+}, the crystal expands, leading to an increase in lattice parameters.

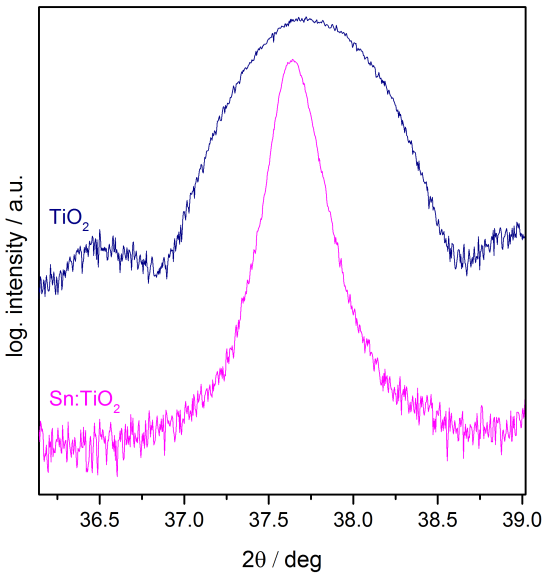


Figure 7.20: Expanded view of the anatase (004) reflection from X-ray diffraction of undoped and Sn-doped TiO_2.

The influence of Sn on the absorbance of TiO_2 was observed using UV-Vis spectroscopy (see figure 7.21. Whilst the undoped TiO_2 sample shows a clear drop in absorbance at around 3.2 eV, the Sn-doped sample only shows a slow decrease at higher energies.

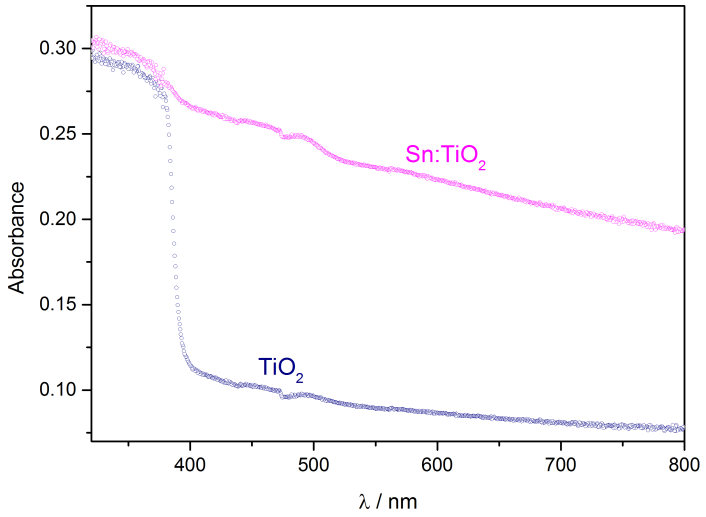


Figure 7.21: Absorbance of an undoped and a Sn-doped anatase TiO_2 thin film.

The electronic properties of Sn-doped TiO_2 from sol-gel dip-coating were further investigated using conventional laboratory and hard X-ray synchrotron based XPS (see chapter 8).

7.4 Concluding Remarks

A Design of Experiments approach, coupled with Raman spectroscopy and atomic force microscopy, was successfully employed to specify the optimum growth conditions for TiO_2 from a sol-gel dip-coating setup. Continuous films could be achieved by choosing specific parameter settings and improving the substrate cleaning process. The annealing temperature and number of dips per sample could be identified as the main influencing factors on the quality and characteristics of the thin films.

The high quality of the resulting thin films is confirmed not only by AFM, but even more so by laboratory- and synchrotron-based X-ray diffraction, where Laue or Pendellösung fringes were observed. From these fringes film thicknesses could be

calculated with high accuracy.

Three dimensional reciprocal space maps of anatase thin films gave a highly detailed view of the thin film Bragg reflections. Truncation rods, which previously were only observed as spikes on line scans, could be observed in their entirety, and for off-specular reflections the substrate peak from which they originate was also shown.

The influence of the temperature on the thin films, particularly in terms of strain, was probed by heating of thin film samples on the sample stage of the diffractometer at the XMaS beamline, and recording Bragg peaks at different temperatures. It was shown that the expected thermal expansion was almost exactly cancelled out by Poisson contraction.

Two further influencing factors, the substrate and Sn-doping, were probed by XRD. Depending on the substrate, either anatase or rutile thin films could be grown using exactly the same setup. Sn-doping of an anatase thin film influences the electronic properties, resulting in a change in absorbance. This will be further investigated using XPS in the following chapter.

7.5 References

[1] O. Carp, C. Huisman, and A. Reller, Progress in Solid State Chemistry **32**, 33 (2004).

[2] K. Tanaka, M. F. Capule, and T. Hisanaga, Chemical Physics Letters **187**, 73 (1991).

[3] A. L. Linsebigler, G. Lu, and J. T. Yates, Chemical Reviews **95**, 735 (1995).

[4] U. Diebold, Surface Science Reports **48**, 53 (2003).

[5] R. Shao, C. Wang, D. E. McCready, T. C. Droubay, and S. A. Chambers, Surface Science **601**, 1582 (2007).

[6] X. Weng, P. Fisher, M. Skowronski, P. Salvador, and O. Maksimov, Journal of Crystal Growth **310**, 545 (2008).

[7] S. Chambers, C. Wang, S. Thevuthasan, T. Droubay, D. McCready, A. Lea, V. Shutthanandan, and C. W. Jr, Thin Solid Films **418**, 197 (2002).

[8] S. A. Chambers, S. Thevuthasan, R. F. C. Farrow, R. F. Marks, J. U. Thiele, L. Folks, M. G. Samant, A. J. Kellock, N. Ruzycki, D. L. Ederer, and U. Diebold, Applied Physics Letters **79**, 3467 (2001).

[9] L. Xu, M. Yang, X. Li, P. Hu, and S. Li, Scripta Materialia **63**, 113 (2010).

[10] M. Murakami, Y. Matsumoto, K. Nakajima, T. Makino, Y. Segawa, T. Chikyow, P. Ahmet, M. Kawasaki, and H. Koinumaa, Applied Physics Letters **78**, 2664 (2001).

[11] Y. Matsumoto, M. Murakami, T. Shono, T. Hasegawa, T. Fukumura, M. Kawasaki, P. Ahmet, T. Chikyow, S. Koshihara, and H. Koinuma, Science **291**, 854 (2001).

[12] B. H. Park, J. Y. Huang, L. S. Li, and Q. X. Jia, Applied Physics Letters **80**, 1174 (2002).

[13] R. J. Kennedy and P. A. Stampe, Journal of Crystal Growth **252**, 333 (2003).

[14] S. R. Shinde, S. B. Ogale, S. D. Sarma, J. R. Simpson, H. D. Drew, S. E. Lofland, C. Lanci, J. P. Buban, N. D. Browning, V. N. Kulkarni, J. Higgins, R. P. Sharma, R. L. Greene, and T. Venkatesan, Physical Review B **67**, 115211 (2003).

[15] D. Kurita, S. Ohta, K. Sugiura, H. Ohta, and K. Koumoto, Journal of Applied Physics **100**, 096105 (2006).

[16] G. E. Jellison, L. A. Boatner, J. D. Budai, B.-S. Jeong, and D. P. Norton, Journal of Applied Physics **93**, 9537 (2003).

[17] M. Schuisky, A. Hårsta, A. Aidla, K. Kukli, A.-A. Kiisler, and J. Aarikb, Journal of the Electrochemical Society **147**, 3319 (2000).

[18] H. S. Jung, J.-K. Lee, J. Lee, B. S. Kang, Q. Jia, and M. Nastasi, Journal of Physical Chemistry C **112**, 4205 (2008).

[19] S. Tanemura, L. Miao, P. Jin, K. Kaneko, A. Terai, and N. Nabatova-Gabain, Applied Surface Science **212-213**, 654 (2003).

[20] W. H. Baur and A. A. Khan, Acta Crystallographica B **27**, 2133 (1971).

[21] M. Horn, C. F. Schwerdtfeger, and E. P. Meagher, Zeitschrift für Kristallographie, Kristallgeometrie, Kristallphysik, Kristallchemie **136**, 273 (1972).

[22] Y. A. Abramov, V. G. Tsirelson, V. E. Zavodnik, S. A. Ivanov, and I. D. Brown, Acta Crystallographica B **51**, 942 (1995).

[23] A. Nakatsuka, O. Ohtaka, H. Arima, N. Nakayama, and T. Mizota, Acta Crystallographica Section E **61**, i148 (2005).

[24] F. E. Oropeza, K. H. L. Zhang, R. G. Palgrave, A. Regoutz, and R. G. Egdell, The Journal of Physical Chemistry C **117**, 15221 (2013).

[25] K. Hinkelmann and O. Kempthorne, *Design and Analysis of Experiments* (John Wiley & Sons, Hoboken, 2008).

[26] R. L. Plackett and J. . P. Buman, Biometrika **33**, 305 (1946).

[27] O. Frank, M. Zukalova, B. Laskova, J. Kürti, and J. K. A. L. Kavan, Physical Chemistry Chemical Physics **14**, 14567 (2012).

[28] N. Kato and A. R. Lang, Acta Crystallographica **12**, 787 (1959).

[29] N. Kato, Acta Crystallographica **14**, 526 (1961).

[30] K. V. K. Rao, S. V. N. Naidu, and L. Iyengar, Journal of the American Ceramic Society **53**, 124 (1970).

[31] D. de Ligny and P. Richet, Physical Review B **53**, 3013 (1996).

[32] X. G. Ma, P. Liang, L. Miao, S. W. Bie, C. K. Zhang, L. Xu, and J. J. Jiang, Physica Status Solidi b **246**, 2132 (2009).

[33] L. Borgese, M. Gelfi, E. Bontempi, P. Goudeau, G. Geandier, D. Thiaudière, and L. Depero, Surface and Coatings Technology **206**, 2459 (2012).

[34] N. Ishizawa, T. Miyata, I. Minato, F. Marumo, and S. I. Iwai, Acta Crystallographica B **36**, 228 (1980).

[35] T. Sasaki and S. Zembutsu, Journal of Applied Physics **61**, 2533 (1987).

[36] R. D. Shannon and C. T. Prewitt, Acta Crystallographica B **25**, 925 (1969).

8 Hard X-Ray Photoemission Spectroscopy of TiO_2 and Sn-doped TiO_2 Thin Films

8.1 Introduction

TiO_2 is one of the most promising photocatalytic materials. However, the band gaps of the rutile and anatase polymorphs are both above 3 eV. Therefore their ability to facilitate photocatalytic reactions in visible light is limited. Visible region activation of TiO_2 was achieved when Asahi *et al.* reported increased photocatalytic activity upon nitrogen doping.[1] Since then, nitrogen has remained the most widely used dopant[2–10], but in addition metal dopants such as V[11], Nb[12], Ta[12], and co-doped Rh/Sb[13,14] have also been successfully employed.

The Egdell group recently demonstrated that Sn-doped *rutile* has superior photocatalytic activity to N-doped *anatase*.[15] Solid solutions of the form $Sn_xTi_{1-x}O_2$, which have the rutile structure, can be prepared by high temperature solid state reactions.[16–18] An increase in the band gap would be expected when doping of the wider gap SnO_2, which has a band gap of 3.596 eV[19], into the lower gap TiO_2. However, pronounced band gap bowing has been observed at low Sn concentrations,

with the band gap reaching a minimum value at $x = 0.02$.[20]

Although anatase is thermodynamically unstable compared to rutile, and therefore not accessible through the solid state route, it can be stabilised as epitaxial layers up to higher temperatures. Recently the Egdell group has investigated Sn-doped TiO_2 anatase films with X-ray photoemission spectroscopy.[21] Figure 8.1 shows valence band XPS of Sn-doped anatase TiO_2, which shows a weak peak at the bottom of the main O $2p$ valence band. This peak increases in intensity with increasing Sn doping level. A peak at this position could stem from hybridisation between Sn $5s$ and O $2p$ states. However, hydroxides on the sample surface can also lead to a peak at this binding energy and assignment to Sn $5s$ states proved controversial with referees.

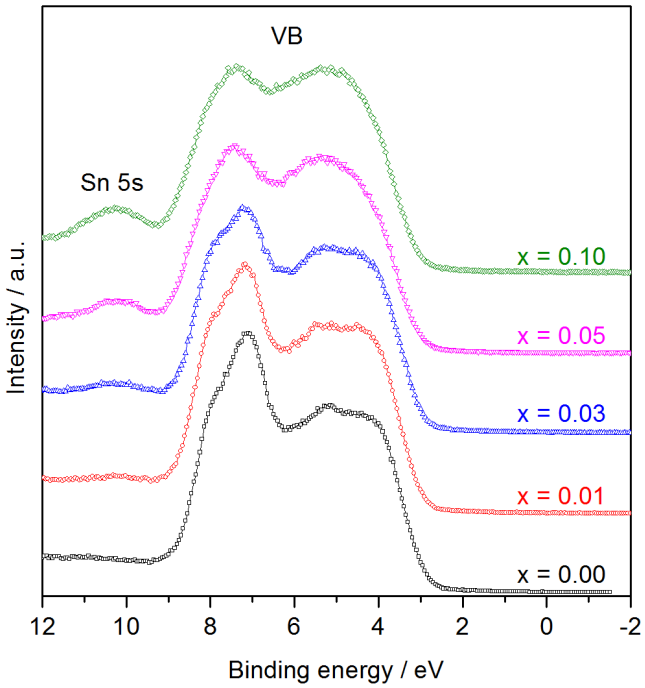


Figure 8.1: Expanded view of the valence band region of $Sn_xTi_{1-x}O_2$. A weak Sn $5s$ peak is observed at the bottom of the valence band.[21]

The main aim of the following investigation is to confirm that this peak is indeed associated with Sn $5s$ states, and to present a thorough analysis of hard X-ray

photoemission spectra (HAXPES) of doped and undoped anatase. The collected valence band spectra are compared to calculations of the density of states.

8.2 Experimental

Thin films of TiO_2 and Sn-doped TiO_2 on 0.5% Nb-doped $SrTiO_3$ (001) were grown via sol-gel dip-coating. A Nb-doped substrate was chosen to ensure a high conductivity. The three thin film samples investigated here are TiO_2 on 0.5% Nb-doped $SrTiO_3$ (001), Sn-doped TiO_2 on 0.5% Nb-doped $SrTiO_3$ (001), and an uncoated 0.5% Nb-doped $SrTiO_3$ (001) substrate. Henceforth, they shall be referred to as TiO_2, Sn:TiO_2, and Nb:$SrTiO_3$.

30 mL of the precursor solutions were prepared in a N_2 atmosphere in a glove box. For the TiO_2 sample a precursor solution of Ti(IV)isopropoxide in 2-propanol with a propoxide concentration of 0.25 mol/L was prepared. A mixed alkoxide solution of Ti(IV)isopropoxide (99.999% trace metals basis, supplied by Sigma-Aldrich Inc.) and Sn(IV)isopropoxide (10 % (w/v) in isopropanol/toluene, 99.99% trace metals basis supplied by Sigma-Aldrich Inc.) in 2-propanol with an overall concentration of 0.25 mol/L was prepared for the Sn:TiO_2 sample. The molar ratio between the Sn- and Ti-precursor was 0.1 to 0.9 giving a doping level of 1%. To both solutions 150 μL of nitric acid HNO_3 were added as a catalyst. The substrates were cleaned with 2-propanol and dried under N_2 flow. Both samples were dipped eight times at a removal speed of 0.35 cm/min.

All three samples were annealed for 5 hours in air at 600°C, and under a constant N_2 flow for 5 hours at 800°C. Both times the cooling rate was set to 5°C per

minute. The N_2 was used at higher temperatures to avoid oxidation of the substrate crystals, giving rise to defects which could compensate the n-type doping due to Nb and reduce the conductivity. This would lower the conductivity of the substrates leading to potential problems due to sample charging when conducting HAXPES experiments.

Core level and valence band spectra of the three samples were investigated by Al $K\alpha$ ($h\nu$ = 1486.6 eV) and hard X-ray photoelectron spectroscopy ($h\nu$ = 6472 eV). Al $K\alpha$ XPS measurements were performed by Dr. R. Palgrave on a Thermo Scientific K-Alpha system at University College London. Hard XPS (HAXPES) was conducted at the BL12XU beam line at SPring-8 in Japan (for a detailed description of the experimental set up, please refer to 3.4.4). Calculations of the density of states for undoped and Sn-doped anatase were conducted by Prof. G. Watson at Trinity College, Dublin.

8.3 Computational

The density functional theory (DFT) calculations were performed using the HSE06 (Heyd-Scuseria-Ernzerhof) hybrid functional as proposed by Krukau *et al.*[22] A reasonably small $2 \times 2 \times 1$ anatase cell with one Sn atom, i.e 1 Sn, 15 Ti and 32 O atoms, was chosen.

8.4 Results and Discussion

8.4.1 Core Level Spectra

Figures 8.2 and 8.3 show conventional XPS and HAXPES survey spectra for all three samples, respectively. All peaks could be assigned to core levels of the elements expected in the samples.

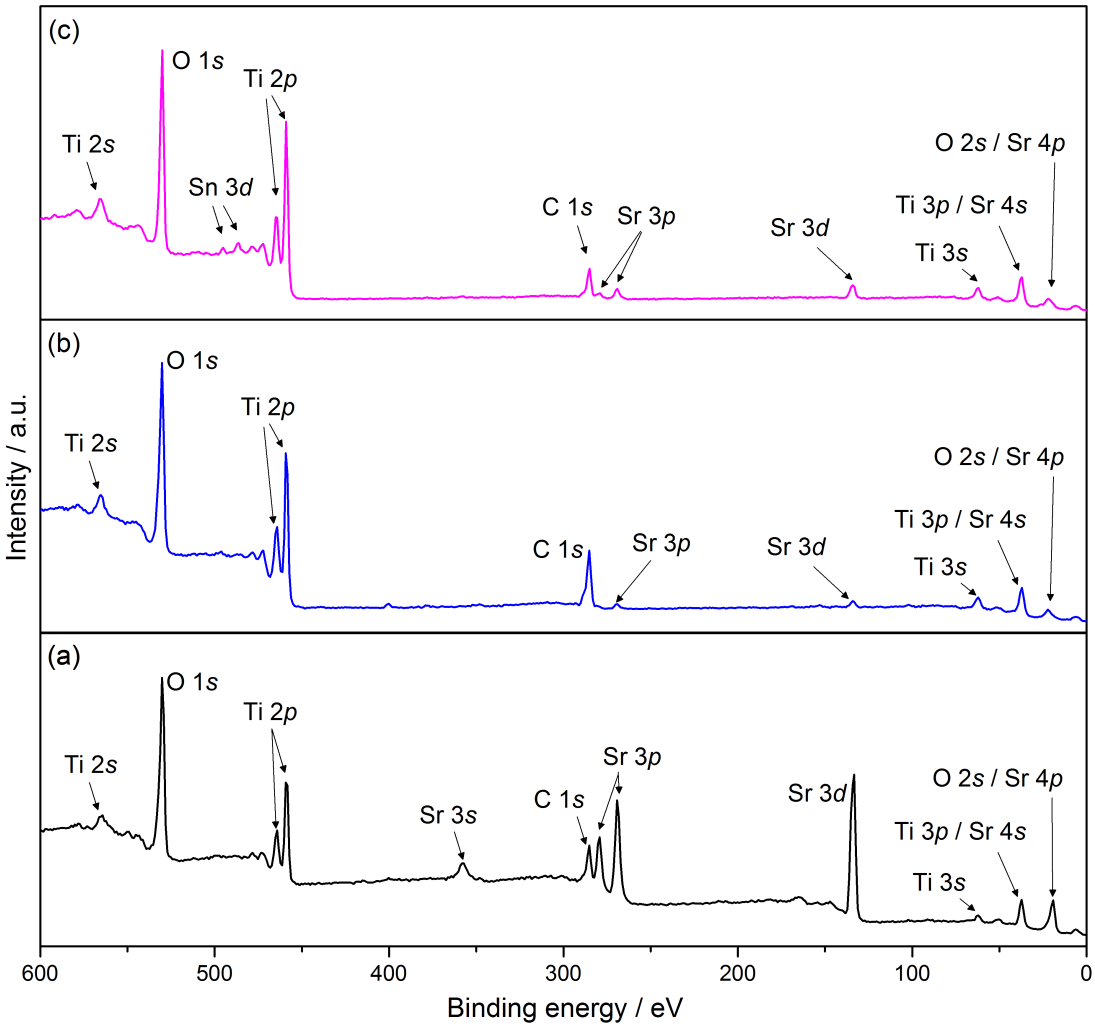


Figure 8.2: Al $K\alpha$ ($h\nu$ = 1486.6 eV) XPS survey spectra for (a) Nb:$SrTiO_3$, (b) TiO_2, and (c) Sn:TiO_2. The spectra were aligned assuming the binding energy of C 1s to be 285.0 eV.

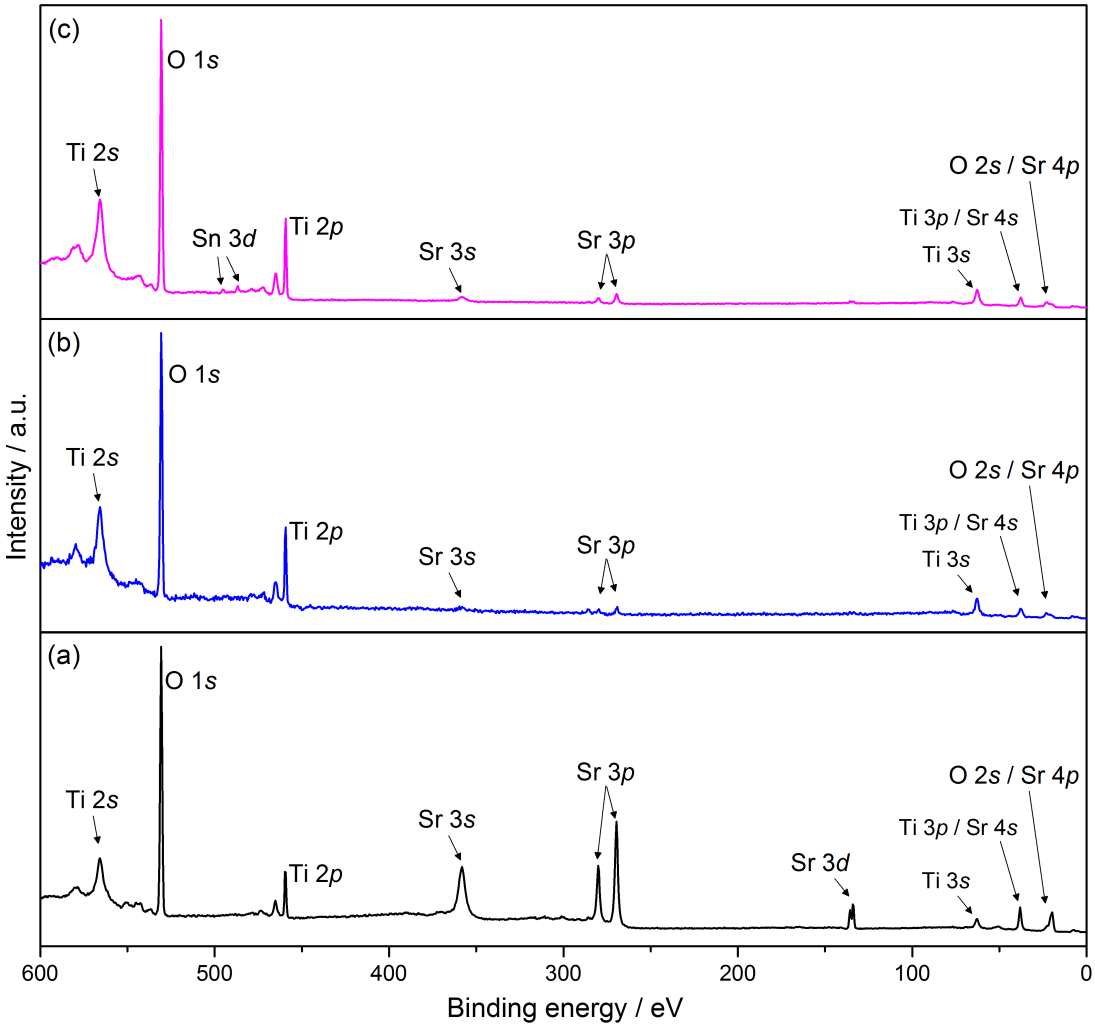


Figure 8.3: HAXPES ($h\nu = 6472$ eV) survey spectra for (a) Nb:$SrTiO_3$, (b) TiO_2, and (c) Sn:TiO_2. The spectra were aligned using the Fermi edge of a gold reference.

Due to the difference in photoelectron cross sections between conventional and hard XPS, the relative intensities of the core levels vary as a function of photon energy. Table 8.1 gives theoretical cross sections calculated by Scofield for the main peaks observed in the survey spectra of the three samples investigated here.

Table 8.1: Computed photoelectron cross sections for filled orbitals σ and for one electron in the orbital σ/e^- for core levels observed in the XPS and HAXPES spectra of Nb:$SrTiO_3$, TiO_2, and Sn:TiO_2. Values for σ at two energies, 1500 eV and 6000 eV, were taken from Scofield.[23] The energies are close to the ones used in the work presented here, 1486.7 eV and 6472 eV respectively. σ_{rel} and $\sigma_{\mathrm{rel}}/e^-$ are the relative cross sections compared to the highest cross section at each energy.

	1500 eV				6000 eV			
Core level	σ	σ/e^-	σ_{rel}	$\sigma_{\mathrm{rel}}/e^-$	σ	σ/e^-	σ_{rel}	$\sigma_{\mathrm{rel}}/e^-$
Sr $3s$	25018	12509	12.72	36.71	1716	858	80.36	82.82
Sr $3p_{3/2}$	58439	14610	29.71	42.88	1807	452	84.62	43.61
Sr $3p_{1/2}$	30176	15088	15.34	44.28	996	498	46.65	48.07
Sr $3d_{5/2}$	39579	6597	20.12	19.36	276	46	12.95	4.45
Sr $3d_{3/2}$	27255	6814	13.86	20.00	195	49	9.13	4.71
Sr $4s$	3910	1955	1.99	5.74	252	126	11.81	12.17
Sr $4p_{3/2}$	6822	1705	3.47	5.01	211	53	9.90	5.10
Sr $4p_{1/2}$	3545	1772	1.80	5.20	117	58	5.46	5.63
Ti $2s$	43447	21724	22.09	63.76	2071	1036	97.03	100.00
Ti $2p_{3/2}$	69340	17335	35.25	50.88	851	213	39.85	20.53
Ti $2p_{1/2}$	35766	17883	18.18	52.49	450	225	21.06	21.71
Ti $3s$	6333	3166	3.22	9.29	283	142	13.27	13.67
Ti $3p_{3/2}$	7141	1785	3.63	5.24	102	26	4.78	2.46
Ti $3p_{1/2}$	3680	1840	1.87	5.40	54	27	2.52	2.60
Ti $3d_{5/2}$	107	18	0.05	0.05	0.34	0.06	0.02	0.01
Ti $3d_{3/2}$	73	18	0.04	0.05	0.24	0.06	0.01	0.01
Ti $4s$	475	238	0.24	0.70	21	11	0.99	1.02
O $1s$	38989	19495	19.82	57.21	682	341	31.95	32.93
O $2s$	1872	936	0.95	2.75	37	18	1.71	1.77
O $2p_{3/2}$	170	42	0.09	0.12	0.84	0.21	0.04	0.02
O $2p_{1/2}$	86	43	0.04	0.13	0.43	0.21	0.02	0.02
Sn $3d_{5/2}$	196710	32785	100.00	96.22	2135	356	100.00	34.35
Sn $3d_{3/2}$	136290	34073	69.28	100.00	1531	383	71.73	36.96
Sn $4d_{5/2}$	21139	3523	10.75	10.34	283	47	13.26	4.55
Sn $4d_{3/2}$	14725	3681	7.49	10.80	204	51	9.57	4.93

In addition to the difference in cross sections, a second apparent difference is the lack of the C $1s$ core levels in the HAXPES spectra. Due to the high energy X-rays used in HAXPES, bulk sensitivity can be achieved. The higher inelastic mean free path compared to XPS makes HAXPES relatively insensitive to contaminants such as hydrocarbons and hydroxides on the sample surface.

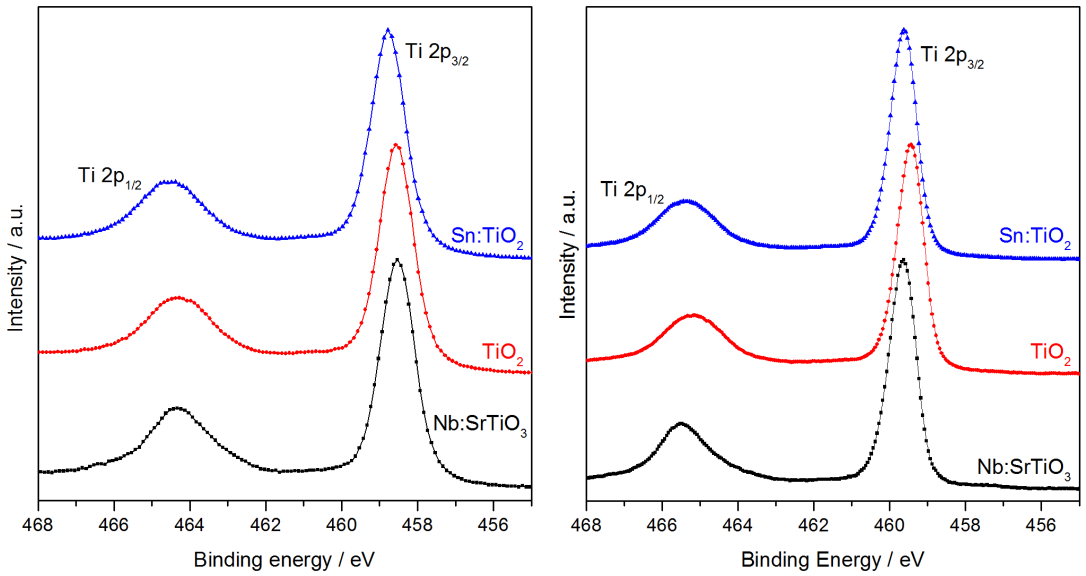


Figure 8.4: Ti $2p$ core level spectra for Nb:$SrTiO_3$, TiO_2, and Sn:TiO_2 measured with (a) conventional XPS and (b) HAXPES.

Figure 8.4 shows the Ti $2p$ core level for all three samples, both measured by conventional XPS and HAXPES. A shift in binding energies between the XPS and HAXPES spectra is apparent. Table 8.2 summarises the positions of the Ti $2p$ peaks from peak fits. Al $K\alpha$ XPS spectra were calibrated assuming the C $1s$ binding energy was 285.0 eV, and HAXPES spectra were calibrated using the Fermi edge of a gold reference. The shift in binding energy is most likely an artefact arising from poor electrical contact between the samples and the manipulator: the samples were mounted using double sided carbon loaded sticky tape. The slightly increased spin orbit splitting (S.O.S.) for the Nb:$SrTiO_3$ sample measured in the HAXPES data is due to the asymmetry of the Ti $2p_{1/2}$ core level in HAXPES and the better experimental resolution in the HAXPES experiment which better reveals the intrinsic line shape.

Table 8.2: Binding energies E_B (subject to an uncertainty of ±0.4 eV) and spin orbit splitting (S.O.S.) for Ti $2p_{3/2}$ and Ti $2p_{1/2}$ measured by conventional XPS and HAXPES. The shift between XPS and HAXPES is also given.

	Sample	$E_B(XPS)$ / eV	$E_B(HAXPES)/eV$	Shift / eV
Ti $2p_{3/2}$	Nb:$SrTiO_3$	458.55	459.64	1.09
	TiO_2	458.56	459.44	0.88
	Sn:TiO_2	458.78	459.63	0.85
Ti $2p_{1/2}$	Nb:$SrTiO_3$	464.31	465.49	1.18
	TiO_2	464.31	465.17	0.86
	Sn:TiO_2	464.52	465.37	0.85
S.O.S.	Nb:$SrTiO_3$	5.76	5.85	
	TiO_2	5.75	5.73	
	Sn:TiO_2	5.74	5.74	

Figure 8.5 shows the Sr $3p$ core level for the three samples measured with Al $K\alpha$ XPS and HAXPES. Strong attenuation of the core levels is apparent in the thin film samples, indicating good coverage of the substrate. The attenuation is very similar in XPS and HAXPES with the intensity of the Sr $3p_{3/2}$ core level of the TiO_2 thin film dropping to below 4% and to below 10% for the Sn:TiO_2 thin film.

The observation that the attenuation is not more pronounced in Al $K\alpha$ than in HAXPES cannot be rationalised assuming complete and uniform coverage of the $SrTiO_3$ substrate by a film ∼24 nm thick. Instead, the results imply that a fraction of around 4% (undoped film) and 10% (doped film) of the film area must consist of pinholes.

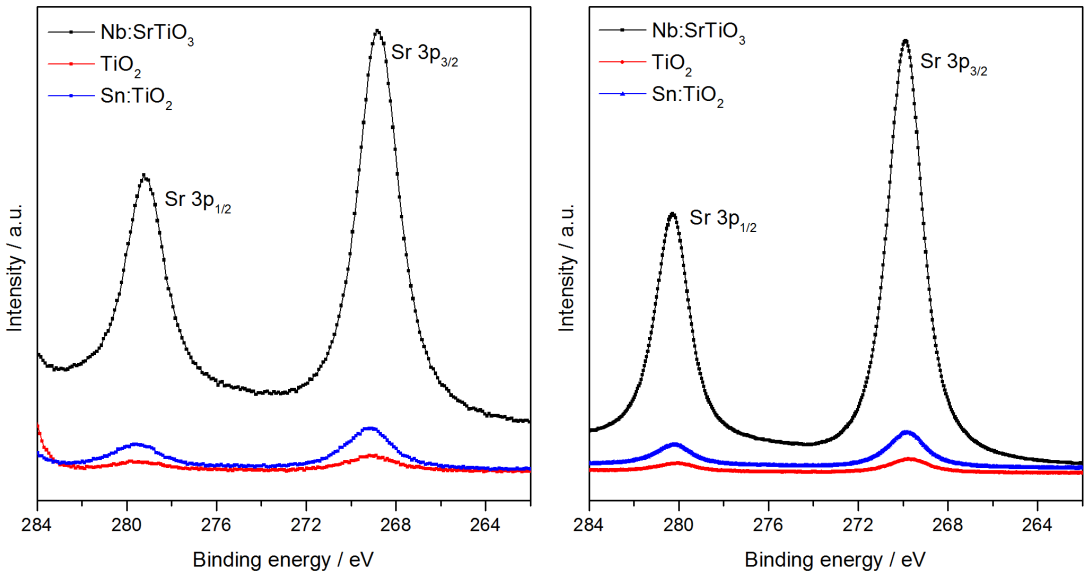


Figure 8.5: Sr $3p$ core level spectra for Nb:$SrTiO_3$, TiO_2, and Sn:TiO_2 measured with (a) conventional XPS and (b) HAXPES.

A similar trend as seen in the Sr $3p$ core level can be observed for the Sr $3d$ core level shown in figure 8.6.

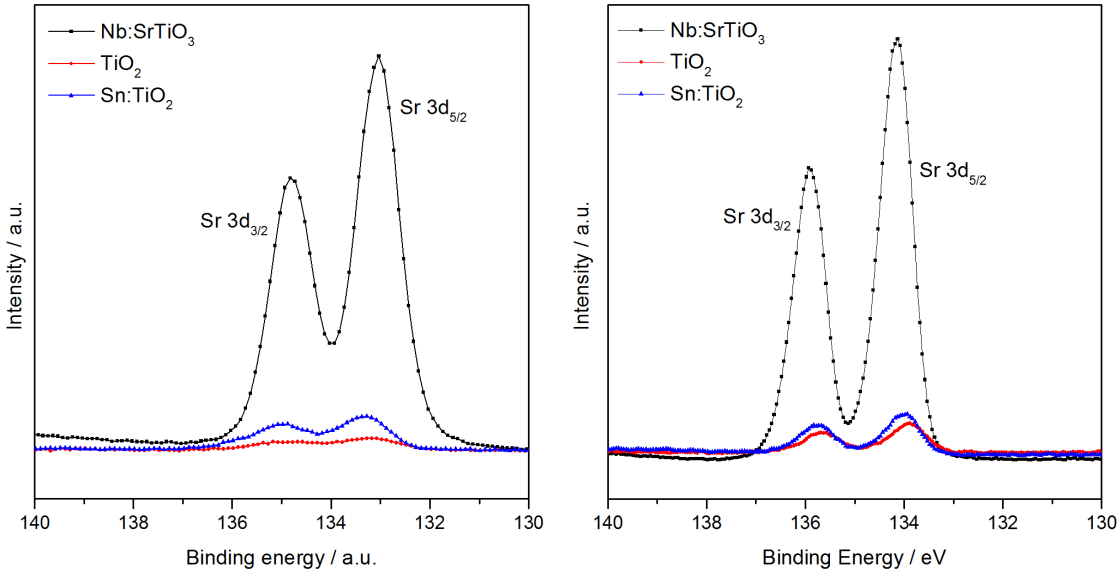


Figure 8.6: Sr $3d$ core level spectra for Nb:$SrTiO_3$, TiO_2, and Sn:TiO_2 measured with (a) conventional XPS and (b) HAXPES.

Table 8.3 summarises the attenuation of the Sr $3p$ and $3d$ core lines for the TiO_2

and Sn:TiO_2 thin film samples compared to the substrate Nb:$SrTiO_3$ for XPS and HAXPES. Values for the residual intensity are derived from the peak areas of the core levels fitted by pseudo-Voigt functions.

Table 8.3: Residual intensity α of the Sr $3p$ and $3d$ core levels for the two thin film samples compared to the substrate for both XPS and HAXPES measurements. All values are subject to an uncertainty of ± 0.05)

Core level	Sample	$\alpha(XPS)$ / %	$\alpha(HAXPES)$ / %
Sr $3p_{3/2}$	TiO_2	5.10	3.42
	Sn:TiO_2	9.58	9.39
Sr $3p_{1/2}$	TiO_2	6.78	3.92
	Sn:TiO_2	10.97	9.66
Sr $3d_{5/2}$	TiO_2	3.57	6.92
	Sn:TiO_2	8.63	9.67
Sr $3d_{3/2}$	TiO_2	3.83	8.74
	Sn:TiO_2	15.17	11.54

The differences in attenuation between XPS and HAXPES stem from the morphology of the sample. Both thin films show a varying density of pin holes across the surface. This combined with the small spot measurements leads to a slight variation in attenuation.

8.4.2 Satellites in the Ti 2*p* and O 1*s* Core Levels

The satellite structures in core levels are of interest as the energy separation between them and the intensity of the peaks can give information about the chemistry of the compounds. Good quality, high resolution XPS data is necessary to identify satellite structures. Here, the first high quality HAXPES study of the Ti $2p$ core levels of Nb:$SrTiO_3$, TiO_2, and Sn:TiO_2 is presented. The core lines and satellites are shown in figure 8.7. The intensities of the spectra are normalized using the Ti $2p_{3/2}$ peak.

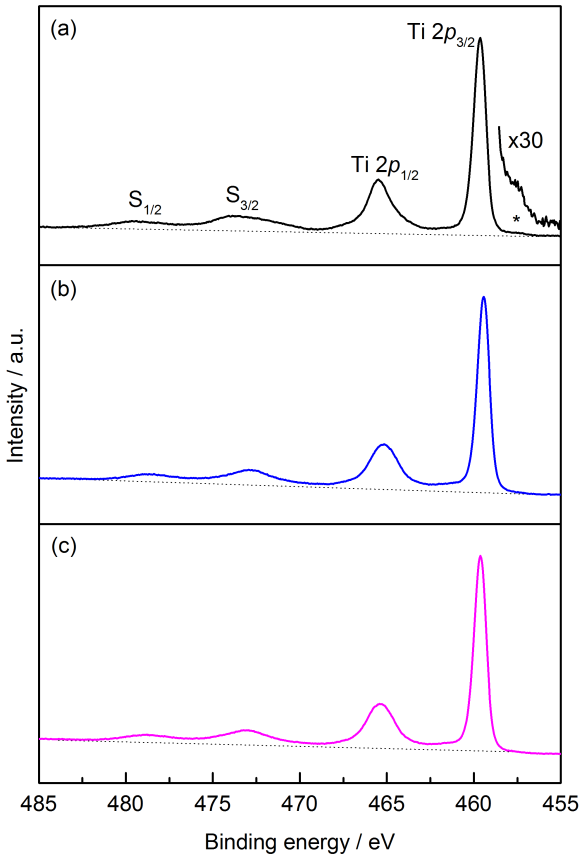


Figure 8.7: HAXPES Ti $2p$ core level spectra for the three samples (a) Nb:$SrTiO_3$, (b) TiO_2, and (c) Sn:TiO_2 are shown. The intensity associated with Ti^{3+} ions is marked with *.

All three spectra show two satellites at the higher binding energy side of the core lines. Whilst the satellite peaks are symmetric in the two thin film samples, the substrate $2p_{1/2}$ line has an asymmetric profile. In addition, the spectrum for the Nb:$SrTiO_3$ substrate shows intensity at the lower binding energy side of the Ti $2p_{3/2}$. This is attributed to a small number of Ti^{3+} ions present due to Nb doping.[24,25]

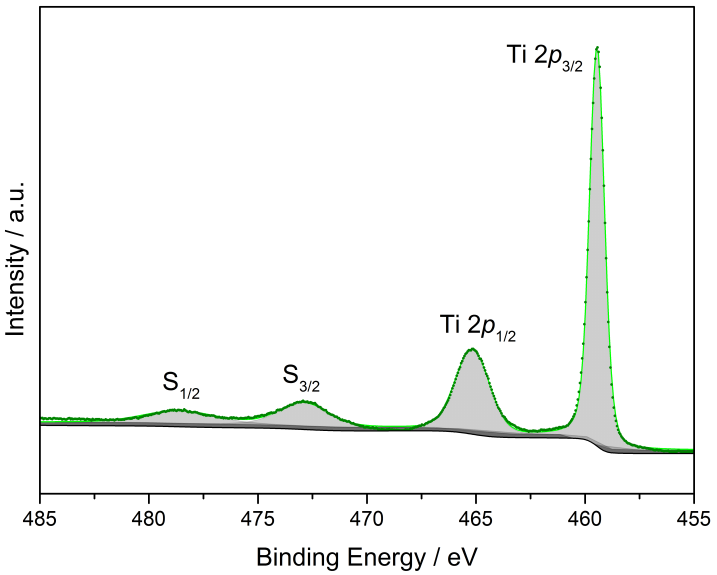


Figure 8.8: Ti $2p$ core level for the TiO_2 sample fitted with pseudo-Voigt functions.

Figure 8.8 shows the Ti $2p$ core level for the TiO_2 sample fitted to pseudo-Voigt functions. From fits of all three samples, satellite separations were derived and are summarised in table 8.4. Only one satellite per core level could be identified. Adding of additional satellite peaks at around 5 - 6 eV separation was not successful as their intensity always converged toward zero.

Table 8.4: Satellite separations ΔE for the $2p$ core lines and relative intensities of the satellites $I_{3/2}$ and $I_{1/2}$ in comparison to the intensities of $2p_{3/2}$ and $2p_{1/2}$ main core lines.

	Separation / eV		rel. Intensity	
System	Ti $2p_{1/2}$	Ti $2p_{3/2}$	Ti $2p_{1/2}$	Ti $2p_{3/2}$
$SrTiO_3$	13.99	13.65	0.18	0.24
TiO_2	13.54	13.47	0.17	0.24
Sn:TiO_2	13.43	13.49	0.16	0.29

The separation energies reported here agree with values from the literature (see table 8.5 for a summary). The difference in relative intensities compared to data from the literature is due to the fact that all previously reported data stemmed from conventional XPS, whereas here HAXPES was used.

A very low intensity plasmon loss related peak at 25.6 eV separation from the Ti $2p_{3/2}$ core line could be observed.

Satellites in the XPS spectra of $2p$ core levels of transition metals and their compounds have been well known since the 1970s. Most research focused on the late transition metals (TMs) where satellites arise mainly due to charge transfer mechanisms.[26–30]

Table 8.5: Separation energy and relative intensity (in relation to the main core level) of satellites of the Ti $2p$ core lines as reported in the literature. A and R indicate the TiO_2 polymorphs anatase and rutile.

	Separation / eV		rel. Intensity	
System	Ti $2p_{1/2}$	Ti $2p_{3/2}$	Ti $2p_{1/2}$	Ti $2p_{3/2}$
TiF_3[31]	12.7	12.4	-	-
TiO_2[32]	12.6	13.3	-	-
TiO_2 (R & A)[33]	13.6	13.6	-	-
TiO_2 (R)[34]	13.4	13.0	0.24	0.25
	25.0	25.4	0.05	0.06
TiO_2 (R & A)[35]	5.0	5.1	0.07	0.07
	13.4	13.5	0.40	0.25
	25.7	25.6	0.14	0.12
TiO_2 (R)[36]	13.4	13.4	-	0.20
	25.7	-	0.13	-
TiO_2 (R)[37]	13.2	13.2	-	-
$SrTiO_3$[34]	13.7	13.6	0.2	0.19
	29.2	29.8	0.1	0.08
$SrTiO_3$[37]	13.2	13.2	-	-
$BaTiO_3$[36]	13.1	13.2	-	-
	24.5	-	0.20	-

A number of experimental studies of the Ti $2s$ and $2p$ core levels exist, which all show satellites on the high binding energy side of the core level peaks. Table 8.5 summarises values from the literature for the separation and relative intensities of

satellites observed on the Ti core levels for TiO_2, TiF_3, $SrTiO_3$, and $BaTiO_3$.

From this overview, it is apparent that in all reported cases one satellite per core line is observed at a separation energy of approximately 13 eV from the main core lines. However, some references report further satellites. The existence of the additional satellites has been subject to debate.

To add to the controversy surrounding these satellite peaks, the physical mechanisms leading to the satellites still provoke controversy. The main satellite peaks observed at 13 eV separation from the core lines are agreed to be shake-up satellites. Shake-up is a process where a second electron from a filled orbital is excited to a higher unfilled orbital during the photoionisation from a core level. However, there is ongoing discussion on the nature of the filled and empty states involved. Four main explanations have been proposed in the literature:

1. Charge transfer from a ligand p to a metal $3d$ level.[35,36,38–40]
2. Charge transfer from a ligand p to a metal $4s$,p orbitals[33,41,42]
3. An excitonic or polaronic process, where shake-up occurs from the outermost p state to the unoccupied s state of the ligand.[43,44]
4. Charge transfer as in 1, but where the final state is strongly influenced by hybridisation between metal d and ligand p orbitals in the final state.[26,45,46]

The simple charge transfer models proposed in 1 and 2 were initially widely accepted, but de Boer *et al.*[44] pointed out that they cannot account for the fact that satellite energies in Sc_2O_3 are smaller than in TiO_2, even though the separation between valence and conduction bands are larger. However, it has subsequently been noted by Okada *et al.*[26,45] that neither of the first three models can cope with the relative intensities of the satellite peaks compared to the core levels. They proposed

a revised charge transfer model which takes hybridisation between metal d and ligand p orbitals in the final state into account. This model gives reasonable separation energies and relative intensities.

The higher satellites, which are sometimes observed at approximately 25 eV separation from the main peak, are attributed to valence electron plasmon loss processes.[33,34,37]

In addition to the satellite structures observed on the Ti $2p$ core level the O $1s$ core line also shows a complex satellite structure. Figure 8.9 shows a detailed view of the satellite structure of the O $1s$ core line for all three samples. In the Nb:$SrTiO_3$ spectrum five satellite components could be identified, indicated in the figure as I-V. They appear at the following separations from the main core line: 6.30 eV (I), 11.89 eV (II), 14.10 eV (III), 16.94 eV (IV), and 19.45 eV (V).

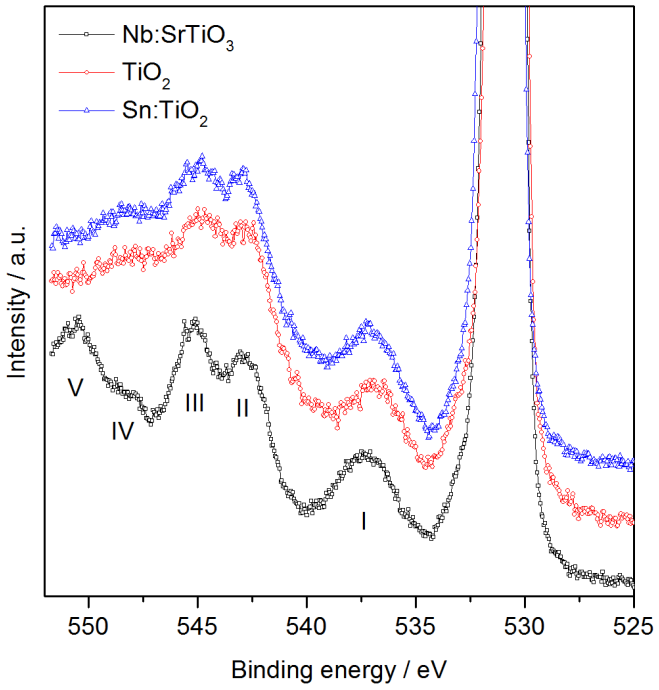


Figure 8.9: Satellites of the O $1s$ core line for Nb:$SrTiO_3$, TiO_2, and Sn:TiO_2 measured by HAXPES.

The observed satellite peaks are in agreement with data reported by Kohiki *et al.*[47] They interpreted the satellite peaks using first principle calculations as follows:

1. I is due to interband transitions from the O $2p$ valence band into the ligand field split t_{2g} and e_g Ti $3d$ levels.
2. II and III were interpreted as arising from O $2p$ valence electron plasma excitation, strongly shifted from the expected value of 20 eV by interaction with other excitations.
3. IV and V could not be interpreted with confidence. They were thought to be caused by excitation of valence or semicore states.

8.4.3 Valence Band Spectra

Figure 8.10 shows the valence band spectra for all three samples measured with conventional XPS and HAXPES. The shape of the valence band changes due to the differences in cross sections between the two methods.

The intensity above the bottom of the valence band in the conventional XPS of the undoped film, or for the bare substrate, cannot be attributed to the hybridisation between Sn $5s$ and O $2p$ states. It must arise from hydroxide contamination of the surface. This assignment of the structure in conventional XPS is controversial. In HAXPES however, hydroxide peaks are not observed, so that the occurrence of the peak can be, without doubt, attributed to the Sn states.

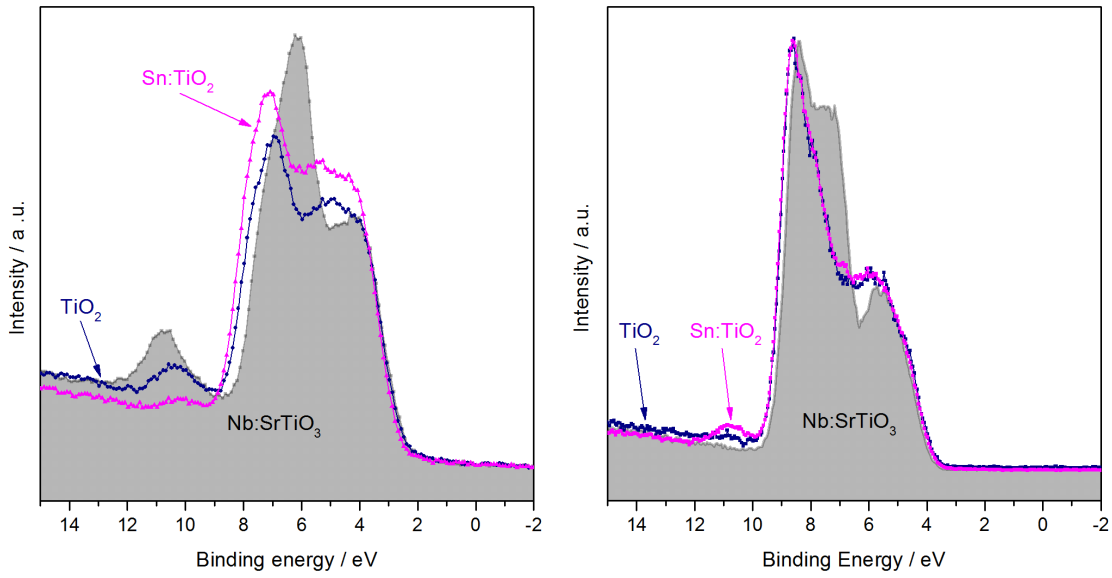


Figure 8.10: Valence band spectra for Nb:$SrTiO_3$, TiO_2, and Sn:TiO_2 measured with (a) conventional XPS and (b) HAXPES.

Figure 8.11 shows a wide view of the valence band, which also includes the Sr $4p$ and O $2s$ core lines. The Sn-doped sample shows the Sn $4d$ core levels. From previous measurements on Sn-doped TiO_2 conducted by the Egdell group, the Sn doping level in the thin films used here could be estimated to be approximately 1%.[21]

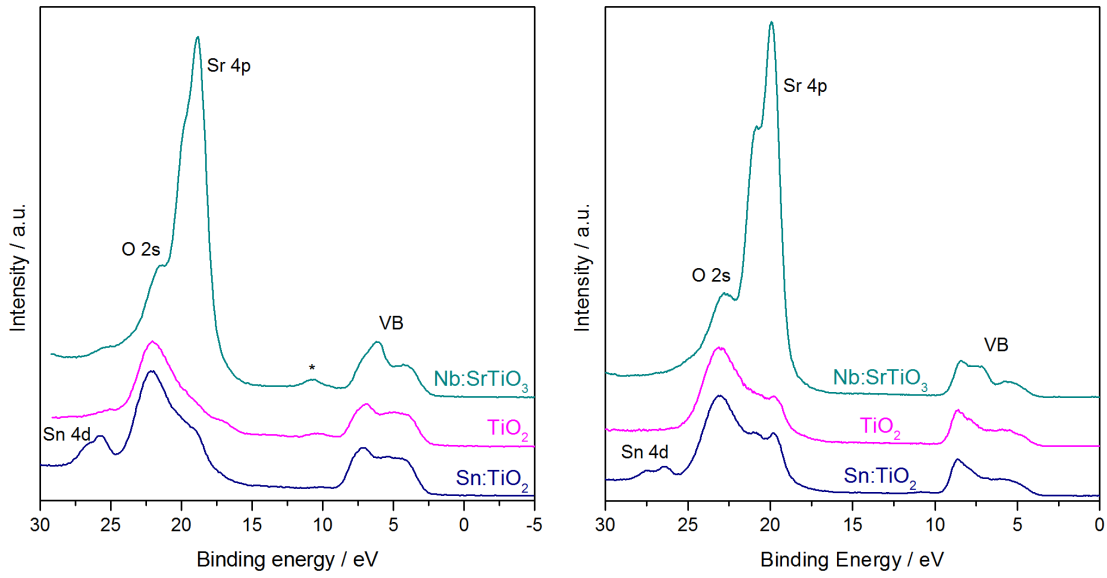


Figure 8.11: Valence band spectra for $Nb:SrTiO_3$, TiO_2, and $Sn:TiO_2$ measured with (a) conventional XPS and (b) HAXPES. * marks the hydroxide peak in the conventional XPS spectra.

8.4.4 Polarisation in Valence Band Spectra

Spectra of the Sn-doped TiO_2 thin film at two different electron optical geometries, horizontal and vertical, are shown in figure 8.12. In horizontal geometry, the angle between electron emission and the polarization vector of the synchrotron beam θ is 0°, whereas in vertical geometry θ is 90°. This causes a change in the differential (i.e. angle resolved) photoionisation cross sections and results in different relative intensities of orbitals in the XPS spectra.

Depending on the geometry, intensity appears above the bottom of the valence band. This is the state attributed to hybridisation between Sn $5s$ and O $2p$. Due to its predominantly s character, the peak mostly vanishes in vertical geometry.

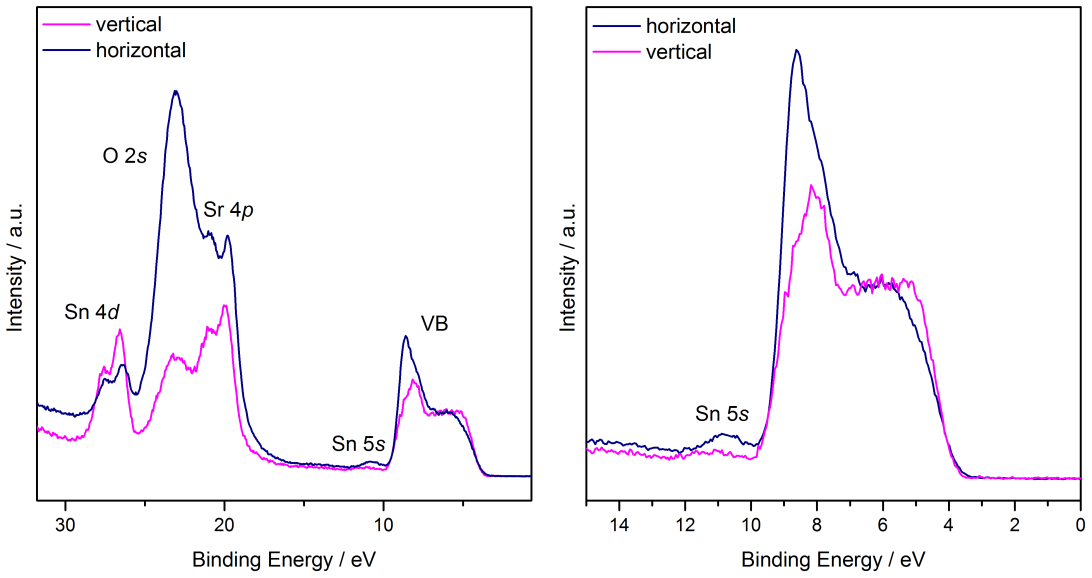


Figure 8.12: HAXPES spectra of the low binding energy region for a thin film of Sn:TiO_2. (a) shows the valence band (VB) and core levels up to a binding energy of 32 eV, (b) shows an expanded view of the valence band ans the Sn 5*s* state.

These experimental results were compared to density of state calculations prepared by Prof. G. Watson, Trinity College, Dublin. To correct for the difference in cross sections, subshell cross section values from Scofield[23] for 6 keV and 8 keV were divided by the number of electrons present, and interpolated for the actual experimental value of 6472 eV. From the following equation, which was first presented in chapter 2, we derived differential (i.e. angle resolved) cross sections from Scofield using asymmetry parameters calculated by Trzhaskovskaya *et al.*[48–50]

$$\frac{d\sigma_i}{d\Omega} = \frac{\sigma_i}{4\pi}\left[1 + \frac{\beta}{2}(3\cos^2\theta - 1) + (\delta + \gamma\cos^2\theta)\sin\theta\cos\varphi\right] \tag{8.1}$$

For both detectors, horizontal and vertical, φ is 90° leading the second angle dependent term to go to zero. For the horizontal geometry $\theta = 0°$ the cross section is multiplied by $1 + \beta$ and for the vertical geometry with $\theta = 90°$ the cross section is multiplied by $1 - \beta/2$. Values for β at 5 and 10 keV were taken from the work of Trzhaskovskaya *et al.*[48–50] These were then interpolated to an energy of 6472 eV to

be equivalent to the cross sections from Scofield.

The Scofield cross sections, beta values and the corrected cross sections are given in table 8.6. For Ti $4p$ the situation is slightly complicated as it is not occupied in the ground state of Ti. As an approximation the values for Ti $4s$ were divided by a factor of two.

Table 8.6: Cross sections from Scofield[23] σ_i, one electron cross sections σ_i/e^-, β values for 5 and 10 keV from Trzhaskovskaya *et al.*[48–50] and interpolated value for 6472 eV, and cross sections for horizontal $\sigma_i(hor)$ and vertical geometry $\sigma_i(ver)$.

orbital	σ_i	σ_i/e^-	β_{5keV}	β_{10keV}	β_{6472eV}	$\sigma_i(hor)$	$\sigma_i(ver)$
Ti $4s$	18.593	9.296	1.975	1.977	1.976	27.662	0.113
Ti $4p$	9.296	4.648				13.831	0.057
Ti $3d_{5/2}$	0.283	0.239	0.301	0.227	0.279	0.371	0.247
Ti $3d_{3/2}$	0.196		0.301	0.227	0.279		
O $2s$	31.558	15.779	1.953	1.963	1.956	46.642	0.348
O $2p_{3/2}$	0.705	0.266	0.148	0.062	0.123	0.299	0.250
O $2p_{1/2}$	0.359		0.136	0.083	0.121		
Sn $5s$	79.003	39.502	1.992	2.000	1.994	118.282	0.111
Sn $5p_{3/2}2$	19.889	15.975	1.474	1.257	1.410	38.501	4.712
Sn $5p_{1/2}$	12.060		1.474	1.257	1.410		
Sn $4d_{5/2}$	239.888	41.328	0.895	0.641	0.820	75.299	24.377
Sn $4d_{3/2}$	173.390		0.927	0.675	0.853		

The partial densities of state for Ti, O, and Sn in undoped and 1% Sn-doped TiO_2 in horizontal and vertical geometry are shown in figures 8.13 and 8.14.

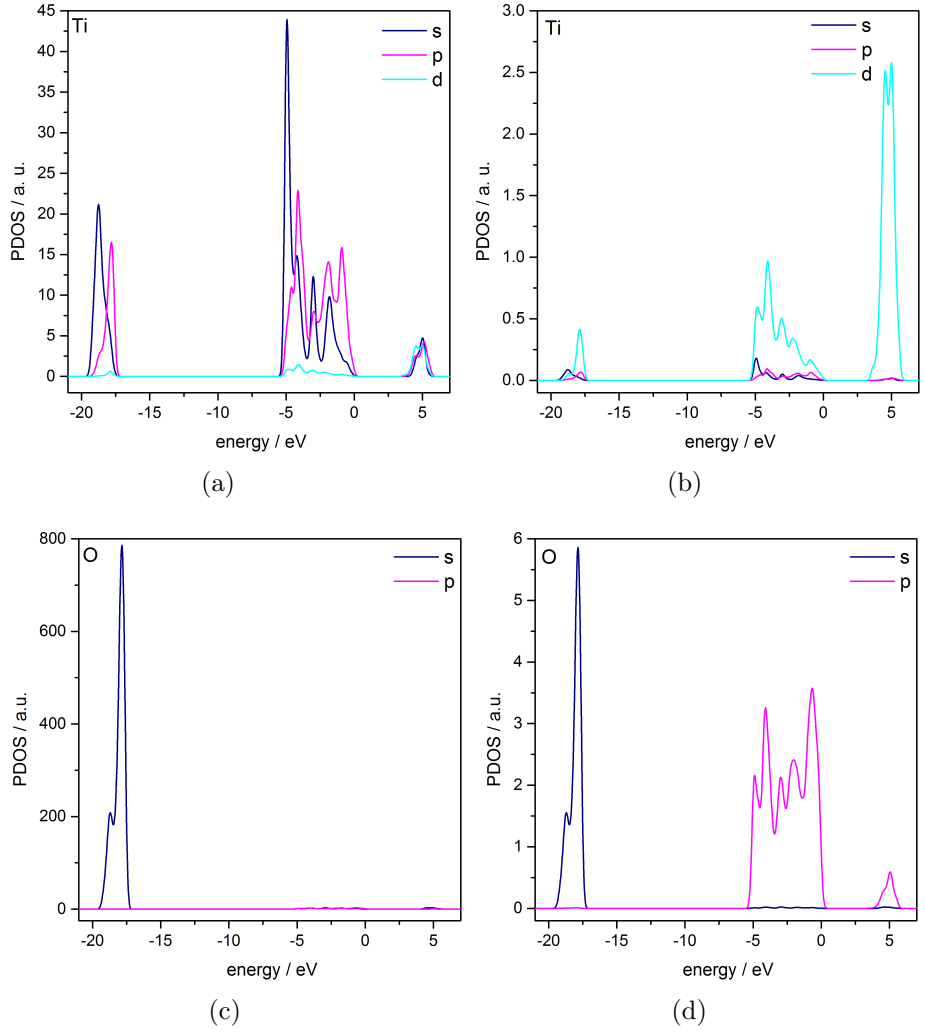


Figure 8.13: Partial densities of state for Ti and O in undoped TiO_2 in (a) and (c) horizontal and (b) and (d) vertical geometry.

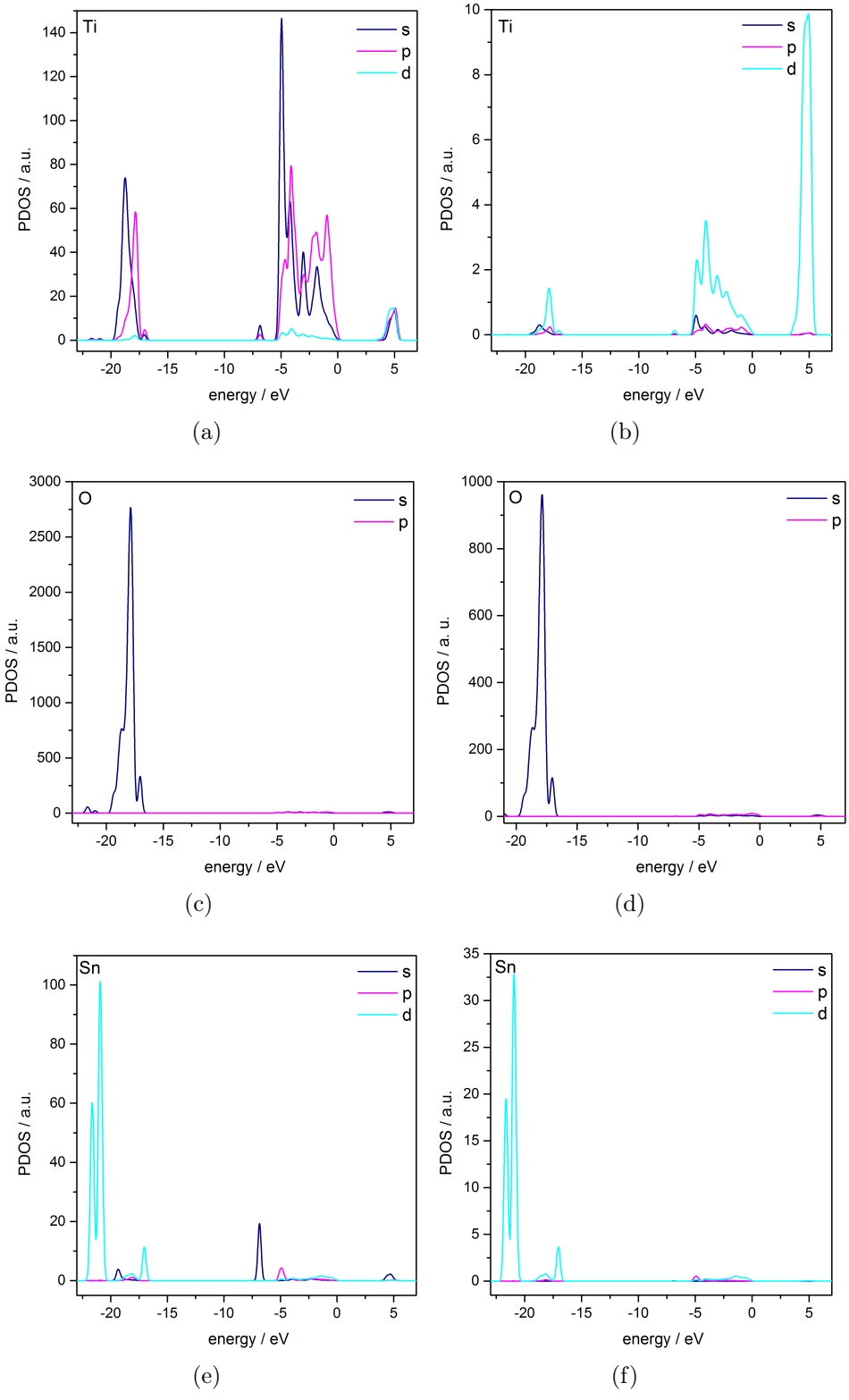


Figure 8.14: Partial densities of state for Ti, O, and Sn in 1% Sn-doped TiO_2 in (a), (c) and (e) horizontal and (b), (d), and (f) vertical geometry.

From the partial densities of state total densities of state for 1% Sn-doped TiO_2 were calculated (see figure 8.15). The calculated density of states fits the experimental data remarkably well.

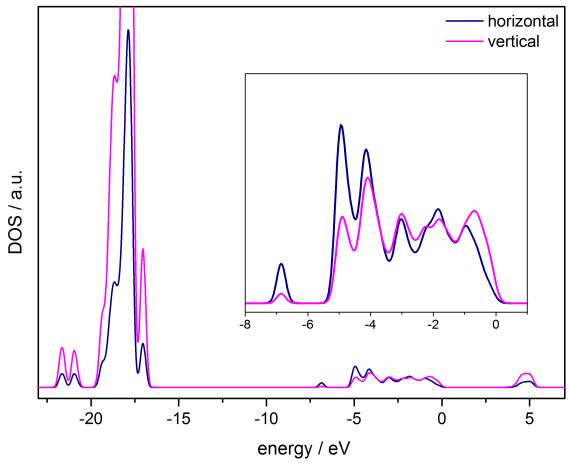


Figure 8.15: Calculated total densities of state for 1% Sn-doped TiO_2 in horizontal and vertical geometry.

The most apparent differences between horizontal and vertical geometry that are obvious in both experimental data and DOS calculations are as follows:

1. The relative intensity of the Sn 5s state is lower in the vertical geometry.
2. At the bottom of the valence band the intensity of the first two peaks changes, leading to the intensity maximum being at lower binding energy for vertical geometry compared to horizontal geometry.
3. At the top of the valence band the intensity on the vertical geometry increases.

8.5 Concluding Remarks

Three samples of TiO_2, Sn:TiO_2, and Nb:$SrTiO_3$ were analysed using soft and hard x-ray photoemission spectroscopy (HAXPES). Core levels were studied, in particular the satellites present around the Ti 2p and O 1s peaks, which was only possible due to the high quality of the HAXPES data.

It is shown that the peak above the bottom of the valence band can indeed be attributed to a Sn state, and is not due to hydroxide contamination of the surface.

Due to the special setup of the beam line at SPring-8, which has two analysers at different geometries, an in depth analysis of the valence band was possible. The resulting spectra were compared to DFT calculations by Prof. G. Watson. After correcting the density of states with the asymmetry parameters and different cross sections the data was in excellent agreement with the calculations.

8.6 References

[1] R. Asahi, T. Morikawa, T. Ohwaki, K. Aoki, and Y. Taga, Science **293**, 269 (2001).

[2] C. D. Valentin, E. Finazzi, G. Pacchioni, A. Selloni, S. Livraghi, M. C. Paganini, and E. Giamello, Chemical Physics **339**, 44 (2007).

[3] X. F. Qiu and C. Burda, Chemical Physics **339**, 1 (2007).

[4] C. D. Valentin, G. Pacchioni, A. Selloni, S. Livraghi, and E. Giamello, Journal of Physical Chemistry B **109**, 11414 (2005).

[5] S. Livraghi, M. C. Paganini, E. Giamello, A. Selloni, C. D. Valentin, and G. Pacchioni, Journal of the American Chemical Society **128**, 15666 (2006).

[6] F. Napoli, M. Chiesa, S. Livraghi, E. Giamello, S. Agnoli, G. Granozzi, G. Pacchioni, and C. D. Valentin, Chemical Physics Letters **477**, 135 (2009).

[7] S. Livraghi, A. Votta, M. C. Paganini, and E. Giamello, Chemical Communications **4**, 498 (2005).

[8] S. Livraghi, M. R. Chierotti, E. Giamello, G. Magnacca, M. C. Paganini, G. Cappelletti, and C. L. Bianchi, Journal of Physical Chemistry C **112**, 17244 (2008).

[9] Y. X. Zhao, X. F. Qiu, and C. Burda, Chemistry of Materials **20**, 2629 (2008).

[10] H. Irie, Y. Watanabe, and K. Hashimoto, Journal of Physical Chemistry B **107**, 5483 (2003).

[11] S. Klosek and D. Raftery, Journal of Physical Chemistry B **105**, 2815 (2001).

[12] R. Niishiro, H. Katoa, and A. Kudo, Physical Chemistry Chemical Physics **7**, 2241 (2005).

[13] R. Niishiro, R. Konta, H. Kato, W.-J. Chun, K. Asakura, and A. Kudo, Journal of Physical Chemistry C **111**, 17420 (2007).

[14] F. E. Oropeza and R. G. Egdell, Chemical Physics Letters **515**, 249 (2011).

[15] F. E. Oropeza, B. Davies, R. G. Palgrave, and R. G. Egdell, Physical Chemistry Chemical Physics **13**, 7882 (2011).

[16] W. R. Sinclair and T. C. Loomis, Angewandte Chemie **70**, 603 (1958).

[17] D. L. Drobeck, A. V. Virkar, and R. M. Cohen, Journal of the Physics and Chemistry of Solids **51**, 977 (1990).

[18] M. Radecka, K. Zakrzewska, and M. Rekas, Sensors and Actuators B **47**, 194 (1998).

[19] K. Reimann and M. Steube, Solid State Communications **105**, 649 (1998).

[20] M. H. Harunsani, F. E. Oropeza, R. G. Palgrave, and R. G. Egdell, Chemistry of Materials **22**, 1551 (2010).

[21] F. E. Oropeza, K. H. L. Zhang, R. G. Palgrave, A. Regoutz, and R. G. Egdell, Journal of Physical Chemistry C **117**, 15221 (2013).

[22] A. V. Krukau, O. A. Vydrov, A. F. Izmaylov, and G. E. Scuseria, Journal of Chemical Physics **125**, 224106 (2006).

[23] J. H. Scofield, Theoretical photoionization cross sections from 1 to 1500 keV, 1973.

[24] D. Morris, Y. Dou, J. Rebane, C. E. J. Mitchell, R. G. Egdell, D. S. L. Law, A. Vittadini, and M. Casarin, Physical Review B **61**, 13445 (2000).

[25] M. S. J. Marshall, D. T. Newell, D. J. Payne, R. G. Egdell, and M. R. Castell, Physical Review B **83**, 035410 (2011).

[26] K. Okada and A. Kotani, Journal of the Physical Society of Japan **61**, 4619 (1992).

[27] J. Park, S. Ryu, M.-S. Han, and S.-J. Oh, Physical Review B **37**, 10867 (1988).

[28] D. D. Sarma and A. Taraphder, Physical Review B **39**, 11570 (1989).

[29] J. Zaanen and G. A. Sawatzky, Physical Review B **33**, 8074 (1986).

[30] A. E. Bocquet, T. Mizokawa, T. S. A. H. Namatame, and A. Fujimori, Physical Review B **46**, 3771 (1992).

[31] B. Wallbank, C. E. Johnson, and I. G. Main, Journal of Physics C: Solid State Physics **6**, L340 (1973).

[32] B. Wallbank, C. E. Johnson, and I. G. Main, Journal of Physics C: Solid State Physics **6**, L493 (1973).

[33] I. Ikemoto, K. Ishii, H. Kuroda, and J. M. Thomas, Chemical Physics Letters **28**, 55 (1974).

[34] K. S. Kim and N. Winograd, Chemical Physics Letters **31**, 312 (1975).

[35] S. K. Sen, J. Riga, and J. Verbist, Chemical Physics Letters **39**, 560 (1976).

[36] H. Chermette, P. Pertosa, and F. M. Michel-Calendini, Chemical Physics Letters **59**, 240 (1980).

[37] Y. Tezuka, S. Shin, T. Ishii, T. Ejima, S. Suzuki, and S. Sato, Journal of the Physical Society of Japan **63**, 347 (1994).

[38] S. Larsson, Journal of Electron Spectroscopy and Related Phenomena **8**, 171 (1976).

[39] M. Braga and S. Larsson, International Journal of Quantum Chemistry **11**, 61 (1977).

[40] D. C. Frost, C. A. McDowell, and B. Wallbank, Chemical Physics Letters **40**, 189 (1976).

[41] J. A. Tossell, Journal of Electron Spectroscopy and Related Phenomena **8**, 1 (1976).

[42] J. A. Tossell, Chemical Physics Letters **65**, 371 (1979).

[43] V. der Laan G, Physical Review B **41**, 12366 (1990).

[44] D. K. G. de Boer, C. Haas, and G. A. Sawatzky, Physical Review B **29**, 4401 (1984).

[45] K. Okada, T. Ouzumi, and A. Kotani, Journal of the Physical Society of Japan **63**, 3176 (1994).

[46] A. E. Bocquet, T. Mizokawa, K. Morikawa, A. Fujimori, S. R. Barman, K. Maiti, D. D. Sarma, Y. Tokura, and M. Onoda, Physical Review B **53**, 1161 (1996).

[47] S. Kohiki, M. Arai, H. Yoshikawa, S. Fukushima, M. Oku, and Y. Waseda, Physical Review B **62**, 7964 (2000).

[48] M. B. Trzhaskovskaya, V. I. Nefedov, and V. G. Yarzhemsky, Atomic Data and Nuclear Data Tables **77**, 97 (2001).

[49] M. B. Trzhaskovskaya, V. I. Nefedov, and V. G. Yarzhemsky, Atomic Data and Nuclear Data Tables **82**, 257 (2002).

[50] M. B. Trzhaskovskaya, V. K. Nikulin, V. I. Nefedov, and V. G. Yarzhemsky, Atomic Data and Nuclear Data Tables **92**, 245 (2006).

9 A Sol-Gel Approach to Growth of In_2O_3 Thin Films

9.1 Introduction

Following on from the growth of In_2O_3 epitaxial thin films using molecular beam epitaxy (MBE), and the sol-gel dip-coating method developed for TiO_2, the next step was to combine the approaches from both to attempt a sol-gel dip-coating approach for the growth of nanostructured epitaxial In_2O_3 thin films.

As described in chapter 4, the orientation of the Y-stabilised cubic zirconia, $Zr_{1-x}Y_xO_{2-x/2}$ or YSZ, substrate has a critical influence on the growth morphology of the In_2O_3. Whilst (110) substrates result in nano rods, (100) substrates show square islands. Here, the sol-gel method was employed to grow In_2O_3 thin films both on YSZ (110) and (100). The amount of In_2O_3 deposited in "limited dip" sol-gel dip-coating is significantly lower compared to MBE with film thicknesses expected to be in the range of a few nm. The low deposition rates are mainly due to comparatively dilute precursor solutions which become necessary due to the instability of the precursor towards premature hydrolysis.

Laboratory-based X-ray diffraction could not be used to characterise the samples

due to the the almost vanishing intensity of epilayer reflections close to substrate Bragg peaks. Here we use reciprocal space maps from synchrotron-based XRD in combination with AFM results to study the nanostructured thin films.

9.2 Experimental

Thin films of In_2O_3 were grown via a sol-gel dip-coating method based on the previously developed method for TiO_2. 30 mL of the precursor solutions were prepared under N_2 atmosphere in a glove box to prevent premature hydrolysis of the indium precursor. A solution of In(III)isopropoxide (5 % (w/v) solution in isopropanol, $\geq$99.9%, supplied by Sigma-Aldrich Inc.) in 2-propanol with a propoxide concentration of 0.1 mol/L was also prepared. The concentration was kept lower, compared to the TiO_2 precursor, as the indium precursor is less stable, but can be acceptably stabilised at lower concentrations. It must be noted that the shelf life of the indium solution lies under 24 hours, compared to a few days for the titanium based solutions.

The precursor solution was immediately removed from the glove box and transferred into a wide necked round bottom flask for the dip-coating. Single crystal YSZ (110) and (100) substrates were cleaned with 2-propanol and dried under N_2 flow. The substrates were then dipped into the solution and held stationary for one minute, after which they were withdrawn from the solution at a removal speed of 0.35 cm/min. Thereafter, they were hydrolysed in a stream of wet nitrogen gas for five minutes. This process was repeated until the desired number of dips was reached. The number of dips varied between two and eight.

Dip-coated samples were placed in recrystallised alumina boats and annealed at

1000°C in a muffle oven for five hours. The cooling down rate for all experiments was set at 5°C per minute.

AFM in combination with synchrotron-based reciprocal space mapping was used to characterise the samples. XRD was conducted on beam line I16 at the Diamond Light Source, Didcot, UK. Data were acquired using a Pilatus 100K area detector with the long axis of the detector in the scattering plane. Images for construction of 3D data sets were collected in a single θ scan which ensured variation in both longitudinal and transverse wavevector transfer within the scattering plane. As in chapter 7, a series of images was used to construct an evenly spaced mesh of points of intensity as a function of h, k, l, and in some cases these data were used to construct 3D isosurfaces, with processing and visualisation using a Matlab code written by Prof. S. Collins. Unfortunately, the Matlab code was only available remotely and processing a single data set took several hours. It was therefore found to be more informative and efficient to present the data simply using the 2D image plate frame capturing maximum intensity in the scattering after conversion of the data from pixel coordinates into 3D reciprocal space.

9.3 Results and Discussion

9.3.1 Influence of the Substrate on Surface Morphology of Thin Films of In_2O_3

As found on MBE grown samples, the orientation of the YSZ substrate determines the surface morphology of the thin films. Due to the low precursor concentration used for the sol-gel dip-coating, the size of the structures drops significantly. Nanorods grown on YSZ (110) at 1000°C using MBE have a length of up to 15 μm,

whilst sol-gel dip-coating grown nanorods have lengths of approximately 190 nm and widths of below 50 nm. Islands grown on YSZ (100) with MBE at 900°C have side lengths of 1 μm, whilst sol-gel dip-coating islands grown at 1000°C have sides which are approximately 125 nm long. Figure 9.1 shows two AFM images of nanorods and islands grown via sol-gel dip-coating which are representative for all samples grown.

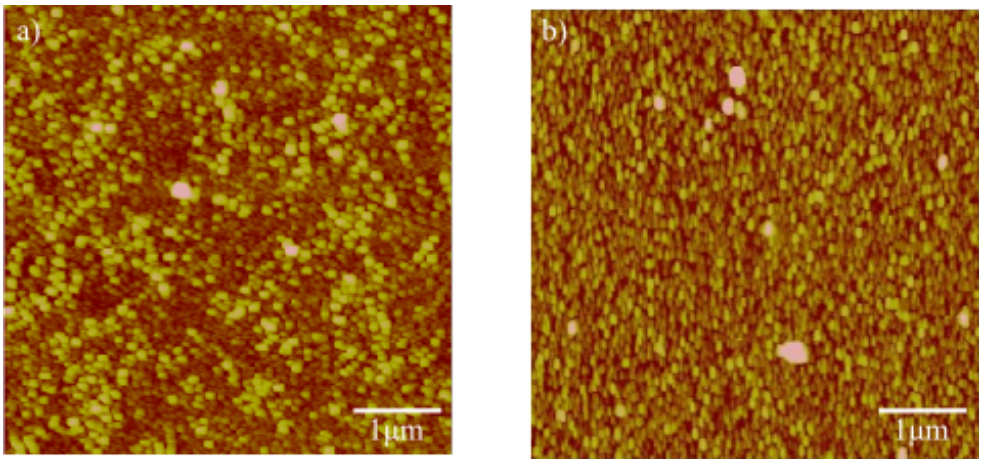
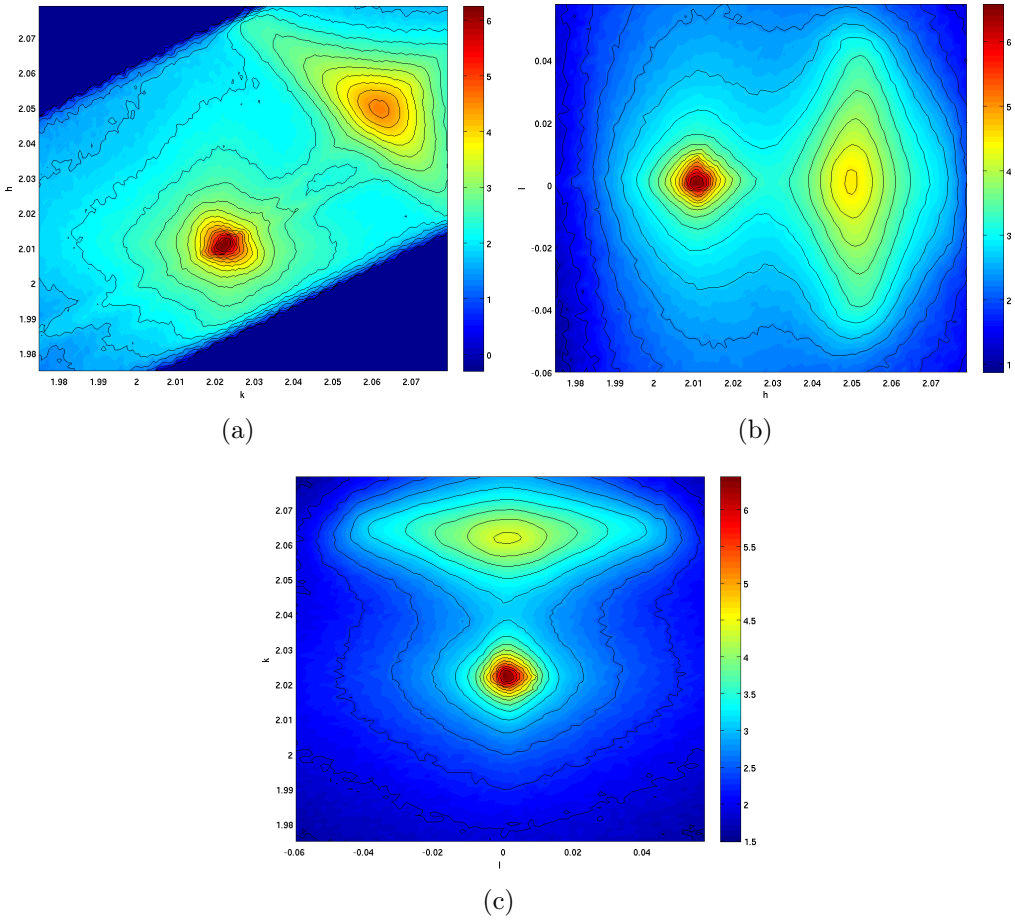


Figure 9.1: AFM images of In_2O_3 nano structures on (a) (100) and (b) (110) YSZ.

9.3.2 Reciprocal Space Maps of Thin Films Grown on YSZ (110)

Prior to measuring the sol-gel dip-coated sample, a molecular beam epitaxy prepared sample of In_2O_3 on YSZ (110) was investigated. Reciprocal space maps of this sample are shown in figures 9.2 and 9.3. The two dimensional maps in figure 9.2 show the (440) thin film reflection in close proximity to the more intense (220) substrate reflection. The thin film Bragg reflection is elongated along the l direction, corresponding to the transverse [001] direction perpendicular to the long axis of the rods.



(a) (b)

(c)

Figure 9.2: 2D reciprocal space maps around the (440) reflection of an MBE-grown In_2O_3 epitaxial thin film. The second, brighter signal stems from the substrate (220) reflection. h, k, and l are given in reciprocal lattice units of the substrate.

Figure 9.3 shows the very weak (220) film reflection which has no nearby substrate Bragg peak, and is also elongated in l. The (220) reflection is 400 times weaker than the (440) reflection as shown in laboratory-based X-ray diffraction (see figure 4.9). This reflection was used to give isosurfaces of the Bragg reflection in three dimensions (see figure 9.4). As observed in both (440) and (220) reflections, an elongation in l is present.

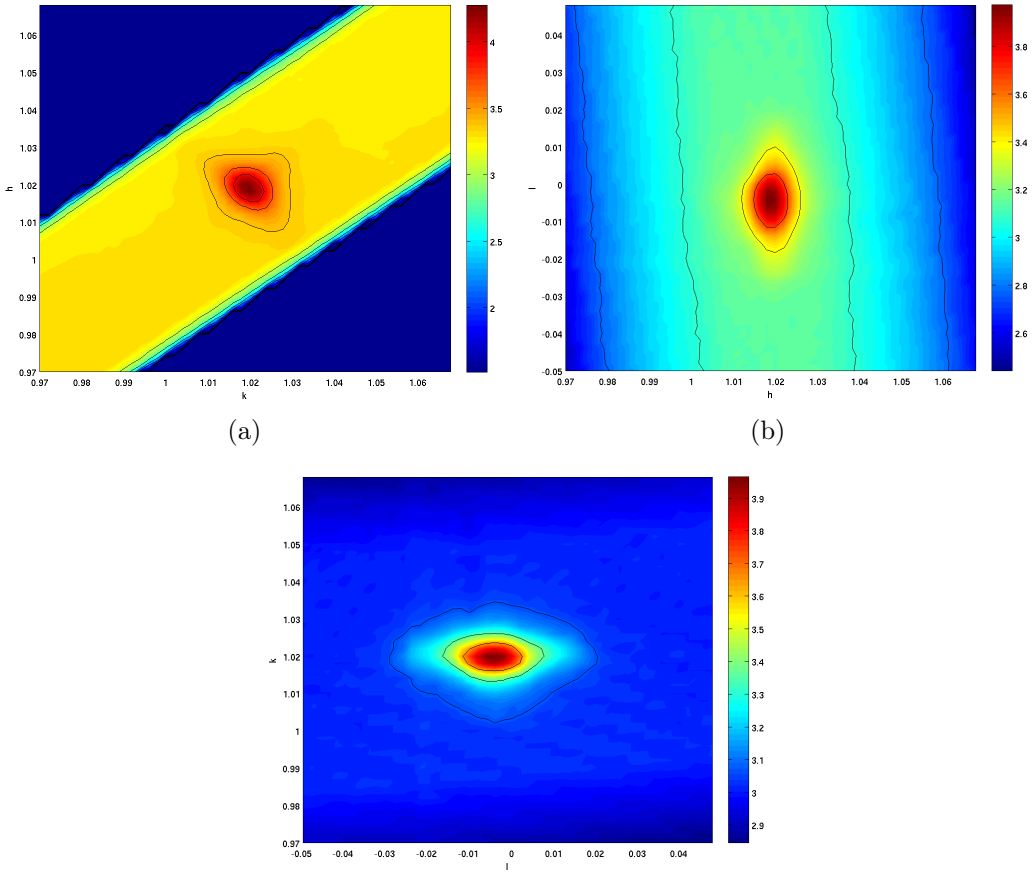
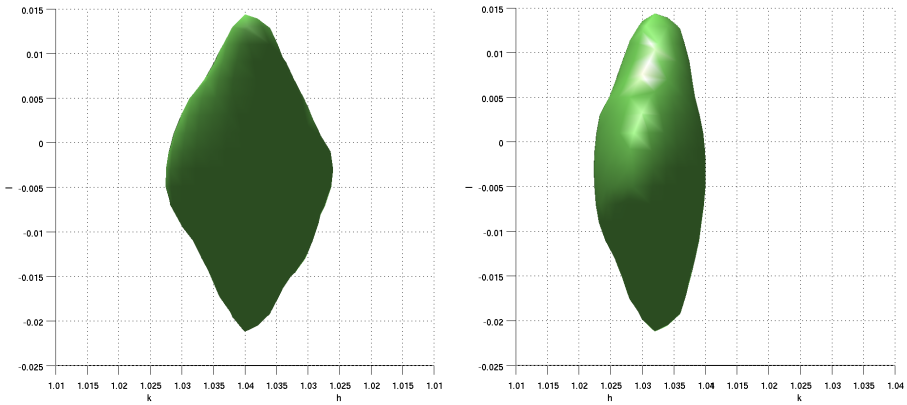
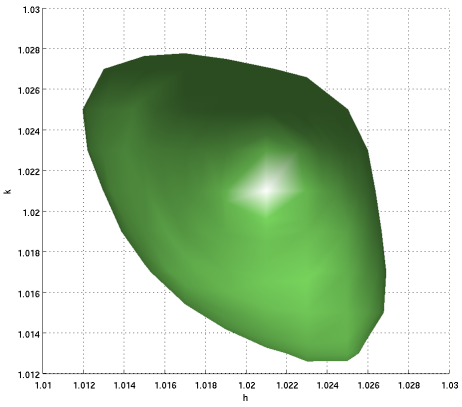


Figure 9.3: 2D reciprocal space maps around the (220) reflection of an MBE-grown In_2O_3 epitaxial thin film. h, k, and l are given in reciprocal lattice units of the substrate.



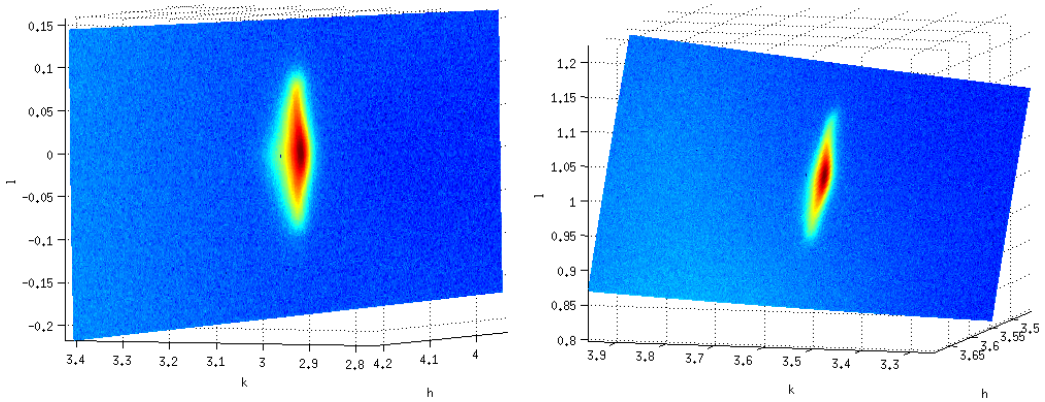
(a) (110) (b) $(1\bar{1}0)$



(c) (001)

Figure 9.4: Isosurfaces of the (220) reflection of an MBE-grown In_2O_3 epitaxial thin film. h, k, and l are given in reciprocal lattice units of the substrate.

Unfortunately the (220) reflection was too weak to allow acquisition of data from sol-gel grown samples, but it was possible to confirm film growth of In_2O_3 by locating off-specular (860) and (772) reflections where transverse wave vector transfer is along $[1\bar{1}0]$ and [001] directions respectively. These off-specular reflections for the MBE grown sample are shown in figure 9.5.



(a) (860) (b) (772)

Figure 9.5: 2D reciprocal space maps around the (a) (860) and (b) (772) reflections of an MBE-grown In_2O_3 epitaxial thin film. h, k, and l are given in reciprocal lattice units of the substrate.

Reciprocal space maps for two sol-gel samples taken around the epilayer (860) and (772) reflections are shown in figure 9.6. Both samples were grown on YSZ (110) which were dipped into the precursor solution two and seven times respectively. The reciprocal space maps clearly show the Bragg peak from the thin film, with the thicker seven-dip sample showing an elongation along l comparable to the MBE-grown sample. In comparison, the thinner two-dip sample shows an almost circular diffraction spot consistent with the non-elongated real space morphology. The diffuse intensity on the left of all four maps stems from the substrate.

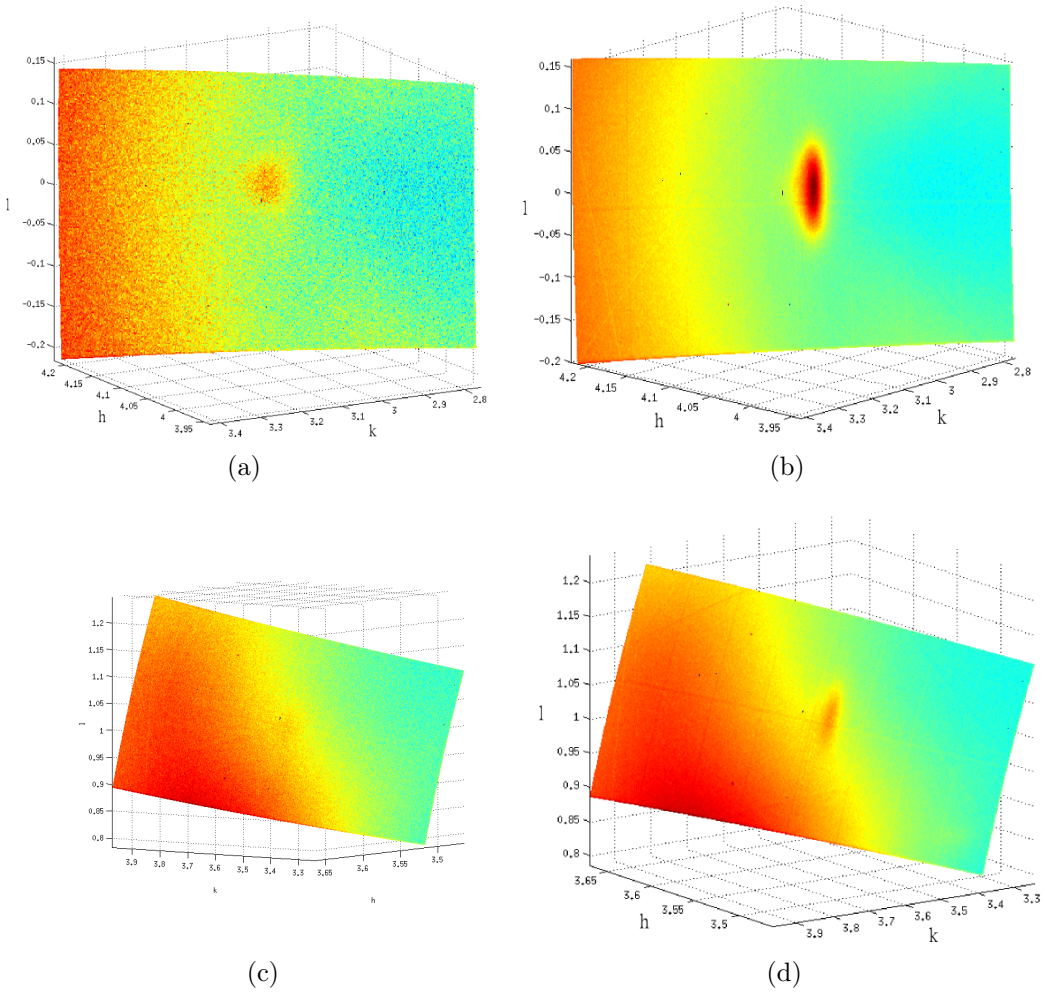


Figure 9.6: Reciprocal space maps around the (a) and (b) (860), and (c) and (d) (772) reflection of the In_2O_3 epilayer of (a) and (c) a two-dip, and (b) and (d) a seven-dip sample on YSZ (110).

From the reciprocal space maps the coordinates of the maximum intensity of the thin film reflection were extracted. They are summarised in table 9.1.

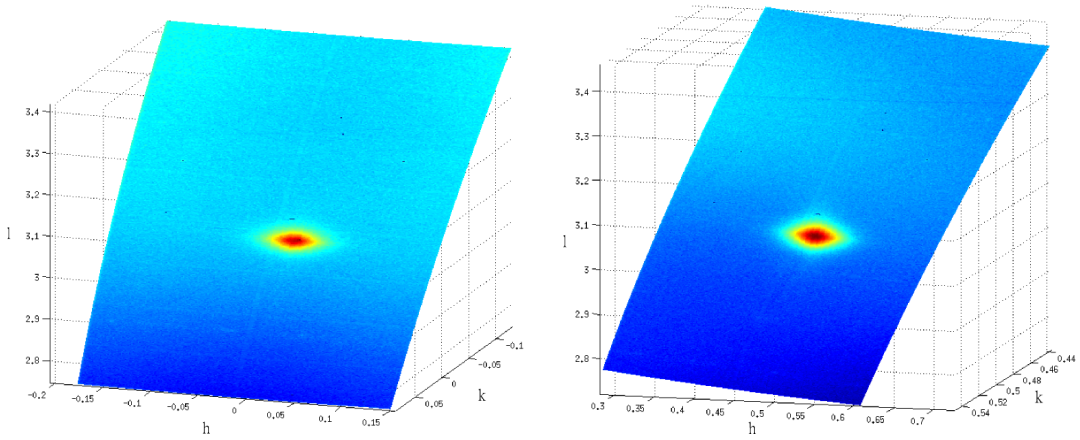
Table 9.1: Coordinates of the point of maximum intensity from the epilayer in the reciprocal space maps of In_2O_3 grown on YSZ (110) and coordinates of the bulk reflection. h, k, and l are given in lattice units of the substrate and are subject to an uncertainty of ± 0.002. 2d and 7d refers to two and seven dip samples, respectively.

sample	hkl_{refl}	hkl_{bulk}	h	k	l
2d	(860)	(4.067 3.050 0)	4.089	3.083	0.018
	(772)	(3.559 3.559 1.017)	3.575	3.586	1.002
7d	(860)	(4.067 3.050 0)	4.073	3.045	0.001
	(772)	(3.559 3.559 1.017)	3.567	3.556	1.006

The non-zero l values for the (860) reflection may reflect misalignment or possibly tilt in the epilayer. The lattice parameters indicate a small contraction of the epilayer lattice spacings in h and k directions and an elongation in l for the two-dip sample.

9.3.3 Reciprocal Space Maps of Thin Films Grown on YSZ (100)

As well as samples grown on YSZ (110), thin films on YSZ (100) were prepared and investigated by synchrotron-based XRD. Figure 9.7 shows reciprocal space maps of the (006) and (116) reflection of the In_2O_3 epilayer of a six-dip sample. Here, the epilayer peak is slightly elongated in h.



(a) (b)

Figure 9.7: Reciprocal space maps around the (a) (006) and (b) (116) reflection of the In_2O_3 epilayer of a six dip sample on YSZ (100).

The coordinates of the maximum intensity of the thin film reflection were extracted from the reciprocal space maps, which are summarised in table 9.2. For both reflections the l values are slightly increased in comparison to values expected for unstrained In_2O_3, and a small displacement in h and k from zero for the (006) reflection is indicative of either tilt or misalignment.

Table 9.2: Coordinates of the point of maximum intensity from the epilayer in the reciprocal space maps of In_2O_3 grown on YSZ (100) and coordinates of the bulk reflection. h, k, and l are given in lattice units of the substrate and are subject to an uncertainty of ± 0.002. 6d refers to the six dip sample.

sample	hkl_{refl}	hkl_{bulk}	h	k	l
6d	(006)	(0 0 3.050)	0.003	0.002	3.052
	(116)	(0.508 0.508 3.050)	0.513	0.511	3.051

9.4 Concluding Remarks

Based on the results of TiO_2 thin films, it has been possible to show growth of In_2O_3 thin films via the sol-gel dip-coating process. Due to the increased reactivity of the indium precursor, the solution had to be diluted, leading to very thin films. Al-

though AFM images showed the expected nanorods and islands as have previously been observed on MBE grown samples, the laboratory-based XRD could not give a diffraction pattern.

Therefore, synchrotron-based XRD was used, which showed diffraction spots for all three investigated samples and consequently provided proof for the growth of epitaxial crystalline thin films.

10 Conclusions

This thesis aims to further the understanding of fundamental characteristics of some of the most widely used oxides. A wide range of characterisation methods has been employed, including a number of synchrotron-based experiments covering reciprocal space mapping, and soft and hard X-ray photoelectron spectroscopy. Furthermore a new approach to the growth of high quality thin films is presented. It is shown that sol-gel dip-coating can produce epitaxial, highly ordered thin films. A brief summary of the work completed is presented below.

Chapter 4 connects to previous research performed by the Egdell group and in many ways presents the motivation for the research presented in this thesis.[1–5] In_2O_3 thin film and nanostructured samples, grown on (111) and (110) YSZ substrates by MBE, were investigated using reciprocal space mapping in conjunction with AFM.[6] The primary focus lay on strain in the thin films, and Poisson ratios were determined. In addition, an explanation of the growth of nanorods on YSZ (110), based on minimisation of surface and interface energies, was presented.[7]

Chapters 5 and 6 investigated doping of In_2O_3 with gallium and thallium in bulk samples. Ga is shown to reduce the band gap of In_2O_3 significantly through diffuse reflectance spectroscopy and X-ray photoemission spectroscopy (XPS). A pronounced surface segregation of gallium is shown in XPS and low energy ion scattering

(LEIS). In the case of thallium doping calculations by Dr. D. O. Scanlon showed a significant decrease in the band gap and subsequently provided the motivation to investigate this system. Due to the health and safety risks associated with thallium and its compounds analysis was restricted compared to the Ga-doped system. Nevertheless, it could be shown that the band gap did decrease as predicted, and significant surface segregation of the dopant was observed.[8]

Chapter 7 introduces the problem of high quality growth of metal oxide thin films. MBE is a highly sophisticated method which leads to epitaxial thin films or nano structures that are of very high quality, as presented in Chapter 4. However, it can be time consuming, and due to the necessary ultra high vacuum systems the experimental effort can be substantial. One of the set goals for this research was to develop a sol-gel dip-coating method which could compete with MBE prepared samples. To achieve this, the TiO_2 system was investigated first and, based on earlier experiments by Dr. F. E. Oropeza in the Egdell group, a design of experiments approach was selected.[9] Ideal growth conditions were identified and the resulting epitaxial thin films of anatase TiO_2 were investigated using laboratory- and synchrotron-based X-ray diffraction (XRD), where well resolved Laue or Pendellösung fringes were observed. 3D reciprocal space maps were prepared which present an extended view of the thin film Bragg reflections, including these fringes and truncation rods. Furthermore, strain caused by an increase in temperature was investigated using synchrotron-based XRD. Whilst $SrTiO_3$ substrates resulted in the described anatase films, R-plane Al_2O_3 substrates used in the same sol-gel solution lead to rutile thin films.

Chapter 7 concludes with the introduction of Sn-doping of TiO_2, and Chapter 8 follows up with the investigation of doped and undoped samples using soft and hard

X-ray photoelectron spectroscopy. It was confirmed that intensity at the bottom of the valence band which was previously observed, does present a Sn state and not hydroxide contamination.[10] HAXPES measurements were able to show the satellite structures on Ti $2p$ and O $1s$ core levels at very high resolution. An in-depth analysis of the valence band at two different HAXPES geometries was shown and compared to density of state calculations.

Chapter 9 closes the circle by presenting In_2O_3 thin films prepared by the new sol-gel dip-coating method. As the films were extremely thin, synchrotron-based 2D reciprocal space maps were collected which show the Bragg peaks from the epitaxial films. AFM images showed the same type of nano structures as observed on MBE grown sample although on a much smaller scale.

From this thesis two major avenues for future work present themselves. Firstly, the results from bulk Ga-doped In_2O_3 in combination with the knowledge regarding the effects of strain on In_2O_3 thin films could be employed to investigate such effects in Ga-doped In_2O_3 thin films. Secondly, the developed sol-gel method could be extended to other metal oxide systems and substrates.

10.1 References

[1] K. H. L. Zhang *et al.*, Chemistry of Materials **21**, 4353 (2009).

[2] K. H. L. Zhang *et al.*, Nano Letters **10**, 3740 (2010).

[3] K. H. L. Zhang *et al.*, Journal of Physics: Condensed Matter **23**, 334211 (2011).

[4] K. H. L. Zhang *et al.*, Physical Review B **84**, 233301 (2011).

[5] K. H. L. Zhang *et al.*, ACS Nano **6**, 6717 (2012).

[6] A. Regoutz, K. H. L. Zhang, R. G. Egdell, D. Wermeille, and R. A. Cowley, Journal of Materials Research **27**, 2257 (2012).

[7] A. Regoutz, R. G. Egdell, D. Wermeille, R. A. Cowley, and K. H. L. Zhang, Nanoscale **5**, 7445 (2013).

[8] D. O. Scanlon, A. Regoutz, R. G. Egdell, D. J. Morgan, and G. W. Watson, Applied Physics Letters **103**, 262108 (2013).

[9] F. Oropeza *et al.*, Crystal Growth & Design **13**, 1438 (2013).

[10] F. E. Oropeza, K. H. L. Zhang, R. G. Palgrave, A. Regoutz, and R. G. Egdell, The Journal of Physical Chemistry C **117**, 15221 (2013).